Temporal Dynamics of Early Brain Activity Explored using EEG and Computational Models

Caroline Hartley

Centre for Mathematics and Physics in the Life Sciences and Experimental Biology (CoMPLEX)

University College London

A thesis submitted for the degree of Doctor of Philosophy.

I, Caroline Hartley confirm that the work presented in this thesis is my own. Where information has been derived from other sources, I confirm that this has been indicated in the thesis.

Abstract

This thesis considers the temporal structure of burst dynamics in early brain activity through the analysis of human very preterm electroencephalograph (EEG) recordings and computational neural network models.

A novel algorithm for the detection of the discontinuous bursts of activity in the preterm EEG is developed and the temporal structure of burst occurrence, size and duration are assessed. The dynamics are shown to exhibit long-range temporal correlations (LRTCs) indicating a temporal complexity within early brain activity not previously appreciated. This result is replicated in a larger population of preterm children and the effect of gestational age and postnatal age on the degree of LRTCs is examined.

A possible mechanism underlying the generation of burst activity that exhibits LRTCs is investigated in a stochastic excitatory neural network model. It is shown that burst dynamics occur in the model when there is a balance between the activity of an individual neuron and the number of neurons it in turn activates. Furthermore, it is shown that correlations in the temporal statistics of these bursts exist over a wide range and extend across an infinite range in the limit of system size. The behaviour of the model with respect to different network topologies is also investigated.

In summary, it is shown that complex temporal dynamics exist even in early brain activity and such dynamics can be observed in a simple model. In light of this, the evidence that the brain exhibits self-organised criticality - a theoretical framework suggested by previous authors as an explanation for LRTCs in a systems dynamics - is discussed. Overall, the observation of complex temporal structure of activity in the early developing brain suggests that the temporal organisation of this activity may play an important developmental role. This thesis therefore provides strong motivation for future work in this area.

Acknowledgements

First and foremost I would like to thank my supervisors, Luc Berthouze and Simon Farmer, for their enthusiasm, encouragement and guidance. I would also like to thank my collaborators at University College Hospital London: Neil Marlow, Sean Mathieson and Janet Rennie; at the University of Oslo: Tom Stiris, Eva Schumacher and Pål Larson; and at University College Cork: Geraldine Boylan, who recorded and provided the EEG data sets. Also Istvan Kiss and Timothy Taylor at the University of Sussex and Maria Botcharova and Nick Ward at University College London.

Additionally I would like to thank the patients and their parents for their cooperation in this research. Finally, I would also like to acknowledge my departments - Faraneh Vargha-Khadem and the DCNU; and CoMPLEX as well as their funding bodies (including the EPSRC and BHF) without which this work would not have been possible.

†

Contents

List of Abbreviations

ANOVA ... Analysis of variance

BNOs ..... Burst of nested oscillations

DFA ..... Detrended fluctuation analysis

EEG ..... Electroencephalograph

EMG ..... Electromyograph

FGN ..... Fractional Gaussian noise

fMRI ..... Functional Magnetic Resonance Imaging

GA ..... Gestational age

GABA ..... γ-Aminobutyric acid

IAI ..... Inter-avalanche interval

IBI ..... Inter-burst interval

IEI ..... Inter-event interval

IVH ..... Intra-ventricular haemorrhage

LRTCs ..... Long-range temporal correlations

MDI ..... Mental development index

MEG ..... Magnetoencephalograph

MRI ..... Magnetic Resonance Imaging

PDI ..... Psychomotor development index

SATs ..... Spontaneous activity transients

SOC ..... Self-organised criticality

SOqC ..... Self-organised quasi-criticality

TMQ ..... Total motor quotient

List of Figures

List of Tables

Chapter 1

Introduction

The brain allows us to perform complex motor actions, interact with our environment with speed and accuracy, remember facts and autobiographical events, and internally generates our perceptions. Like all other organs it is a collection of cells, yet the combined properties of these cells gives rise to the complex functions needed for everyday life. How the brain achieves this is still poorly understood. However, normal brain function can only be achieved as a product of the brain's development. To fully understand adult brain functioning, both in health and disease, we must understand how the brain develops.

Brain development is itself a complex process worthy of study. Early in development cells must be generated, migrate to their correct position and make functional connections with other neurons. Indeed, in the most part, neurons are not replaced throughout the life of the animal (including humans)[1] and so the early developmental period is vital for the later functioning of the brain. The early developing brain is also crucially different when compared with the adult brain: before full-term birth the nervous system has altered neurotransmitter effects, with GABA (γ-Aminobutyric acid - the main inhibitory neurotransmitter in the more mature brain) having a depolarising effect on postsynaptic neurons [2–5]. Furthermore, thalamic axons do not project directly to the cortex but form synapses with a transient population of neurons known as the subplate [6–10]. The subplate neurons in turn form synaptic connections with cortical neurons, creating a pathway for sensory input which is unique to the early developmental period.

In addition to genetic factors, activity-dependent mechanisms play a critical role during the early developmental period [11, 12] and continue to occur long after birth, with synaptic pruning lasting into adolescence [13] and plasticity mechanisms persisting

[1] Exceptions include evidence of adult neurogenesis in the olfactory bulb and dentate gyrus as well as tentative evidence in other areas including the neocortex [1].

throughout life [14]. It is this activity-dependence, meaning that the brain is not pre-programmed and deterministic, which importantly allows the brain to adapt in relation to the external environment. A well studied example of activity-dependence in the developing brain is that of retinal waves. Several weeks before eye opening (and sensory driven activity occurs) mammalian retinal ganglion cells have been shown to fire spontaneously as bursts of neuronal activity that are correlated with neighbouring cells and spread as waves across the retina [11, 15–17]. These waves are thought to drive the formation of eye-specific layers in the lateral geniculate nucleus of the thalamus which are formed before eye opening [11, 18]. Similar examples of correlated spontaneous activity, and the advantageous effect it has on connectivity formation, has also been observed in the spinal cord [19–21] and between motoneurons and muscles [22]. The cerebral cortex exhibits spontaneous activity *in vitro* [23] and electrophysiological recordings *in vivo* of local field potentials in early developing rats have revealed spontaneous synchronous bursts of activity which have also been suggested as critical for connectivity formation [24, 25].

Despite the fact that activity dependence is crucial for normal brain development, relatively little is understood about the activity in the early human nervous system compared with the extensive analysis that has been carried out of adult nervous system dynamics. The EEG (electroencephalograph) of premature human neonates provides a unique opportunity as a 'window into the brain' during very early development. In stark contrast to the normal EEG later in life, preterm EEG is discontinuous with activity occurring in bursts [26–28]. These bursts are thought to be a result of spontaneous activity endogenously generated in the nervous system as well as external sensory input [29, 30]. Extensive analysis of this activity will be crucial in understanding the activity-dependent development of the human brain.

The temporal organisation of activity plays a role in the adult brain, for example in plasticity mechanisms [31] and the coordinated functioning of different brain areas [32–34]. Moreover, as has been discussed, temporal organisation of activity is important in the developing brain in, for example, the temporal correlations of the wave patterning formed by synchronous firing in the retina. As this is the case it seems possible that the temporal organisation of the bursts themselves may also be important in the developing brain (i.e. the order in time of the bursts and not just the correlated firing within the burst itself). However, there has been no thorough investigation of the temporal organisation of activity in the preterm EEG. The length of the EEG recordings in preterm subjects (up to 72 hours [35]) provide a wealth of information with which to investigate this question.

Before embarking on analysis of this type it is useful to consider whether what is known about the temporal dynamics of the adult brain can guide us in our analysis of preterm brain activity. The EEG of the adult brain is characterised by oscillatory activity at

different frequencies. Theoretically it has been proposed that to react to the external environment in an efficient manner the (fully developed) brain must in some way be optimal. But what is meant by 'optimal' and how is optimality achieved? In physical systems theory, systems which exhibit *power-law* dynamics (defined and discussed in more detail below) have been shown to exhibit an optimal wide dynamic range [36–38]. This means that the system is able to differentiate - with different output responses - the most (i.e. widest) number of different input stimuli when compared with systems which are perturbed away from this dynamic state. When the system's parameters are such that power-law dynamics are not observed then the system is less able to distinguish between stimuli (for example two large input stimuli may both lead to the same indistinguishable saturated response) and so the system has a reduced dynamic range [38]. Power-law dynamics have been observed in the fluctuations of oscillation amplitude in human EEG and MEG (magnetoencephalograph) [39–45]. More specifically, power-law dynamics are exhibited by the *temporal organisation* of the amplitude of oscillations. Power-law dynamics have also been observed in the human brain in synchronisation measures of resting state fMRI (functional magnetic resonance imaging) [46], in intracranial-EEG recordings [47] and in inter-spike intervals [48]. Additionally, a number of *in vitro* and *in vivo* experiments have shown that neuronal firing can occur in cascades known as neuronal avalanches [49–54] and that these neuronal avalanches exhibit power-law distributions of avalanche sizes. Thus, power-law dynamics appear to be present at many different scales from local neuronal firing through to large population measures.

If adult nervous system dynamics appear to be optimal and exhibit power-laws, what does this mean for the developing brain? A number of theoretical frameworks have been proposed to explain how power-law dynamics arise [55–58]. The most influential of these, in terms of interest in the literature, is *self-organised criticality* (SOC) [55, 59]. SOC systems will self-organise without any external tuning (i.e. without any pre-programmed 'hard-wired' dynamics) to a 'critical' state (explained in detail below) at which, even though the interaction between elements is simple and short-range (i.e. interactions are between neighbouring elements only), long-range spatiotemporal interactions with power-law distributions emerge [55, 56, 60]. The observation of power-law dynamics in neuronal systems has led to the hypothesis that the brain is a SOC system [39, 49, 60]. While this might seem an attractive proposition, since the system will achieve its optimal state without the need for an external driving or tuning, there is very little evidence to suggest that this is the case [54]. A number of alternative modelling approaches have shown that (apparent) power-law distributions can occur through other mechanisms that are just as plausible [57, 61, 62]. It may well be that one of these paradigms is more applicable to the brain. Further evidence is required to determine which of these paradigms (or an alternative) correctly describes brain dynamics. If the brain is a SOC system then a period of self-organisation would be

expected to occur. Indeed, models which exhibit SOC do display a period of self-organisation during which they do not exhibit power-law dynamics. Thus, a key question is whether there is evidence for self-organisation during brain development, i.e. at what stage in brain development do critical dynamics emerge?

At present only a small number of investigations have examined the occurrence of power-laws in the developing brain. In the early postnatal rat cortex - an equivalent age to late gestation in humans - neuronal avalanches have been observed *in vivo* and *in vitro* [51] suggesting that power-law distributions are an attribute of the early nervous system as well as in the adult. In humans, two recent publications by separate groups have examined changes in the power-law dynamics in the amplitude of oscillations across a wide age-range from early childhood into adulthood [44, 45]. Both studies observed power-law dynamics in temporal correlations across all age-ranges studied, which in *Berthouze et al.* [44] was as young as 0 months of age. Although a trend was observed across childhood by *Smit et al.* [45], both studies indicate that power-law dynamics can be observed even at a young age. Thus, if a period of self-organisation were to occur it must do so before full-term age. This is perhaps not surprising since, in contrast to foetal development, after birth the brain must already be in a 'suitable' dynamic state to adapt and react to the external environment. Finally a study by *Tetzlaff et al.* [54] investigated the development of avalanche activity in neuronal cell cultures between 13 and 95 days *in vitro* - a period during which connections are developing. They found that the activity passes through a super-critical then sub-critical state before reaching a critical state where the avalanches follow a power-law distribution. This suggests that a period of self-organisation exists *in cultures* and is the first evidence that self-organisation to a critical state occurs in neuronal systems. However, it remains to be seen whether a self-organisation process occurs *in vivo*.

Is there evidence for a period of self-organisation to a critical state in the human brain in the EEG recordings of preterm infants? The results of *Tetzlaff et al.* [54], which appear to exhibit self-organisation over a period of connectivity development in cultures, suggest that the very preterm brain (the period of which spans a phase where the dominant developmental process is synaptogenesis) may also exhibit self-organisation. This thesis will address this question by examining the temporal organisation of the burst dynamics of EEG recorded from very preterm human neonates. Given that power-laws are observed in the temporal organisation of oscillation amplitudes in the EEG of more mature subjects, this thesis will investigate whether the preterm EEG also exhibits a complex temporal organisation. The critical nature of the dynamics will be examined across different gestational ages in order to ascertain whether there is a period of self-organisation in the early developing brain. The evidence that SOC is a plausible framework for brain dynamics will be discussed. In light of these results a computational model will be developed to examine a possible mechanism by which burst dynamics with the same temporal behaviour as the EEG can occur. As mentioned previously, the

immature nervous system has altered neurotransmitter responses, with GABA having a depolarising effect on postsynaptic neurons [2–5]. While presynaptic inhibition is fully operational throughout the period of early development [63], the differences in relation to GABA will have an effect on the dynamics of the early developing brain compared with that of the more mature nervous system. Indeed, it has been suggested that the "immature brain is at risk for seizures because of the imbalance between excitation and inhibition" [63], with the imbalance towards a more excitatory system. The computational model considered in this thesis will examine the most 'extreme case' that the immature nervous system might be in - a purely excitatory system. With this approach it will therefore be possible to determine the type of dynamics that can arise in such a system and in particular whether bursts of activity (separated by periods of inactivity) can occur in a purely excitatory system. If such dynamics can be observed this will generate future research in the area of dynamical systems and experimental studies to investigate the overall level of excitability in the developing brain. The model could then be extended to incorporate these experimentally derived levels of inhibition.

This thesis is organised as follows. In Chapter 2 the temporal organisation of the burst activity of the very early human preterm EEG is investigated. In Chapter 3 this investigation is extended to a larger data set in order to examine if the dynamics are related to age, time since birth and also if there are correlations with cognitive outcome later in life. In Chapter 4 a computational model is introduced to examine how the dynamics observed in the preterm EEG might occur. Finally, in Chapter 5 this model is extended to investigate how the dynamics might be affected by different connection topologies and in turn how the temporal characteristics of the dynamics themselves might affect synaptic connectivity formation. However, before embarking on the work of this thesis, a more detailed review of the relevant literature is given in what follows.

1.1 Background

1.1.1 Early brain development

From as early as embryonic day 33 neurogenesis starts to occur in humans [64] and neurons begin migrating from a subcortical region known as the ventricular zone up into the region beneath the meninges [7, 10]. This population of the first generated neurons form a layer known as the *preplate* or primordial plexiform zone [7]. Later generated cells, from embryonic day 50, migrate to a position in between earlier generated preplate cells splitting it into two regions known as the *marginal zone* and *subplate* [7, 10]. The marginal zone is the upper layer, below the pia mater and will become cortical layer I [7]. The subplate lies below the newly generated cells and is a transient zone which is no longer present after the early stages of development [7, 65, 66]. The later generated cells

form a region known as the *cortical plate*, which will become cortical layers II-VI, in an inside-out fashion, with earlier migrating neurons forming layer VI and younger neurons forming the outer layers[2] [68]. While in rodent development later migrating cells all form the cortical plate, the subplate of primates (including humans) continues to grow while cells are migrating into the cortex and probably involves the addition of new cells [7]. This difference in behaviour between rodents and primates, which is also highlighted by the fact that the subplate in primates is larger (in terms of relative proportion to the cortex) than it is in rodents, indicates that the subplate region is not just a by-product of evolution but is of functional importance in humans [66].

From 24 weeks of gestation the dominant developmental process switches from cell migration to connectivity formation in the cortical plate [69]. Connectivity formation is believed to rely on activity-dependent mechanisms [11, 12] as well as on genetic/molecular cues [70]. Activity-dependent mechanisms are initiated both by spontaneously generated activity (that is generated by the cortex itself [12, 24] and also spontaneous activity that is generated by subcortical regions, the spinal cord and the peripheral nervous system [11, 12, 15–17, 19, 20, 24, 29, 30]) as well as activity from external sensory input [11, 12, 70, 71]. During the main period of cortical connectivity formation, sensory input from the thalamus is received via functional connections from the subplate [6, 8], and it is not until approximately 34 weeks gestational age in the human foetus that thalamocortical connections have established functional synapses with layer IV (the main input layer) of the cortex [9], see Fig. 1.1. Ablation of the subplate before thalamocortical connections have developed leads to weak thalamocortical synapses and an effective decoupling of the cortex from the thalamus [72–74]. Furthermore, ablation of the subplate has also been shown to prevent the formation of ocular dominance columns [75] and normal patterning within the somatosensory barrel region of the cortex in rodents [74], as well as preventing the switch in GABA from a depolarising effect to the mature hyperpolarising effect [73]. Coinciding with the formation of direct thalamocortical connections, subplate cell death begins between approximately 30 and 35 weeks (depending on the brain region) in humans, with the majority of subplate neurons having apoptosed by term [65]. Fig. 1.2 shows histological sections from human foetuses at different ages. Changes in subplate thickness with gestational age can clearly be seen, including an initial increase in subplate thickness, followed by a decrease which occurs first at the bottom of cortical sulci.

Increases in cortical folding with gestational age have been seen in histological studies (see Fig. 1.2) and more recently have been shown *in vivo* through MRI imaging [78], see Fig. 1.3. This figure clearly highlights the stark contrast in cortical folding at the early

[2]Cortical cell migration in this stage of development is a clear example of where molecular cues play an important role in development: cells in the marginal zone produce the protein reelin which is thought to provide a signal for the migrating neurons [10, 67].

Figure 1.1: **Figure removed from online version of the thesis due to copyright - see *Kanold, 2009* [76].** Thalamocortical wiring at different stages of development. Early in development thalamic connections project to subplate neurons which in turn project to cortical layer IV. The precise target of these subplate-cortical connections are unknown (indicated by '?'). From approximately 26 weeks gestational age in humans thalamic axons begin to project to the cortex, with subplate connections still remaining intact at this state [9]. This period has been termed the 'critical period' as during this time refinement of synaptic connections in the cortex are particularly influenced by sensory input [76]. After this, beginning at approximately 30 weeks gestational age in humans, subplate neurons apoptose leaving the direct thalamocortical connections. Figure from *Kanold, 2009* [76]. 'Glu-R' indicates glutamate receptors and '$GABA_A$-R' indicates $GABA_A$ receptors.

Figure 1.2: **Figure removed from online version of the thesis due to copyright - see *Kostović and Judas, 2002* [77].** Acetylcholinesterase stained sections through the brains of human foetuses at age (A) 18, (B) 24, (C) 28 and (D) 32 weeks. Overlay indicates different regions (CP = cortical plate, SP=subplate, IZ= intermediate zone) and major cortical afferents (thalamocortical afferents - dashed lines, basal forebrain afferents - solid lines, callosal afferents - dotted lines, and ipsilateral long association fibres - dotted and dashed lines). Note that these lines indicate some connections only and at 28 weeks (C) thalamic axons project to both the cortical plate and subplate, see Fig. 1.1. The change in thickness of the subplate with age can clearly be seen, reaching its peak thickness at around 28 weeks (C). Subplate dissolution begins at approximately 30 weeks and occurs first at the bottom of sulci (D). From these figures it is also possible to observe the increase in gyration with age, see also Fig. 1.3. Figure from *Kostović and Judas, 2002* [77].

preterm age compared with full-term neonates. The MRI study also indicated differences in the rates of gyration between the two hemispheres, with the right hemisphere presenting gyral complexity earlier than the left. This may be a sign of early arrangements leading to future functional specialisation [78] - for example, language is usually left lateralised (first reported by Broca in 1861, reviewed by *Toga and Thompson* [79]). For further reviews of early development see *Sidman and Rakic* [80], *Allendoerfer and Shatz* [6], *Bystron et al.* [7] and *Kanold and Luhmann* [66].

Figure 1.3: **Figure removed from online version of the thesis due to copyright - see *Dubois et al. 2008* [78].** 3D images of the cortical surface at different gestational ages reconstructed from measurements of the interface between the developing cortex and white matter/subplate zone on T2-weighted MRI images [78]. The colours indicate the surface curvature. Numbers indicate the gestational age of the subject in weeks (left) and the sulcation index (right). The sulcation index was defined as the ratio between the areas of sulci from the lateral, ventral and vertex surfaces; and the closed surface of the cortex (defined by a smooth envelope mask over the cortex). The image clearly shows increases in cortical sulcation with gestational age. Note that the images are not scaled with the size of the brain. Figure from *Dubois et al. 2008* [78].

As there are rapid anatomical changes and the subplate is an anatomical feature unique to this developmental period, this leads to the question of whether there are also changes in, for example, EEG activity and neurophysiological markers that might be indicative of subplate activity and its influence on the cortex. Moreover, the fact that neuronal activity is important during this stage of development necessitates the characterisation

of the activity that can be observed in humans during these developmental stages.

1.1.2 Preterm EEG

Premature human neonates now survive from as early as 23 weeks gestational age. As was discussed above, the cortex at this age is still far from fully formed. The subplate is a major neuro-anatomical structure and connectivity formation is on-going and being shaped through activity-dependent mechanisms. Thus, much can be learned from studying brain activity in this population.

The first EEG of a human preterm neonate was carried out in the 1950s by Dreyfus-Brisac and colleagues [81] and since then numerous studies have examined both 'normal' and pathological EEG characteristics. The normal EEG pattern of a preterm infant is discontinuous with bursts of high amplitude activity interspersed within periods of very low amplitude background activity (virtually electrically silent) [26–28]. An example of a section of an EEG recorded from a preterm at 26 weeks gestational age is shown in Fig. 1.4 in which these relatively long periods of very low amplitude activity can be clearly seen. This discontinuous activity pattern, referred to in the literature as *tracé discontinue* [82], is present in the earliest recorded preterm subjects at 23 weeks gestational age and lasts until approximately 35 weeks of age [26, 83]. The degree of discontinuity within the EEG decreases as gestational age increases, with the periods between the bursts of activity (known as the inter-burst interval, IBI) decreasing [83–86]. Combined with this IBI decrease, the bursts of activity increase in length leading to periods of more continuous oscillatory activity as gestational age increases [83–86]. Additionally, changes in spectral band power have been shown to occur with age [35, 87, 88] reflecting the change in pattern and occurrence of activity.

The bursts of EEG activity can be characterised as slow wave activity (delta waves in the range 0.5-2 Hz) with nested oscillations of higher frequencies [27, 83, 89]. This activity has been shown to occur following tactile [29, 90, 91] and noxious [91] stimuli, as well as in relation to spontaneous limb movement [29]. It also occurs frequently in background EEG recordings, as was seen in Fig. 1.4. The nested oscillations in the preterm EEG have been suggested to be homologous with nested oscillations, known as spindle bursts, in the early developing rat brain [24, 25]. Spindle bursts also occur in response to spontaneous movement and persist, though are reduced, following spinal cord transection [24]. They have been shown to occur in response to retinal waves, stimulation of the optic nerve and endogenously in the visual cortex [92]. Thus, spindle bursts, and by association nested oscillations in the human preterm, are not entirely a result of peripheral input to the cortex but also result from intrinsic cortical events. As work has shown that spontaneous activity is important for proper connectivity formation in animals [11, 72–75], the spontaneous activity observed in

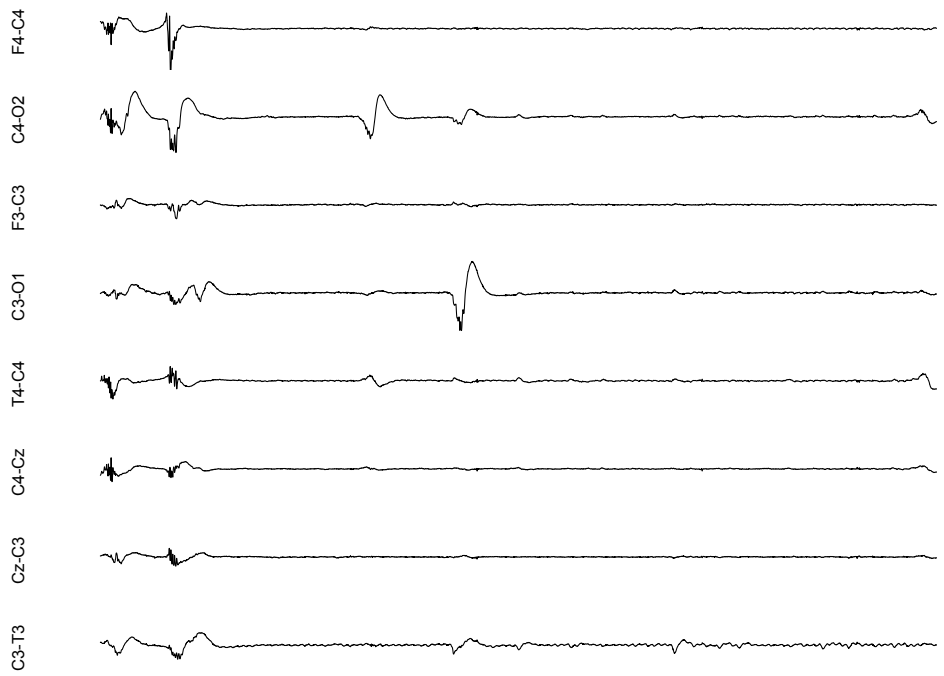

Figure 1.4: 50 second section of EEG recorded from a preterm subject at 26 weeks gestational age. High amplitude activity can be observed interspersed within periods of very low amplitude - the EEG is discontinuous. This EEG recording was filtered with a high pass filter at 0.5 Hz, a low pass filter at 70 Hz and a notch filter at 50 Hz.

electrophysiological data in humans (originating from any region of the nervous system) will also likely play a role in cortical connectivity formation and refinement [29].

Most EEG recordings are AC-coupled and employ a high-pass filter at 0.5 Hz. Recent DC-coupled recordings without the need for this filtering have revealed very slow waves (0.1-0.5 Hz) with nested higher frequency oscillations, termed spontaneous activity transients (SATs) [93–95]. Filtering of these SAT events produces a delta wave with nested higher frequencies, indicating that the nested events on AC-coupled recordings correspond to SATs or periods within SAT events [94]. Consistent with the observations in AC-coupled recordings, SATs have been shown to co-occur with spontaneous movement, often occurring after single limb movements but preceding startle events (movements occurring simultaneously in at least three limbs) [30].

In the preterm the neurophysiological mechanisms underlying the EEG are not well understood [96]. As the age of the subjects coincides with the period during which thalamic input is via the subplate, the subplate likely plays a role in modulating the activity observed in the EEG [96]. Ablation of the subplate in rodents leads to almost complete loss of spindle burst activity [74]. From other animal studies it has been suggested that the delta wave which carries the nested oscillations reflects the action of the subplate on the cortex [97]. Additionally, *in vitro* studies of the intact cortex of newborn mice show that bursts of oscillations are synchronised within cortical columns

through gap junction coupling in the subplate [23]. However, another study has suggested that the developmental disappearance of the discontinuous burst pattern is associated with the maturation of GABAergic inhibition [95]. Future work is needed in this area to fully understand how all the developmental features affect the EEG.

Sawtooth patterns (oscillations in the theta range, 4-8 Hz) are another characteristic burst behaviour which commonly occur in the occipital [98] and temporal [27, 83, 98] regions in EEG recordings of preterms before 30 and 32 weeks of age respectively. Other types of activity are usually indicative of pathology, such as abnormal (including rolandic) sharp waves [99, 100], as are prolonged IBIs or an immature EEG in relation to gestational age [28, 101]. Abnormal EEG activity recorded during the preterm period is a useful diagnostic tool of neurological sequelae [99, 102–106] and has been suggested to be predictive of outcome [28, 100, 101, 103, 104, 107–110].

Although preterm EEG provides an invaluable method through which early brain activity can be analysed, it is important to remember that preterm subjects probably develop differently to foetuses *in-utero*. Even without overt brain problems such as haemorrhage, evidence suggests that children born extremely prematurely are much more likely to have social and cognitive problems later in life [111–113]. These problems may be related to the abnormal extra-uterine environment, with abnormal sensory stimuli, within which the preterm child develops. It is important that the potential of the EEG as an early diagnostic tool is maximised. This is particularly crucial given that the survival rate of premature neonates is increasing [114]. Thus, any study of the preterm EEG is of importance not just for understanding the development of the brain but also from a clinical perspective. Full analysis of early brain activity may aid in the understanding of why some premature children have problematic outcome while others do not.

While a number of studies have examined mean or maximum inter-burst interval (IBI) [27, 83, 86, 98, 101, 115] and how this changes with gestational age, no thorough investigation of the temporal organisation of the burst activity of the preterm EEG has been carried out. An analysis of this type seems an obvious extension to the current literature, and may aid in the clinical assessment of abnormal EEGs. For example, if a very long IBI occurs only once in an entire recording of one subject but in the recording of another subject IBIs of that length occur many times, will the latter subject have a worse outcome? What does it mean if all these long IBIs occur together in the recording? While this question will not be directly addressed in this thesis it clearly highlights that examining the distribution and temporal organisation of activity is a worthwhile endeavour from a clinical perspective, as well as a scientific one.

1.1.3 Other imaging modalities and the developing human brain

Foetal MEG has shown that the spontaneous brain activity of the developing foetus is similar to that observed on the preterm EEG, with a discontinuous behaviour and bursts of nested oscillations [116]. Evoked magnetic fields in the foetus have been observed in response to auditory [117] and visual [118] stimuli. It is not yet clear exactly how well foetal brain activity, as recorded on the MEG, compares with preterm EEG. This comparison is important for our understanding of early brain activity and is a key question for future work.

Recent work has investigated fMRI in preterm neonates, showing activation in response to sensory stimuli in preterm infants [119] and the progressive emergence of resting state networks which are fully present by full-term [120]. Though preterm fMRI has currently been investigated only in a small number of infants, as the field develops it may provide interesting evidence to suggest the anatomical localisation of spontaneous neurological activity, and may prove to be a promising methodology with which to investigate the functional role of the subplate in human neonates.

1.1.4 Key characteristics of the EEG recordings of older subjects

By full-term the EEG is largely continuous and is characterised by low-frequency waves with higher frequency nested oscillations [26], see Fig. 1.5. As discussed above, this switch to more continuous behaviour may reflect the development of thalamocortical connections and GABAergic inhibition. Some authors have noted differences in EEG activity of children born prematurely and recorded at full-term age compared with term born controls, including differences in band power [121] and differences in the amplitude of evoked potentials in response to painful stimuli [122]. However, preterm subjects should have a continuous EEG by term age and a discontinuous EEG at term equivalent age, either in subjects born preterm or those born at term, is indicative of severe pathology [26, 123].

The characteristics of the EEG continue to change with age and a number of studies have examined the maturational features of the EEG from childhood into adulthood. Key characteristics of the EEG recorded from older subjects and changes with respect to age are briefly described here. These characteristics further highlight the importance of fully examining the temporal properties of EEG activity.

Power spectra

The adult EEG exhibits different oscillations depending on the state of the individual (e.g. sleep state or level of arousal). Typically for an alert adult with eyes open the

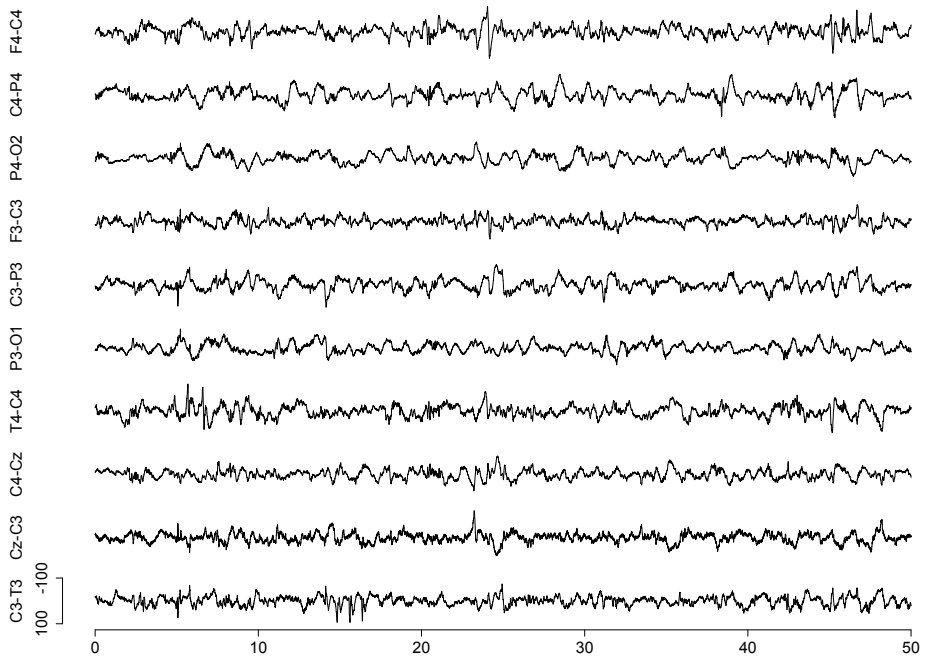

Figure 1.5: 50 second section of EEG recorded from a full term subject (gestational age 39 weeks). The activity at this age is now continuous and lower amplitude (compare with Fig. 1.4, which shows the starkly contrasting discontinuous activity of the preterm neonate). This EEG recording was filtered with a high pass filter at 0.5 Hz, a low pass filter at 70 Hz and a notch filter at 50 Hz.

oscillations will be in the beta range (14-25 Hz), as was identified by Berger in the 1920s in the first human EEG recordings (reviewed in *Buzsaki* [124]). With lower levels of arousal and during sleep the oscillations are typically of lower frequencies. From childhood to adulthood there is a decrease in the power of the low frequency oscillations and a relative increase in oscillations in the higher frequency ranges (alpha - 8-13 Hz - and beta) [125–127]. It has been hypothesised that these changes are due to synaptic pruning and changes in frequency have been shown to correlate with changes in cortical thickness [125]. Interestingly, when plotting the logarithm of the power against the logarithm of the frequency of oscillations within the EEG a straight line relationship is observed indicative of a power-law (see below) [124].

Synchrony

The synchronised action of populations of neurons has been proposed as a means of communication, linking information processed in distinct regions of the nervous system [33, 34]. For example, synchrony has been observed between spatially separated areas of the visual system [32], between areas of the sensorimotor cortex [128] and between the motor cortex and EMG recorded in the hand during contraction [129]. Increased synchrony also occurs with attention to a particular stimulus [130]. Abnormal

synchrony has been linked with pathology - for example there is increased synchrony in patients with epilepsy in inter-ictal EEG [131] and decreased synchrony in patients with schizophrenia [132]. Across childhood and adolescence there is an increase in temporal synchrony between areas of the nervous system: EEG-EMG coherence between the primary motor cortex and the contralateral wrist extensor muscle has been shown to increase with age [133].

Power-law scaling has been observed in synchronisation within adult fMRI recordings [46]. This indicates that phase locking (the measure of synchronisation used in this study) can react to the needs of the environment [46]. In this way distinct areas of the nervous system might communicate in an 'optimal' manner.

Long-range temporal correlations

While synchrony between populations is a property of two or more signals, one might wonder whether the signals from individual areas themselves (recorded on single EEG channels) have particular temporal patterns. Does the signal appear to behave like a random process or does it have a complex temporal ordering? As described earlier, the temporal organisation of continuous EEG oscillations have been analysed through examining fluctuations in the amplitude of the oscillations. A number of studies have shown that these fluctuations exhibit so-called *long-range temporal correlations (LRTCs)* [39–45]. LRTCs are a power-law decay in the autocorrelation of a signal (temporal correlations within the signal) which implies that correlations between temporally distant events exist and the magnitude of the temporal correlations has no distinct scale. Thus, to understand LRTCs we must first understand what a power-law is.

1.1.5 Power-law distributions

The function $f(x)$ is said to be a *power-law* if

$$f(x) = cx^{-\gamma}$$

for all values of x where c and γ are constants and γ is known as the *exponent* of the power-law.

A key property of power-laws is that they are *scale invariant*. This means that there is no characteristic scale of the distribution (unlike, for example, a periodic function which has a characteristic scale of the period of that function). This can be seen from the fact that

$$\frac{f(kx)}{f(x)} = \frac{ck^{-\gamma}x^{-\gamma}}{cx^{-\gamma}} = k^{-\gamma}$$

i.e. the relative change for any value of k is independent of x. Thus, the dynamics do not occur with a typical scale and a system whose dynamics follow a power-law does not therefore have a typical behaviour (and a wide range of behaviours is possible within the system).

Taking logarithms of both sides of the equation of a power-law we see that:

$$log(f(x)) = log(cx^{-\gamma}) = -\gamma log(x) + log(c)$$

Thus, a power-law follows a straight line on a double-logarithmic plot and the gradient of this line is the exponent of the power-law. Power-law distributions have been observed in many different contexts from city populations to word distributions [134]. They have also been commonly observed in nature in such varying situations as earthquakes [135], landslides [136], snow avalanches [137], solar flares [138] and neuronal avalanches [49–53].

Fig. 1.6 shows the method used to extract neuronal avalanches from electrophysiological recordings and an example of the distribution of neuronal avalanche size. Avalanches are determined from multi-electrode recordings by first extracting points at which the local field potential recorded at a given electrode passes a negative threshold. Activity is divided into time frames and a neuronal avalanche is defined as a temporal cluster of electrodes below the threshold, with the start and end of an avalanche determined by time frames either side which do not contain any activity. The distribution plot on a double-logarithmic scale shows a linear relationship (up to the size of the system - see below) indicating power-law scaling.

Figure 1.6: **Figure removed from online version of the thesis due to copyright - see *Beggs and Plenz* [49, 50].** (A) Extraction of neuronal avalanches from neuronal activity recorded on a multi-electrode array. Cortical slices were cultured on multi-electrode arrays and the spontaneous activity was recorded (top left). When the local field potential (LFP) recorded at an electrode (top right) passes a negative threshold this electrode might be thought of as 'active'. The distribution of active electrodes throughout the array (middle plot) shows clusters of events which, when examining their temporal structure in closer detail (bottom plot), are not completely synchronised. Dividing the activity into time frames of size Δt (bottom plot), avalanches are defined as successive frames with at least one active electrode. Figure from *Beggs and Plenz* [50]. (B) Probability distribution of avalanche size defined as either the number of active electrodes or the sum of the negative LFP at all the active electrodes. Both exhibit a power-law relationship (a power-law with an exponent of $\gamma = 1.5$ is indicated by the red line). Figure from *Beggs and Plenz* [49].

1.1.6 Long-range temporal correlations (LRTCs)

Let $\Gamma(\tau)$ be the autocorrelation function of a time series where τ is the delay. LRTCs can be simply put as correlations that do not die out, even in an infinitely long time

series. Mathematically this can be written as [139]:

$$\sum_{\tau=-\infty}^{\infty} |\Gamma(\tau)| = \infty$$

Conversely, a time series where the correlations are absolute, i.e.

$$\sum_{\tau=-\infty}^{\infty} |\Gamma(\tau)| < \infty$$

is said to have *short-range temporal correlations*.

The interest in signals which exhibit LRTCs stems from the fact that such signals can be considered to be long-memory processes; the signal is affected by all previous values of the signal (though to varying degrees) and so 'carries a memory' of past events. LRTCs have been observed in many natural systems including river levels [140], inter-heartbeat intervals [141] and, as stated above, the brain's oscillatory dynamics. Additionally, in neuropathological states LRTCs have been shown to be altered with respect to healthy control states [47, 142–144].

The presence of LRTCs in empirical data can be assessed through estimation of the *Hurst exponent, H* (see below). The Hurst exponent is related to the autocorrelation of the signal by

$$\Gamma(\tau) \sim \tau^{2H-2}$$

as $\tau \to \infty$ [145]. Thus, we see that LRTCs are a power-law decay in the autocorrelation of the signal. By the *Wiener-Khinchin theorem*[3], the Hurst exponent is also related to the exponent of the power spectral density of the signal [145].

1.1.7 Mechanisms of generating power-laws and LRTCs

Power-law distributions are known to occur at the *critical point of a second-order phase transition* - a concept from thermodynamics, discussed in *Binney et al.* [146] - and so this has led to the suggestion that natural systems that exhibit power-law distributions may also be at a critical point [56, 58]. The idea of a system being at a critical point further implies that when perturbed away from this critical point the system will no longer exhibit power-law dynamics. A well known example of a computational model with critical dynamics is the *Ising model* which represents ferromagnetic spins. At low temperatures the system is very ordered, at high temperatures the spins are random, while the system exhibits power-law spatial and temporal correlations at a critical

[3]The Wiener-Khinchin theorem states that the power spectral density of a signal is the Fourier transform of the autocorrelation function. So from the relationship of the Hurst exponent and the autocorrelation of the signal it is possible to derive the equivalent exponent of the power spectral density.

temperature value [60, 146]. In order to reach this temperature and display the power-law distributions the system must be tuned to that temperature value. However, many of the natural systems (including neuronal systems) for which power-law statistics have been observed do not do so following an obvious tuning of a parameter. A possible solution to this problem came with the seminal work of Bak, Tang and Wiesenfeld in 1987 and their introduction of the concept of self-organised criticality (SOC) [55].

Self-organised criticality

SOC can be simply explained as a system that self-organises to a critical state. That is to say the system's dynamics (over time) reach a state which is critical (so that it exhibits power-law decay in spatial and temporal correlations) without any external forcing or parameter tuning [55, 56, 58, 147, 148]. The now classical example that the authors gave to demonstrate their theory was a model of a sandpile [55]. Grains of sand are added randomly to the system (a lattice grid) until a site reaches a threshold level of grains. This site then topples releasing a grain of sand to each of its four neighbours and decreasing its own height by four. If a site is at the edge of the lattice then the grain is dissipated, falling off the edge of the system. A grain toppling into a neighbouring site may lead to this site itself being above threshold and in this way avalanches of sand can occur. Only once all sites have returned to below their threshold is a new grain of sand added randomly to the lattice, possibly restarting another avalanche. The authors showed that this system will organise without the aid of parameter tuning to a critical state in which avalanche sizes and the duration of avalanches both follow power-law distributions [55]. However, note with reference to our developmental perspective, that during the period before the system has reached the critical state (the period of self-organisation), the avalanche dynamics do not follow a power-law and in general only small avalanches occur.

A self-organised model which attempted to explain neuronal avalanches was developed by *Levina et al.* [149] who showed that activity-dependent synapses led to self-organisation towards critical state dynamics. While it was believed initially that this model exhibited SOC, it was shown by *Bonachela et al.* [150] that this model does not exhibit true SOC as the system, unlike the sandpile model, is not conservative. For example, if a sandpile model were constructed so that when a cell topples it loses 6 grains of sand but only the 4 nearest neighbours each receive a single grain, then overall 2 grains of sand are lost from the system and the system is therefore not conservative. If such a non-conservative system has a driving force which counterbalances the dissipation in energy then it can appear critical as the system can 'hover around' a critical point. When a system is near to a critical point it can display apparent power-law dynamics which are very close to, but not true, power-laws. The system will only be truly critical when the driving exactly balances the dissipation. In order to achieve this parameter

tuning is required and so this cannot be considered to be a proper SOC system (as SOC systems self-organise, i.e. they do not require parameters to be tuned) [58]. This has therefore been termed *self-organised quasi-criticality (SOqC)* [58]. However, what is important to note here is that this type of system can display apparent power-law distributions. Along with the model of neuronal avalanches by *Levina et al.*, a number of other non-conservative self-organising models have also been shown to display apparent power-law distributions [151–154]. Given that experimental observations are inherently noisy it seems unlikely that one could determine from the distribution of data alone whether it results from a true power-law or an apparent power-law relating to a system being close to a critical point. Therefore, this paradigm provides an approach to understanding the dynamics which is just as plausible as true SOC.

The observation of power-law distributions in neuronal avalanches and LRTCs in the amplitude of cortical oscillations has led to the suggestion that the brain is a SOC system [39, 49, 60]. However, as previously discussed, there is currently very little evidence to confirm that this is the case. It is possible that an alternative mechanism underlies the apparent power-law distributions observed in nervous system dynamics.

Alternative mechanisms of generating power-law distributions

A number of alternative *non-critical* mechanisms have been suggested to account for power-law distributions. The simplest example shows that thresholding of a purely stochastic (i.e. non-critical) process can lead to the observation of power-laws in peak size [155]. These power-laws do not pass more stringent tests such as the Kolmogorov-Smirnov test but this emphasises the need for testing power-law distributions more rigorously than through a simple double-logarithmic plot, as discussed below [155]. A number of authors have shown that the superposition of processes with short-range dependence and with different characteristic timescales can lead to data with apparent power-law long-range dependencies [57, 156, 157]. For example, the summation of only three random processes with different exponential timescales yields almost perfect power-law structure [57]. This framework has been suggested to have biological relevance in the analysis of inter-heartbeat intervals, which have been been shown to display LRTCs [141, 156]. In this context different timescales are present, e.g. the fast timescales of the autonomic nervous systems and the much slower timescales of the sleep-wake cycle and the circadian clock, which provide the basis for the timescales of the suggested exponential processes [156]. Moreover, this framework has been suggested from a neurocognitive perspective - neural processes could be determined by many independent groups of neurons, each with their own timescale [158].

Specifically in the field of computational neuroscience, neuronal network models have

been formulated to suggest a possible underlying mechanism for the generation of neuronal avalanches (with power-law distributions) which do not have self-organising dynamics [61, 62, 159]. These models all found that power-law distributions, i.e. true neuronal avalanches, occurred when there was a balance between excitation and inhibition within the network, which gives rise to a critical state. Experimentally, neuronal avalanches have also been shown to occur only when there is a balance of excitation and inhibition [37, 62]. Furthermore, this balance coincides with an optimal dynamic range [37], optimal information transfer [160] and maximal variability but moderate levels of phase synchrony [62]. These results emphasise the advantageous nature of networks operating at a critical state, but suggest that this critical state need not be obtained through SOC. Balance of excitation and inhibition is also an attractive mechanism that seems intuitively plausible [38]. Too much excitation would lead to run-away activity, which is pathologically observed in epilepsy. On the other hand, too much inhibition would lead to activity that dies out quickly. However, the early developing brain has altered neurotransmitter effects compared with the mature nervous system with an imbalance between excitation and inhibition [2–5, 63]. Considering the extreme example, how might a balanced critical state be attained in a purely excitatory system?

1.1.8 Empirical evaluation of power-laws and LRTCs

In this thesis data from both preterm EEG and the constructed computational model will be analysed in terms of the distribution of the overall data (for example, does the distribution of burst size follow a power-law as was seen in neuronal avalanches?) and through assessing the presence of LRTCs in the organisation of the activity (are the bursts of activity temporally random or do they exhibit a more complex temporal structure?). In this section the methods which will be used are briefly reviewed.

Power-law distributions

As shown in section 1.1.5, power-laws follow a straight line on a double-logarithmic axis. This property is often utilised as a test to determine whether empirical data follows a power-law distribution (for example see [49, 50, 134, 136–138]). However, other functions can also appear linear over a range of values [134] and so linearity in experimental data, which will also be inherently noisy, should be taken with caution to suggest a power-law distribution [155]. With this in mind, statistical methods have been developed to compare power-law distributions with other plausible distributions in order to better ascertain whether empirical data is likely to be power-law distributed [134]. This statistical assessment currently provides the best approach to test empirical data which appears to have a power-law distribution and will be used in this thesis. Briefly,

the algorithm of *Clauset et al.* [134] estimates the exponent γ (of the power-law distribution) and value of x_{min} (the minimum value for which the power-law holds) which gives the best goodness-of-fit to the data. From this a p-value (the test statistic for the power-law distribution) is calculated by generating 1000 distributions of the same size and with the same exponent and x_{min}. These are compared to the power-law using the Kolmogorov-Smirnov statistic (this is a non-parametric test based on the maximum distance between the cumulative distribution functions of the data and the model), as is the empirical data. The p-value is calculated as the *proportion of times that the empirical data is a better fit* to the power-law than the generated data. Thus, a *high* p-value is obtained if the empirical data frequently fits the exact power-law better than the generated data. As in *Clauset et al.* [134], a p-value *greater* than 0.1 will be taken in this thesis to suggest that the hypothesis that the empirical data follows a power-law distribution is a good one.

Another test which can be used to assess the presence of power-laws in empirical data is to see whether the data exhibits *finite-size scaling*. While true power-laws extend across all scales, for systems of a finite size the power-law often does not occur across the whole distribution and a crossover in the distribution to exponential decay occurs for a certain scale [56]. This *finite-size effect* has, for example, been observed in neuronal systems in the case of neuronal avalanches [49–53], where the crossover and 'limit of the power-law' in avalanche size occurs at the size of the multi-electrode array used for the recording, see Fig. 1.7. If a system is truly critical then the crossover inherent from any finite-size effect will scale with respect to the system size, as was shown to be the case with neuronal avalanches [49]. Furthermore, measurements for different system sizes should be related to each other by a rescaling of variables - a phenomenon known as finite-size *scaling*, see Fig. 1.7. For a system to be critical it does not suffice for power-law statistics to be observed but the system must also exhibit finite-size scaling [58]. However, this is also a necessary but not sufficient condition of criticality [58].

Figure 1.7: **Figure removed from online version of the thesis due to copyright - see *Klaus et al.* [161]** (A) Neuronal avalanches exhibit the finite-size effect - probability distribution of neuronal avalanche size (s) recorded from an organotypic culture of rat somatosensory cortex on a 60 electrode array. The size of the array is indicated by the arrow and a clear drop-off is observed at this size with power-law scaling up to avalanches of this size. (B) Schematic of the approach used to assess finite-size scaling. The left plot shows a number of avalanche size distributions before scaling which were 'recorded' on electrode arrays of different sizes. With larger electrode arrays the distributions extend to larger avalanche sizes. The right panel shows that after rescaling (by normalising by the array size N) the distributions for all array sizes collapse onto the same distribution, with the drop-off occurring at the same point. This figure is modified from Figures 1 and 2 of *Klaus et al.* [161]. The authors showed that finite-size scaling can be observed in neuronal avalanches.

In this thesis the preterm EEG was recorded from a relatively small number of electrodes (due to the small size of the subjects' heads) and so finite size scaling cannot

readily be assessed in this data. However, this relationship can be examined in data from computational models, for example by examining neural networks of different sizes as will be assessed in this thesis.

LRTCs

The presence of LRTCs in data is assessed through estimating the Hurst exponent, H. For data with no correlations or for short-range correlations only $H = 0.5$. If $0.5 < H < 1$, this indicates persistent long-range correlations in the data, while if $0 < H < 0.5$, then the data has persistent anti-correlations. As empirical data is necessarily finite it is only possible to obtain an estimate of the Hurst exponent - LRTCs exist across all scales, not just those measured in a finite sample, however, estimates will be asymptotic to the true value of the Hurst exponent. There are a number of methods with which an estimate can be calculated, many of which are reviewed in *Taqqu et al.* [162]. As the exponent can only be estimated it is recommended practice to check the consistency of results using two methods [145]. Furthermore, for each of these two methods it is also best practice to randomly shuffle the original time series and calculate the exponent of the shuffled time series. Randomly shuffling the time series will destroy any correlations in the data, and so the shuffled sequences should have an exponent consistent with the theoretical asymptotic value of 0.5 for uncorrelated noise. The shuffling should then be repeated a large number of times (in this thesis data is compared with at least 500 shuffled sequences) and the resulting distribution of exponents from the shuffled data can be compared to the exponent from the original time series. If the actual exponent is significantly different from the distribution of exponents of the shuffled data, we can be confident that the exponent of the original sequence is the result of LRTCs in the data.

Throughout this thesis the two estimates of the Hurst exponent which are used to assess LRTCs in the data (both physiological and computational signals) are detrended fluctuation analysis (DFA) [141, 163] and the Whittle estimator [162]. These techniques were chosen as they produce more accurate estimates than other methods [162]. Furthermore they are calculated in different domains - DFA is a graphical method constructed in the time domain, whereas the Whittle estimator is a non-graphical method calculated in the frequency domain. These differences in methodology, combined with the rigorous statistical comparison with shuffled data, mean that any spurious estimates can be detected. These methods have been described elsewhere [141, 162, 163] but for completeness they are briefly described here.

Detrended fluctuation analysis (DFA)

Let x be the signal for which the Hurst exponent is being estimated, N the length of the signal and y the integrated signal. The signal is divided into boxes of equal length n.

Figure 1.8: **Figure removed from online version of the thesis due to copyright - see *Peng et al.* [141].** An example of an inter-burst interval sequence of 1000 heart beats (upper plot) and the integrated signal $y(k)$ (lower plot). The vertical lines indicate boxes of size $n = 100$ and the straight line segments indicate the trend across the box according to a least-squares fit. Figure from *Peng et al.* [141]

For each box, a least squares fit, $z(k)$, to the integrated signal, $y(k)$, is calculated and y is detrended by subtracting this local trend. From this detrended signal the root mean square fluctuation, F(n), is calculated:

$$F(n) = \sqrt{\frac{1}{N}\sum_{k=1}^{N}\left(y(k) - z(k)\right)^2}$$

The process is then repeated for a number of different box sizes. The average fluctuation $F(n)$ is compared to the box size n on a double-logarithmic plot, with a linear relationship indicating the presence of scaling. If a linear relationship is found, the gradient of this straight line is the estimate of the Hurst exponent. Fig. 1.8 and 1.9 show examples of DFA exponent calculation in inter-heart beat intervals and the fluctuations in oscillation amplitude recorded using whole-scalp MEG respectively. DFA calculations were carried out in this thesis using the MATLAB code of *McSharry* [164].

Figure 1.9: **Figure removed from online version of the thesis due to copyright - see *Linkenkaer-Hansen et al.* [39, 40].** (A) An example of an MEG signal, filtered at 10 Hz (passband 6.7-13.3 Hz), recorded with the subject resting and with their eyes closed. The thicker line indicates the amplitude envelope of the signal calculated using the Hilbert transform. This type of amplitude signal can be analysed using DFA (B,C). (B) The amplitude of the signal from a single recording of length 1200 seconds (top). The integrated signal is calculated (middle) and this signal is separated into set box sizes (also known here as a window) and the least-squares fit calculated (bottom plot). (C) The signal is detrended by subtracting the linear fit (top) and this process is repeated for multiple box sizes. The average fluctuation is then compared against box (window) size on a double-logarithmic axis (bottom). In this case the exponent was found by calculating the slope of the line in between the two arrow heads. For lower window sizes temporal correlations were affected by the wavelet filtering of the original signal. The arrow indicates the window size shown in the other plots of this figure. Figure (A) from *Linkenkaer-Hansen et al.* 2004 [40] and (B,C) from *Linkenkaer-Hansen et al.* 2001 [39].

The Whittle estimator

The Whittle estimate is the value of η which minimises Q:

$$Q(\eta) = \int_{-\pi}^{\pi} \frac{I(\lambda)}{f(\lambda, \eta)} d\lambda$$

where $f(\lambda, \eta)$ is the spectral density at frequency λ and $I(\lambda)$ is the periodogram given by

$$I(\lambda) = \frac{1}{2\pi N} \left| \sum_{k=1}^{N} x_k e^{ik\lambda} \right|$$

For all calculations in this thesis the function FDWhittle in the R package fractal was used, with sdf.method='wosa' - Welch's Overlapped Segment Averaging.

1.1.9 Power-law scaling on different levels

As described above, power-law scaling has been observed on different levels - from neuronal avalanches, to LRTCs in EEG oscillations recorded at the level of the entire brain. However, whether and how these observations are related is currently an unresolved issue. Recent work by *Poil et al.* [159] showed that a computational model can exhibit neuronal avalanches with a power-law distribution and, for the same parameters, but on a longer timescale, oscillations which display LRTCs in amplitude fluctuations. From this result they have proposed the concept of multi-level criticality in which power-law dynamics emerge on multiple levels of a hierarchical system. This work suggests that neuronal avalanches and LRTCs may both be a product of the same system at criticality, however, experimental work is required to confirm this result.

There is also some evidence to suggest that the burst activity in the developing brain may relate to neuronal avalanches: bursts of nested theta and beta/gamma activity recorded in young rats has been shown to organise as neuronal avalanches [51]. While this activity occurs at a later developmental stage than spindle bursts in rats, the activity is a discontinuous burst pattern suggesting that bursts of activity and neuronal avalanches in the developing brain may be related. Additionally recent experimental and computational observations have suggested neuronal avalanches may occur at different rates in relation to *up and down neuronal states*. Up and down states refers to the observation that some neurons have a two-state sub-threshold membrane potential behaviour - a more hyperpolarised level known as a down state and a more depolarised membrane potential known as an up state [165], see Fig. 1.10. The neuron is more likely to fire when in the up state as it is closer to the action potential threshold, but can still fire when in the down state. *Lombardi et al.* [166] measured the inter-avalanche intervals (IAIs) of neuronal avalanches recorded in culture and showed that the distribution of

Figure 1.10: **Figure removed from online version of the thesis due to copyright - see *Wilson and Kawaguchi* [165] and *Lombardi et al.* [166].** (A) An example of up and down states from an intracellular recording *in vivo* of neostriatal spiny neurons in anaesthetised rats. The top trace shows the membrane potential in the absence of an applied current, in the bottom trace a small hyperpolarsing current was passed through the electrode preventing action potentials. Figure from *Wilson and Kawaguchi* [165]. (B) Distribution of waiting times (inter-avalanche intervals) measured experimentally (green) in cultures and in a neuronal network model (black squares, for details see *Lombardi et al.* [166]). The insets show the distributions evaluated separately in the up and down states for the experimental (lower inset) and simulated (upper inset) data. Δt was estimated for each culture as the average time between negative local field potentials (which are used in analysis of neuronal avalanches) and ranged from 3-6 ms. Figure from *Lombardi et al.* [166].

IAIs had two different behaviours. Firstly, there was an approximately power-law section for small IAIs which the authors suggest correspond to the IAIs between avalanches that occur when neurons are in the up state. For larger IAIs the distribution exhibits a 'hump' which the authors suggest corresponds to avalanches that occur during the down state, see Fig. 1.10.

Thus, there are developing theories connecting the power-laws observed at different scales with each other and with other brain activity. However, future work is needed before it can be determined whether all the signatures of criticality observed in brain dynamics are as a result of the whole system being at a critical state.

1.2 Summary

Activity-dependent mechanisms are crucial for brain development and are thought to play a role in the proper formation of synaptic connections. It is therefore of interest to fully understand activity dynamics during the developmental period. Preterm EEG provides a unique opportunity with which to study activity in the early developing human brain.

Analysis of adult EEG has shown that fluctuations in the amplitude of oscillations exhibit LRTCs [39–45], indicating a complex temporal patterning. Combined with other observations of power-law distributions in neural systems, this has led to the suggestion that the brain is a SOC system [39, 60]. However, other frameworks can give rise to apparent power-law scaling and there is currently very little evidence of a period of self-organisation of brain dynamics to a critical state. This leads to the question of whether there is evidence of a period of self-organisation to a critical state during (human) brain development. Previous research has shown that LRTCs are exhibited by the oscillatory activity of the EEG in very young children [44, 45]. Therefore if there is a period of self-organisation it must occur at a younger age. This thesis examines this question in the very early human preterm, whose EEGs are recorded at a time period

during which the main developmental process is cortical connectivity formation. In addressing this question, this thesis will provide an extensive analysis of the temporal dynamics of the preterm EEG and so will also enhance research in this area and the understanding of activity in early brain development.

This thesis will firstly investigate markers of criticality in the preterm neonate through assessment of power-law distributions and LRTCs in the burst dynamics of their discontinuous EEG recordings. The effect of the Hurst exponent on gestational and postnatal age will be examined in order to evaluate evidence for a self-organisation period towards a critical state. Correlations between the Hurst exponent and outcome measures later in life will also be determined. Any correlations are of interest from a clinical perspective and it is important when investigating preterm EEG that the clinical needs of this group are considered, and the potential of EEG recordings are maximised.

An excitatory neuronal network model will also be examined to address the question of whether a simple purely excitatory network can exhibit the type of dynamics observed in the preterm EEG. During development there are altered neurotransmitter effects with delayed postsynaptic inhibition. Therefore, this model will generate an hypothesis as to how the brain exhibits the type of activity observed in the preterm EEG. How connectivity formation (i.e. the dominant process during this period of development) might be affected by the dynamics is also investigated.

1.3 Aims and hypotheses

- To construct an algorithm for the extraction of activity bursts from the preterm EEG. This will make use of the known characteristics of these bursts.
- To assess the distribution of the characteristics of the bursts of activity in the preterm EEG (size, duration and intervals between them) to better understand the spontaneous activity of the early developing brain. Evidence of power-law scaling in these distributions will be investigated.
- To examine markers of criticality in very preterm human EEG by assessing the presence of LRTCs in the bursts. I hypothesise that the emergence of power-law dynamics occurs as a function of brain maturation and so a convergence towards a 'critical' power-law relationship will be observed with increasing gestational age. This would be consistent with the hypothesis that the brain is a SOC system.
- To investigate whether the degree of the LRTCs (if they exist) are affected by postnatal age. Other EEG parameters have been shown to be affected by time since birth [35, 167], perhaps indicating an adaptation to the *ex-utero* external environment, and so I hypothesise that this will also be the case with the degree of correlations.

- To ascertain whether the Hurst exponent is correlated with measures of outcome later in life. I hypothesise that any measures of complexity may well be correlated with outcome; studies have shown that LRTCs are affected by pathologies in older subjects [47, 142–144].

- To investigate a possible underlying mechanism producing the observed dynamics in the preterm EEG using a computational model. As the early developing brain has altered neurotransmitter effects with GABA having a depolarising effect and delayed maturation of other forms of postsynaptic inhibition [63], I will examine the question of whether and how a purely excitatory system can produce bursts of activity which exhibit the same temporal patterning as the bursts of activity in the preterm EEG.

- To investigate effects of topology (i.e. changes in connectivity type, which is relevant from a developmental perspective) on the dynamics of this model. Other authors have shown that topology can have a large effect on dynamics [168–171] and so I anticipate that this will also be the case with the model here.

- To investigate the effect of the dynamics on connectivity formation, the dominant developmental process in the brain during the period at which the preterm subjects were recorded. I hypothesise that any temporal structuring in the dynamics may have an effect on connectivity formation as, for example, the temporal relationship[4] of activity is known to be important later in life in synaptic plasticity [172] and similar mechanisms to synaptic plasticity have been shown to be related to activity-dependent connection formation in the developing brain [173].

[4]Note that the specific temporal relationship shown by LRTCs has, however, not been investigated in relation to plasticity mechanisms or activity-dependent connection formation.

Chapter 2

Long-range temporal correlations in human preterm EEG

2.1 Introduction

As described in the introduction the EEG of very preterm babies is discontinuous with bursts of high amplitude activity separated by periods of very low amplitude apparent inactivity. In this chapter the temporal characteristics of these burst dynamics will be assessed. While summary statistics (mean and maximum) of burst amplitude, duration and IBI (inter-burst interval) have previously been described in the literature [27, 83, 86, 98, 101, 115], a thorough examination of the distributions of these characteristics has not been carried out. Furthermore, no examination of the temporal ordering of these events has been made. Here the distribution of the burst characteristics and the presence of LRTCs in the data are assessed. This analysis aims to determine the temporal dynamics of burst activity during this period of brain development in which activity-dependent mechanisms are crucial and may shed light on the hypothesis that the brain is a (self-organised) critical system.

The bursts of activity can be characterised by slow waves with nested higher frequency oscillations. The slow wave activity is within the delta EEG frequency band (0.5-2 Hz) and so this type of activity has been referred to as a *delta brush* [26]. However, some authors suggest more restrictive definitions of a delta brush based on age, narrow frequency ranges [27] or the phase within the slow wave at which the nested behaviour occurs [83]. Activity in the delta range with nested higher frequency oscillations is present in subjects as young as 23 weeks (the current limit of survival) and this type of activity was clearly present in all the subjects analysed in this study. To avoid confusion in nomenclature, bursts of slow wave activity in the delta range with nested higher frequency oscillations will be referred to in this thesis as *bursts of nested oscillations*

(BNOs).

Before continuing it is important to make clear the other distinctions and similarities between the nomenclature used in this thesis and the terms as they are used in the clinical literature. In particular, while here we consider a BNO to be a single channel event, in previous literature a burst usually refers to activity which takes into account multiple channels. For example, in their investigation *Biagioni et al.* defined a burst as emergent activity (i.e. coming after a period of very low electrical activity) 'in at least half of the leads' [108, 174]. Additionally, inter-burst intervals are usually defined as periods of apparent electrical silence (very low amplitude activity) in all channels. BNOs should therefore not be confused with bursts of activity as described by previous authors, rather BNOs are single channel events which may or may not occur at the same time as activity in other channels. This distinction was chosen as the method of extraction developed directly leads to measurements in individual channels of the recording. From these events it is then possible to examine activity across multiple channels (i.e. bursts as defined in the literature) as will be investigated at the end of the results section of this chapter. Having said this, it is worth noting that 'bursts' of activity have also been described previously by *Palmu et al.* who analysed single channel EEG recordings, i.e. they described bursts as activity in a single EEG channel. By extension to the definition of a BNO as a burst event in a single channel, the terms discontinuity and continuity (though not specifically analysed) can also be thought of here as in terms of a single EEG channel as well as the broader terms used in the literature to refer to the degree of continuity across all electrodes.

Temporal organisation and spatial organisation are also terms that are used with a slightly different meaning in previous literature/the clinical setting. In general in relation to preterm EEG the temporal organisation describes the overall temporal patterning in the EEG, in particular in relation to whether the EEG is largely discontinuous or more continuous, see for example *Anderson et al.* [83]. In this thesis the term temporal organisation also describes the patterning of the EEG across time but the term is used more specifically in terms of the exact ordering in time of BNO events. That is to say, whether the temporal occurrence (i.e. exact timing) of previous BNOs affects the temporal occurrence of future BNOs.

In the literature the term spatial organisation refers to the topographical patterning of the EEG activity. For example, *Anderson et al.* with reference to spatial organisation noted that activity in the delta frequency range was more prominent in occipital regions [83]. Similarly, here differences in activity in relation to topographical locations of electrodes will be investigated[1]. However, the differences investigated will be in terms of the temporal organisation of BNOs at different EEG channel locations and not the spatial organisation of frequencies as was the case in the example given here from

[1]Note that the investigation of effects of EEG channel location is carried out in Chapter 3.

Anderson et al. [83].

This study will analyse the EEG of very young preterm infants born and recorded between 23-30 weeks gestational age. Firstly, a novel algorithm for the efficient detection of the BNOs is developed. Markers of critical dynamics will be examined through assessment of the distributions of burst characteristics (amplitude, duration and the intervals between the bursts) and LRTCs in the organisation of the bursts. I hypothesise that LRTCs will develop with maturation and therefore in the youngest subjects, which lack mature cortical connections, LRTCs are unlikely to be present. I further hypothesise that the distributions of the characteristics may not initially exhibit power-laws but that power-law distributions will be exhibited by the older infants only. As the subjects are recorded at ages which span the period of cortical connectivity formation, the pattern of distributions may be similar to that of *Tetzlaff et al.* [54] who over a period of connectivity formation in cultures observed firstly a super-critical stage (increased number of large events compared with a power-law), followed by a sub-critical stage (fewer large events than is expected by a power-law with activity dying out faster on average), before finally observing critical power-law distributions of the neuronal avalanches.

The main results of this chapter relating to LRTCs in the temporal occurrence of EEG bursts were presented in *Hartley et al.* (2012) [175].

2.2 Methods

Note that all EEG recordings analysed in this thesis, both in this chapter and the following chapter, were recorded by medical staff and I was not involved with these recordings. However, all the analysis and methods of analysis was decided upon and carried out by myself.

2.2.1 Subjects

In this study EEG recordings from 11 preterm babies were analysed. All subjects were born extremely prematurely - with a gestational age of between 23 and 30 weeks and were recorded within the first few weeks of life (median age since birth at the time of recording was 1 day, range: 0-23 days). Recordings were requested by the treating clinician on clinical grounds and recorded in the neonatal intensive care unit. All infants were treated and recorded at either University College Hospital, London, UK or Cork University Hospital, Ireland. Only subjects who did not have abnormal/seizure activity and whose EEG was classified as normal for age by an experienced clinical

neurophysiologist were included in the study. Ethical approval and written parental consent was obtained for use of the data for research purposes.

Subjects were recorded for a median duration of 21.6 hours (range 5.2-24.0 hours). Tables 2.1 and 2.2 list subject details including age, days since birth, recording duration and ultrasound information. Note that 4 out of the 11 subjects had intracranial haemorrhages as observed on transcranial ultrasound. While the difference between subjects with and without intracranial haemorrhage will be examined briefly in the results section, this study did not aim to examine the difference between these two groups. Rather the aim of the study was to firstly develop an extraction method for BNOs and from this to ascertain whether there are signatures of complex dynamics present in the BNOs. However, as haemorrhages are a prevalent problem in this clinical population it is of interest to see whether the BNO dynamics appear to be affected by this neurological sequelae.

2.2.2 EEG recordings

Subjects were monitored using the NicOne digital video-EEG system (Carefusion, Wisconsin USA) with a V32, C32 or O32 amplifier. Electrodes were applied to the scalp using soft paste to achieve impedances of below 5 $k\Omega$ and secured using tape and an elasticated hat. Depending on the subject (and chosen by clinicians depending on the size of the subjects head), two different bipolar montages were used (see Fig. 2.1 and Table 2.2), with electrode positioning according to the 10:20 measuring system modified for neonates [176]. All EEGs were recorded with a midline cephalic reference electrode at FCz and remontaged for bipolar derivation. EEGs were recorded with a sampling rate of 250, 256 or 1024 Hz (see Table 2.2) and were filtered with a low pass filter of 70 Hz, a high pass filter of 0.5 Hz and a 50 Hz notch filter.

Artefact rejection was carried out by visual inspection of the data and sections of recording were rejected on the basis of very high amplitude noise due to loss of electrodes. An example of an artefact of this type is shown in Fig. 2.2. The BNO detection algorithm (see next section) was robust to short artefacts, for example high amplitude activity (spikes) caused by subject movement and lasting for less than a few seconds, such as the example in Fig. 2.2. As these short artefacts were not detected as BNOs there was no need to reject them from the EEG signal passed to the BNO detection algorithm. On the other hand, long high amplitude artefacts preclude the detection of BNOs and so were rejected prior to BNO extraction.

Subject Index	Gestational Age at Birth (weeks + days)	Corrected Age at recording (weeks + days)	Time Since Birth (days)	Ultrasound details	Further details/Follow up
1	23+3	23+4	1	Normal	Normal at 6 months.
2	23+5	23+5	0	Normal	Chronic lung disease.
3	24+5	24+5	0	Normal	Normal at 10 weeks.
4	25+5	25+5	0	Normal	Normal at 9 months.
5	25+5	26+2	4	Intraventricular/ parenchymal haemorrhage (grade 4) left hemisphere, intraventricular haemorrhage (grade 3) right hemisphere.	Laser treatment for retinopathy, developed a left porencephalic cyst, chronic lung disease.
6	24+1	27+3	23	Left germinal matrix haemorrhage (grade 4).	Left transparietal shunt in situ, dilation of lateral, third and fourth ventricles. Porencephalic cyst secondary to germinal matrix haemorrhage, retinopathy of prematurity, chronic lung disease.
7	25+1	27+4	16	Bilateral germinal matrix haemorrhage (grade 1) and cystic changes in post-ventricular white matter.	Died from necrotising enterocolitis.
8	26+1	28+0	13	Bilateral intraventricular haemorrhage involving parenchyma on the right (grade 3 left, grade 4 right)	Chronic lung disease.
9	26+3	28+2	13	Normal	Normal at 12 weeks.
10	30+1	30+1	0	Normal	Discharged at term, well.
11	30+5	30+5	0	Normal	Normal at 6 weeks.

Table 2.1: Subject Age and Clinical Details. This includes gestational age (age at birth) and corrected age (age at recording calculated as the gestational age at birth plus age since birth). Note that 4 out of the 11 subjects had intracranial haemorrhages at the time of their EEG recordings.

Subject Index	Bipolar Montage	Sampling Rate (Hz)	Recording Duration (Hours)
1	1	256	24.00
2	1	256	5.23
3	1	256	12.50
4	1	256	23.98
5	1	250	22.80
6	2	250	18.48
7	2	250	21.59
8	2	250	22.74
9	2	250	12.36
10	2	250	23.96
11	1	1024	10.03

Table 2.2: EEG recording details for each subject. Two different bipolar montages were used: 1=F4-C4, C4-O2, F3-C3, C3-O1, T4-C4, C4-Cz, Cz-C3, C3-T3; 2=F4-C4, C4-P4, P4-O2, F3-C3, C3-P3, P3-O1, T4-C4, C4-Cz, Cz-C3, C3-T3. See also Fig. 2.1.

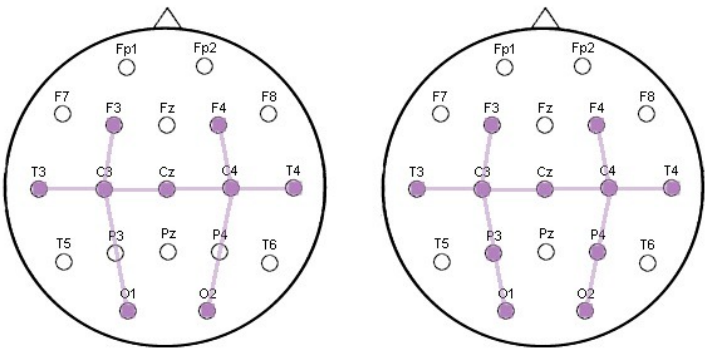

(A) (B)

Figure 2.1: The two bipolar montages used in the study. (A) Montage 1=F4-C4, C4-O2, F3-C3, C3-O1, T4-C4, C4-Cz, Cz-C3, C3-T3; (B) Montage 2=F4-C4, C4-P4, P4-O2, F3-C3, C3-P3, P3-O1, T4-C4, C4-Cz, Cz-C3, C3-T3.

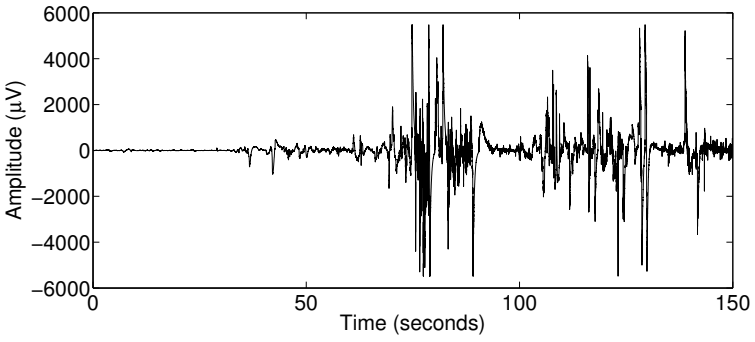

(A)

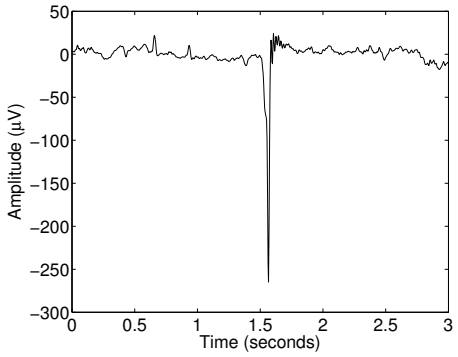

(B)

Figure 2.2: (A) An example of a high amplitude artefact lasting for longer than a few seconds and likely due to the loss of the electrode or an increase in the electrode impedance. Note the departure from normal activity at around 30 seconds in this epoch. High amplitude artefacts remained for the rest of the record in this particular EEG channel (subject 4, C3-O1) and so this channel was rejected throughout this period - see Table 2.4. (B) An example of a short artefact which the BNO extraction algorithm is robust to (i.e. this is not detected as a BNO).

2.2.3 Extraction of BNOs

BNOs have a complex nature, with higher-frequency activity nested within slow wave oscillations, and so any extraction algorithm should make use of these characteristics. Simple thresholding on the basis of the amplitude of the EEG activity alone would increase the number of false-positives compared with a more complex extraction algorithm, as, for example, high amplitude activity is observed in the EEG due to movement artefacts, see Fig. 2.2. A further argument against a simple threshold is that others have shown that thresholding (i.e. with a single value) of a stochastic signal can produce a signal with power-law statistics [155]. However, extraction of a well-defined characteristic through combining frequency and amplitude measures implies that if, for example, power-law statistics are observed, they will necessarily relate to this type of activity within the signal.

Previous authors have devised algorithms for the automated detection of bursts which have been based on single amplitude thresholds of the EEG signal [84] or through thresholds applied to the results from wavelet analysis (of short epochs) [29, 91]. *Palmu et al.* [177] use a more complex approach in the form of a non-linear energy operator. This takes into account the amplitude of a band-pass filtered signal at several consecutive time points and requires the resulting value to be above a threshold for a minimum duration. However, this algorithm only takes into account a single band-pass filtered signal and so again does not fully utilise the complexity of the data.

A novel extraction method which considers the co-occurrence of each of the components, a slow wave (0.5-2 Hz) and higher frequency oscillations (8-22 Hz), was devised. These frequency ranges were obtained from the literature as frequencies that encapsulate BNO activity [83, 178].

The BNO extraction algorithm is as follows. Let $x(t)$ be the EEG signal from a single channel. From $x(t)$ three time series are obtained:

- $x_1(t)$, the low-pass filtered signal at 2 Hz,
- $x_2(t)$, the band-pass filtered signal at 8-22 Hz and
- $x_3(t) = x(t) - x_1(t)$, the signal with the low-frequency components removed.

For each of these three signals, the absolute value of the Hilbert transform was taken: $h_{i=1,2,3}$. The absolute value of the Hilbert transform defines the amplitude envelope of the signal, which at each point is the maximum of the rectified signal (for examples see Fig. 2.3). Calculation of the Hilbert transform can therefore lead to an extraction algorithm which is based on the amplitude of each of the three signal components. Importantly it is based on the rectified signal, which is of interest here as bipolar EEG

signals are analysed and so a negative deflection carries as much information as a positive deflection from baseline.

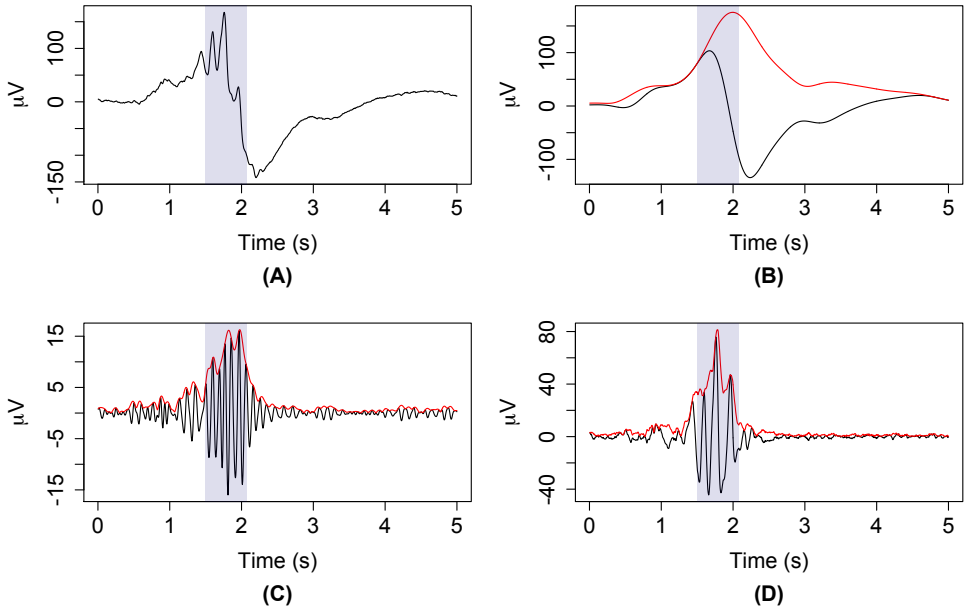

Figure 2.3: (A) A section of EEG signal $x(t)$ (for signal annotation see text) which contains a BNO. Note that the EEG signal is filtered with a high pass filter at 0.5 Hz, a low pass filter at 70 Hz and a notch filter at 50 Hz prior to extraction of BNOs and the data shown here is after these filters have been applied. (B) The low-pass filtered signal, $x_1(t)$. (C) The band-pass filtered signal, $x_2(t)$. (D) The signal with the low-frequency components removed, $x_3(t)$. The absolute value of the Hilbert transforms of each are shown in red. The highlighted region indicates the section of the signal extracted by the algorithm as a BNO.

For each of the signal components a confidence value $c_{i=1,2,3}$ relating to the amplitude of the component is calculated:

$$c_i(t) = 1 - exp\left(\frac{ln(0.05)h_i(t)^2}{q_i(t)^2}\right)$$

where $q_1 = 50,\ q_2 = 10,\ q_3 = 10$ are amplitude thresholds for the slow and nested high-frequency components of the BNO taken from the literature [83, 178]. The values of c_i are between 0 and 1 and if $h_i = q_i$ this yields a value of $c_i = 0.95$. Thus, where the signal components have a high amplitude (i.e. an amplitude greater than q_i) the value of $c_i > 0.95$.

The final step of the algorithm combines these measures for the three components, leading to a value reflecting whether all three components co-occur with significant amplitude. It can therefore be thought of as a confidence value on the presence of nesting:

$$c(t) = \prod_{i=1}^{3} \sqrt[3]{c_i(t)}$$

From this, a BNO event was defined as a contiguous section of data for which c was greater than or equal to the *extraction threshold*, see below. Consecutive events that occurred within 0.5 seconds of one another were counted as one. Similarly any events of duration less than 4/22 of a second were discounted to ensure that there was at least one entire oscillation at the lowest frequency of the high-frequency component (8 Hz) but also 'sufficient' (so as to be less effected by noise) higher frequency activity (22 Hz). As consecutive values of c may fluctuate between values that are above and below the extraction threshold, a moving average of c was taken, with a window size of 0.5 seconds, to smooth the time series before extracting the events. This window size was chosen as it is the largest interval that does not interfere with intervals between consecutive events.

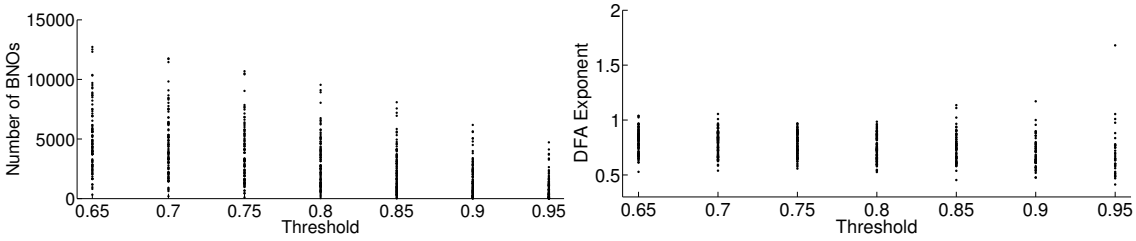

(A) (B)

Figure 2.4: Detection of BNOs was carried out initially at different thresholds in order to determine a suitable detection threshold. (A) The number of events detected from each subject and channel at different threshold levels. (B) DFA exponent of IEI sequences - one of the measures used in analysis, see the next section - plotted for different thresholds. The DFA exponents are relatively robust to changes in threshold, though for higher thresholds the variance increases due to the lower number of detected BNOs. Also, for high thresholds some BNOs in the data were missed (observed through visual inspection). For future analysis the threshold was set to 0.80.

Initial analysis was carried out on a range of extraction thresholds between 0.65 and 0.95. Analysis carried out for each of the extraction thresholds, see Fig. 2.4, revealed that the degree of correlations (that is the Hurst exponent, used to quantify LRTCs in the data - see below) were robust to changes in the threshold provided that the number of events remained sufficiently large for correlations to be examined (see below). Larger thresholds led to the detection of fewer events, missing BNO events that can be observed by visual inspection of the data. On the other hand, a low threshold increased the likelihood of false positives. Therefore, a threshold of 0.80 was chosen as this corresponds to high thresholds for each of the three components c_i ($0.8 > 0.92^3$).

To summarise, this novel algorithm combines amplitude and frequency measures to extract areas of the signal (BNOs) which are characteristic of the preterm EEG. The combination of both amplitude and frequency components produces an extraction method that is much more robust than simple thresholding of signal amplitude.

2.2.4 Analysis of BNO activity

From the extraction algorithm, BNO events were defined by a start and end time. Three key characteristics of the BNOs were considered:

- The time between BNO events defined as the difference between the start time of one event and the end time of the event immediately preceding it. This will be termed the *inter-event interval (IEI)*, see Fig. 2.5.
- The *duration* of a BNO, defined as the difference between the end time and start time of an event.
- The *amplitude* of the BNO.

Two measures of BNO amplitude were assessed. The *peak amplitude* was defined as the maximum of the rectified signal during the BNO. Secondly, the *total amplitude* of the BNO was calculated as the sum of the rectified signal. This definition takes into account the event as a whole and is perhaps more reflective of the underlying activity. For example, an event which is formed from a large number of neurons firing may have a very high amplitude and be short in duration or it may have a relatively low amplitude but have a longer duration and therefore the second method will reflect this better. On the other hand, peak BNO activity may reflect more synchronised activity and so is also of interest.

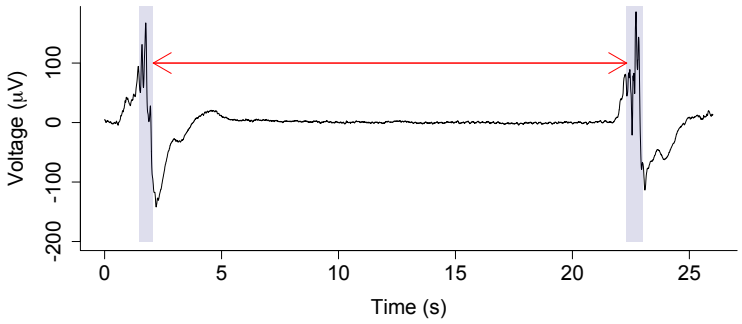

Figure 2.5: An example of two consecutively detected BNOs (shaded area). The arrow indicates the IEI - the time between the events. This EEG signal was filtered with a high pass filter at 0.5 Hz, a low pass filter at 70 Hz and a notch filter at 50 Hz.

Note that the definition of an IEI is not the same as the definition of an inter-burst interval (IBI) in the preterm EEG literature. Previous research has defined IBIs as periods of low amplitude in *all* electrodes/channels [86, 98, 108, 174]. Here an IEI is a period of no BNOs in a *single* channel and thus we are likely to obtain IEIs that are much longer than the maximum IBIs observed in previous studies. The IEI definition was chosen as it is a clearly defined statistic which comes directly from the extraction

method. However, IBI and synchronicity across channels will also be briefly examined at the end of this chapter to compare with previous results.

For each of the characteristics of the BNO activity (IEI, duration and amplitude) firstly the distribution will be examined. Secondly, the presence of LRTCs will be assessed in the temporal sequence of BNOs. These measures will allow us to assess the 'critical' nature of preterm brain activity.

Data distributions

The probability distribution of each of the BNO characteristics (IEI, duration, peak and total amplitude) will be assessed. As discussed in Chapter 1 a power-law distribution is linear on a double-logarithmic plot and so each of the probability distributions will be assessed in this way. However, whilst this method can be used to easily rule out a power-law distribution if the plot is not linear, if it is linear (over a range) this is not a robust method for determining a power-law. Thus, the statistical testing of *Clauset et al.* [134] will also be used to test the likelihood that the data follows a power-law distribution. As described previously, this analysis calculates the power-law, with exponent γ which best-fits the data, from a starting point x_{min} up to the largest data point (i.e. it fits the tail of the distribution, or the whole distribution if the lower data points follow the same distribution as the points with larger values). The p-value is calculated by comparing distributions with the same number of points as the empirical distribution drawn at random from this power-law distribution with the empirical distribution itself. So in this case a p-value $p \geq 0.1$ indicates that the data is well fit by the power-law distribution.

Analysis will be carried out for each channel of the EEG separately and also for the pooled distribution (combining data from all channels) if the distribution from each channel appears similar. This pooled approach can be used when analysing the distribution as it does not matter about the order of the data only the data values (the data ordering can be shuffled and it will still have the same distribution). This will not be possible when examining LRTCs, where temporal ordering is important and shuffling the data does not give the same result.

Note that the extraction algorithm makes use of amplitude statistics and therefore also imposes an effective minimum amplitude on the data (though as the extraction algorithm examines three different components there is no strict threshold in the overall BNO amplitude itself). Similarly, a minimum IEI of 0.5 seconds and a minimum duration of 2/11 seconds was imposed by the algorithm. This was necessary to avoid spurious results of, for example, very short "BNOs" which are actually noise or the separation of a single BNO into two events. However, it is important to bear these constraints in mind when analysing the distribution of these characteristics.

LRTCs in BNO amplitude, duration and IEIs

As the EEG of very premature neonates is discontinuous LRTCs cannot be assessed in the same way as previous authors investigating neurological data have done - by examining fluctuations in the amplitude of continuous oscillations. Instead an approach that has been used for examining inter-heartbeat intervals (i.e. discontinuous data) is used [141]. For each of the BNO characteristics the corresponding *sequence* for each EEG channel was defined as the sequence of the data given by the temporal order in which the data values occurred within the EEG recording. For example, if through BNO extraction a particular EEG channel has an IEI of 1.20 seconds, then the next IEI is 0.67 seconds, and the next is 5.34 seconds and so on, then the IEI sequence will necessarily be given in the order $\{1.20, 0.67, 5.34, ...\}$. Similarly, if the BNOs preceding these IEIs were such that the first BNO had a peak amplitude of 55 μV, a total amplitude of 342 μV and a duration of 0.54 seconds, then the next BNO has a peak amplitude of 84 μV, total amplitude of 921 μV and a duration of 2.3 seconds, and the next BNO has a peak amplitude of 121 μV, a total amplitude of 1025 μV and a duration of 2.1 seconds, then the sequence of peak amplitudes will necessarily be given in the order $\{55, 84, 121, \ldots\}$, the sequences of total amplitudes will be in order $\{342, 921, 1025 \ldots\}$ and the sequence of durations will be $\{0.54, 2.3, 2.1\}$.

The presence of LRTCs in these sequences were assessed through estimating the Hurst exponent. The presence of LRTCs in the sequences would indicate a temporal complexity in BNO IEI, duration or amplitude. For example, LRTCs in BNO IEI would indicate that the temporal occurrence of BNOs follows a complex temporal pattern with, on average, long (short) IEIs followed by long (short) IEIs. Similarly, BNOs with long (short) durations will be followed by BNOs with long (short) durations and BNOs with high (low) amplitude will be followed by BNOs with high (low) amplitude. As was stated in Chapter 1, in this study we used DFA and the Whittle estimator to calculate estimates of the Hurst exponent. These methods were chosen as they have been shown to produce more reliable estimates than other methods [162].

Sequences of length less than 1000 were excluded from the analysis to ensure that robust estimates of *long*-range correlations were obtained (i.e. LRTCs cannot be examined across very short sequences as these correlations are, by virtue of the sequence length, short and it cannot be ascertained whether they continue beyond the sequence length). With regards to DFA, the minimum box size was set to 5 (that is the minimum box size was set to include 5 data values). The maximum was set as 1/10 of the length of the sequence unless otherwise stated, which is the recommended maximum box size for DFA [179] and analysis was carried out with 25 different window sizes equidistantly placed on a logarithmic scale. For IEI sequences (see results section), DFA was also carried out with a maximum box size of 1/4 of the length of the IEI sequence. Such analysis should be taken with caution as with increased box sizes averages are necessarily taken across

fewer values (for example with a box size of 1/4 of the length of the data, as the boxes do not overlap, 4 boxes encompass the whole data and an average fluctuation value for this box size is therefore calculated from these 4 values) and so the statistics become less robust at larger box sizes. However, if there is a strong correlation between the exponent calculated for larger box sizes and that calculated with the more conservative maximum box size of 1/10 of the length of the data, combined with a DFA plot with the same trend for larger box sizes as for smaller box sizes, then this provides evidence that correlations (if they exist) extend across a broader range of timescales [44]. This is important as it suggests further that any correlations observed are perhaps only limited by the length of the recording and that they are proper long-range correlations.

Statistical Analysis

In order to ascertain whether the results are significant the exponents of the actual sequences were compared to exponents obtained from randomly shuffling the data sequences. This method is chosen as it retains most of the information from the original sequence, such as mean, minimum, maximum and the overall distribution of the data, while changing the characteristic of interest - the temporal organisation of the sequence. Any temporal correlations that are present in the original sequence will be destroyed by the shuffling process and so shuffled sequences should have a Hurst exponent of approximately 0.5 (0.5 is the asymptotic limit for an infinite sequence length).

For each BNO characteristic, each sequence was shuffled 5000 times and the exponents for the shuffled sequences calculated using both DFA and the Whittle estimator. Then for each subject, and for both estimates of the Hurst exponent, the original exponents were compared with the distribution of the shuffled exponents using two approaches. Firstly, the difference in the means of the distribution of the exponents of the original sequences for each subject (for all channels) are compared with the pooled distribution of shuffled sequences for that subject using the non-parametric Wilcoxon Mann-Whitney test. This test was used after applying the Anderson-Darling test of normality to the shuffled data. In most cases the null hypothesis (that the data has a normal distribution) was rejected and so a non-parametric test for comparison of the exponents was carried out. This test provides an understanding of the overall distribution of exponents for that subject.

To examine the significance of the exponents of individual sequences (i.e. not just the distribution for the subject across all channels), the individual exponents were also compared directly with the distribution of exponents for the shuffled data of that sequence. The individual sequence was considered to exhibit LRTCs if the exponent of the original sequence fell in the upper 5% tail of the shuffled distribution. This approach was used previously by *Linkenkaer-Hansen et al.* 2005 [142]. As this compares a single sequence to the corresponding shuffled distribution it provides a more stringent test

than the first approach when considering the exponents on an individual basis rather than across the subject as a whole.

Subject Comparison with Fixed Length Sequences

As the recording length for each subject differed and the number of BNOs also differed (between subjects and also within a single subject between channels) in order to better compare subjects, fixed length sequences were also analysed. The sequence length for this analysis was chosen as 1000, the minimum sequence length included in the study. Each fixed length sequence was taken as the first 1000 points in the original sequence. For fixed length sequences both DFA and Whittle estimates of the Hurst exponents were calculated.

The effect on the estimates of the Hurst exponent of the corrected age (gestational age plus age since birth) of the subject was assessed for both the full-length and the fixed length sequences. Effects were assessed using a linear regression comparing the Hurst exponent with respect to corrected age.

2.3 Results

BNO events were detected in all channels of all the subjects assessed in this study. The average number of BNOs per hour was 200.3 (range: 85.4 - 329.3). Table 2.3 lists the average number of BNOs for each subject, averaging over all channels and also averaging over only those channels remaining for analysis once the channels with data sequences less than 1000 (i.e. those channels where LRTCs were not able to be assessed) were rejected. Table 2.4 lists EEG electrodes that were rejected, both because of artefacts and also those with short sequence lengths.

Previous studies have shown that neurological outcome is worse in patients with longer inter-burst intervals (defined as a period of low electrical activity in all electrodes) [101, 104]. In line with this, the subjects in this study with intraventricular haemorrhages had significantly (Mann-Whitney test, $p = 2.46 \times 10^{-10}$) lower numbers of events per hour (110.1 ± 38.9) compared to subjects without intraventricular haemorrhages (251.7 ± 55.1). Fig. 2.6 shows the number of BNOs per hour plotted against the corrected age for all the subjects. As all the subjects with haemorrhages had a similar age (and these subjects were found to have significantly lower numbers of BNOs) in the middle of the age range assessed, it was difficult to ascertain whether the number of BNOs varied with age.

Subject Index	BNO rate (before rejection)	BNO rate (rejected)
1	262.0	262.0
2	197.9	236.5
3	286.3	286.3
4	247.6	247.6
5	168.1	168.1
6	67.5	85.5
7	63.7	94.4
8	86.9	92.3
9	329.4	329.4
10	101.8	148.6
11	195.2	251.8

Table 2.3: Average number of BNO events per hour for each subject (also averaged across all channels for that subject). 'Before rejection' includes all channels for which BNO detection was carried out (i.e. except those that are rejected due to artefacts, see Table 2.4). 'Rejected' includes only those channels whose sequences are long enough for LRTC sequence analysis, see Table 2.4. If a sequence was rejected because it was too short (had less than 1000 data points) then, as the length of the sequence depends on the number of BNOs, this channel will also have a low average number of BNOs per hour. When this is removed from the statistics the average number of BNOs per hour will necessarily increase - as is seen in the table. Those subjects whose averages do not change after rejection are the subjects that did not have any rejected channels, see Table 2.4. Note that subjects 5-8 had haemorrhages as observed on ultrasound.

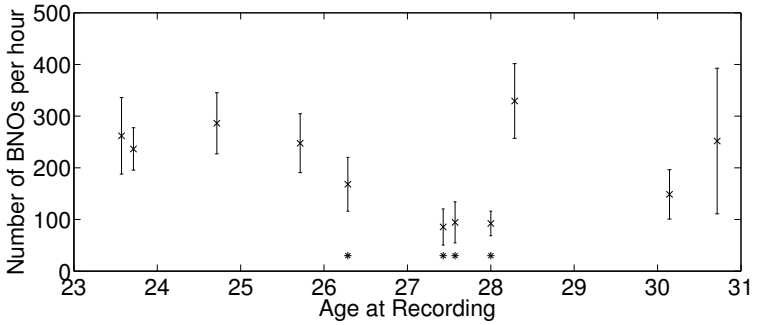

Figure 2.6: Average number of BNO events for each subject plotted against corrected age (age at time of recording calculated as gestational age at birth plus age since birth). Error bars indicate standard deviation. Averages were calculated after excluding those channels with less than 1000 BNOs - see also Table 2.3. Asterisks indicate subjects with intraventricular haemorrhages.

Subject Index	Remaining channels	Reasons for channel exclusion	Other exclusions
1	All	NA	Channels 1,2,5 and 6 were analysed from the start to 13.54 hours. Channels 3,4,7,8 were analysed from the start to 22.83 hours.
2	1-3,5,7,8	IEI sequences less than 1000.	None
3	All	NA	Channels 6 and 7 were analysed from 2.09 hours to the end of the recording.
4	All	NA	Channels 6 and 7 were analysed from the start to 9.88 hours. The other channels were analysed from the start to 20.41 hours.
5	All	NA	None
6	1,5-7,9,10	Channel 4 rejected due to large artefacts throughout. Others had IEI sequences less than 1000.	None
7	1,4,5,7,10	IEI sequences less than 1000.	None
8	1-8,10	IEI sequences less than 1000.	None
9	All	NA	None
10	1,4,6-8,10	IEI sequences less than 1000.	Channels 1,2 and 7 were only analysed from 3.01 hours to the end, channels 5 and 6 from 10.67 hours to the end and channels 8 and 9 from 10.69 hours to the end.
11	1,2,4-6,8	IEI sequences less than 1000.	None

Table 2.4: Channels that were rejected from analysis for each subject. Most rejections were due to the low number of BNO events detected in the signal of that channel. 'Other exclusion' indicates sections of channels that were rejected, before the extraction algorithm was applied, due to the occurrence of high amplitude artefacts likely caused by loss of the recording electrode/an high impedance between the electrode and the subjects scalp.

2.3.1 Distributions of the data

Distributions for each of the characteristics (IEI, duration and peak and total amplitude) were analysed for each channel and subject separately. Some subject differences between the distributions were observed for IEIs, but not the other three characteristics. Thus, for duration, peak amplitude and total amplitude only the pooled (from all subjects and channels) distribution is shown here and is sufficient to understand fully the distribution of these characteristics.

IEI distributions

Across all subjects and channels (including those with less than 1000 IEIs) the mean IEI was 21.5 seconds and the median was 9.0 seconds. Excluding those channels with less than 1000 IEI the mean IEI was 18.3 seconds, median 8.5 seconds.

For each channel of the same subject the IEI distribution appeared approximately the same (data not shown), though some of the channels had few IEIs and so the distribution could not be properly evaluated. However, the similarity of the distributions enabled the IEIs to be pooled across channels to obtain a subject distribution. The distribution for each individual subject is given in Fig. 2.7. Differences in the distributions between subjects can be seen - some subjects have a 'humped' distribution while other subjects have a smoother distribution. Interestingly, with the exception of subject 10, those subjects with a 'humped' distribution were also those with intraventricular haemorrhages.

Fig. 2.8 shows the IEI distribution pooled across all subjects and channels along with the cumulative plot of this distribution. The distribution does not appear to follow a power-law when examining the log-log plot by eye - the distribution appears to have a change in behaviour at larger IEI values. The cumulative distribution is used in the method of *Clauset et al.* [134] in order to calculate the goodness of fit of the data to a power-law distribution. The cumulative distribution appears to have perhaps two different linear trends. The statistical analysis necessarily fits the tail of the distribution and yielded a p-value of $0.066 \not\geq 0.1$. Therefore, this result indicates that the (tail of) the distribution of IEI is not well-fit by a power-law. Note that an inherent problem with this method is that it will only fit the tail of the distribution. As there is a lower probability of observing these high IEI values, this analysis also fits the smaller part of the distribution and the section that is likely to be most noisy. However, from examining the distribution by eye, in this case it is not surprising that the distribution failed to pass the statistical testing in comparison with a power-law distribution.

Though the IEI distribution does not appear to be a power-law, it does appear to have a so-called 'fat tail', i.e. there are a number of very large IEIs. Another type of

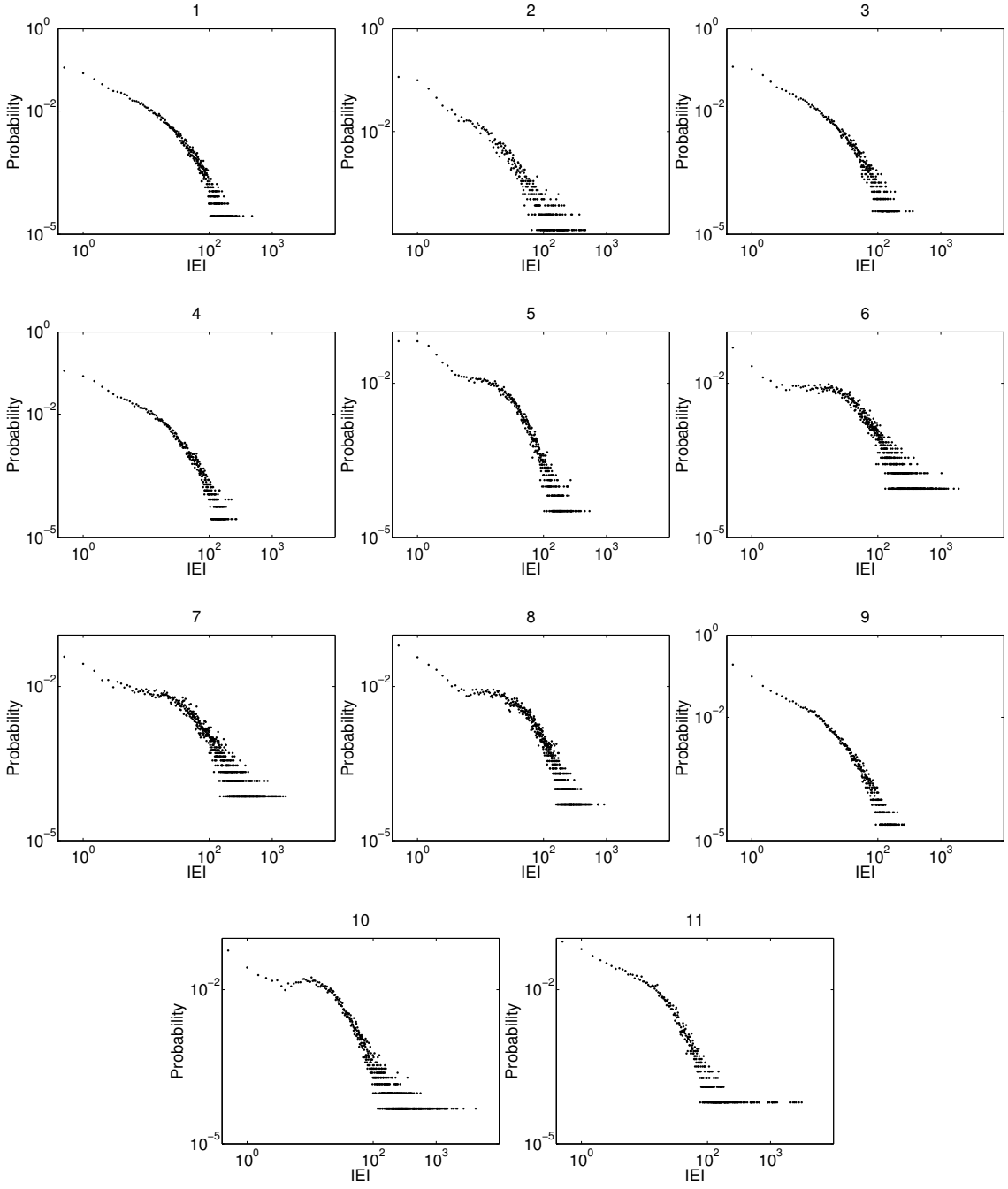

Figure 2.7: IEI distribution for each of the subjects (as labelled: 1-11). The distribution is obtained by pooling the IEIs from all channels (including those with less than 1000 IEI). Note that some distributions (subjects 5-8,10) appear to have a 'hump' while others are smoother. Interestingly except for subject 10 these subjects are the subjects with haemorrhages.

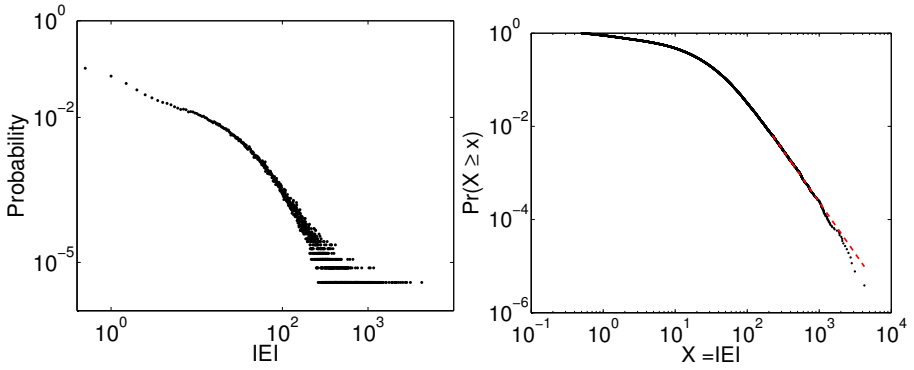

(A) (B)

Figure 2.8: (A) IEI distribution pooled from all subjects. (B) The corresponding cumulative distribution and the best-fit of the distribution to a power-law (red). This is calculated using the method of *Clauset et al.* [134] which finds the portion of the data (from a start size of x_{min} to the largest data point) best fit by a power-law. The best fit to the data yielded values of $\gamma = 3.21,\ x_{min} = 223.9,\ p = 0.066$.

distribution that has a fat tail is a log-normal distribution. To examine evidence for this type of distribution the logarithm of the data was examined, see Fig. 2.9. This logarithmic data appeared to have distributions with two peaks, though the first peak was not apparent in all subjects. This result suggests that the IEIs may in fact have a bimodal log-normal distribution. Unlike the presence of a power-law this does not suggest that the brain is in a critical state. Having said this, it is worth recalling that other critical systems do not exhibit power-law distributions in all characteristics. For example, the sandpile model has an exponential distribution of inter-avalanche intervals [56, 138]. It is important to consider other characteristics and signatures of critical dynamics before concluding anything about the critical nature of the early developing brain.

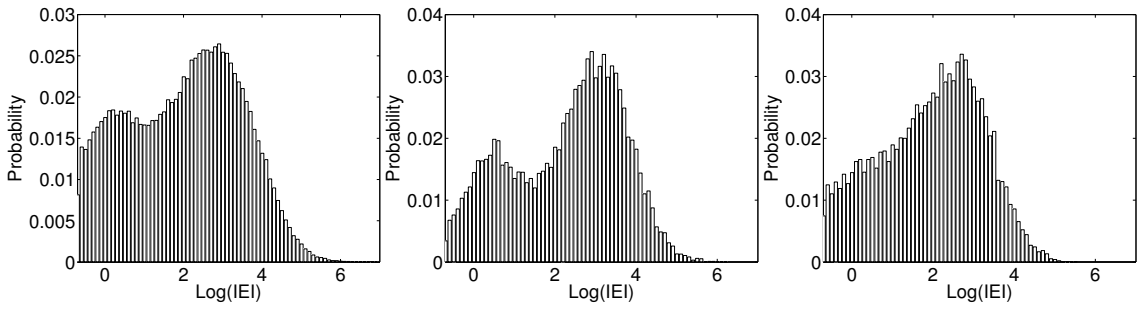

(A) (B) (C)

Figure 2.9: (A) Pooled distribution across all subjects of the logarithm of IEIs. The distribution appears to have two peaks, though this was clearer in some subjects than others. (B) The distribution of the logarithm of IEIs for subject 5 - this subject showed the clearest 2 peaks in its distribution. (C) The distribution of the logarithm of IEIs of subject 11. This subject did not have a clear first peak in the distribution.

BNO duration distributions

Across all subjects the mean BNO duration was 0.64 seconds, median 0.48 seconds. Fig. 2.10 shows the distribution of BNO durations pooled from all subjects and plotted on a double-logarithmic scale. Individual subject distributions were similar (data not shown). The distribution does not appear to follow a power-law, and this is also apparent following the statistical analysis which found $p = 0.04 \not\geq 0.1$.

Fig. 2.11(A) shows the distribution of the logarithm of BNO durations. This suggests that the durations may follow a log-normal distribution with a single peak, though the distribution does appear to be slightly skewed.

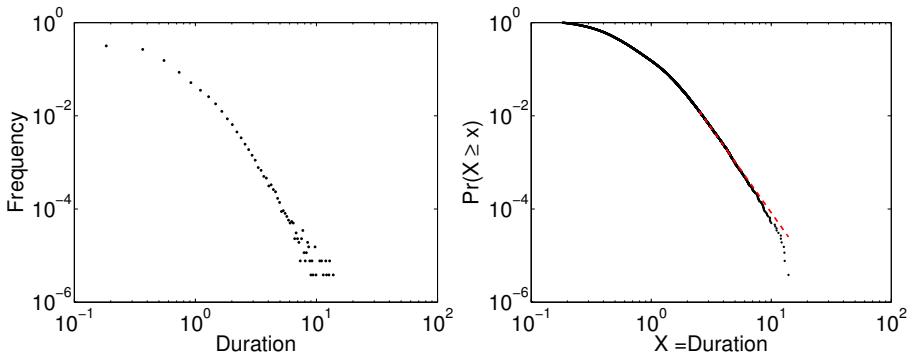

(A) (B)

Figure 2.10: (A) Distribution of BNO duration pooled from all subjects. (B) The corresponding cumulative distribution. The best-fit of the data to a power-law is shown by the red line which has $\gamma = 4.63,\ x_{min} = 2.50,\ p = 0.04$.

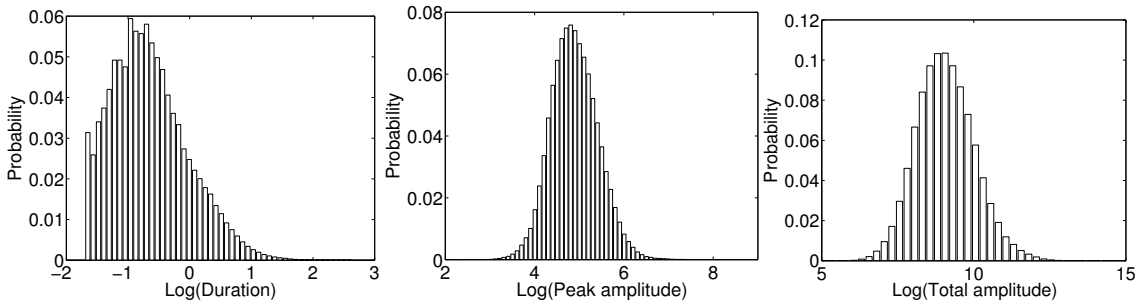

(A) (B) (C)

Figure 2.11: Pooled distributions of the logarithm of (A) BNO duration, (B) peak amplitude and (C) total amplitude. Both amplitude distributions appear from this to be log-normal distributed. The duration distribution may also be log-normal distributed, though there is evidence for a slightly skewed distribution.

BNO amplitude distributions

Across all subjects the average peak amplitude was 154.3 μV (mean) and 130.0 μV (median). The distribution of amplitudes pooled across all subjects is shown in Fig. 2.12 along with the cumulative distribution. There was no evidence of the distribution following a power-law through statistical testing ($p = 0$). Furthermore, in the overall distribution there are clearly fewer BNOs with low amplitude than would be expected from a power-law. This likely relates to the BNO extraction algorithm, which imposed a threshold on amplitudes of the different frequency signals of interest. Note that the detected events with very low amplitudes are lower than the amplitude of the slow wave (50 μV) that leads to a value of $c_1 = 0.95$. For such events to be above threshold they must have amplitudes in the other two components that are much higher than their threshold values. Therefore, BNOs with low amplitudes are less likely to be detected and this distribution at low amplitude values should be taken with caution.

Considering the other end of the distribution there are several very high amplitude 'BNOs'. These are clearly outliers and unphysiological noise that was detected. The largest realistic (i.e. physiological activity) BNO recorded on the EEG is likely to approximately 1000 μV. For example, *Vanhatalo et al.* [94] stated that the largest amplitude of the *slow* wave activity (of SAT events) was 700 μV (note the average age of the subjects in this study was 35 weeks conceptional age). Similarly, *Biagioni et al.* [108] observed delta waves within delta brushes with a maximum amplitude of 450 ± 122.5 (mean $\pm$ standard deviation, across one group of children aged 27-28 weeks). From visual examination of the detected BNOs the maximum amplitude appeared to closer to 1000 μV. This difference is likely due to the fact that our amplitude includes the whole BNO and not just the slow wave and the fact that some of the subjects were younger than the subjects studied by the other authors. Additionally, the recordings studied were much longer than those studied by the other authors (which were up to 2 hours). As these large events are very rare, then a longer recording time is more likely to lead to their detection than a shorter recording. However, the 'BNOs' that were detected by the extraction algorithm but had an amplitude larger than this did not appear to be physiological. Considering 'BNOs' with a peak amplitude greater than 1000 μV as outliers, 0.09% of all the detected BNOs (across all subjects) was classed as an outlier. These were removed from the sequence analysis when investigating LRTCs. The total amplitudes of the corresponding BNOs were also removed when analysing the sequences of BNO total amplitude.

Across all subjects the average total BNO amplitude (recall that this is the sum of the amplitude of the rectified signal throughout the BNO) was 14217 μV (mean) and 8277 μV (median). Fig. 2.13 shows the pooled distribution of total amplitudes across all subjects and the corresponding cumulative distribution. This distribution has a similar shape to that of peak amplitude and for the same reasons should be taken with caution.

Interestingly, the distribution did pass statistical testing of a power-law distribution ($p = 0.90$). However, this test (as can be seen in Fig. 2.13) does just test the tail of the distribution.

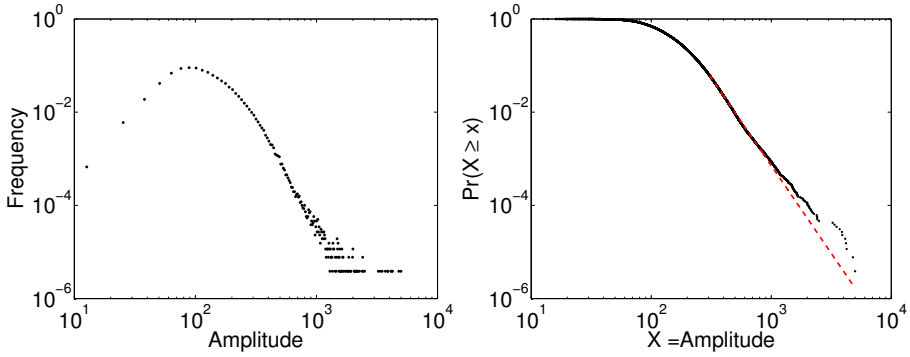

(A) (B)

Figure 2.12: (A) Distribution of peak amplitude pooled across all subjects and channels. (B) The equivalent cumulative distribution. The red line indicates the best power-law fit to the data with $\gamma = 4.77,\ x_{min} = 307.01,\ p = 0$.

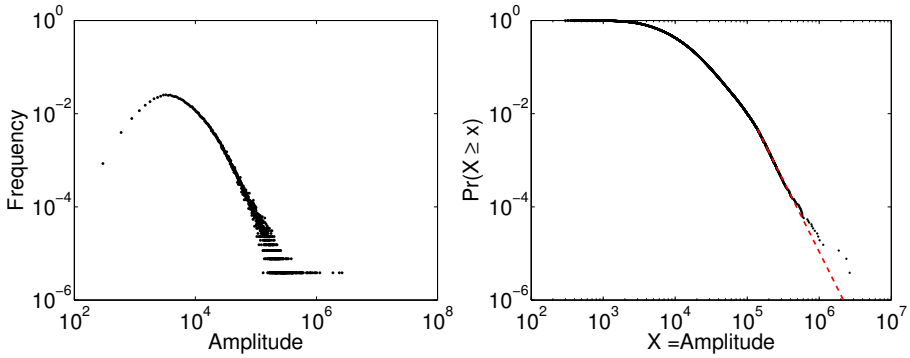

(A) (B)

Figure 2.13: (A) Distribution of amplitudes calculated using the second approach and pooled from all subjects. (B) The corresponding cumulative distribution. The best fit to a power-law is found to be the red line where $\gamma = 4.08,\ x_{min} = 1.40 \times 10^5,\ p = 0.90$.

The distribution of the logarithm of the data for both peak and total amplitude appeared to show that the data was log-normally distributed, see Fig. 2.11(B,C). These distributions were much clearer than in the cases of IEI and duration distributions. However, again some caution is needed when considering the amplitude distributions as they are likely to be affected at low values by the necessary amplitude thresholds imposed on the different BNO components.

A note on the analysis of distributions

All the BNO characteristics take real values and so there is no straightforward way in which to bin the data as would be the case if only integer values could be taken. The histograms in previous plots (and in future plots apart from in this section) where constructed with bins of interval width set to the minimum value of that characteristic. This was chosen as it provides a consistent binning measure. However, note that if a different bin width is used then the distribution can appear completely differently, see Fig. 2.14 - using a different bin width when examining the amplitude distributions they now appear closer to a power-law then was the case with the previous binning, see Figs. 2.12,2.13. Some analysis by previous authors has not encountered this problem if the values investigated were integer values which give rise to clearly defined values with which to plot the data. For example, neuronal avalanche size is defined by the number of electrodes that contribute to that avalanche[2]. However, this further highlights the need for caution when assessing power-laws in data. The same is true for the binning of the logarithmic data (Figs. 2.9,2.11).

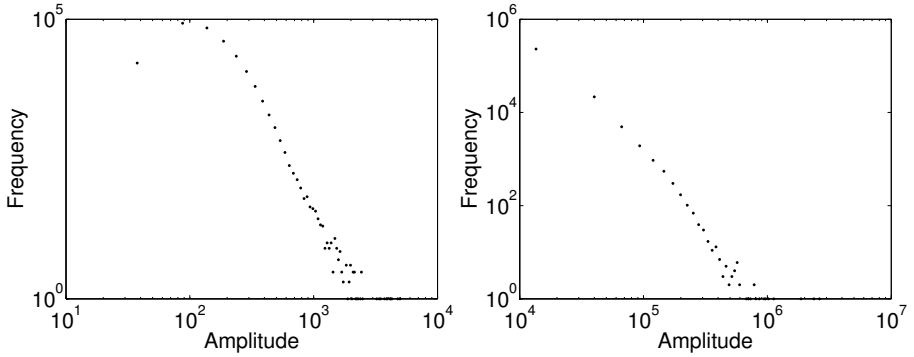

(A) (B)

Figure 2.14: (A) Distribution of peak amplitudes and (B) total amplitudes pooled from all subjects, constructed from 50 equally spaced (on a linear scale) bins. These plots should be compared with Figs. 2.12,2.13 respectively to see the difference the bin width can have on the appearance of the distribution.

2.3.2 Analysis of LRTCs in data sequences

LRTCs in sequences were assessed through estimation of the Hurst exponent. Sequences were constructed according to the temporal ordering of data (IEI, BNO duration and amplitude) as it occurred in the EEG recording. Recall that a Hurst exponent of 0.5 indicates no or short-range correlations in the data, while a Hurst exponent of

[2]However, neuronal avalanche analysis involves thresholding of activity at electrodes to determine whether an electrode is 'active' at a particular time [49, 50]. Therefore changing this threshold may change the distribution.

$0.5 < H < 1.0$ indicates LRTCs in the data. The Hurst exponent of sequences was estimated using DFA and the Whittle estimator.

It is important to note that while the distributions of the characteristics did not exhibit power-law distributions, assessing the Hurst exponent of the temporal sequences of the data is still a worthwhile analysis. LRTCs (a power-law in the autocorrelation of the signal) can result from data with any distribution not just a power-law. For example, fractional Gaussian noise is a well known example of a process that exhibits LRTCs but the underlying distribution of the points is a Gaussian [139] (see also Appendix 1). It is the *temporal relationship* of the points that is important in this analysis not the distribution of the points. LRTCs in temporal sequences of data implies that there is a 'memory' effect in the data such that large (small) data values are on average followed by large (small) data values. Conversely, a power-law distribution in the data does not imply the existence of LRTCs in the data ordering. For example, drawing points at random from a power-law distribution will not give rise to a process with LRTCs. This is because there is no memory effect from drawing data at random.

IEI sequences

Fig. 2.15 shows an example IEI sequence and the corresponding DFA plot. For both DFA and Whittle analysis, all IEI signals had Hurst exponent estimates greater than 0.5 indicating the presence of LRTCs. Across all the sequences, the average Hurst exponents were 0.68 (DFA, range 0.55-0.81) and 0.63 (Whittle, range 0.53-0.77). There was no difference in Hurst exponents between subjects with and without intraventricular haemorrhage in either DFA ($p = 0.07$, Wilcoxon Mann-Whitney test) or the Whittle estimates ($p = 0.06$).

For DFA, all resultant plots were analysed (see example in Fig. 2.15) and it was observed that they followed a single straight line behaviour. This is important, as it indicates that the same trend occurs across all box sizes, i.e. the same degree of correlations were observed and there is no other behaviour present. Spurious estimates of the Hurst exponent can occur if, for example, there are underlying trends in the data which can lead to so-called crossover behaviour in the DFA plot [179]. However, this was not the case for any of the plots here.

Each of the IEI sequences was randomly shuffled 5000 times and the DFA and Whittle estimates of the Hurst exponents calculated for these new sequences. The shuffled sequences had distributions of exponents with mean $\pm$ standard deviation of 0.51 ± 0.02 (DFA) and 0.50 ± 0.02 (Whittle). Thus, the shuffled distributions have exponents which are consistent with the theoretical asymptotic value of $H = 0.5$ for uncorrelated noise, as is expected from randomised data. Fig. 2.16 shows the average exponent for each subject along with the pooled distribution of the exponents from the shuffled data for

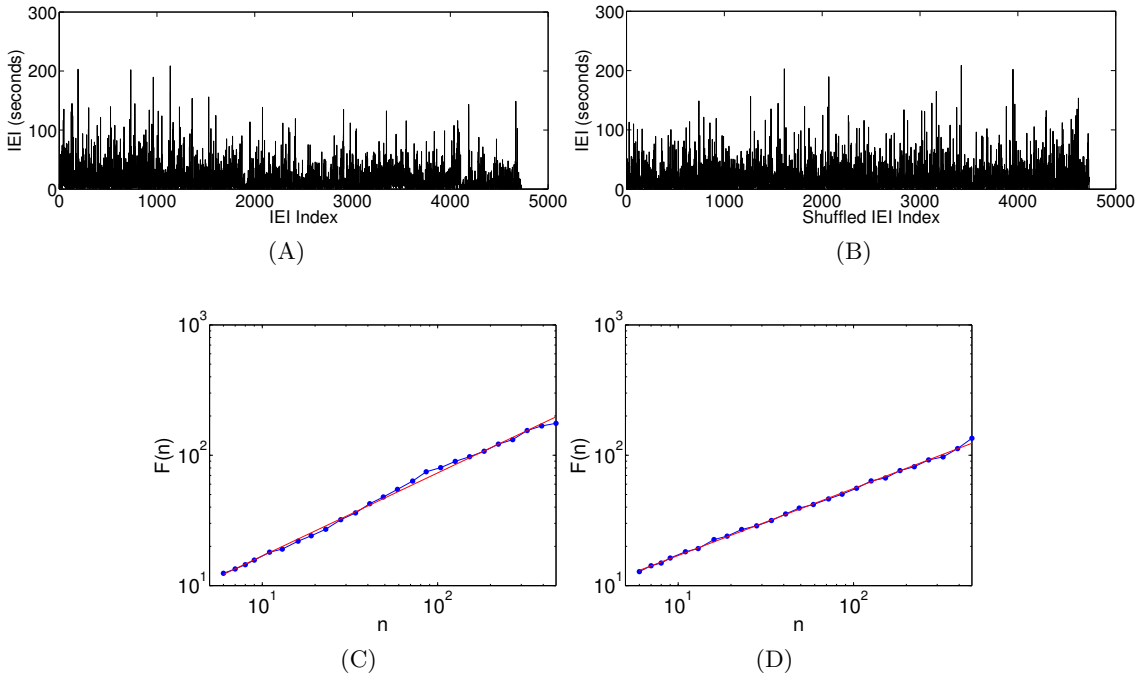

Figure 2.15: (A) An example IEI sequence from subject 1 channel 8 (C3-T3). (B) The same sequence randomly shuffled. (C,D) The corresponding DFA plots. As expected the DFA of the shuffled sequence (D) yields an exponent of 0.51 which is close to 0.50. For the actual sequence the DFA exponent was 0.64 indicating LRTCs. Note that the DFA plot shows that the same trend is present for all box sizes, i.e. the points are well fit by a single straight line.

both the DFA (Fig. 2.16A) and the Whittle exponents (Fig. 2.16B) of the IEI sequences. It is clear from the figure that the shuffled distributions are distinct from the exponents of the actual IEI sequences. IEI exponents were found to be significantly different from those of the shuffled distributions ($p < 0.001$) using the Wilcoxon Mann-Whitney test. The average difference in the means of the shuffled distributions with the distributions of the exponents for the actual sequences was 0.17 (DFA, range 0.11-0.26) and 0.14 (Whittle, range 0.09-0.20). Only one subject (subject 6) had a single exponent of the actual sequences (for both DFA and Whittle) that was in the lower 95% of the distribution of the corresponding shuffled sequences. All other exponents of the actual sequences fell in the upper 5% tail of the distributions from the shuffled sequences. This statistical analysis strongly indicates the presence of LRTCs in the IEI sequences, and therefore in the temporal occurrence of BNO events in the EEG, of every subject studied.

DFA analysis was also carried out for all signals with a maximum box size of 1/4 of the length of the data. Whilst this is larger than the recommended maximum box size of 1/10 of the length of the data [179] as studied above, the results observed for this maximum box size did not show deviation from the trend in the DFA plot for smaller box sizes. Further, the exponents calculated for this maximum of 1/4 were strongly

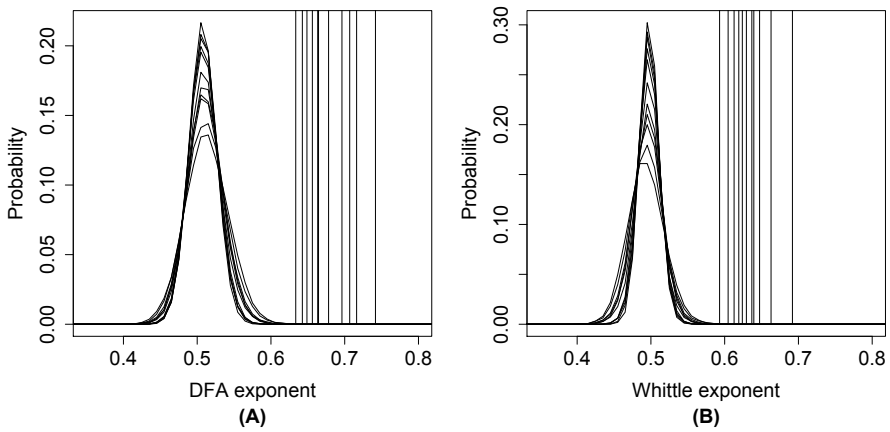

Figure 2.16: DFA (A) and Whittle (B) exponents for the IEI sequences (vertical lines) averaged across all channels recorded for each subject (each vertical line corresponds to the average exponent of a single subject) compared with the pooled probability distribution of the shuffled data for each subject. The data is plotted using the same format as in Figure 4 [142].

correlated ($R^2 = 0.79$, slope 0.83, intercept 0.11) with exponents found with a maximum box size of 1/10 of the IEI sequence length (see Fig. 2.17A). This result suggests that the LRTCs extend across larger box sizes. The distribution of exponents of shuffled sequences (calculated with this larger maximum box size, see Fig. 2.17B) was significantly different from the actual IEI exponents ($p < 0.001$, Wilcoxon Mann-Whitney test) once again indicating the presence of LRTCs in the IEI sequences. For this larger maximum box size the average difference between the means of the distribution from shuffled sequences and the distribution of exponents of the original sequences was 0.16 (range 0.07-0.25) and all exponents of the actual sequences fell in the upper 5% tail of the distribution of the corresponding shuffled sequences.

In order to better compare the data between subjects, given that for all subjects and all channels the IEI sequences are different in length, further analysis was carried out on fixed length IEI sequences. These were constructed from the first 1000 IEI of each full length IEI sequence. Both Whittle and DFA estimates of the Hurst exponent were calculated, and due to the shorter length of the sequences and the positive results achieved above, DFA exponents were calculated using a maximum box size of 1/4 of the length of the signal, i.e. 250 IEI. Averaging over all of the fixed length sequences analysed, the Hurst exponents were estimated as 0.66 (DFA, range 0.53-0.84) and 0.62 (Whittle, range 0.50-0.76). Comparison of the exponents of the fixed length sequences with the exponents for the whole sequences (with a maximum box size of 1/4 the length of the sequence) through linear regression showed a strong correlation with a slope of 0.90, intercept 0.05, $R^2 = 0.53$ for DFA and for Whittle a slope of 0.95, intercept 0.02 and $R^2 = 0.50$. Again the exponents of the actual fixed length sequences were significantly different from the distributions of the shuffled sequences ($p < 0.001$) and the average difference in the means between the distributions is 0.16 (DFA, range

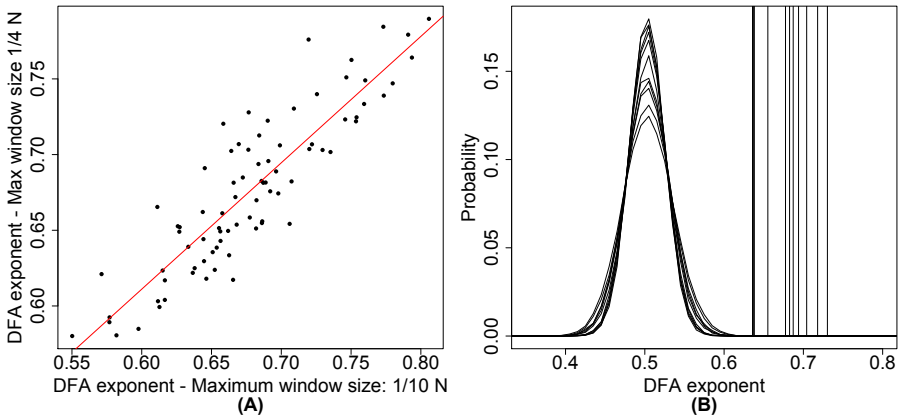

Figure 2.17: (A) Relationship between DFA exponents calculated with a maximum box size of 1/10 of the length of the signal and those calculated with a maximum box size of 1/4 of the length of the signal. The exponents are strongly correlated ($R^2 = 0.79$) suggesting that LRTCs extend over larger box sizes. (B) DFA exponents calculated with a maximum box size of 1/4 of the length of the signal (vertical lines, taking averages across channels within each subject - each vertical line corresponds to the average for a single subject) were again significantly different from the probability distributions of the exponents of the shuffled data (calculated with this larger box size).

0.07-0.25) and 0.13 (Whittle, range 0.07-0.23). For the Whittle exponents all but 2 and for the DFA exponents all of the exponents of the original sequences are in the upper 5% tail of the distribution of shuffled exponents.

BNO duration sequences

Across all sequences of BNO duration, from all subjects and channels, the average Hurst exponent was 0.56 (DFA, range: 0.47-0.67) and 0.54 (Whittle, range: 0.47-0.65). Fig. 2.18 compares the average exponent values for each subject with the shuffled distributions. Shuffled distributions had a mean ± standard deviation of 0.51 ± 0.023 (DFA) and 0.50 ± 0.018 (Whittle) consistent with uncorrelated data. However, unlike the average exponents for the IEI sequences (Fig. 2.16) there is some overlap between the shuffled distributions and the average exponents of the actual sequences of BNO duration, see Fig. 2.18. This was also reflected in the statistical analysis: for DFA there was a significant difference ($p < 0.01$) between the exponents of the actual and shuffled sequences for subjects 1 and 4-11. However, subject 3 was significant at the 5% significance level ($p = 0.037$) only and subject 2 did not show a significant difference ($p = 0.065$). The average difference in the means of the distributions was 0.05 (minimum 0.02, maximum 0.08) across all subjects. Only in the case of subject 5 did all the DFA exponents of the original sequence lie in the upper 5% tail of the distribution for the corresponding shuffled sequences. For the other subjects an average of 3.5 of the DFA exponents were within the lower 95% of the corresponding distribution of shuffled sequences. For the Whittle exponent all subjects exponents except from subject 2

($p = 0.081$) were significantly different from the shuffled distributions ($p < 0.005$). The difference between the means of the distributions was on average 0.04 with a maximum of 0.09. All subjects had at least one exponent in the lower 95% of the corresponding shuffled distribution, with an average of 2.9 exponents per subject lying in this region. These results indicate that, while some BNO duration sequences do not exhibit LRTCs, overall BNO durations do exhibit LRTCs. Unlike in the case of the IEI sequence exponents, there was also a significant difference (at the significance level of $p = 0.05$) between the exponents of the subjects with and without intraventricular haemorrhage ($p = 0.03$ DFA and $p = 0.04$ Whittle).

For fixed length sequences of the first 1000 BNO durations (maximum box size 1/4 the length of the sequence), the average exponents were 0.54 (DFA, range 0.45-0.69) and 0.52 (Whittle, range 0.43-0.64).

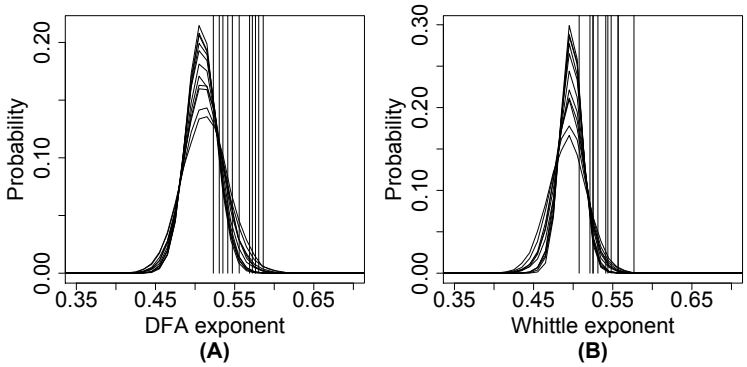

Figure 2.18: Comparison of the average exponents - (A) DFA and (B) Whittle - of the sequences of BNO duration (vertical lines - each line corresponds to the average for a single subject) with the distributions of the exponents of the shuffled sequences. Exponent subject averages for the actual data are taken across all channels and shuffled distributions are pooled from 5000 shuffled sequences for each channel.

BNO amplitude sequences

Sequences of peak amplitudes yielded average exponents of 0.59 (DFA, range: 0.49-0.70) and 0.58 (Whittle, range: 0.49-0.69). Fig. 2.19 shows the average exponents for each subject compared with the shuffled distributions. The shuffled distributions had exponents of 0.51 ± 0.024 (DFA, mean $\pm$ standard deviation) and 0.50 ± 0.017 (Whittle). There was some overlap between the average exponents and the shuffled distributions. The Wilcoxon Mann-Whitney test of each subject's DFA exponents compared with the pooled shuffled distributions showed significant differences ($p < 0.05$) for all subjects. The average difference in the means of the distributions of the actual sequences compared with the shuffled sequences was 0.08 (range 0.03-0.14). Eight of the eleven subjects had exponents which fell within the lower 95% of the corresponding distribution of exponents of shuffled sequences and of these subjects there was an

average of 2.5 exponents within this region. However, the Whittle exponents were significantly different for all subjects and 4 out of 11 subjects had an average of 2 exponents in the lower 95% of the distribution of the exponents of the shuffled sequences. The other subjects did not have exponents of the actual sequences in the lower 95% of the shuffled distributions. There was no significant difference in the exponents of those subjects with and without intraventricular haemorrhages ($p = 0.34$ DFA and $p = 0.98$ Whittle). The average exponent for the fixed length sequences was 0.56 (DFA, range 0.45-0.72) and 0.55 (Whittle, range 0.42-0.71).

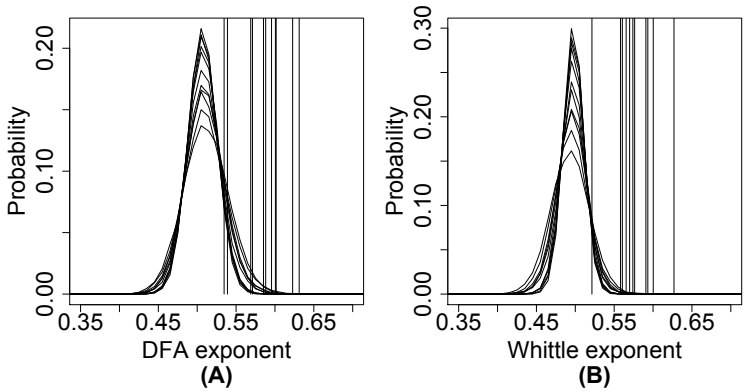

Figure 2.19: Average (A) DFA and (B) Whittle exponents of peak amplitude compared with the distributions of shuffled sequences. Average exponents for each of the subjects are plotted as vertical lines (each line corresponds to a single subject). The shuffled distributions are formed from the pooled distributions of exponents of 5000 shuffled sequences for each of the sequences.

Across all subjects, the average exponents for the sequences of BNO total amplitude was 0.56 (DFA, range: 0.45-0.68) and 0.56 (Whittle, range: 0.49-0.72). Fig. 2.20 shows the average exponents for each subject compared with the shuffled distributions. The pooled shuffled distributions had a mean $\pm$ standard deviation of 0.51 ± 0.025 (DFA) and 0.50 ± 0.017 (Whittle). Again there was some overlap of the average exponents and the tails of the distributions. Wilcoxon Mann-Whitney test for each of the subjects actual DFA exponents compared with the pooled shuffled distributions showed significant differences ($p < 0.05$) for subjects 1-2,4-5 and 7-11. The average difference between the means of the distribution of the actual and shuffled exponents was 0.06 (range 0.01-0.1). Nine of eleven subjects had at least one exponent which fell within the lower 95% of the distribution of the exponents of the shuffled sequences, with an average of 3.3 exponents per subject falling within this region. All Whittle exponent distributions were significantly different from the shuffled sequence exponent distributions ($p < 0.05$) and only 7 subjects had exponents in the lower 95% of the distribution of the exponents of the shuffled sequences with an average of 2.1 exponents falling in this region. The statistics for the comparison with shuffled sequences for all BNO characteristics is summarised in Table 2.5. Again there was no significant difference between subjects with or without intraventricular haemorrhages ($p = 0.35$ DFA and $p = 0.61$ Whittle). The fixed length sequences of BNO total amplitude had

average exponents of 0.54 (DFA, range 0.46-0.68) and 0.53 (Whittle, range 0.42-0.69).

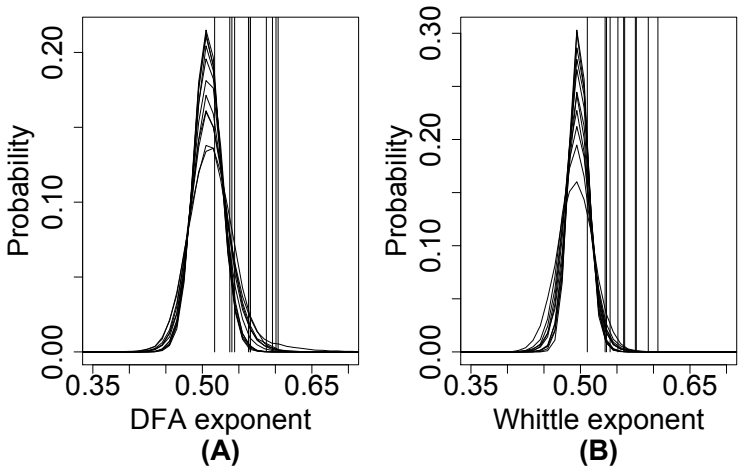

Figure 2.20: (A) DFA and (B) Whittle exponents averaged over channels for each subject (vertical lines - each line corresponds to the average for a single subject) compared with the pooled distributions of 5000 randomly shuffled sequences for each original sequence.

In summary, LRTCs were observed in the sequences of all BNO characteristics. However, they were only robustly observed in IEI sequences, where the exponents of the actual sequences were significantly different from the distributions of the randomly shuffled sequences for all subjects. This is highlighted by the differences listed in Table 2.5, which shows that the IEI sequences have the largest difference in the means of the distributions and virtually all exponents fell in the tail of the distributions of the exponents of the shuffled sequences.

Relationship between the Hurst exponent and the subject's corrected age

In this section the effect of corrected age (age at recording given as gestational age plus the time since birth) on the Hurst exponent is examined. This is calculated for both the full length sequences and the fixed length sequences. It is worth remembering that the full length sequences should give better estimates of the actual Hurst exponent - the Hurst exponent is a measure over an infinite sequence and the estimate calculated from a finite sequence is asymptotic to the true value. However, fixed length sequences are also considered so as to standardise the measures across subjects.

As different EEG montages were used when the data was recorded, in order to standardise the number of points per subject for the analysis, average exponents were calculated with respect to channel locations. The channel regions were defined as frontal, central and posterior classed as: frontal = F4-C4, F3-C3; central = T4-C4, C4-Cz, Cz-C3, C3-T3; posterior = C4-O2, C3-O1 (montage 1) and frontal: F4-C4, F3-C3; central = T4-C4, C4-Cz, Cz-C3, C3-T3; posterior = C4-P4, P4-O2, C3-P3, P3-O1 (montage 2).

	DFA		
	Average difference in means	Number of subjects	Average number of exponents
IEI	0.17	1	1
Peak amplitude	0.08	8	2.5
Total amplitude	0.06	9	3.3
Duration	0.05	10	3.5
	Whittle		
	Average difference in means	Number of subjects	Average number of exponents
IEI	0.14	1	1
Peak amplitude	0.08	4	2
Total amplitude	0.06	7	2.1
Duration	0.04	11	2.9

Table 2.5: Tables showing the summary statistics for the comparison of the actual sequences with the shuffled sequences. The average difference in the means between the distribution of the exponents of the actual sequences and the distribution of the exponents of the corresponding shuffled sequences (averaged across subjects) is listed in the second column. The column 'Number of subjects' indicates the number of subjects that had at least one exponent for that characteristic that fell within the lower 95% of the distribution of the exponents of the shuffled sequences (indicating a sequence which did not display LRTCs). For these subjects the average number of exponents that did so is given under 'Average number of exponents'. Recall that the number of subjects in this study was 11.

Fig. 2.21 plots the DFA and Whittle exponents with respect to corrected age for both the full IEI sequences and the fixed length (1000) IEI sequences (averaged across the three channel locations). For the fixed length sequences there was a significant effect of age for the DFA exponents of the IEI sequences ($p = 0.046$) but not for Whittle exponents, through linear regression analysis. Tables 2.6,2.7 show the results from linear regression analysis for the full length and fixed length sequences for all the BNO characteristics (indicating the slope of the regression, the intercept - i.e. at age 0, and the R and p-value).

BNO	DFA exponents				Whittle exponents			
characteristic	Slope	Intercept	R	p-value	Slope	Intercept	R	p-value
IEI	0.0056	0.53	0.31	0.08	0.0016	0.59	0.09	0.62
Duration	0.0022	0.50	0.16	0.37	0.0015	0.50	0.14	0.42
Peak amplitude	0.0034	0.49	0.19	0.29	0.0005	0.56	0.031	0.86
Total amplitude	0.0044	0.45	0.25	0.17	0.0032	0.47	0.21	0.24

Table 2.6: Results for linear regression of the exponents from the full length sequences (averaged across channel locations) with respect to corrected age of the subjects for each of the BNO characteristics. For all BNO characteristics none of the analyses showed significant p-values, indicating that there was no trend in the exponents (of the full-length sequences) with respect to corrected age.

No significant effects were observed for any of the BNO characteristics in the exponents of the full-length sequences. However, there was a significant effect of age for duration, peak and total amplitude in the case of the fixed length exponents for both the DFA and Whittle estimator. For example, for BNO duration a trend in fixed length

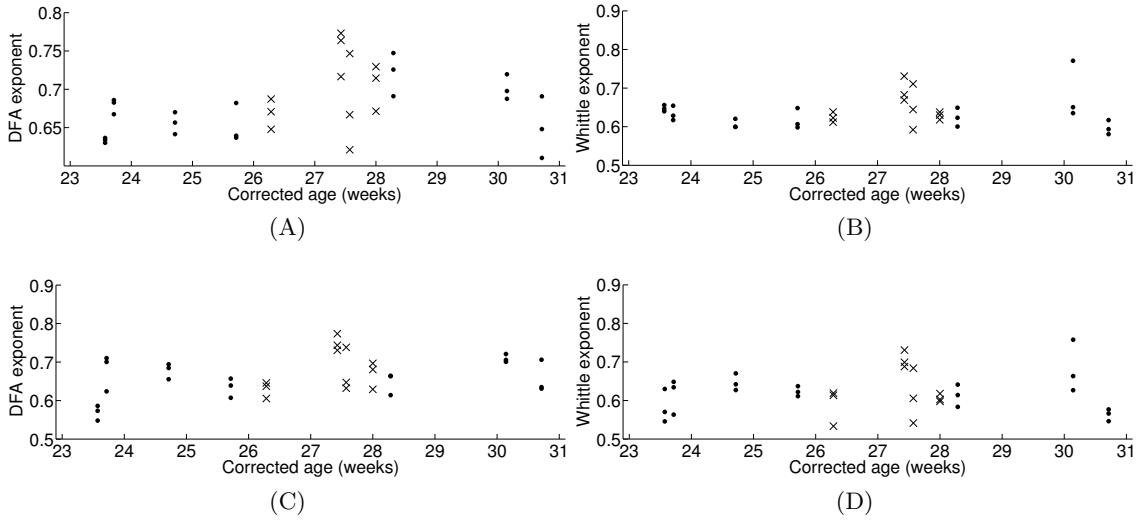

Figure 2.21: Exponents of IEI sequences plotted with respect to corrected age (gestational age at birth plus age since birth). (A) DFA and (B) Whittle exponents for full length sequences, (C) DFA and (D) Whittle exponents for fixed length sequences of 1000 IEI. Exponents are averages taken across the three channel groups (see main text). Crosses indicate subjects with haemorrhages.

BNO	DFA exponents				Whittle exponents			
characteristic	Slope	Intercept	R	p-value	Slope	Intercept	R	p-value
IEI	0.0079	0.45	0.35	0.046	0.0017	0.58	0.075	0.68
Duration	0.0069	0.36	0.41	0.019	0.0063	0.36	0.49	0.0038
Peak amplitude	0.0104	0.29	0.48	0.0048	0.0073	0.36	0.49	0.0035
Total amplitude	0.0090	0.31	0.52	0.0021	0.0070	0.35	0.54	0.0013

Table 2.7: Results of the linear regression analysis of the exponents of the fixed length sequences (averaged across channel locations) for each of the BNO characteristics with respect to subject's corrected age. DFA exponents were calculated with a maximum box size of 1/4 of the length of the sequence. Results from the full length sequences were given in Table 2.6.

sequences was observed in both DFA and Whittle exponents, with slopes of 0.0069 and 0.0063 respectively. This indicates that across the 7 week age range studied there is an increase in the Hurst exponent estimate of 0.048 for DFA estimates and 0.044 for Whittle estimates. This is an interesting finding, perhaps reflecting the increase in cortical connectivity over the age range studied, and warrants further investigation in a larger data set.

Inter-burst intervals and synchronicity of the BNOs

Previous authors examining preterm EEG have investigated inter-burst intervals (IBIs) defined as periods of silence in *all* electrodes [27, 83, 86, 98, 101, 115]. This choice of characteristic was in part probably due to the fact that most analysis in these studies was carried out by hand and so determining silence in all electrodes is much quicker than analysing the data on a per channel basis. However, this means that the analysis carried out here, examining IEIs, cannot be directly compared to the previous literature. Therefore, in this section we will also examine IBIs in this data set. An IBI was defined as a period in which there were no BNOs in any EEG channel. As with IEIs, there was a minimum IBI imposed of 0.5 seconds. Table 2.8 lists the IBI statistics for each subject. Note that the subjects with haemorrhages have longer IBIs. The mean IBI is comparable to a previous result: *Anderson et al.* found a mean IBI between 4-16 seconds in a population of neonates between 27 and 31 weeks conceptional age [83]. The maximum IBI was slightly higher than some other authors have found (46 seconds [27], 88 seconds [83], 62 seconds [98]). However, this is likely to be due to the difference in definition of IBI that was used here - as can be seen in Fig. 2.5 the BNO is only detected as the nested portion of the event and does not include all of the delta wave. Also, the analysis here was carried out over a very long recording period owing to our automated technique. Previous analysis was carried out on much shorter sections (around 30 mins) [27, 83]. As can be seen from the IBI distribution (see Fig. 2.22), very long IBIs are rare and so would be less likely to be detected in a short recording.

Fig. 2.22 shows the distribution of IBIs pooled from all subjects. The distribution is similar in shape to the distribution of IEIs (Fig. 2.8) but the maximum IBI is much lower as would be expected (as IEIs are evaluated in a single EEG channel). Table 2.8 also lists the DFA exponent of the IBI sequences, all of which indicated LRTCs in the data. The mean DFA exponent for IBI sequences was 0.73. Comparison with shuffled sequences showed that the distribution of DFA exponents for the actual IBI sequences was significantly different to the pooled distribution of shuffled data ($p < 0.001$, one-sample Wilcoxon signed rank test). The shuffled data had mean of 0.51 and a standard deviation of 0.017.

Other authors have also investigated the degree of synchronicity of bursts of activity in

Subject	Mean IBI (secs)	Median IBI (secs)	Maximum IBI (secs)	DFA exponent
1	6.3	3.2	113.4	0.68
2	7.5	3.1	133.3	0.71
3	5.7	2.7	95.7	0.69
4	5.8	2.6	105.8	0.67
5	9.4	4.8	123.2	0.69
6	12.4	7.9	157.9	0.86
7	14.9	9.6	212.8	0.68
8	15.2	9.0	221.7	0.73
9	4.0	1.9	72.1	0.76
10	8.9	6.4	73.1	0.72
11	5.0	2.8	61.2	0.81

Table 2.8: IBI statistics for each subject. IBIs are periods without BNO activity in all EEG channels. Note that the subjects with intraventricular haemorrhages (5-8) have longer IBIs. DFA exponent is the exponent of IBI sequences constructed according to the temporal ordering of the IBIs.

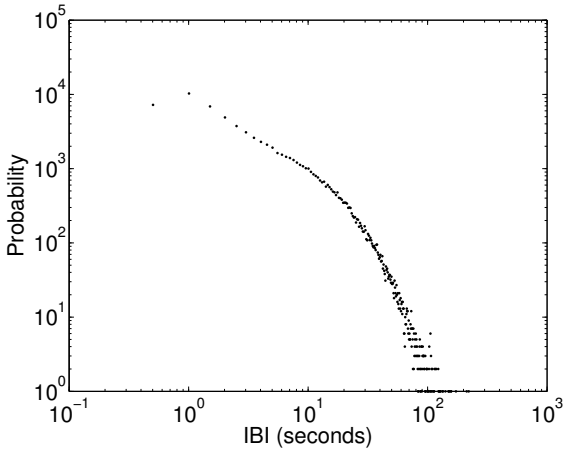

Figure 2.22: Distribution of IBIs pooled across all subjects. As might be expected there is a similarity between this distribution and the distribution of IEIs (Fig. 2.8) though the maximum IBI is much shorter than the maximum IEI.

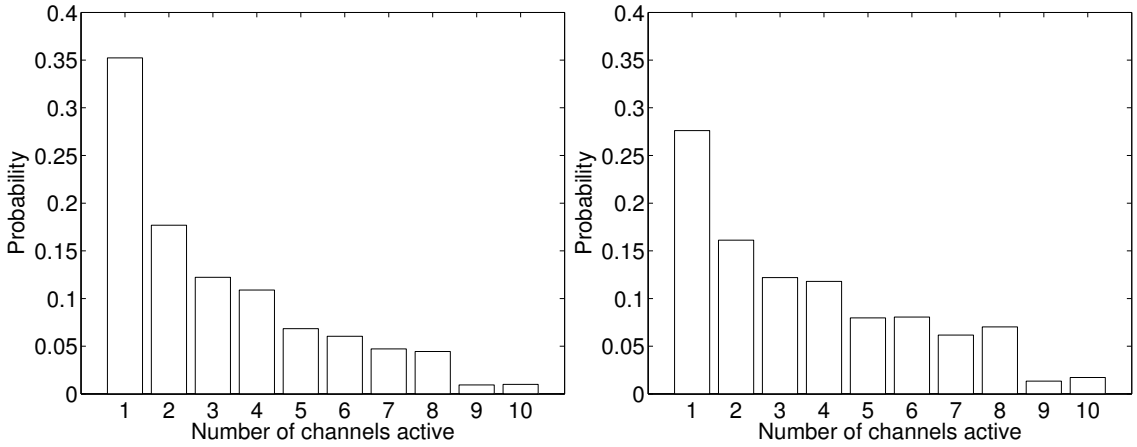

Figure 2.23: Number of channels active within an active period (a period in the EEG which is not defined as an IBI). Note that only some subjects had 10 channels rather than 8 so the probability of having 9 or 10 channels active within an active period is artificially low in these plots. (A) The minimum IBI was set to 0.5 seconds. (B) The minimum IBI was increased to 2 seconds.

the EEG suggesting that activity often occurs synchronously at multiple electrodes [27, 83, 89]. The degree of synchronicity of BNOs within the EEG was assessed here by examining the number of channels active within an active period (where an active period was defined as the period in which there is at least one channel with a BNO, i.e. a period which is not an IBI). If a channel was active more than once it was only counted once, thus the maximum number of active channels is 10. Fig. 2.23 shows the probability distribution of the number of channels active within an active period.

With the minimum IBI set to 0.5 seconds it was found that $\sim 35\%$ of active periods were comprised of a BNO in just one channel. This at first seems to contradict some previous results in the literature that have suggested bursts occur synchronously [27, 83, 89]. However, firstly it is worth noting that this percentage implies that $\sim 65\%$ of active periods were synchronous activity in more than one EEG channel. Furthermore, again those authors used a different definition of bursts of activity and some used a much broader definition of when bursts occur synchronously - bursts within 2 seconds of each other were defined as synchronous by *Anderson et al.* [83]. Increasing the minimum IBI to 2 seconds, see Fig. 2.23B, as would be expected the number of channels active within the periods of activity on average increases. In this case the percentage of active periods with only a single active channel decreases to $\sim 28\%$. Furthermore, other studies have reported that, while activity can occur across multiple electrodes, it can be "spatially confined" [29] and exhibit "periods of asynergy" (local or unilateral activity) [85]. The results here are consistent with these latter papers, suggesting that BNOs can occur locally as well as being events that span multiple cortical regions.

2.4 Discussion

The results of this chapter provide, to my knowledge, the first demonstration of LRTCs in the BNO activity of human preterm EEG. LRTCs were consistently observed in all subjects and in the sequences of all BNO characteristics, but were observed most robustly in IEI sequences where exponents were always significantly different from the exponents of the shuffled sequences. Prior research examining BNO characteristics has investigated the spectral properties [35, 87, 88], average amplitude [27, 83, 98], and, in terms of the temporal properties of activity, the mean or maximum IBI only [27, 83, 86, 98, 101, 115]. The results presented here therefore indicate a complex temporal ordering to the BNO activity not previously appreciated.

Older subjects, as young as a few weeks post-term age, exhibit complex temporal dynamics in the form of LRTCs in the fluctuations of oscillation amplitude [39–45]. The discontinuous nature of the preterm EEG prevented analysis of oscillation amplitude. However, the temporal ordering of burst activity is no less interesting, indicating a complexity in the brain's dynamics at a much younger developmental stage. This is also particularly interesting given that the brain at this stage is still undergoing major developmental changes which are known to be activity-dependent. Might the temporal properties of this activity observed here be important for development? Nested oscillations recorded in rats during the second postnatal week (a period equivalent to a slightly older age than the preterm subjects studied here) organise as neuronal avalanches with long-range *spatial* correlations and this spatial patterning has been hypothesised to provide a template for cortical circuit formation [51]. Future work is needed to determine the role of LRTCs (and long-range spatial correlations) in cortical development.

In terms of the IEI sequences, the Hurst exponents are comparable with those observed in an analysis of inter-spike intervals recorded intracranially from human hippocampus [48] which provides evidence of this kind of temporal patterning in waiting times (i.e. periods of inactivity) in the adult. Long-range correlations have also been observed in the inter-burst intervals of the spontaneous synchronous burst activity in cultures [180]. Though this data lacked the nested oscillations seen in the bursts in the preterm EEG this data adds to the empirical evidence of LRTCs in neuronal systems. Future work is required to understand the possible mechanisms which might result in this type of temporal pattering. One possible mechanism will be addressed in Chapter 4 of this thesis.

While LRTCs were observed in all BNO characteristics, indicating a power-law relationship in the autocorrelation function, the distribution of the data (i.e. probability distribution of the data points which does not relate to their temporal ordering) did not exhibit a power-law and in fact the data was shown to be log-normally distributed.

Interestingly the 'humped' IEI distribution observed for some of the subjects on a double logarithmic axis (see Fig. 2.7) is similar to recent results shown by *Lombardi et al.* [166] of the distributions of inter-avalanche intervals. The authors recorded neuronal avalanches in organotypic cultures and compared their results with neuronal network simulations, see Fig. 1.10. Their results suggest that the short inter-avalanche intervals (i.e. the lower portion of the distribution) are recorded during up states[3] of the network while the hump in the distribution is related to down states. While the inter-avalanche intervals are on a much smaller timescale than the IEIs measured here (of the order of milliseconds rather than seconds) I speculate that the similar distribution observed here may relate to the brain being in more or less excitable ('up' and 'down') states. Future research would be needed to ascertain whether this is the case. Moreover, as the IEI distributions appeared to be bimodal log-normally distributed, reassessment of the data of *Lombardi et al.* in terms of the distribution of the logarithm of the data may be worthwhile.

There did not appear to be any change in the data distributions with respect to the corrected age of the subjects. Given the work of *Tetzlaff et al.* [54] who showed a change in distribution of neuronal avalanches over a period of connectivity formation in cultures this is perhaps initially surprising. However, during the period of development studied here cortical connectivity is forming, yet the subplate is already densely connected [9]. Sensory input via the subplate drives the cortical plate during this period [6, 8]. A neuronal network developing in culture is a much more simplified system than that examined here.

There was evidence of an increase in exponent across age in the fixed length sequences. In particular, this was a significant trend in the fixed length sequences of BNO duration, peak and total amplitude. Interestingly the trends in these sequences all start from close to 0.5 at 23 weeks and increase across the age range studied (though note that the trend in IEI sequences starts at a much higher value of approximately 0.6). This is perhaps tentative evidence for some form of self-organisation process starting at a non-critical state (i.e. no LRTCs). However, due to the small number of subjects and the fact that there are several confounds with this data set (discussed below) future analysis in this area is necessary to fully determine whether the Hurst exponent is affected by the age of the subject.

2.4.1 Methodological considerations

While all the preterms studied had EEG which was classed as normal for age, we cannot assume that the EEG dynamics detected here will be present in a normally developing foetus *in-utero*. The preterm is exposed to an abnormal *ex-utero* environment and it is

[3]For a description of up and down states see Chapter 1.

not currently understood whether or how this environment affects the neurological development of the child. EEG studies have shown cortical activity in preterm infants in response to painful medical procedures [91] that a normally developing foetus would not be subject to. At term equivalent age, infants born very prematurely have increased responses to painful stimuli [122] compared with children born at term and lower brain volumes, including region specific changes [181]. Furthermore, children born extremely prematurely are more likely to have special educational needs and lower IQ than their term-born peers later in life [111–113]. This suggests that the preterm brain may develop along a different trajectory to the healthy developing foetus and results from preterm studies cannot be assumed to hold true for the normal developing brain. On the other hand, foetal MEG studies have observed spontaneous activity in the foetus which appears as nested oscillations within discontinuous traces [116]. Foetal MEG recordings have also shown neurological responses to light [118] and auditory stimuli [117] suggesting that the foetus may in some way be affected by the external environment. Future work is needed in this area to understand how preterm brain dynamics differ from foetal dynamics. Foetal MEG recordings may provide a method for the analysis of the temporal dynamics of foetal activity similar to the work undertaken here. Nonetheless, the results of this study provide a unique insight into the early developing brain.

The BNO extraction method combined frequency and amplitude criteria in order to robustly extract events. However, the algorithm was based on amplitude criteria taken from the literature [83, 178]. Due to the nature of the extraction algorithm BNO events with amplitude lower than these thresholds can still be detected. In general though, lower amplitude BNOs may not be detected. This leads to a distortion in amplitude distribution at low values. A threshold level was also applied to the duration and IEI statistics. However, these have less of an effect, particularly for IEIs, as the thresholds are small in comparison with the range of the data.

The EEG recordings in this chapter were carried out with two different electrode montages. These recordings were all conducted as part of clinical testing and so the electrode positions were determined by medical staff. However, it is important to consider whether these different montages may have had an effect on the analysis. In particular, montage 2 has more electrodes and the spacing between the bipolar electrodes differs compared with the first montage. For example, in montage 1 the bipolar pair C3-O1 is assessed, whereas in montage 2 the P3 electrode was also used during recording and so the bipolar montage included C3-P3 and P3-O1 but not C3-O1. Thus, the second montage had a reduced electrode spacing between the bipolar pairs over the posterior region of the brain. Interelectrode distance has been noted to be important when examining coherence between electrodes where small distances between electrodes can artificially increase the coherence due to volume conduction effects (the same signal being detected at both electrodes) [182]. Different electrode spacing may

also alter the frequency content of a signal - as slow frequencies are transmitted across a wider range and the joint signal detected by the two electrodes may differ with increasing space between them. Additionally, the amplitude of the EEG signal increases with distance between the electrodes [183]. It is therefore possible that for different bipolar pairs the amplitude and frequency content of the BNOs as detected on the EEG trace are slightly altered. However, the difference in spacing of the electrodes in the two different montages is minimal - the majority of bipolar pairs remain the same in the two montages and the subjects head is relatively small. Moreover, the analysis undertaken in this study is according to the temporal ordering of BNOs and so is not a direct measure of frequency or amplitude but is only related to frequency and amplitude in-so-far as extraction. If the frequency or amplitude of a wave were to be altered slightly it is possible that this could lead to the miss-detection of a BNO. However, LRTCs were observed in the signals from all EEG channels irrespective of the distance between the electrodes. Interelectrode spacing therefore does not change the results of this study. It may be interesting in future research to compare the spacing between electrodes as well as differences between EEG channel locations and the effect on the degree of LRTCs.

During the recording period the subjects were connected to a ventilator and subject to normal nursing and medical care. Trends in data sets that result from extraneous factors can lead to erroneous estimation of the Hurst exponent [179]. Trends in the data can be observed by 'crossover' points, where for a certain box size the trend in the detrended fluctuations either side of that box is different, i.e. if a single linear trend does not occur at all box sizes [179]. The data presented here had a single linear trend for all box sizes suggesting that the Hurst exponent was not affected by external stimuli.

Due to the clinical nature of the recordings in this data set, there are a number of confounds with the data which need to be considered. Firstly, the number of subjects in this study was small, with few subjects at each corrected age. Also the subjects recorded in the middle of the age range all had intraventricular haemorrhages. While there was no difference between the Hurst exponents of the subjects with haemorrhages compared to those without (except in duration sequences), given that these subjects were necessarily compared with those of a different age, this may still have an effect on trends examined within the data. Furthermore, as the EEG recordings were carried out based on clinical grounds, they were recorded at different times in relation to subject birth. Other authors have observed in longitudinal recordings that there are changes in spectral band power [35, 167] and a decrease in the duration of IBIs [167] with time since birth and that there is a change irrespective of the gestational age at birth. Thus, for example, a subject born at 25 weeks and recorded at 1 week old may not be comparable with a subject born at 26 weeks and recorded soon after birth. In this chapter trends in the exponent across corrected age were examined. However, this research by other authors suggests that in doing so two 'competing' factors may have been analysed: the effect of gestational age and the effect of time since birth (perhaps reflecting an adaptation to the

external environment). Therefore, future analysis in this area should examine subjects recorded at the same postnatal age to give a true indication if the Hurst exponent varies with respect to gestational age. A longitudinal analysis would also enable examination of the Hurst exponent with respect to time since birth. However, these limitations do not detract from the fact that LRTCs were observed in all subjects studied - a strong indication of the complex temporal organisation of the early preterm EEG.

2.4.2 Directions for future work

As mentioned above, a confound with this data set is that, due to clinical reasons, subjects were recorded at different ages after birth. It would therefore be of interest to record subjects at the same time after birth to determine whether the Hurst exponent does in fact vary with gestational age. Previous studies [35, 167] have found an effect of age since birth which may reflect an adaptation to the external environment or alternatively perhaps a return to 'base-line' after a traumatic birth experience, or indeed a combination of the two. A longitudinal study, following subjects at different ages after birth which also compares subjects born at different gestational ages would also be of interest.

When analysing EEG from preterm subjects it is important to remember the clinical nature of the recordings and the amount of health care that these subjects require. Any research in this age group should therefore try to combine analysis that elucidates brain development with that which increases understanding of how and why the preterm brain develops abnormally in the ex-utero environment. This must include understanding why patients without overt neurological sequelae can develop neurological impairments later in life while others of the same age at birth do not. This can perhaps only be achieved fully through longitudinal studies which attempt to correlate preterm EEG features with outcome data much later in life. It would be interesting to see if values of the Hurst exponent correlate with outcome.

Previous work has suggested that subjects with long maximum IBIs may have a poor outcome later in life [101]. Given the distributions observed in this work, with few very long IEIs/IBIs, the number of long IBIs may also be important. The length of the recording may also affect the likelihood of observing a long IBI. Therefore, future clinical assessment of the EEG of very young preterm children should take this into account.

Despite the lower number of BNOs per hour in subjects with intraventricular haemorrhage, there was no difference in Hurst exponents in any of the BNO characteristics between those subjects with and without this neurological sequelae. However, the subject groups are small and the age at recordings differ so further investigation would be needed in a future study before a concrete conclusion can be drawn. Previous research has shown that subjects with lesions but with normal EEG at

birth often have favourable outcome later in life [107]. We do not have long-term follow-up for these subjects and it may be that these subjects will have a good outcome. Investigation of children with lesions and abnormal EEG would therefore also be of interest in such a study.

Chapter 3

Factors affecting long-range temporal correlations in preterm EEG

3.1 Introduction

In the last chapter it was shown that the early preterm EEG exhibits LRTCs in the sequences of BNO amplitude, duration and IEI, implying that the dynamics of the preterm brain are complex even at a very early age range. This result was most robustly observed in IEI sequences, i.e. the temporal occurrence of BNOs. As discussed it was not possible to concretely address whether the Hurst exponent varied with gestational or postnatal age due to the clinical constraints imposed upon the recordings. In this chapter, a much larger data set of subjects, also born at ages 24-30 weeks gestational age, is examined. This will first enable confirmation of the results (LRTCs) in a wider data set. Additionally, all the subjects in this data set were recorded across the first three days of life. Therefore, this makes it possible to properly examine the effect of both gestational age and time since birth on the Hurst exponent. Thus, this chapter will better determine whether a self-organisation process to a critical state appears to occur over this preterm period as was the original hypothesis.

Additionally, all children in the data set studied in this chapter have had follow-up investigations at two years of age assessing motor and cognitive levels. Therefore, the existence of correlations between these follow-up measures and the Hurst exponent as calculated from the EEG at birth, will be investigated. It is of interest to see whether the EEG at birth may be able to predict outcome in later life so that the complications of preterm birth can be better understood. A number of studies have shown that abnormal EEG in the neonatal period is predictive of poor outcome later in life

[28, 100, 101, 103, 104, 107–110]. This includes results indicating that longer inter-burst intervals are a predictor of poor outcome [28, 101], suggesting a disruption to the temporal occurrence of BNOs.

LRTCs in adults (in the fluctuations of oscillation amplitude) have been shown to differ in conditions such as epilepsy [47], depression [142], Alzheimer's disease [143], schizophrenia [144] and Parkinson's disease [184] suggesting that the Hurst exponent may be affected by a number of pathological conditions. In the epilepsy study the epileptogenic hippocampal region exhibited slower decay of temporal correlations (an increased Hurst exponent) than the control region [47], whereas in other studies the patients with pathologies had lower Hurst exponents [142–144], though in all cases LRTCs were observed. To my knowledge, no studies investigating LRTCs of discrete neurological events (such as bursts of activity) and variation with pathology have been carried out. However, the work on LRTCs in continuous amplitude fluctuations suggests that pathological states lead to a decrease in the Hurst exponent - closer to uncorrelated noise - perhaps relating to a decrease in the communication and ordering of the network. The exception to this decrease in Hurst exponent in relation to pathology was shown in the case of epilepsy. However, epilepsy is a hyper-synchronised state and so we might expect to see an increase in correlations. LRTCs in discontinuous network activity may relate to the Hurst exponent in the same way. Therefore, I hypothesise that the Hurst exponent will be lower in subjects with poorer outcome. This would reflect a faster decay of temporal correlations relating to a less correlated pathological state.

The EEG recordings analysed in this chapter have been examined previously in *Schumacher et al.* 2011 [35]. This work demonstrated that continuous EEG monitoring over the first three days of life is feasible in this population and can be achieved alongside other medical procedures, including ultrasounds, required by these patients [35]. The authors also analysed the total absolute band power at different frequency bands and found that, at all ages and in all frequency bands, total absolute band power increased over the first three days of life. Furthermore, dividing the subjects into two age groups of extremely preterm ($24 \leq GA < 28$) and very preterm ($28 \leq GA < 31$) neonates, the authors observed an increased total absolute band power with gestational age which is present from the first day of life [35]. This study therefore highlights the importance of taking into account the postnatal age as well as the gestational age when comparing preterm subjects.

This study by *Schumacher et al.* [35] and another study by *Victor et al.* [167] indicate that there are changes in the neural activity observed on the EEG over the first few days of life. This may reflect a reaction to the abnormal *ex-utero* environment and some sort of adaptation process. As discussed in Chapter 1 there are a number of EEG changes observed with respect to gestational age which reflect brain development. As these studies suggest that there are changes with respect to gestational and postnatal

age it is worthwhile investigating whether there is an effect of either or both of these factors on LRTCs. As previously stated, LRTCs might be expected to increase with gestational age reflecting brain maturation. I also hypothesise that there will be an increase in Hurst exponent with postnatal age across the first three days of life reflecting an increased adaptation to the environment. A higher Hurst exponent would reflect a slower decay of the temporal correlations, i.e. an increase in the temporal ordering. The foetal brain may not need to be in a critical state as it does not need to be able to react to the environment in the same optimal way in which it would do *ex-utero*. Therefore, an adaptation process after birth may result in an increase in the Hurst exponent.

3.2 Methods

3.2.1 Subjects

EEG was analysed from 41 preterm neonates born between 24 and 30 weeks gestational age, see Table 3.1. All EEGs were recorded in the neonatal intensive care unit of Oslo University Hospital, Norway. Ethical approval and written parental consent was gained for the use of the data for research purposes. Five infants had intraventricular haemorrhages grade II or above as detected by cerebral ultrasound. Note that these 5 infants were not included in the original analysis by *Schumacher et al.* [35]. Also 6 subjects that were included in the original study were not included in the analysis here as they did not have outcome measures obtained at two years. The reasons for this were that two died at 3 weeks of life (one through complications of surgery, one unknown cause), two children moved away from Oslo and the surrounding area and did not return for assessment and two children had congenital disorders that would mean they would have problems with the tests unrelated to their premature birth. To our knowledge this data set is the largest data set ever recorded of preterm subjects across the earliest days of life.

Gestational Age (weeks)	Number of Subjects
24	3
25	5
26	7
27	7
28	7
29	6
30	6

Table 3.1: Subject age details.

3.2.2 EEG recordings

EEG monitoring was carried out within 12 hours of birth and subjects were recorded over the first 3 days of life for an average of 71.37 hours (range: 61.09-77.44 hours, including impedance check times - see below). Eight EEG electrodes were used for monitoring, placed at Fp1, P3, O1, T3, Fp2, P4, O2 and T4 positions according to the 10-20 system modified for neonates. These were chosen to enable ultrasound access over the anterior fontanelle. The electrodes were held in place using a specially designed cap (see [35]). Analysis was carried out using a bipolar montage: Fp1-T3; T3-O1; Fp2-T4; T4-O2; Fp1-P3; P3-O1; Fp2- P4; P4-O2; T3-P3; P4-T4, see Fig. 3.1.

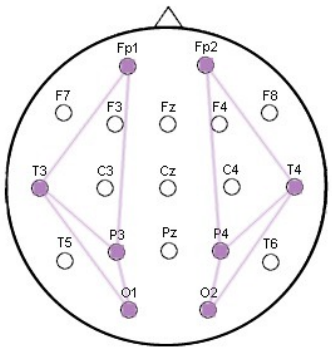

Figure 3.1: The bipolar montage used for analysis of EEG data in this study: Fp1-T3; T3-O1; Fp2-T4; T4-O2; Fp1-P3; P3-O1; Fp2- P4; P4-O2; T3-P3; P4-T4. Note that due to differences in the electrodes this montage is different from the montages used in Chapter 2. These electrodes were used in the recording of these subjects to allow access to the central region for ultrasounds. The montage is the same as that of *Schumacher et al.* [35].

EEG was recorded using the NicoletOne version 5.2 (CareFusion, CA) and a sampling rate of 256 Hz. A high-pass filter of 0.5 Hz, a low-pass filter of 70 Hz and a notch filter at 50 Hz were applied. To sustain an adequate EEG recording throughout the 3 day period electrode impedances were checked regularly. Electrodes with high impedances were then replaced (an electrode was defined as having high impedance when the impedance was $> 40\ k\Omega$). However, as will be discussed in detail below, these impedance checks interrupted the recording of the EEG for varying lengths of time and so this needed to be taken into account when analysing the data and the effect that this had on temporal sequences of BNOs needed to be considered. Note that this was not required for the previous analysis of this data set by *Schumacher et al.* [35] as their analysis was based on averaging across epochs of EEG and the temporal ordering of the data or missing data was not important. Also note that in the recordings analysed in the previous chapter, impedance checks that stopped the recordings were not carried out and so this was not a problem with the analysis there.

3.2.3 EEG analysis

Artefacts were rejected from the EEG (prior to BNO extraction) based on visual inspection of the data on a channel-by-channel basis. As in Chapter 2, single artefacts in the EEG such as an artefact lasting only a few seconds due to subject movement and low levels of EMG were not rejected prior to applying the BNO extraction algorithm as the algorithm was robust to these events. Long periods (more than a few seconds) were rejected as they were likely to preclude the detection of underlying BNOs. All subjects had cerebral ultrasounds during the EEG recording which often caused around 10 minutes of high amplitude noise in the EEG and so led to a period of rejection. The other common reason for a period of artefact rejection was the loss of an electrode - as was the case in Chapter 2. Periods of artefact that were rejected were set to zero in the EEG data set or the data was segmented - discussed below. This method of artefact rejection was different to that used by *Schumacher et al.* as they considered 1 second epochs of data and rejected those with the greatest 5% power [35]. However, this method of rejection does not consider continuous sections of data, such as those where an electrode is unattached, and is more likely to break up the data. Therefore, while it was suitable for the previous analysis carried out by *Schumacher et al.*, the method used in Chapter 2 is more suitable when considering the temporal dynamics of activity and so was used in this instance of data analysis.

As mentioned above, impedance checks were carried out during the EEG recording approximately every three hours and involved the recording being switched off for a period of time. Across all subjects the average duration of an impedance check was 9 seconds (median, range 1 second - 2.18 hours). As we are interested in the temporal ordering in the BNO statistics these impedance checks and the disruption they cause must be taken into account when analysing the data. Similarly long periods of artefacts and the disruption to the temporal sequencing must also be taken into account. For very short impedance checks (or artefacts) it seems unlikely that a BNO is missed - in the last study the average IEI was 21.5 seconds (median 9 seconds). Therefore for very short impedance checks and artefacts it is possible to join the two sections of EEG - using appropriate zero padding to ensure the times between the sections of EEG are correct - and treat this data as normal. However, as the length of the impedance check increases, a BNO is increasingly likely to be missed leading to a change in the sequence of BNOs. As we are interested in long-range correlations we require the longest sections of data possible for analysis but we do not want to have spurious estimates of the Hurst exponents caused by missed BNOs from artefacts and impedance checks. Thus, a criteria was required so that data is segmented if the impedance check or artefact is 'too' long but which also maximises sequence lengths.

Segmentation of the data

Using the data from the previous study (Chapter 2) the effect that impedance checks/artefacts had on the data was simulated by setting a period of the EEG, with a randomly chosen start time, to zero. Thus, this introduced an effective period during which the EEG was not recorded or an artefact precluded BNO detection. The number of BNOs that were missed and the effect that this had on the estimation of the Hurst exponent of the sequence of IEIs was calculated. This was simulated a number of times and the effect of different 'impedance check' lengths was examined. The results from these simulations are shown in Fig. 3.2. Note that it was found that some of these artificial impedance checks led to an increased estimation of the Hurst exponent in the new sequences, while some led to a decrease. Therefore, the absolute value of the difference is plotted, for both DFA and Whittle exponents.

As expected, as the length of the artificial impedance check was increased the number of missed BNOs increased and the difference in the estimates of the Hurst exponent also increased. From these results the threshold for the maximum length impedance check/artefact in the data analysed in this chapter that would be allowed before the data was segmented was set to *300 seconds*. This threshold value was chosen as the effect on both estimates of the Hurst exponents was on average approximately 0.01 or less and should also mean that the data does not require segmentation too frequently thus leading to sequences which are long enough for Hurst exponent estimation. For impedance checks or artefacts longer than 300 seconds the data is segmented, yielding two sections of data and so two sequences of BNOs that will be analysed separately. On the other hand, if the impedance check or artefact is less than 300 seconds long the data is padded with zeros or set to zero (respectively) for the corresponding time, leaving the data as one segment. The results will be compared with a more stringent segmentation threshold of 30 seconds in section 3.3.5, to ensure that no spurious results have been introduced with the higher thresholding.

Data sections

During recording, EEG data was saved in sections of 3 hours. These stored files had an average gap between them of 4 seconds, and all gaps between files were much less than the threshold value for segmenting the data (the largest time lapse between files was 61 seconds). Thus, files were joined together with a zero padding of length equal to the time lapse between the two consecutive files.

However, occasionally (for 8 out of 41 subjects) EEG recording was stopped during the data collection, due to poor electrode impedances. In this case there was a gap between the recorded files (range 6.13 minutes to 4.31 hours). As these gaps were greater than

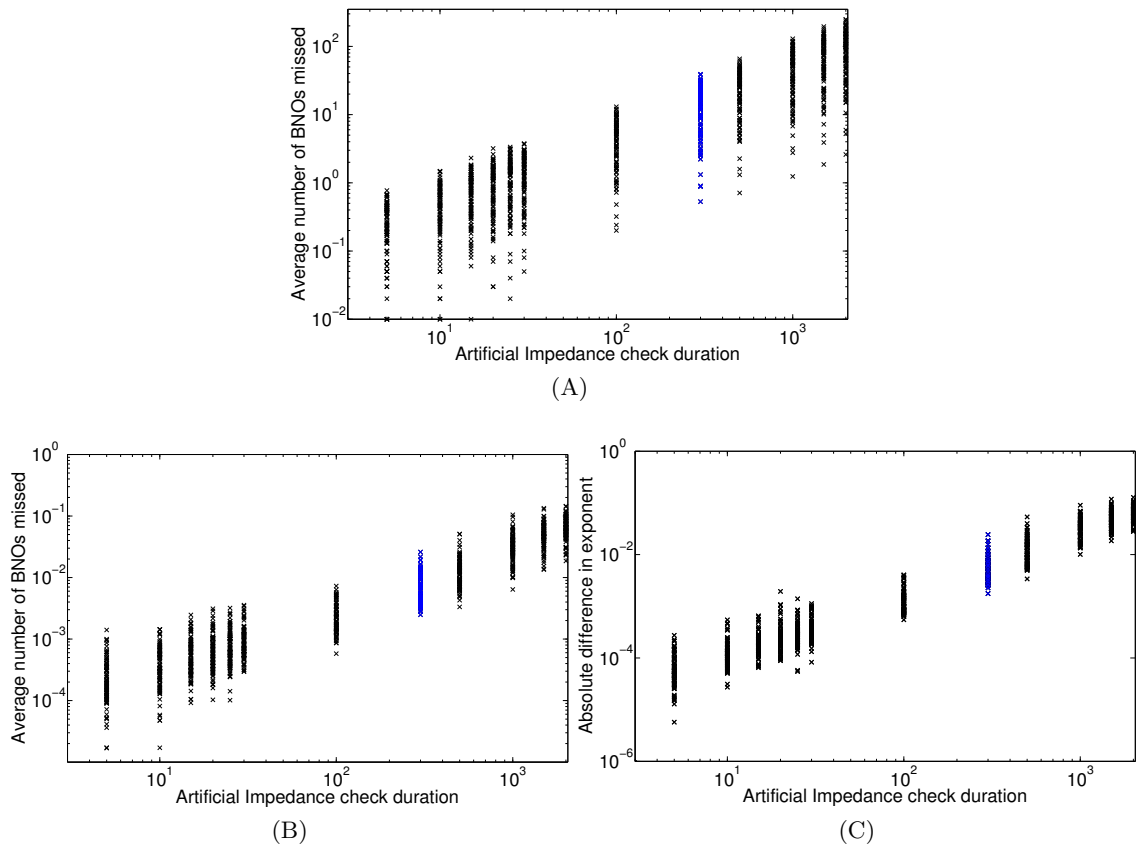

Figure 3.2: (A) Number of BNOs missed and difference in Hurst exponent estimates - (B) DFA and (C) Whittle - following addition of artificial impedance checks to the data from Chapter 2. For each IEI sequence one artificial impedance check with duration as indicated was added. The process was repeated 100 times and an average taken. Blue points highlight artificial impedance checks of duration 300 seconds - the threshold taken for segmentation of the data in this chapter. For this value of the artificial impedance checks the difference in Hurst exponent estimates was approximately 0.01 or less. Note the logarithmic scaling on both axes.

the threshold level this led to segmentation of the data.

Analysis of BNOs

BNOs were extracted from the segments of EEG using the same approach as in Chapter 2 and IEI, amplitude (peak and total) and duration were analysed. However, unlike for the data in Chapter 2, for each subject and channel there were a number of segments (depending on impedance checks and artefacts), each of which had a Hurst exponent estimated through both DFA and the Whittle estimator. As before, a minimum sequence length of 1000 data (IEI, amplitude or duration) points were required for analysis of LRTCs within a sequence to prevent spurious observations of the correlations. Exponents were compared to those exponents estimated from 5000 shuffled sequences to test whether the Hurst exponents of the actual sequences were significant. This process was carried out for each data segment.

The effect of gestational age (GA), time since birth and regional differences on the Hurst exponent (DFA and Whittle estimate) was examined. The subjects were divided into 2 groups according to their GA: group 1 included those subjects less than 28 weeks GA (i.e. $24 \leq GA < 28$ weeks), group 2 included those subjects equal to or older than 28 weeks GA (i.e. $28 \leq GA < 31$ weeks). These groups are the same as those used by *Schumacher et al.* [35] and the group sizes are approximately equal (group 1: $n = 22$, group 2: $n = 19$). Time since birth was assessed across the three days of the recording by further segmenting the data into day 1 (≤ 24 hours), day 2 (24-48 hours) and day 3 (48-72 hours).

Regional differences in the Hurst exponent were examined according to EEG channel location, separating the channels into two groups: those that included frontal electrodes (Fp1-T3; Fp2-T4; Fp1-P3; Fp2- P4) and those that did not (T3-O1; T4-O2; P3-O1; P4-O2; T3-P3; P4-T4). These groups were chosen as there is evidence to suggest regional differences in brain development with frontal regions developing later. This includes differences in the level of gyration in the preterm period, with gyration beginning in the central region [78, 185] and progressing in an occipito-rostral direction [78], differences in subplate apoptosis - the subplate exists in the frontal region for the longest period (until after full-term equivalent age) [65, 186], as well as differences in older children with peak synaptic density known to occur later in the prefrontal cortex compared with the auditory cortex [13]. Furthermore, regional differences have been observed in the preterm EEG by previous authors: total EEG power is increased in occipital and to a lesser extent frontal regions compared with other regions during both active and quite sleep [187]. In a study examining burst spectral power alone (i.e. excluding inter-burst intervals) across the preterm period the largest change in power with age was seen in the frontal and temporal regions [188]. These results suggest there

are regional differences in the EEG and therefore regional differences in the Hurst exponent may also be apparent. I hypothesise that if there is a difference, then lower correlations (closer to 0.5) will be observed in the frontal regions as this area may be underdeveloped in comparison with more posterior regions.

So three different factors were investigated: gestational age, day of recording (time since birth) and EEG channel location. For each subject for each day of recording and for each EEG channel a summary statistic was calculated. This was the average (mean) exponent of all the segments. The reason that an average was taken was as follows. For each subject there were different numbers of segments, with some only having a single segment for a particular channel and day and other subjects having a number of segments. Two ways in which to approach this data from a statistical perspective might be to treat the subjects with fewer segments as having 'missing data' or perhaps to weight the exponents in some way leading to a greater 'confidence' in exponents which are an average across more segments. However, subjects with fewer segments do not have missing data. In fact, a subject with a single segment will have a longer sequence. LRTCs are more robustly estimated over longer sequences and so subjects with single segments should have better estimates of the exponents. A subject with several shorter segments will have several estimates of the Hurst exponent from shorter sequences. Due to the minimum sequence length threshold imposed (sequences must have 1000 data points), for each sequence these estimates will be reliable estimates of the Hurst exponent for that sequence. Taking an average of the exponents is therefore the 'best' measure for that subject.

Effects were analysed using a mixed design ANOVA (type III sum of squares) with age as a between subjects factor and two within subject factors: day of recording and channel location. To obtain a single value for each subject, average exponents were calculated within days (as discussed above) and EEG channel locations (frontal or posterior). Sphericity was tested using Mauchly's sphericity test. If data did not pass this test (with $p < 0.05$) the Greenhouse-Geisser corrected p-values were used. Post-hoc comparisons were carried out where there was a significant difference (of day of recording - the other factors had only two groups) using paired two-sample t-tests with Bonferroni correction for multiple comparisons. As in Chapter 2, analysis was also carried out with fixed length (first 1000) sequences, again averaging over all the segments and using the same methods of statistical testing.

3.2.4 Subject follow-up

Neurodevelopmental outcome was assessed in each of the subjects at 2 years of age using the Bayley Scales of Infant Development and the Peabody Developmental Motor Scales. For the Bayley assessment two subscales were used: the Mental Development

Index (MDI) and the Psychomotor Developmental Index (PDI). Both of these sub-tests were administered on the same day, always in the order of the MDI test followed by the PDI test. The Peabody assessment was administered on a separate day and measured the Total Motor Quotient (TMQ).

A child was said to have poor outcome at this 2 year follow-up age if one of the tests had a score of less than 85, i.e. the outcome was abnormal if $MDI < 85$ or $PDI < 85$ or $TMQ < 85$. It was observed that a number of the children (7) had an abnormal PDI score, but normal scores in the other two tests. This was thought to relate to the ordering of the tests, with the two Bayley subtests being carried out on the same day. The child may have been tired or bored when taking the PDI test leading to artificially low scores. Therefore, this test was removed from the analysis and a child was considered to have normal outcome if they had a normal MDI and TMQ, but to have abnormal outcome if they had $MDI < 85$ or $TMQ < 85$.

The subjects were then divided into 2 groups - those with normal outcome and those with abnormal outcome. For each of the subjects in these groups the average exponent across all segments and channels was calculated (yielding one average exponent value for each subject). Differences in the Hurst exponent between the two groups were assessed using a Mann-Whitney test following assessment of normality of the groups using the Anderson-Darling test. This comparison was carried out with subjects in the two age groups (as defined above) separately.

3.3 Results

Across all subjects and channels the average total length of EEG recording was 65.16 hours (range: 29.40 - 73.65 hours, excluding long artefacts and impedance checks, an average of 71.37 hours, range 61.09 - 77.44 hours including artefacts and impedance checks). Across all subjects and channels the average length of the individual segments analysed was 6.69 hours (range: 6 seconds to 71.86 hours). Note that the segment of length 71.86 hours corresponded to a segment which encompassed all of the data recorded from a channel in one of the subjects, i.e. no segmentation was required for this channel of this subject (other than the segmentation into the three days of recording which was carried out after initial analysis). The average number of segments per subject and channel was 9.69 (range 1 - 25).

3.3.1 BNO statistics

Across all subjects, channels and segments with more than 1000 data points the average number of BNOs per hour was 293.9 (range: 49.8 - 645.8). Fig. 3.3 shows the average

number of BNOs per hour with respect to age group, day of recording and EEG channel location. A mixed ANOVA with age as a between subject factor and day of recording and channel location as within subjects factors showed no significant effect of age group with respect to the average number of BNOs per hour. However, there were significant effects of both day of recording ($p < 0.001$) and channel location ($p < 0.01$). There was also a significant day-channel interaction. Post-hoc comparison of the effect of day using paired t-tests with Bonferroni correction showed significant effects ($p < 0.001$) between all days. Thus, the results indicate a significant increase in the average number of BNOs across the first three days of life and it is worth recalling that this is a longitudinal data set so this result is not caused by analysing different subjects.

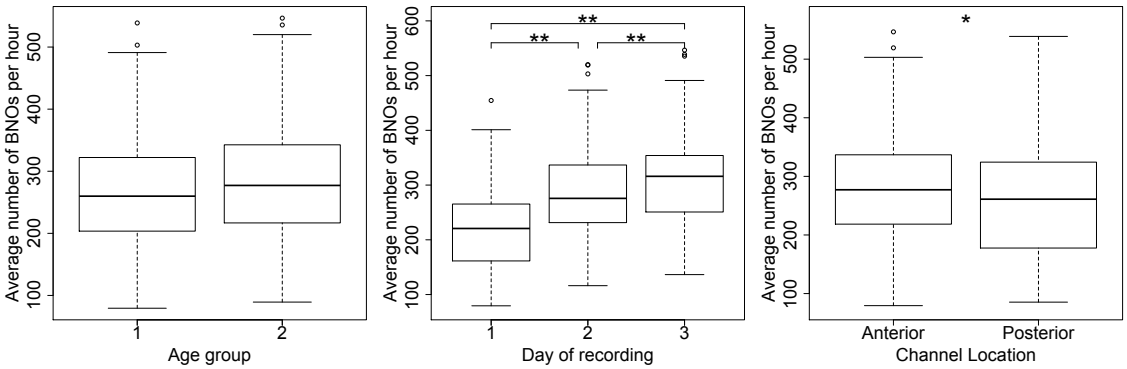

(A) (B) (C)

Figure 3.3: Average number of BNOs per hour with respect to (A) age group, (B) day of recording and (C) channel location. 'Anterior' indicates those channels that included frontal electrodes (Fp1-T3; Fp2-T4; Fp1-P3; Fp2- P4) and 'posterior' indicates those that did not (T3-O1; T4-O2; P3-O1; P4-O2; T3-P3; P4-T4). Asterisks indicate significant differences between the groups with $**$ indicating $p < 0.001$ and $*$ indicating $p < 0.01$.

As was the case in the last chapter, there was a significant difference ($p < 0.001$, Mann-Whitney test) between the average number of BNOs per hour (including all three days of recording) of those subjects with intracranial haemorrhage (mean $\pm$ standard deviation: 234.9 ± 96.4) compared with those subjects without haemorrhages (274.4 ± 111.9). However, in this data the average number of BNOs per hour in the subjects with intracranial haemorrhage is not as low as it was for those subjects analysed in Chapter 2. Consistent with previous results in the literature [101], the average number of BNOs per hour was also significantly lower ($p < 0.001$, Mann-Whitney test) in those subjects with haemorrhages with abnormal outcome at 2 years (200.8 ± 94.3, $n = 3$) compared with those subjects with haemorrhages but with normal outcome at 2 years (257.2 ± 91.7, $n = 2$).

Across all subjects the average (median) IEI was 6.1 seconds, average duration was 0.49 seconds and the average amplitude was 133.9 μV (peak amplitude) and 8301.4 μV (total amplitude). The distribution of each of the four BNO components, pooled from

all subjects is shown in Fig. 3.4 along with the distribution of the logarithm of the data. The distributions for all four characteristics were of similar shape to the distributions in the previous chapter. Note that (as in chapter 2) some outliers can be detected in the distribution of BNO peak amplitude. Those outliers with peak amplitude greater than 1000 μV accounted for 0.19% of the data and were rejected from the analysis of BNO amplitude sequences.

3.3.2 Hurst exponent statistics

LRTCs were assessed in sequences of BNO amplitude, duration and IEIs as in the previous chapter. For each of the DFA analyses, the value of R^2 was calculated for the linear fit. To avoid spurious exponents resulting from non-linear trends across box sizes a threshold of $R^2 = 0.95$ was set and those sequences with $R^2 < 0.95$ were excluded from analysis. No peak amplitude sequences had an $R^2 < 0.95$. Five IEI sequences, 8 duration sequences and 20 total amplitude sequences were rejected based on this criteria (out of a total of 1804 sequences for each characteristic assessed).

Taking these rejections into account, the exponent statistics are given in Table 3.2. As with the previous data, Hurst exponents indicative of LRTCs were observed in all four of the BNO characteristics. These exponents were compared with the exponents of randomly shuffled sequences. Fig. 3.5 shows the comparison of the exponents of the shuffled sequences with the average (for each subject) exponents of the actual sequences, for both Whittle and DFA. For all characteristics and both DFA and Whittle exponents the means of the distributions of the actual exponents compared with the pooled distributions of exponents of the shuffled sequences were significantly different ($p < 0.01$, Wilcoxon Mann-Whitney test). However, some of the differences in the means of these distributions were small for duration, peak amplitude and total amplitude - see Table 3.3 - indicating only a small increase in the exponents of the actual sequence with respect to the randomised uncorrelated sequences. The number of exponents that fell in the lower 95% of the corresponding shuffled distribution was also higher in the case of duration and amplitude data compared with the exponents from IEI sequences, see Table 3.4. Thus, as with the data in Chapter 2 there is strong evidence to indicate the presence of LRTCs in the IEI sequences of all subjects studied. There is also evidence of the presence of LRTCs in the sequences of BNO duration, peak amplitude and total amplitude, however, these results are less robustly observed.

There was a significant difference in the exponents of the subjects with and without haemorrhages only in DFA and Whittle exponents of the duration sequences ($p < 0.001$, Mann-Whitney test), as was the case in the previous chapter. There was also a difference ($p = 0.03$) in the DFA of peak amplitude sequences though the difference in the means of the two groups was actually only 0.007. Note there is a large difference in

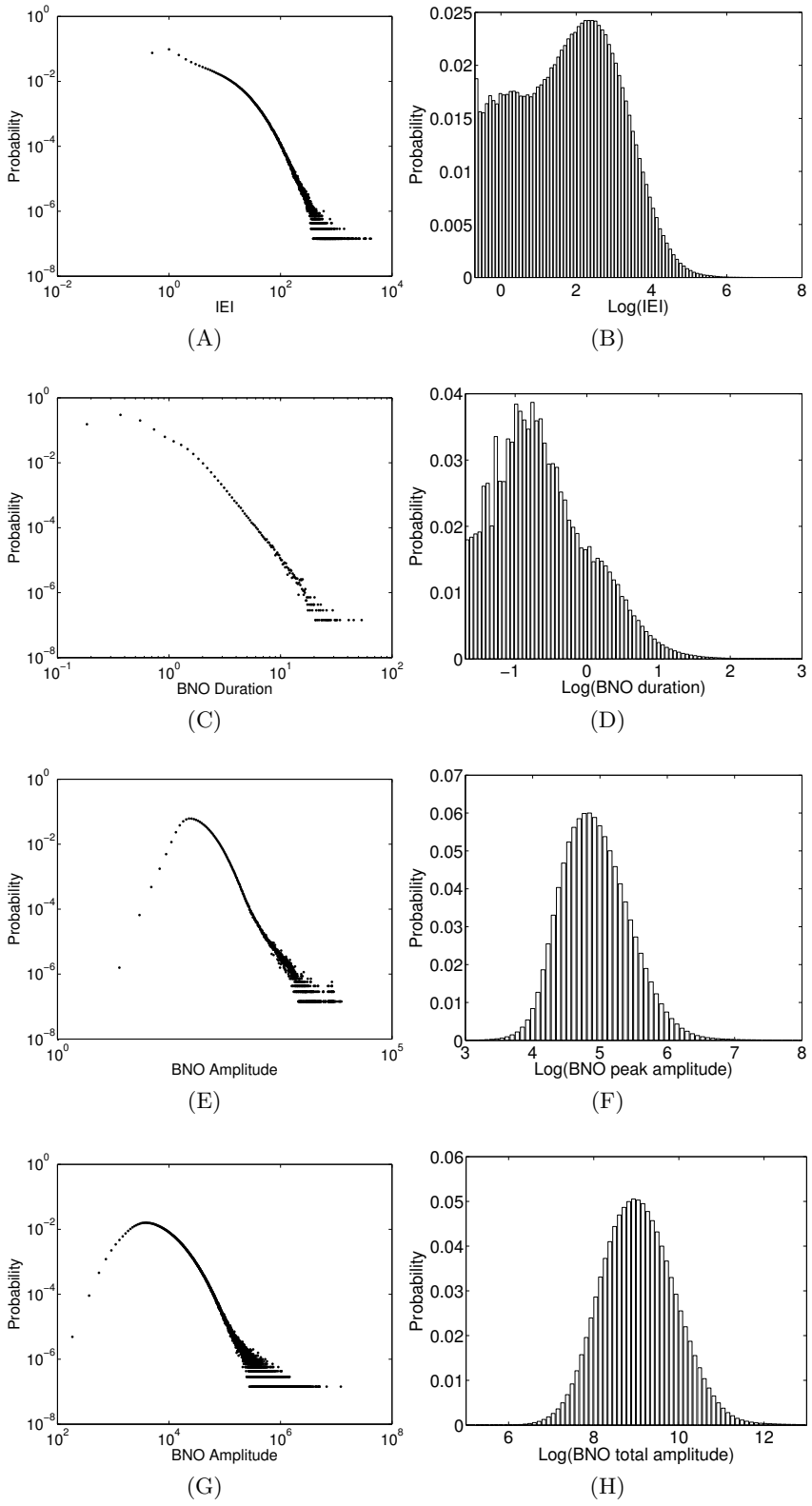

Figure 3.4: Distributions (A,C,E,G) and the distributions of the logarithm (B,D,F,H) of IEIs (A,B), peak amplitude (C,D), total amplitude (E,F) and duration (G,H), with data pooled from all subjects.

	DFA exponent			Whittle exponent		
	Mean	Minimum	Maximum	Mean	Minimum	Maximum
IEI	0.66	0.46	0.86	0.61	0.46	0.77
Peak Amplitude	0.60	0.44	0.82	0.58	0.46	0.83
Total Amplitude	0.59	0.45	0.86	0.57	0.45	0.87
Duration	0.58	0.41	0.88	0.56	0.42	0.91

Table 3.2: Summary statistics of the DFA and Whittle exponents of each of the four BNO characteristics, calculated across all subjects, channels and segments.

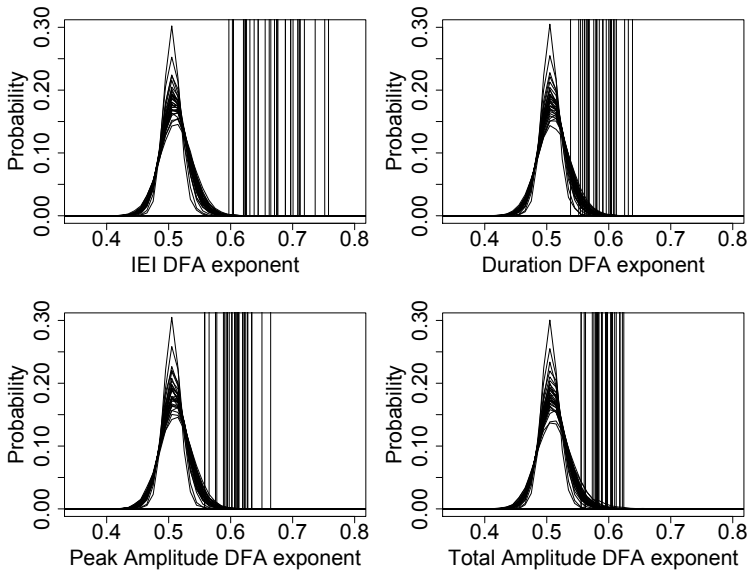

(A)

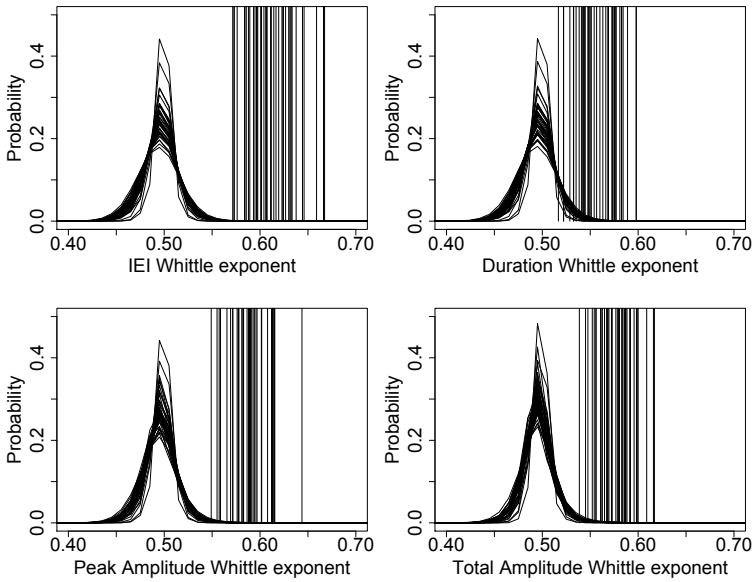

(B)

Figure 3.5: Comparison of (A) DFA and (B) Whittle exponents for the actual sequences and shuffled sequences, with the BNO characteristic as indicated on the x-axis of each plot. Distributions are the pooled shuffled distributions for each subject. Vertical lines indicates the average exponent for each subject (averaged across EEG channels and segments).

	Difference in means - DFA			Difference in means - Whittle		
	Mean	Minimum	Maximum	Mean	Minimum	Maximum
IEI	0.16	0.06	0.26	0.12	0.07	0.17
Peak Amplitude	0.09	0.04	0.16	0.09	0.05	0.12
Total Amplitude	0.08	0.03	0.12	0.07	0.04	0.12
Duration	0.07	0.02	0.14	0.06	0.02	0.10

Table 3.3: Summary statistics of the differences between the means of the distributions for the original sequences and the pooled distribution of the shuffled sequences. The table shows the differences of these means averaged across subjects, and the minimum and maximum differences across subjects. All distributions of the exponents of the original sequences were significantly different from the shuffled distributions ($p < 0.01$).

	DFA distributions overlap		Whittle distributions overlap	
	Number	Proportion	Number	Proportion
IEI	8	0.15	5	0.10
Peak Amplitude	25	0.18	12	0.14
Total Amplitude	31	0.22	24	0.13
Duration	37	0.33	36	0.29

Table 3.4: Comparison of individual exponents with the corresponding shuffled distributions. Table shows the number of subjects (out of 41) who had at least one of the original sequence exponents within the lower 95% of the shuffled distribution. 'Proportion' indicates the proportion of exponents of original sequences that lie within the lower 95% of their corresponding shuffled distributions, averaging across those subjects that have at least one exponent within this lower 95% region. Note that this test was carried out for all sequences (for all channels and segments) and so the number of exponents for each subject varied, hence a proportion rather than the absolute value is indicated.

the sizes of the subject groups (36 subjects in the group without haemorrhage - which was classed as those with IVH grade I or below - and only 5 subjects in the group with haemorrhages). Interestingly, the average exponents for the duration sequences were higher in the case of subjects with haemorrhage - see Fig. 3.6.

As with the previous chapter, due to the natural differences in BNO numbers within the EEG recordings, exponents were also calculated for fixed length sequences of the first 1000 data points (i.e. IEI, duration, peak or total amplitude) from every sequence. This enables a more direct comparison of the sequence exponents. The summary statistics for the exponents of the fixed length sequences are given in Table 3.5. As was the case with the data in Chapter 2, the fixed length sequences have on average slightly lower exponents. However, exponents indicating LRTCs were still consistently observed.

	DFA exponent			Whittle exponent		
	Mean	Minimum	Maximum	Mean	Minimum	Maximum
IEI	0.62	0.52	0.79	0.60	0.49	0.72
Peak amplitude	0.58	0.48	0.72	0.57	0.46	0.77
Total amplitude	0.57	0.46	0.72	0.56	0.47	0.73
Duration	0.56	0.47	0.69	0.56	0.49	0.69

Table 3.5: Summary statistics of the exponents of the fixed length sequences (first 1000 data points).

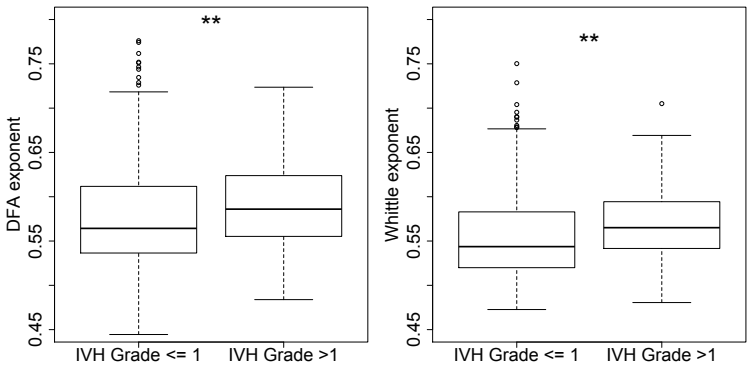

(A) (B)

Figure 3.6: (A) DFA and (B) Whittle exponents for duration sequences for those subjects without (IVH grade I or below) or with haemorrhages. There was a significant difference between these two groups in this case (i.e. duration sequences). Asterisks indicate the significant difference between the two groups with $p < 0.001$.

3.3.3 The effect of gestational age, time since birth and channel location on the Hurst exponent

As described in the methods section, subjects were divided into two groups according to their gestational age (group 1: $24 \leq GA < 28$, group 2: $28 \leq GA < 31$). For each subject the Hurst exponent estimates were calculated for each of the three days of recording (averaging across segments) and were divided into two EEG channel locations according to whether the channel included a frontal electrode or did not (averaging over exponents from the channels within the group). A mixed ANOVA was used to test differences between the means of each of the factors as well as factor interaction. This was computed for each of the burst attributes and the DFA and Whittle exponents separately. Note that most of the data had a p-value $p > 0.05$ according to Mauchly's sphericity test indicating that the variances between pairs of groups are equal and the repeated measures ANOVA assumption of sphericity within the data was not violated. The exceptions to this were: DFA exponents - IEI sequences for day-channel interaction and day-channel-age interaction; Whittle exponents - IEI sequences for day-channel interaction, peak amplitude for day-channel and day-channel-age interaction, and duration for day and day-age interaction. In these cases the Greenhouse-Geisser corrected p-value was used.

There was no effect of gestational age defined by the two groups observed for any of the burst attributes for either the DFA or Whittle exponent. Fig. 3.7 shows the DFA exponents of IEI sequences for the two age groups, including the exponents from each channel location and day of recording for all subjects.

There was a significant effect of day of recording for the DFA ($p = 0.018$) and Whittle ($p = 0.012$) exponents of IEI sequences. In these cases there was also a significant effect

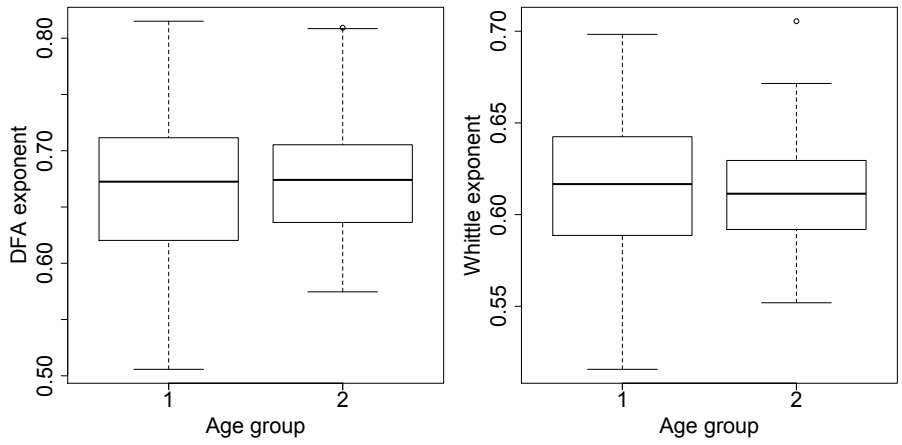

(A) (B)

Figure 3.7: (A) DFA and (B) Whittle exponents of IEI sequences for each of the two age groups (group 1: $24 \leq GA < 28$, group 2: $28 \leq GA < 31$). For this box plot exponents were included from both EEG channel locations and also from all three days of recording. There was no effect of age group for any of the burst characteristics with DFA or Whittle exponent.

of day-channel interaction ($p = 0.0015$ DFA, $p = 0.00029$ Whittle). Post-hoc comparisons were carried out with exponents pooled by day, from all subjects and both channel locations, using paired two-sample t-tests with Bonferroni correction. For both DFA and Whittle exponents these tests showed significant differences with $p < 0.01$ between days 1 and 2 but not between days 1 and 3 and days 2 and 3. Fig. 3.8 shows the exponents across each of the three days for the IEI sequences. As can be seen in the figure the average exponent is higher on the first day compared with the average exponent on the other two days.

There was a highly significant effect of EEG channel location ($p < 0.001$) in both the DFA and Whittle exponents of BNO duration. Fig. 3.9 show a box plot of the DFA and Whittle exponents for the two channel locations including all subjects exponents from all the days of recording. Contrary to the hypothesis, the average exponent at the anterior channel locations (i.e. those channels that included frontal electrodes) was higher than the average posterior exponent. There was also a significant difference between the Whittle exponents of the peak amplitude ($p = 0.008$), data shown in Fig. 3.9. However, in this case the difference between the means of the two groups was actually only 0.006 and the average exponent was slightly higher in the posterior location. There was no significant effect of channel location for any of the other burst statistics.

In summary, there was no effect of age group for any of the BNO characteristics. There was a significant effect of day of recording for DFA and Whittle exponents of IEI sequences only with the average exponent for day 1 greater than that for day 2. There was a significant effect of EEG channel location for DFA and Whittle exponents of BNO duration sequences, with the average exponent greater for the anterior region, and for

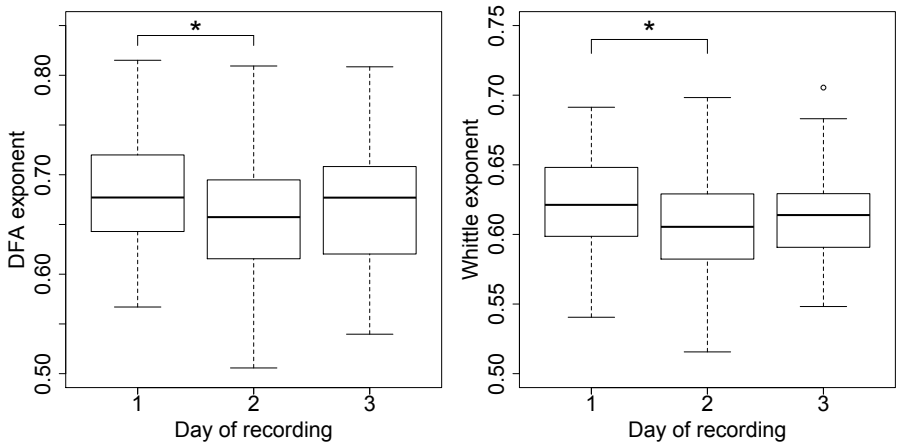

(A) (B)

Figure 3.8: (A) DFA and (B) Whittle exponents for IEI sequences plotted with respect to the day of recording. This includes all subjects and exponents for both channel locations. There was a significant effect of day in both cases. Post-hoc comparison revealed significant differences of the means between day 1 and day 2 only for both DFA and Whittle exponents. Asterisk indicates a significant difference between the two groups with $p < 0.01$.

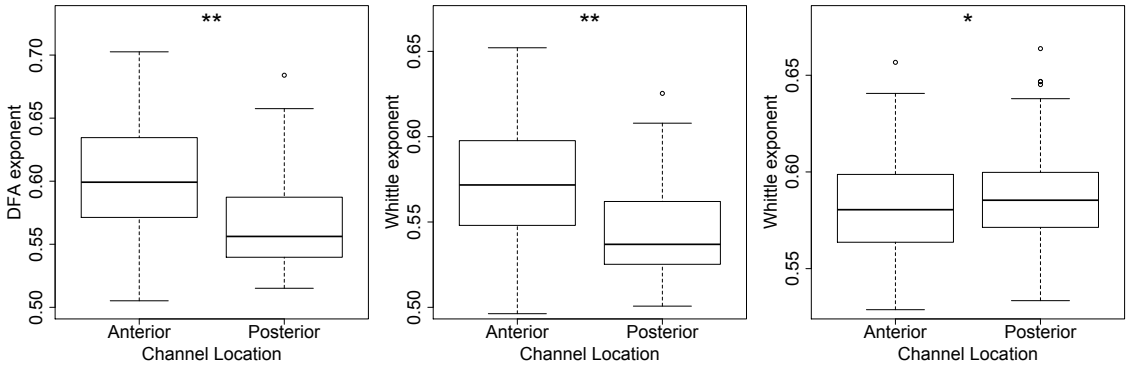

(A) (B) (C)

Figure 3.9: (A) DFA and (B) Whittle exponents for BNO duration sequences and (C) Whittle exponents for BNO peak amplitude sequences for all subjects across all days of recording plotted with respect to EEG channel location. 'Anterior' indicates those channels that included frontal electrodes (Fp1-T3; Fp2-T4; Fp1-P3; Fp2- P4) and 'posterior' indicates those channels that did not (T3-O1; T4-O2; P3-O1; P4-O2; T3-P3; P4-T4). For all three of these exponent sets there was a significant effect of EEG channel location. However, in the case of peak amplitude sequences (C) the difference between the means was actually only 0.006. Significance levels between the two groups are as indicated with $**$ indicating $p < 0.001$ and $*$ indicating $p < 0.01$. There was no significant effect of channel location for the exponents of the other BNO characteristics.

the Whittle exponent of peak amplitude sequences. Examination of the statistics for fixed length sequences showed the same effects except that there was additionally a significant effect of DFA exponent of channel for the peak amplitude sequences (as well as for the Whittle exponent, $p = 0.019$) and post-hoc comparison of the effect of day of recording on DFA exponents of IEI sequences also showed a significant difference ($p < 0.01$) between days 1 and 3.

3.3.4 Does the Hurst exponent correlate with neurological outcome?

All of the subjects were assessed on cognitive and motor performance at 2 years of age. Of the 41 subjects 25 had normal outcome, with neither of the two assessments having abnormal scores. One child did not complete the Bayley test due to non-compliance, but did complete the Peabody test. As this child had a normal outcome on the Peabody test they were placed in the normal outcome category. Sixteen subjects exhibited abnormal outcome with at least one of the tests having an abnormal score. Five children had abnormal scores on both tests. Interestingly, of the 5 subjects with intraventricular haemorrhage grade II or above (as identified on cerebral ultrasound during the first 3 days of life), 3 had normal outcome and one had an abnormal score only for the Bayley test. The subjects were divided into two groups according to normal (no tests with abnormal scores) or abnormal (at least one test with an abnormal score) performances on these follow-up tests.

Fig. 3.10 shows box plots of the average Hurst exponents for the subjects with normal and abnormal outcome also split according to subject age group as was defined before. Exponents for each subject were taken as an average over the values for all the segments and channels of that subject. Comparison of the exponents using a Mann-Whitney test showed no significant differences between the normal and abnormal group for any of the BNO characteristics. This is contrary to the hypothesis that the subjects with abnormal outcome may have lower exponent values. The fact that there is no difference in the Hurst exponent between the two groups is perhaps surprising when considering the adult literature that has shown that the degree of LRTCs is altered with pathology [47, 142–144]. However, this analysis related to LRTCs in the continuous fluctuations of oscillation amplitude and so is a different measurement to the patterning investigated in the discontinuous preterm EEG in this thesis. The pathologies investigated in the adult literature were also different to those investigated here.

Comparison of the fixed length sequences also showed no significant differences between the those subjects with normal and abnormal outcome except in the case of Whittle exponents of the total amplitude sequences which showed a difference boardering on significant ($p = 0.04$, Mann-Whitney test).

Comparison of the exponents and outcome between those subjects who had IVH grade

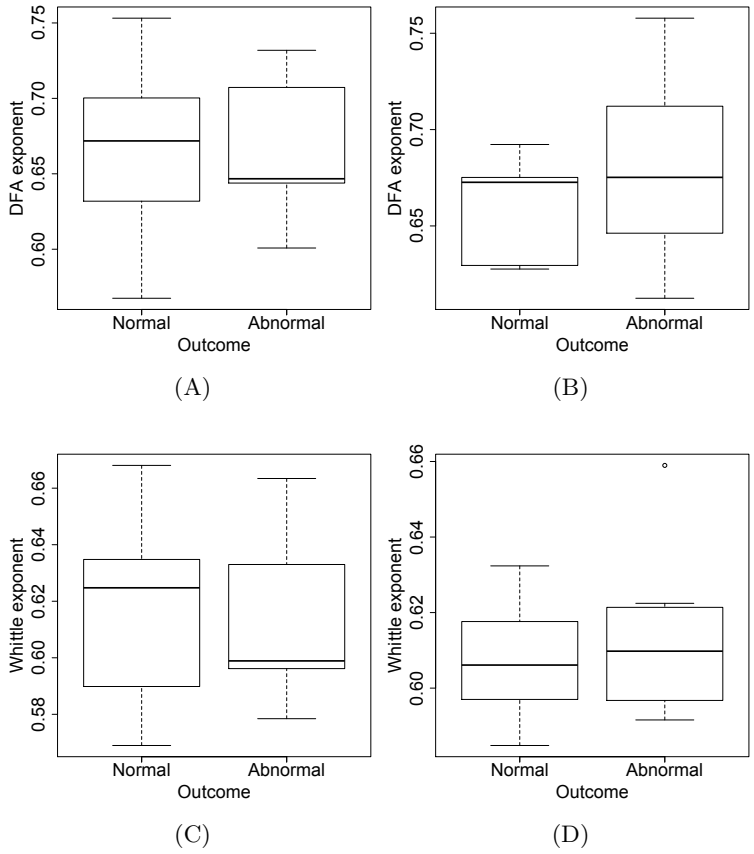

Figure 3.10: (A,B) DFA and (C,D) Whittle exponents of IEI sequences for age group 1 (A,C) and age group 2 (B,D) plot according to follow-up at two years of age (classed as either normal or abnormal). The exponent for each subject was the average across all segments and channels. The age groups were as defined previously with group 1: $24 \leq GA < 28$ and group 2: $28 \leq GA < 31$.

II and above at birth (i.e. comparison of these 5 subjects only split according to outcome) did show significant differences ($p < 0.001$, Mann-Whitney test) for DFA and Whittle exponents of duration sequences and Whittle exponents of peak and total amplitude sequences. Interestingly, the exponents were higher in all four cases in the group with abnormal outcome, see Fig. 3.11. There were no significant differences between the groups for the other BNO characteristics.

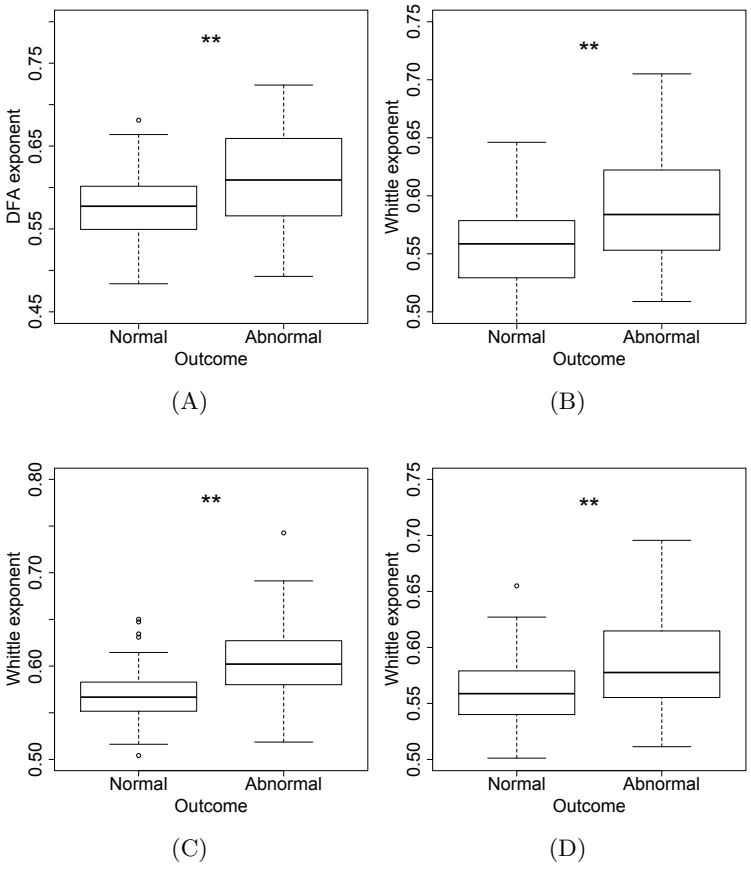

Figure 3.11: Comparison of exponents of those subjects with haemorrhages observed at birth and normal outcome at 2 years ($n = 3$) and those with abnormal outcome ($n = 2$). (A) DFA exponents of the duration sequences. (B) Whittle exponents of the duration sequences. (C) Whittle exponents of the peak amplitude sequences. (D) Whittle exponents of the total amplitude sequences. There was a significant difference ($p < 0.001$) between the two groups in all four of these measures, with higher average exponents in the group with abnormal outcome.

3.3.5 Comparison of results to those with a segmentation threshold of 30 seconds

In the methods section, simulations of artificial impedance checks were used to determine an appropriate threshold for segmentation of the data due to long impedance checks or artefacts. This segmentation threshold was chosen as a compromise between a low value, which would mean that shorter segments were obtained and so estimates of the

LRTCs would be less robust, and a high value which would lead to spurious estimates of the Hurst exponent due to missing data. From the analysis the segmentation threshold was set to 300 seconds and this value has been used throughout the rest of this chapter. In this section we briefly examine a much more stringent threshold set to 30 seconds to determine whether the threshold chosen above had an effect on the results.

The average number of segments with a threshold of 300 was 9.69 (range 1-25 - average across all EEG channels from all subjects) with an average length of the segments of 6.69 hours (range 6 seconds - 71.86 hours). For a threshold of 30 seconds the average number of segments increased to 21.02 (range 2-55) with the average length of the segments decreasing to 3.05 hours (range 5 seconds to 60.70 hours). The summary statistics for IEI, BNO duration and amplitude were approximately the same for both thresholds, with only slight changes (the median value IEI for a threshold value of 300 was 6.11 seconds and for the threshold of 30 was 6.10 seconds). However, this would be expected as changing the impedance check threshold would be expected to affect a single IEI (if the data is not segmented it is set to zeros during an impedance check therefore a BNO cannot be detected in this region which leads to the region being defined as an IEI). While the number of segments is increased with a threshold of 30 seconds, the relative proportion of segments that can be analysed in terms of the LRTCs of the sequences is decreased due to the requirement of 1000 data points and the fact that the segments are shorter. For a threshold of 300 seconds 1804 sequences were analysed (out of a total of 3963 - the sequences that were not analysed were less than 1000 data points long) but with a threshold of 30 seconds only 1983 sequences (from a total of 8599) can be analysed.

Table 3.6 shows the summary statistics for the DFA and Whittle exponents for the sequences obtained from the segments with the 30 second threshold. For this lower threshold the exponents continue to indicate LRTCs in the data. Comparison with Table 3.2, the summary statistics for the exponents with a 300 second segmentation threshold, shows that the exponents (though there are some differences as would be expected) are similar to these previous values.

	DFA			Whittle		
	Mean	Minimum	Maximum	Mean	Minimum	Maximum
IEI	0.66	0.44	0.86	0.61	0.43	0.79
Peak amplitude	0.59	0.42	0.90	0.58	0.46	0.91
Total amplitude	0.58	0.30	0.83	0.56	0.45	0.93
Duration	0.57	0.41	0.82	0.55	0.43	0.75

Table 3.6: Summary statistics of the DFA and Whittle exponents for sequences from segments of data obtained from the stricter segmentation threshold of 30 seconds. This can be compared with the exponents from the original segments (with a segmentation threshold of 300 seconds) listed in Table 3.2.

Statistical analysis with a mixed ANOVA to examine the effects of GA, day of recording

and EEG channel location on the Hurst exponents with a 30 second segmentation threshold showed the same effects as the previous analysis carried out for exponents with a segmentation threshold of 300 seconds: no effect of GA, an effect of channel location for the exponents of the duration sequences and the Whittle exponents of peak amplitude sequences, an effect of day of recording on the exponents of the IEI sequences (with post-hoc comparison indicating a significant effect between day 1 and day 2 and also, in the case of the Whittle exponents only, between day 2 and day 3). Additionally, there was a significant effect of day of recording on the DFA exponents of the total amplitude sequences ($p < 0.01$). Post-hoc comparison showed a significant effect ($p < 0.01$) between day 2 and day 3 only.

Comparison of the exponents of the sequences from a 30 second segmentation threshold and the outcome data at 2 years showed no differences between the exponents of those with normal outcome and those with abnormal outcome.

3.4 Discussion

In this chapter the EEG recordings of 41 preterm subjects, all with gestational ages between 24 and 30 weeks and recorded over the first three days of life, were analysed. This extends the study of the previous chapter to a much larger data set which was also importantly not confounded by differences in postnatal age of the subjects at the time of the recording. Similar shape distributions were observed for BNO amplitude, duration and IEIs compared with those for the data in Chapter 2. Furthermore, LRTCs were observed in sequences of BNO amplitude, duration and IEI, confirming the results of the previous chapter. As with the previous chapter, LRTCs were most robustly observed in IEI sequences for which the exponents were consistently within the upper 5% of the distribution of the exponents of the corresponding randomly shuffled sequences. However, for all BNO characteristics the overall distributions of exponents of the actual sequences were significantly different from the distribution of the exponents of the shuffled sequences, indicating LRTCs in the sequences of all BNO characteristics.

3.4.1 Factors affecting the Hurst exponent

One of the main aims of this chapter was to investigate whether there were changes in the Hurst exponent (i.e. the degree of the LRTCs) with respect to gestational age or postnatal age. Previous work has suggested that there are changes in the EEG in relation to both these factors making them worthwhile variables to consider. Investigation of these factors was also motivated by the hypothesis that self-organisation to a critical state may occur over this developmental time period and that maturation may affect the Hurst exponent. A regional effect on exponents was also examined by

separating the EEG channels into two groups. These were separated according to more anterior or posterior locations as there is evidence to suggest that the brain matures in a rostral-caudal direction.

The effect of gestational age on the Hurst exponent

There was no effect of gestational age observed for any of the BNO characteristics. One of the reasons why this might be the case is the relatively small sample size studied here. *Smit et al.* [45] observed a trend in the degree of LRTCs (in the fluctuations of oscillation amplitude) across childhood which was not observed by *Berthouze et al.* [44], with the former authors suggesting this difference in the results was related to the fact that their sample size was much larger. The large sample size was needed to counteract the fact that there was a large variance in exponents observed at all ages and while the trend showed that there was an increase in the Hurst exponent across childhood, some young children had exponents that were much higher than those exhibited by some adults. Therefore, the Hurst exponent was relatively insensitive to age effects. Given this result, it might be that investigating a much larger population of preterm children would permit the observation of trends with age. However, a sample of preterm subjects recorded in the same way (i.e. at the same postnatal age) which is much larger than the current data set would be difficult to achieve. There was also a large variance in the data observed in this study so, given the effort needed to record a large number of preterm subjects, one might question the need for conducting such a study. Furthermore, there was an effect of time since birth and EEG channel location (for some BNO characteristics) on the exponents (i.e. the sample size was sufficient for such effects to be observed) emphasising the fact that increasing the sample size would only lead to a detection of weak effects of gestational age (if such effects were to exist). However, to this end it is important to perform power calculations which could be used for future analysis and this is discussed below.

Another reason for the lack of effect of gestational age might be the number of possible differences between the subjects within the study. A number of other factors which have not been considered here may have affected their EEG activity. For example, particularly as the subjects were recorded so soon after birth, the reason for premature birth may be a factor, with some subjects perhaps having a more traumatic birth than others. Other factors such as non-neurological medical problems and the amount of medical attention the infant required may influence the neurological activity. On the other hand, splitting the subjects into two age groups should average out any of these effects and *Schumacher et al.* did observe a difference in band power with gestational age in these subjects. Therefore, it seems likely that there is in fact no trend in the Hurst exponent with gestational age in this developmental period, as the result from this sample population indicates.

In the data studied in Chapter 2, there was a significant increase in the exponents of the fixed length sequences of BNO duration and amplitude with the *corrected* age of the subjects. No trend was observed in the exponents for the fixed length sequences with *gestational* age of the subjects in the present chapter. However, the data in this chapter was not confounded by differences in time since birth of the subjects. Some subjects analysed in Chapter 2 were recorded on the first day of life while others were recorded up to two weeks after birth. Previous research has observed effects on the EEG with postnatal age [35, 167] and the results presented here also showed an effect of postnatal age with the IEI exponents higher on the first day of life compared with the second. No longitudinal comparison has been made between exponents of EEG recorded on the first day of life with EEG recorded at two weeks postnatal age. However, this may well have had an effect on the results in Chapter 2 leading to the observed trend with corrected age. The results of this chapter are more robust and provide a strong indication that there is no effect on the Hurst exponent with gestational age across the age range studied.

The effect of postnatal age on the Hurst exponent

For both the DFA and Whittle exponents, there was a significant effect of the day of the recording on the exponents of IEI sequences only. Post-hoc tests showed that there was a significant difference between day 1 and 2, with the mean exponent for day 1 greater than the mean exponent for day 2. For exponents with the 30 second segmentation threshold there was also a significant effect of day for the DFA exponents of total amplitude, but in this case post-hoc comparison showed that there was a significant difference between day 2 and day 3. While in some ways the statistics observed with the more stringent threshold (30 seconds) might be more accurate, due to the higher level of segmentation at this threshold and the minimum required sequence length for analysis, most of the data at this segmentation threshold cannot be analysed. This highlights the problems relating to the impedance checks in the data and if this experiment were to be repeated it should only be done so when impedance checks can be carried out without switching off the recording. Having said this, the fact that the data from the 30 second segmentation threshold (and the fixed length sequences) showed significant effects in all the cases in which the original data also showed significant effects indicates that these results are robust.

The fact that for IEI sequences the exponents were significantly greater on day one compared with day two is contrary to the hypothesis that the Hurst exponent would increase over the first few days of life. This hypothesis came from the idea that the brain may adapt to the *ex-utero* external environment over the first few days of life which may be reflected in an increased Hurst exponent in a similar way to the idea that the Hurst exponent was expected to increase with maturation. *Smit et al.* [45] suggest

that the Hurst exponent will increase with maturation following their results examining LRTCs in the fluctuations of oscillation amplitude. However, as discussed above, the effect they observed was actually fairly weak requiring a large sample size. No effect of age (i.e. maturation) was observed in this data set. Furthermore, LRTCs in the temporal ordering of BNOs, which are discrete events, reflects a different type of ordering to the LRTCs observed in the continuous EEG recordings of older subjects. The different mechanisms generating these contrasting types of activity may therefore mean that changes in the Hurst exponent reflect different processes. I speculate that the higher exponent on the first day may instead be related to the traumatic birth experience and medical procedures required, followed by a return to baseline (adaptation) by the second day.

Regional differences in the Hurst exponent

There was a significant difference between the EEG channel locations in the exponents of duration sequences for both the DFA and Whittle exponents. Contrary to the hypothesis, in this case the average Hurst exponent was greater for anterior channels than for posterior channels. As was discussed above, this hypothesis was related to an investigation of LRTCs in the fluctuation of oscillation amplitude across a period of maturation [45]. However, it appears that the Hurst exponent in this population is not necessarily a marker of maturation (no change was observed with gestational age). Therefore, the increased exponent in frontal regions should not be taken as a contradiction of previous results in the literature suggesting that the frontal region is less mature at this age.

3.4.2 Correlations of the Hurst exponent with later outcome

One of the main questions in the clinical field relating to preterm subjects is whether EEG measures taken early in life can predict later outcome. All the subjects in this study were tested on motor and cognitive development at 2 years of life and so it was of interest to see whether the Hurst exponent was different between those subjects with normal outcome and those subjects with abnormal outcome. In fact, for all BNO characteristics there was no significant difference between the Hurst exponents of the children with normal and abnormal outcome.

On the other hand, comparison of only the 5 subjects with intracranial haemorrhages did reveal significant differences in exponents, with the average exponent greater in the group with abnormal outcome. These differences are between a very small sample size and so this effect would need to be considered in a much larger sample before a

conclusion can be drawn. However, it is still an interesting effect to consider. What might lead to an increased Hurst exponent in subjects with an abnormal outcome?

3.4.3 Do higher Hurst exponents reflect a hyperexcitability within the system?

As described, we have seen increased exponents, reflecting a slower decay of temporal correlations, in cases where we had anticipated observing a lower exponent. In particular, this is surprising when considering the differences in outcome in the group of subjects with intraventricular haemorrhages. However, *Parish et al.* [47] also observed an increased Hurst exponent (albeit in continuous data in the fluctuations of oscillation amplitude) in epileptogenic brain region compared with the contralateral side. As epilepsy is an hyperexcitable state and the preterm brain is a system which is in an altered state of excitability in comparison to the more mature neural system [63] it is possible that the increased Hurst exponents we have observed in some cases in this data set also relate to a hyperexcitable state. If this was the case, then this might explain why subjects with higher exponents (in the haemorrhage group) have abnormal outcome later in life. I speculate that the higher exponent (of duration sequences) on the first day of recording may also reflect an increased excitability of the brain in response to birth, with a decrease back to 'baseline' by day two.

On the other hand, in the case of time since birth there is an increase in total absolute band power across the first three days of life [35] and an increase in the average number of BNOs per hour (see Fig. 3.3). Furthermore, subjects with haemorrhages with abnormal outcome had significantly lower numbers of bursts per hour compared with those subjects with haemorrhages with normal outcome. In both cases this suggests there is less overall BNO activity when a higher exponent was observed. Why then would a higher exponent reflect a hyperexcitable state? Recall that the Hurst exponent reflects the temporal ordering of activity. For example, in the case of IEI sequences, for which the exponent is higher on the first day of life, the Hurst exponent reflects whether a short (long) IEI is likely to follow a short (long) IEI. Several successive short IEIs (which of course have bursts of activity in between them) may indicate a hyperexcitable network period or a disruption of the network excitability that would not be observed from examining the average number of events.

However, note that this section is purely speculative. The discussion is this chapter has highlighted the fact that there is currently no proper understanding in the literature as to the underlying mechanism that gives rise to LRTCs, and more importantly there is no understanding of what different exponents mean. Future research is needed in this area in order to determine how the differences in Hurst exponents observed in various data sets, including the one studied here, arise and whether they point to a

developmental process.

3.4.4 Evidence of self-organisation to a critical state

As was discussed previously, a system at a critical state exhibits power-law dynamics. From the results of this chapter and the previous chapter there is strong evidence to indicate that the preterm EEG exhibits LRTCs in burst dynamics. LRTCs were observed even in the youngest subjects suggesting that the brain may be at a critical state even during this early phase of development.

If the brain is a SOC system then it would be expected to exhibit a period of self-organisation towards a critical state. For example, in the sandpile model (see Chapter 1) there is an initial period during which avalanches are generally small as most cells are well below the threshold needed to topple. The sandpile has an initial period during which a complex pattern of cells just below threshold build up eventually reaching a critical state. However, once a critical state has been reached the dynamics will remain at this critical state unless perturbed away from it by an external force.

While the dynamics investigated here were not avalanche dynamics, as is analysed in the sandpile model, the theory relating to this model still suggests that before a critical state is reached there will be a period of self-organisation in which critical state dynamics are not observed. There is no evidence in the data analysed in this chapter of a period of self-organisation in the early developing brain. LRTCs were present at all ages and there was no effect of gestational age. This is in many ways surprising as across this developmental period cortical connections are forming. One might expect the cortex to exhibit increased signs of complex dynamics as connections form. On the other hand, there is evidence to suggest that the burst dynamics exhibited by the EEG relate to sensory or spontaneous input via the subplate and that the delta waves are the action of the subplate on the cortex [74, 97]. The subplate is densely connected and these connections are functional prior to the youngest age we have examined here [8, 65]. Perhaps the subplate has already self-organised to a critical state? As the subplate drives the cortical plate this may in turn lead to the apparent critical state of the cortex, masking any self-organisation effect of cortical wiring at this age.

Overall, we found no evidence for self-organisation in the very early preterm EEG. It may therefore be the case that self-organisation occurs at an earlier age. However, until such evidence has been obtained it is perhaps premature to suggest that the brain is a SOC system. Moreover, given that a system in a true critical state would be expected to exhibit power-laws for many different characteristics, the data here - with power-laws in the autocorrelation function (LRTCs) but without power-laws in the actual distributions - may suggest that the brain is also not in a truly critical state.

3.4.5 Methodological considerations and extensions

The main limitation in the analysis of this data was caused by the impedance checks. While these checks were necessary when carrying out the records (allowing electrodes with poor impedances to be reattached and thus gaining a better overall recording), they did interrupt the recordings and it is not possible to know whether any BNOs occurred during the impedance checks. Thus, when a long impedance check occurred it was necessary to segment the data as a number of BNOs would have occurred during this period. In the case of short impedance checks this also meant that some BNOs may have been missed leading to slight differences in the sequences analysed than the actual sequence that may have occurred. However, the effect of this should be minimal (only a difference in the Hurst exponent of ~ 0.01 or less) as was assessed using the simulated impedance checks in order to determine the segmentation threshold. There was no crossover (a single linear trend occurred across all box sizes) in the DFA plots indicating that the estimated Hurst exponent is an accurate estimate for that data sequence and that the impedance checks did not introduce spurious estimates of the Hurst exponent.

The analysis was initially carried out with a fairly high impedance check threshold (300 seconds) to avoid excessive segmentation of the data and many short segments for which LRTCs could not be assessed. The results were compared with the much more conservative threshold of 30 seconds. As was expected, at this threshold the proportion of segments that could be analysed was greatly reduced (implying that at this threshold a lot of the data was effectively discarded). However, the exponents were in a similar range to the exponents at the larger threshold and the statistical analysis showed significant effects in all cases for which significant effects had been observed with a threshold of 300 seconds. Considering the segments with the original impedance check threshold, the effect of different length segments and different average burst rates between subjects was minimised by examining fixed length sequences of the first 1000 data points. Analysis of these fixed length sequences also showed consistent observations of LRTCs and the same effects with respect to gestational age, postnatal age and channel location. Thus, both these analyses suggest that the results obtained with the original segmentation threshold are a robust result of this sample population.

The aims of the EEG studies conducted in this thesis were to investigate whether the preterm EEG exhibited complex temporal dynamics and whether there were changes in the temporal occurrence of bursts with respect to gestational age or time since birth. This was inspired by the question of whether the activity was indicative of the brain being at a critical state and whether there appeared to be a period of self-organisation to a critical state. The basis of the study was therefore not clinical. However, due to the medical requirements of this population and the necessity to improve treatment it is important that any study conducted in the area consider whether the analysis can be of benefit from a clinical perspective. From the results of this chapter and the previous

chapter the clinical significance of this analysis is (currently) unclear. Comparison of the Hurst exponents themselves between those subjects with and without intraventricular haemorrhages found no differences. There was also no difference in the Hurst exponents between those children with normal and abnormal outcome at two years of age. While there was a difference between those children with normal and abnormal outcome in those subjects who had intraventricular haemorrhages at birth, this examined a small group of neonates (n=5). Therefore, future research would be needed to ascertain whether there is a clinical interest in investigating the Hurst exponents of sequences of BNO attributes in terms of capturing abnormal outcome or states in preterm infants.

The age range studied in this chapter and the previous chapter covers a wide developmental period, with synaptic connectivity forming in the cortex. Across this age range other authors have identified changes in the EEG including differences in band power [35, 87, 88], an increase in the number of bursts [83–86] and an increase in the degree of continuity [83–86]. It is therefore important to consider whether these changes might have an effect on the analysis carried out in this study. Similarly it is worth considering whether changes between periods of more continuous activity and discontinuous periods within a subjects EEG recording may have an effect. In particular, this is also related to the state of the infant as quiet sleep is characterised by a more discontinuous tracing whereas active sleep is associated with a more continuous trace. From as early as 27 weeks sleep state differentiation is present with the infant either being awake, or in periods of quite or active sleep [189]. Younger infants have less well defined sleep states, however, comparison with eye movements shows that the mean percentage of EEG activity is increased in periods with rapid eye movements suggesting a rough sleep-state differentiation even at younger ages [89]. Therefore, sleep state is a factor that could lead to changes in the temporal patterning of BNOs, particularly in the older neonates for which sleep states can be clearly differentiated.

For the data studied here sleep states were not annotated on the recordings and electro-oculagraphs (EOG) were not recorded meaning that it is not possible to accurately determine sleep states. However, as discussed DFA plots were examined and there were no crossover points in the data indicating that the same linear trend was present across all box sizes. This would not be the case if a periodic signal or a signal with an underlying trend was driving the trend in the data - leading to apparent LRTCs. It is therefore not the case that changes in sleep state or changes in continuity are driving the patterns in the temporal dynamics of the BNOs observed here, i.e. changes in state do not lead to the complex temporal patterning observed. However, it is possible that different sleep states or different levels of continuity do effect the degree of the temporal correlations and that while the overall patterning is not driven by these states changes in state do lead to changes in the Hurst exponent. This would be an interesting question for future research.

Statistical analysis and power calculations

To conduct the statistical analysis one measurement was required for each subject (with one for each of the regional channel locations) and so an average Hurst exponent was calculated, averaging across segments. As was discussed, an average exponent leads to the best subject value given that the subjects with fewer (longer) segments will have better estimates of the Hurst exponent. However, this does reduce the data and so loses some of the information. It would therefore be advantageous to examine long data sets where impedance checks had been carried out without disruption to the recording. Investigation of data without segmentation would also enable an understanding of whether LRTCs consistently extend to very long box sizes. Nonetheless, despite the need for segmentation of the data analysed here, LRTCs were consistently observed across segments and this data set provided a unique opportunity with which to examine LRTCs from data that was recorded continuously over the first three days of life.

To determine a sufficient sample size for analysis it is often appropriate to perform a power calculation before running an investigation. However, in order to do so the effect size must be known or estimated from previous research. As effect on the Hurst exponent of the factors investigated here - gestational age, postnatal age, EEG channel location and outcome at two years of age - had not previously been examined it was not possible to obtain accurate estimates of the effect sizes. A power calculation to determine the sample size was therefore not performed *a priori* for this study and analysis was carried out on a data set which had been collected for a previous investigation by *Schumacher et al.* [35]. However, it is of interest to calculate post-hoc power in order to conclude whether the sample size was sufficient or whether an increase in sample size would be required if future investigations were undertaken.

For mixed ANOVAs, power calculations need to be performed for each of the potential effects including the main effects and interactions. Power calculations were performed for the effects of interest: gestational age, postnatal age and EEG channel location. For each of these factors, and for each of the BNO characteristics, the mean and variance of the data from the sample studied in this chapter was used to calculate the effect size. From the effect size, the sample size and the correlation among the repeated measures, the power ($1 - \beta$, where β is the probability of a type II error) was calculated with a significance level of $\alpha = 0.05$ using the program G*Power 3 [190]. The results of this analysis are shown in table 3.7. Conventionally, a test is considered to be sufficiently powered if the power is 0.8 or above. As can be observed from the tables, particularly in the case of gestational age, the power from this sample population is much lower than this level. To achieve a sufficiently high power a larger sample size would be required.

However, it is important to remember that for any effect size it is always possible to calculate a power value and the required sample size for any given power. That is to say,

DFA	Gestational age		Time since birth		EEG channel location	
	Effect size (f)	Power	Effect size (f)	Power	Effect size (f)	Power
IEI	0.024	0.05	0.20	0.77	0.023	0.09
Duration	0.045	0.07	0.082	0.16	0.47	1.00
Peak Amp.	0.14	0.23	0.069	0.12	0.031	0.081
Total Amp.	0.11	0.18	0.071	0.11	0.045	0.091
Whittle	Gestational age		Time since birth		EEG channel location	
	Effect size (f)	Power	Effect size (f)	Power	Effect size (f)	Power
IEI	0.038	0.06	0.22	0.82	0.011	0.05
Duration	0.012	0.05	0.046	0.08	0.47	1.00
Peak Amp.	0.013	0.05	0.065	0.11	0.12	0.54
Total Amp.	0.013	0.05	0.082	0.14	0.019	0.05

Table 3.7: The effect size (f) and power calculated for each BNO characteristic and for each of the three main effects considered: gestational age, time since birth and EEG channel location. The effect size is calculated from the mean and variances of the data studied in this chapter. The results are shown for the DFA (top) and Whittle (bottom) estimates of the Hurst exponent. Note that Amp. denotes amplitude.

given a large enough sample size any small effect could be determined as significantly different from zero (in terms of the difference in means of the groups). However, this does not mean there is actually a difference between the two groups that is of interest [191]. Some of the effect sizes from this study are so small (see *Cohen, 1992* [192]) that they might be regarded to not constitute meaningful effect sizes. Indeed, it is possible to consider the actual effects of the groups in terms of the difference in means of the groups. For example the difference in means between the DFA exponents of duration sequences for EEG channel location is 0.035 whereas the difference in means between the two age groups of the Whittle exponents of the duration sequences is only 0.001. Given the variation in Hurst exponents and the fact that the Hurst exponent measures are only estimates, do these differences in means constitute meaningful effect sizes? *Taqqu et al.* [162] examined variation in the estimates of the Hurst exponent for sequences constructed with known Hurst exponents. From the values given by the authors, the average standard deviation in Hurst exponent estimates (taken across all sequences studied) was 0.016 using DFA and 0.007 in the case of the Whittle estimator. These values can be interpreted as the level of the noise for these estimates of the Hurst exponent. Therefore, any difference in means between groups that is less than these values could be interpreted as noisy fluctuations within the measurements and should not be considered a meaningful effect.

Table 3.8 lists the difference in means for the different BNO attributes. For those differences that are larger than the threshold values given above the sample sizes required to yield a power of 0.8, given the effect sizes in table 3.7, are also listed. Any future studies investigating these effects should therefore use these sample sizes in order to achieve sufficient power. However, it is worth noting that in 3 of the 6 cases where

the effect size is greater than the value of the noise, the sample size within this study achieved sufficient power (and in one other case the required sample size is 44, where here n=41).

DFA	Gestational age		Time since birth		EEG channel location	
	δ	N	δ	N	δ	N
IEI	0.003	-	0.024	44	0.002	-
Duration	0.005	-	0.009	-	0.035	14
Peak Amplitude	0.013	-	0.008	-	0.002	-
Total Amplitude	0.01	-	0.007	-	0.003	-
Whittle	Gestational age		Time since birth		EEG channel location	
	δ	N	δ	N	δ	N
IEI	0.003	-	0.017	40	2×10^{-7}	-
Duration	0.001	-	0.004	-	0.029	12
Peak Amplitude	0.001	-	0.005	-	0.007	74
Total Amplitude	0.001	-	0.008	376	6×10^{-7}	-

Table 3.8: Difference in means (δ) and required sample size needed in order to achieve a power of 0.8 with the effect size as determined from the data and listed in table 3.7. The required sample sizes are shown only for those distributions where the difference in means was greater than or equal to the average standard deviation of estimates of the Hurst exponent of sequences with known Hurst exponent [162]. In the case of DFA exponents this threshold value was set to 0.016 and for Whittle exponents 0.007. The measures are calculated for the DFA (top) and Whittle (bottom) estimates of the Hurst exponent.

Table 3.9 lists the details of power calculations for the tests comparing the Hurst exponents with outcome at two years of age. Again we see that some of the effect sizes are very small leading to low power. However, as discussed above, a sample size and power can always be computed from any effect size, including in situations when the effect size is small. The table also lists the differences in means between the two groups (those subjects with normal and those with abnormal outcome) and we can see that these differences are small. Given the range observed in the Hurst exponent estimates of sequences with known Hurst exponent, these effects are not of biological importance. Indeed, only in two cases is the difference in means just above the threshold, and the required sample sizes to observe the effect in these cases are listed. More importantly for the analysis, these small effects would not be of value in predicting outcome later in life based on Hurst exponent estimates from EEGs recorded in the neonatal period. This particular analysis is therefore unlikely to be of use in the clinical setting in terms of predicting outcome of patients.

Finally in this section we discuss the validity of the statistics in terms of the number of tests that have been carried out. For any statistical testing, with a significance level (and a p-value) of 0.05 there is a probability of 0.05 that the null hypothesis is in fact true and has been incorrectly rejected. If one were to carry out n statistical tests, each with a significance level of 0.05, then the probability of incorrectly rejecting the null hypothesis in each case is 0.05 and so the probability of incorrectly rejecting one of the

DFA	Difference in means	Effect size (d)	Power	Required sample size
IEI	0.005	0.11	0.063	-
Duration	0.012	0.46	0.28	-
Peak Amp.	0.005	0.19	0.085	-
Total Amp.	0.006	0.29	0.14	-
Whittle	Difference in means	Effect size (d)	Power	Required sample size
IEI	0.001	0.038	0.052	-
Duration	0.008	0.31	0.15	350
Peak Amp.	0.006	0.32	0.16	-
Total Amp.	0.009	0.50	0.32	134

Table 3.9: Difference in means, effect size, power and required sample size (in the cases where the difference in means was above threshold) for the tests of Hurst exponent compared with the subjects outcome at two years of age (split according to subjects with normal and abnormal outcome). The two tables indicate the values for the estimates of the Hurst exponent according to DFA (top) and Whittle (bottom). The threshold for the difference in means where the value could be considered to be above the value of the noise within the estimates of the measures was taken as 0.016 in the case of DFA and 0.007 for the Whittle estimate. Note that Amp. denotes amplitude.

null hypotheses is $0.05n$. For this reason it is important to correct for multiple comparisons when multiple tests are undertaken, thereby reducing the probability that any of the null hypotheses are rejected incorrectly back to 0.05. In the case of post-hoc comparisons of the time since birth this was corrected in this chapter using a Bonferroni correction. However, multiple comparisons were not corrected for across all of the statistical tests that were carried out in this study. This should be taken into account when examining the results of this chapter.

Effects of IEI, peak amplitude, total amplitude and BNO duration were investigated for both DFA and Whittle estimates of the Hurst exponent (8 tests in total). For each of the BNO characteristics a comparison was also made between the Hurst exponents (both DFA and Whittle) and the outcome at two years of age (a further 8 tests). All of these tests were also carried out for fixed length sequences. Additionally counting those test comparing subjects with haemorrhages with those without haemorrhages, a total of 53 comparisons were made. This leads to a revised significance level of $\alpha = 0.05/53 = 0.0009$. Taking into account this revised significance level, there remains a significant effect of EEG channel location on the exponent of duration sequences (for both DFA exponents[1] - $p = 3 \times 10^{-8}$ - and Whittle exponents - $p = 8 \times 10^{-9}$) as well as the significant differences observed in the comparison of outcome in the group with haemorrhage at birth (all p-values < 0.0007) and a significant effect of time since birth on the number of BNOs per hour ($p = 7 \times 10^{-17}$). However, the other 'significant' results do not pass this revised level. This therefore indicates that future analysis is necessary in order to determine whether significant effects exist in terms of these factors.

[1]The stated p-values have not been corrected for multiple comparisons but are lower than the revised significance level

If a future analysis were to be carried out it would be possible to specifically analyse those attributes highlighted in this study as having effects of interest (in particular, the changes in exponents of IEI sequences with postnatal age and the effect of EEG channel location on the exponents of duration sequences) and so reducing the problem of multiple comparisons.

Chapter 4

Burst dynamics in an excitatory neuronal network model

The observation of LRTCs in the burst dynamics of preterm EEG leads directly to the questions of how such dynamics might occur and also how this behaviour in the dynamics might effect changes in the system. Both these questions are of particular interest due to the developmental context within which they have arisen. In this chapter the first of these questions will be addressed, leaving the latter question to Chapter 5 where specific attention will be paid to how the dynamics and connectivity of the system interact.

To generate a hypothesis of how complex temporal patterning of burst dynamics might occur in the premature brain, in this chapter a computational model will be introduced and its dynamics analysed in detail. As with the EEG data, particular attention will be paid to LRTCs in, and the distributions of, burst occurrence, amplitude and duration. Analyses of these characteristics for different parameter ranges should enable an understanding of the sort of model characteristics required to produce such dynamics. This then gives a possible prediction of the requirements of the underlying behaviour of the developing nervous system which yields the dynamics observed in the EEG.

The most robust finding of the last two chapters was that the bursts of activity in the preterm EEG exhibited LRTCs in burst occurrence (i.e. LRTCs in the IEI sequences). However, there is currently no theoretical explanation for such behaviour (power-law statistics of waiting times) in neuronal systems. LRTCs have been observed in inter-heart beat intervals [141] and it was suggested that this behaviour could be understood by a superposition of exponential processes with different timescales [156]. Another paradigm that has been used to explain power-law statistics in waiting times, for example in solar flares [138], is intermittency. This is a type of dynamics where bursts are interspersed within phases of low amplitude activity caused by the interaction

of two variables, with one passing repeatedly through the bifurcation point of the other [193, 194]. I have also observed that thresholding of a LRTC process can give rise to burst activity for which the periods between the bursts themselves exhibit LRTCs, see Appendix 1. These are therefore all candidate mechanisms for the LRTCs in the bursts of activity in the preterm EEG. However, we will take a more direct approach, analysing a neuronal network model to understand the system requirements for LRTCs in the dynamics.

As discussed in Chapter 1, previous computational work has shown that a number of different frameworks can yield dynamics with power-law statistics of size [55–58, 60]. In the case of neuronal systems particular emphasis has been given to both SOC models and models with a balanced level of excitation and inhibition by parameter tuning [38, 61, 62, 149, 159]. However, little consideration has been given to the temporal dynamics of the avalanches seen in these models. Several models have been shown to exhibit exponential distributions, i.e. only short-range correlations, of burst occurrence [56, 138]. Recent work by *Lombardi et al.* [166] showed that a computational model can exhibit IAI distributions with initial power-law scaling but a bump in the distribution at higher values indicative of down states within the network. This distribution was the same as that observed experimentally [166], see also Fig. 1.10. However, the authors did not examine temporal correlations in the ordering of the avalanche activity. *Poil et al.* [159] showed that a balance of excitation and inhibition can lead to power-law scaling of neuronal avalanches and, on much longer timescales, that the same model gives rise to oscillations with LRTCs in amplitude fluctuations[1]. This result is the first observation of power-laws on multiple levels and the authors proposed that this be termed *multi-level criticality*. While this is an interesting result, as it coincides with experimental evidence suggesting that neuronal systems exhibit power-laws at different scales, it also leaves open an intriguing question: do neuronal avalanches themselves exhibit LRTCs (either in the temporal ordering of size, duration or inter-avalanche intervals)? To my knowledge this question has not been examined either in experimental results or in computational models of neuronal avalanches.

Having said this, the model of *Poil et al.* [159] does suggest that LRTCs (in the amplitude of oscillations) can occur through a balance of excitation and inhibition. Could this help us to explain the LRTCs observed in the burst dynamics of the preterm EEG? Recall that before full-term birth the brain has altered neurotransmitter effects: GABA, which after the early stages of development is the main inhibitory neurotransmitter, acts to depolarise the post-synaptic neuron during this period [2–4]. Furthermore, other forms of postsynaptic inhibition are delayed in their maturation

[1] *Poil et al.* determined a balanced level of excitation and inhibition as the level which gives rise to power-law dynamics. A relative change in either the inhibitory or excitatory connectivity led to a reduction in the temporal correlations and either a sub-critical or super-critical distribution [159]. This level is therefore balanced as it is in between states where activity can quickly die out or saturate the system.

leading to an imbalance of excitation and inhibition in the developing nervous system [63]. While presynaptic inhibition is thought to be present throughout development, the differential effects of postsynaptic responses need to be taken into account when examining the dynamics of the preterm nervous system. The LRTCs observed in the temporal ordering of BNOs in the preterm EEG cannot result from a balance of (postsynaptic) excitation and inhibition as is thought to be the case in the mature nervous system. Might a balance of activity be achieved by some other mechanism? To answer this question we will make use of the concept of the *branching parameter* [195] (explained in detail below), for which it is possible to determine system parameter values such that the activity is balanced.

The model considered in this chapter will be a purely excitatory system in terms of the postsynaptic actions. Presynaptic effects of neurotransmitters will not be explicitly formalised in the model and therefore presynaptic inhibition is not included specifically. Having said this, it will not be possible for neurons to fire at every timestep - once a neuron has fired it will need to return to the quiescent state before it can fire again. The length of time for the neuron to return to the quiescent state can therefore be thought of as a refractory period/form of presynaptic inhibition. The effect of neuronal firing on all postsynaptic neurons will be to depolarise the cell and so this coincides with experimental results of the altered effect of GABA and the delayed maturation of other inhibitory postsynaptic neurotransmitters in the developing nervous system [63]. Therefore, by considering a purely excitatory system (in terms of postsynaptic effects) we examine the most 'extreme' case possible of the developing nervous system as suggested by the current experimental evidence. Furthermore, it is of interest from a dynamical systems perspective to see what this property alone means for the dynamics of the system. Can a purely excitatory system actually produce burst dynamics without leading to system saturation? The question that will be addressed in this chapter can be reduced to whether a purely excitatory neuronal network can produce burst dynamics that exhibit LRTCs. The properties of the distributions will also be investigated to examine other markers of criticality (i.e. power-law distributions).

Here a simple stochastic neuronal model is investigated, with individual neurons in one of two states. A simple model is chosen so as to be analytically tractable and therefore allow direct derivation of the parameters required for burst dynamics. In particular this will permit the derivation of the branching parameter, yielding parameters of the neuronal system that will lead to a balance of activity (activity that on average neither quickly dies out nor saturates the system). Through simulations of the system's dynamics the distributions of the burst properties and LRTCs within sequences of the bursts will be investigated. From this it will be determined whether this 'balanced' state of network dynamics can give rise to apparent critical dynamics, as is the case for systems with balanced levels of excitation and inhibition. The simplicity of the model also permits the theoretical derivation of the distributions of inter-burst intervals, burst

size and duration, leading to a better understanding of these distributions.

The model investigated in this chapter is based on that of *Benayoun et al.* [61] who investigated avalanche dynamics in a stochastic model with both excitatory and inhibitory neurons. The authors found that power-law distributions of avalanche size occurred in their model when there was a balance of inhibition and excitation. Unlike other computational approaches investigating neuronal avalanches, *Benayoun et al.* include a source of external input. This interesting extension allows the analysis of dynamics in the time domain[2], and *Benayoun et al.* utilised this when examining inter-spike intervals in their network, which were shown to follow exponential distributions (i.e. a temporally non-correlated process). They did not examine inter-avalanche intervals despite the fact that the addition of external input would have allowed them to do so. This extension into the temporal domain will be used to examine burst (avalanche) characteristics in this work, in particular including the investigation of inter-burst intervals and LRTCs. However, as described above, as the system investigated in this chapter will be purely excitatory, a different mechanism (i.e. not a balance of excitation and inhibition) will be required to achieve balanced activity and with this critical dynamics.

As may have been noticed, in this introduction the terms avalanche and burst have been used somewhat interchangeably. We are interested in investigating burst dynamics yet it has been stated that the model that will be examined in this chapter is one that was originally developed to analyse neuronal avalanche behaviour. Has this been chosen because the burst dynamics of the preterm brain are neuronal avalanches? Recall from Chapter 1 the discussion on the possible relationship between neuronal avalanches and bursts of activity in the developing brain. Bursts of nested theta and beta/gamma activity recorded in young rats has been shown to organise as neuronal avalanches [51]. Thus, though future experimental work is needed, there may be a link between BNOs and neuronal avalanches. However, the particular model was chosen here as it is analytically tractable and it produces discontinuous bursts of activity. While we will not attempt to produce realistic BNO activity in terms of nested oscillatory behaviour, this model will enable examination of the type of discontinuous activity which is required in order to investigate the temporal ordering in a similar manner to that of the EEG analysis.

[2]Note that with specific network connection topology, neuronal systems can give rise to self-sustained but not saturating dynamics [196, 197] which could also be a candidate for investigating the temporal dynamics of avalanche/burst activity.

4.1 The Model

Networks consisted of N neurons with each neuron in one of two states: active, a, or quiescent, q. Each neuron switches between the two states stochastically with certain probabilities - the neurons were modelled as continuous time two-state Markov processes, see Fig. 4.1. In time dt the transition probability of the i^{th} neuron between the two states is given by:

$$P(a \to q, in\ dt) = \alpha dt$$
$$P(q \to a, in\ dt) = g(\bar{a}(t), w_i, h_i(t))dt$$

as $dt \to 0$, where $g(\bar{a}(t), w_i, h_i(t))$ is the activation function, relating the neighbouring (i.e. presynaptic) neurons that are active to the rate at which the postsynaptic quiescent neuron (i) itself becomes active and α is the rate of transition from an active to a quiescent state. $h_i(t)$ is the external input to neuron i at time t, w_i is the vector of synaptic connection strengths w_{ji} from all presynaptic neurons j to neuron i (where $w_{ji} = 0$ indicates that there is no connection between the neurons) and $\bar{a}(t)$ is a vector where the j^{th} element $\bar{a}_j(t) = 1$ if the j^{th} neuron is active at time t and zero otherwise. Note that an important property of the system is that the probability of a quiescent neuron becoming active depends on its input (which is related to the number of presynaptic active neurons) and so this varies at each simulation step.

As the model is of an excitatory network, all synaptic weights and the external inputs are positive. For analytical tractability, we (initially) set $w_{ji} = w > 0\ \forall\ j, i$ and $h_i(t) = h(t) \geq 0\ \forall\ i$, i.e. all synaptic weights are equal to each other, the network is fully connected and the external input to each neuron is the same. Furthermore, unless otherwise stated, the external input will be taken to be a tonic input with $h(t) = h\ \forall t$. These assumptions are somewhat simplified from a real neuronal network. However, as is stated this is done so as to make the model analytically tractable. It is much easier to make these simplifications in order to fully understand network dynamics and then to increase the model complexity and so (hopefully through understanding of the simplified model) understand the parameters of this more complex system, than it is to start with the more complex model.

With these assumptions the input to all quiescent neurons will be equal and is a function of the number of active neurons, A, in the network. We therefore simplify the notation: $g(\bar{a}(t), w_{ji}, h_i(t)) \to g(A)$. Under these conditions, the population is well-mixed and so the mean field equations for the system can be formulated to evaluate the change in population levels of activity.

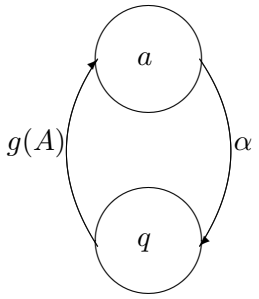

Figure 4.1: Single neuron states and transitions. Each neuron can be in one of two states: a, active or q quiescent. Transitions between the states occur at the rates indicated, where the transition between the quiescent and active state is a function of the number of active neighbours, A.

In a well-mixed population the mean field equations for the system are:

$$\frac{dA}{dt} = g(A)Q - \alpha A$$
$$\frac{dQ}{dt} = \alpha A - g(A)Q$$

where A is the number of active neurons in the system and Q is the number of quiescent neurons. As $A + Q = N$ the equations can be reduced to a single equation:

$$\frac{dA}{dt} = g(A)(N - A) - \alpha A \tag{4.1.1}$$

Before continuing with the model analysis, we introduce the concept of the branching parameter which will enable us to move forward with our approach.

4.1.1 Derivation of the branching parameter

The *branching parameter* σ is defined - in the case of a neuronal system - as the number of active neurons that a single active neuron gives rise to (i.e. activates) [49]. Thus, $\sigma < 1$ implies that for a single active neuron, on average in the next generation there will be less than one 'daughter' neuron, i.e. activity will quickly die out. Similarly, if $\sigma > 1$ then there will be on average more than one daughter neuron for every parent neuron and so we would expect the average activity level to increase and eventually saturate the system. The critical parameter case is where $\sigma = 1$ where on average one parent neuron gives rise to a single daughter active neuron and so activity is on average sustained but does not explode. This balanced level of activity is of interest from the perspective of brain dynamics - intuitively the brain should be in a state where activity does not explode nor quickly die out. Also, this balanced level of activity is akin to that observed at the critical point (transcritical bifurcation) of, for example, the Ising model where activity is neither very ordered nor random but achieves a balance in between the

two states [60]. As power-law dynamics can be observed at such critical points (in the case of the Ising model the size of spatial structures with correlated spins follows a power-law for example [60]), it is of interest from our perspective to find parameters such that the system exhibits this type of critical point.

Analysis of experimental observations of neuronal avalanches reveals an average branching parameter of approximately 1 [49]. Similarly, neuronal avalanches have been shown to occur when there is a balance of excitation and inhibition within the network [37, 62] and this balance is thought to relate to a branching parameter of one (changes in the ratio of excitation to inhibition must alter the spike propagation probability) [38].

A simple feed-forward network of excitatory neurons achieves optimal information transfer when the connections are such that the branching parameter is one [49] highlighting the value of a network being in this balanced state. Similarly, computational networks with a branching parameter of one show maximum dynamic range [36, 37]. The formulation of the branching parameter gives an intuitive understanding of why a branching parameter of 1 can give rise to optimal dynamic range and information transfer. Consider a network of 50 neurons. In the extreme supercritical example of a branching parameter such that when a single neuron is active this will activate on average 50 neurons at the next time-step then no matter which neuron is initially active this information will be lost immediately. If the branching parameter is 0.5 (i.e. subcritical) then on average after a single neuron is activated the activity will immediately die out and again information is lost. Similarly, (and also for less extreme examples) small stimuli die out quickly in subcritical states whereas large stimuli saturate a network in the supercritical regime and are consequently indistinguishable [38]. This optimal dynamic range for a branching parameter of one is characterised by a power-law distribution of the activity in response to stimuli. For branching parameters other than one the distribution deviates from a power-law.

As power-laws are observed in systems with a branching parameter of one, direct calculation of the branching parameter for the model considered in this thesis will be a useful approach to find a parameter region that may produce the type of dynamics we are interested in. It is worth noting that, to my knowledge, none of the investigations of the branching parameter and critical balanced dynamics in models of neuronal avalanches have examined LRTCs in the avalanches themselves[3]. It therefore remains to be seen whether a branching parameter equal to one leads to the desired characteristics in the case of these attributes.

[3]The recent paper by *Poil et al.* showed that a model that exhibits neuronal avalanches also, on a longer timescale, displays oscillations with LRTCs in amplitude fluctuations. However, they did not investigate temporal patterning in the avalanches themselves.

The branching parameter can be calculated as:

$$\sigma = \frac{\lambda}{r} + 1$$

where λ is the dominant eigenvalue of the system at the fixed point and r is the rate at which an active neuron becomes quiescent. So we have that

$$\sigma = 1 \iff \lambda = 0, \quad \sigma < 1 \iff \lambda < 0, \quad \sigma > 1 \iff \lambda > 0.$$

Thus, in order to achieve a branching parameter equal to 1 the eigenvalue at the fixed point must be zero. We introduce the terminology of a *critical fixed point* to denote a fixed point with a critical eigenvalue ($\lambda = 0$). (Note that this is different from the normal mathematical definition of a *critical point* which is just an alternative term for a fixed point, i.e. a point at which the first derivative is zero.)

4.1.2 Initial model analysis

We will consider, unless otherwise stated, the linear activation function $g(A) = \frac{w}{N}A + h$. Note that in *Benayoun et al.* [61] the activation function was taken to be $tanh(\frac{w}{N}A + h)$ as it is a saturating function. However, the linear activation function is chosen here as it is much more analytically tractable and also it is a close approximation to the *tanh* function for small A. As will be seen in section 4.1.4, the probability of having a high number of active neurons is very low and therefore the two functions would be expected to give rise to similar results. With this linear activation function, by equation 4.1.1, the system mean field equation is

$$\frac{dA}{dt} = \left(\frac{w}{N}A + h\right)(N - A) - \alpha A \tag{4.1.2}$$

First, let us briefly consider the system with no external input, i.e. $h = 0$. The main reason for this is to gain a better understanding of the system dynamics. Also it is worth considering as most models of avalanche dynamics do not have an external input and so letting $h = 0$ allows better comparison with these previous systems. The equilibria of this system are $A^* = 0$ and $A^* = N\left(1 - \frac{\alpha}{w}\right)$. The stability of these fixed points is found by calculating the eigenvalue which is given by $\lambda = f'(A^*)$ where $f(A) = \frac{dA}{dt}$. As we have seen above, a branching parameter equal to 1 occurs when $\lambda = 0$. Calculating the eigenvalue for the system (with no external input) we have that

$$\lambda = f'(A) = w - \alpha - \frac{2w}{N}A$$

So for the zero fixed point $A^* = 0$ the eigenvalue is zero if $w = \alpha$. Note also that with

these parameters the positive fixed point is reduced to zero as well, i.e. there is a single critical fixed point.

Simulations of the network firing dynamics were implemented, as in *Benayoun et al.* [61], using the *Gillespie algorithm* [198] for stochastic simulations. Briefly, at each step of the simulation a single neuron is selected probabilistically to switch states based on the rates of transition for all neurons in the network. The time-step to this transition is drawn at random from an exponential distribution with rate which also depends on the sum of the rates of transition within the network. Therefore at each step in the simulation, the time to the next transition changes. This algorithm is used as it is an efficient method with which to simulate a stochastic process [61].

As (in this initial case) there is no external input, when the system has no active neurons the fixed point can be thought of as an absorbing state - once the network has reached this state it will remain there unless perturbed. Each simulation was therefore seeded by setting a single neuron to the active state. An *'avalanche'*, in this zero input case, was defined as the neuronal firing dynamics which occurred until the network returned to the fully quiescent state. The size of the avalanche was defined as the number of neurons that fired during the avalanche, where a neuron is said to *fire* at the *first* simulation-step at which it switches to the active state. For example, if a neuron during the course of a single 100 ms simulation starts in the quiescent state, switches to the active state at 21 ms, then to the quiescent state at 25 ms, back to the active state at 55 ms and returns to the quiescent state at 57 ms; then this neuron is said to fire at 21 and 55 ms. In general in this thesis an avalanche will be defined as a cluster of neuronal firing. Note that in the experimental literature, the term avalanche is usually used to define only those clusters whose size distributions follow a power-law [37, 49]. However, as the avalanches must be defined before their size distribution can be determined, we use the term more loosely to describe any kind of clustered firing.

The network was simulated with three different parameter sets, see Fig. 4.2, such that the branching parameter $\sigma < 1,\ \sigma = 1,\ \sigma > 1$, which will be described as the sub-critical, critical and super-critical case respectively coinciding with the values of their eigenvalues. In the critical case the distribution appears to follow a power-law with an exponent of ~ 1.5. This exponent is of interest as it is the same exponent as has been observed in neuronal avalanches [38, 49] but is also not surprising as this value agrees with the theoretically expected value for a critical branching process [60, 195, 199]. In the sub-critical case the distribution appears to follow a power-law to some extent but 'drops-off' quicker, with few large avalanches, i.e. as expected for a sub-critical parameter set the dynamics die out more quickly compared with the critical case. In the super-critical case there are many large avalanches, which again move the distribution away from the apparent power-law.

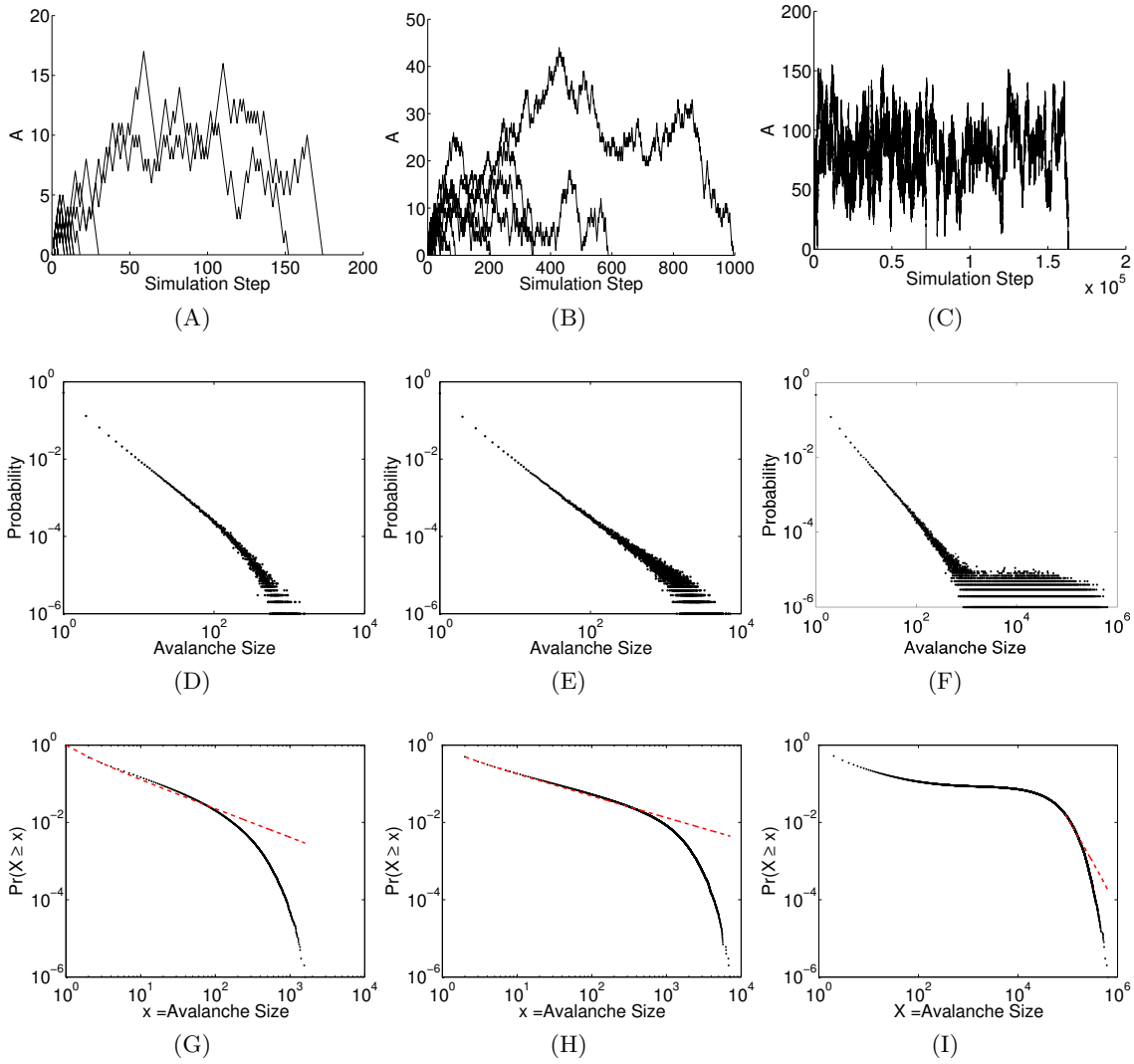

Figure 4.2: (A-C) Number of active neurons, A, at each simulation step for 50 avalanche simulations with parameters that are sub-critical (A), critical (B) and super-critical (C). Each avalanche is initiated by setting a single neuron in the network to the active state. The number of active neurons at each simulation step must either increase or decrease by 1 (as the simulation uses the Gillespie algorithm) and the avalanche ends when the network dynamics return to the fully quiescent state. (D-F) Distribution of avalanches sizes for each of the three parameter sets. (G-I) Corresponding cumulative distribution. Each distribution consists of 100,000 avalanches. For all networks $N = 800$, $w = 1$ and α was varied. For the critical network (B,E,H) $\alpha = 1 \Rightarrow \sigma = 1$, for the subcritical network (A,D,G) $\alpha = 1.1 \Rightarrow \sigma \approx 0.91$ and for the supercritical network (C,F,I) $\alpha = 0.9 \Rightarrow \sigma \approx 1.11$. The best-fit of a power-law to the cumulative distributions is shown in red and calculated using the approach of *Clauset et al.* [134]. This yielded exponents of (G) $\gamma = 1.74,\ x_{min} = 1$, (H) $\gamma = 1.56,\ x_{min} = 2$, (I) $\gamma = 3.22,\ x_{min} = 89436$.

Size distributions are certainly of interest when assessing the dynamical properties of the network. However, while it is important to note that this excitatory neuronal network can produce this sort of apparent critical power-law dynamics, seeding a network which then receives no further input until it has relaxed to a totally quiescent state is not realistic from a neuronal network perspective. Furthermore, as avalanches are initiated 'by hand' this precludes the calculation of waiting time dynamics (inter-avalanche intervals - IAIs) which is a key characteristic observed in the preterm EEG and which was a particular motivation for this study. Therefore, to increase the physiological realism of the model we consider the case of non-zero external input. As stated above, for the system to be analytically tractable this input will be a positive tonic source to every neuron.

In this case we also wish to calculate the parameters such that there is a fixed point with a zero eigenvalue (so that the branching parameter is 1). From equation 4.1.2 we obtain the following equations for the value of the fixed point and the eigenvalue at the fixed point:

$$\begin{aligned} f(A) = \frac{dA}{dt} &= -\frac{w}{N}A^2 + wA - hA - \alpha A + hN = 0 \\ \lambda = f'(A) &= -2\frac{w}{N}A + w - h - \alpha = 0 \end{aligned}$$

Solving these simultaneously we find that $\frac{w}{N}A^2 + hN = 0$, which leads to complex roots (as $w,\ h,\ N > 0$) except in the case where $h = 0$. Thus, it is not possible for this system to have parameters such that there is a (real) critical fixed point. How then can we use the idea of a critical fixed point to find a parameter region such that the dynamics might display power-law characteristics and LRTCs? Mathematically, there are two possibilities - the first being to consider a different system (i.e. a different activation function) which does have a parameter range with a critical fixed point in the case of a non-zero external input. The second is to analyse the dynamics of the original system in the presence of a small external input with parameters such that a critical fixed point is obtained when there is no external input. The idea behind this is that the small external input only perturbs the system away from this critical fixed point a small amount and so the dynamics should remain close to criticality. Recall in Chapter 1 the description of a system that exhibits self-organised quasi-criticality [58, 150]. In this case the system exhibits apparent power-law distributions while being close to a critical point. While here we are not investigating a SOC/SOqC system (the system is tuned to the parameters and does not self-organise) the same principle may apply. The system perturbed slightly from the critical fixed point by a small external input may exhibit the sort of behaviour (apparent power-laws and LRTCs) we are interested in. For completeness, the first approach is examined in Appendix 2. However, as a change in the activation function is not physiologically justifiable (in the appendix it is shown that

a quadratic activation function gives rise to a required parameter region - the linear function examined here is better related to neuronal integration of inputs than a quadratic activation function) we concentrate on the second approach and this will be explored fully in what follows.

4.1.3 The system in the presence of small external input

For the zero input case we have seen that the system has a critical fixed point when $w = \alpha$. For these parameters

$$f(A) = -\frac{w}{N}A^2 + hN - hA$$

So the fixed point is

$$A = -\frac{N}{2w}\left(h \pm \sqrt{h^2 + 4wh}\right)$$

and the eigenvalue at the fixed point is

$$\lambda = -h - 2\frac{w}{N}A$$

Assume that h is small so that the system is only slightly perturbed away from the critical fixed point. Initially we set $h = 1/N$ as on average this will activate one neuron and so it is similar to the random seeding carried out in the zero input case. With $h = 1/N$

$$A = -\frac{1}{2w} \pm \sqrt{\frac{1}{4w^2} + \frac{N}{w}} \tag{4.1.3}$$

Setting $w(= \alpha) = 1$ we find that $A = -\frac{1}{2} \pm \sqrt{\frac{1}{4} + N}$.

As $N \to \infty$ the eigenvalue of this fixed point $\lambda \to 0$, see Fig. 4.3. That is to say, as $N \to \infty$ the branching parameter approaches 1. Note also that for the positive fixed point, the eigenvalue is negative which implies that the branching parameter approaches 1 from the subcritical regime. Therefore, in simulations with a finite number of neurons the network is in a (slightly) subcritical state.

An example of a simulation of the network dynamics with these parameters and $N = 800$ is shown in Fig. 4.4. As the parameters are chosen such that if $h = 0$ the fixed point would be critical, this parameter set will be referred to as 'critical'. In the same figure the dynamics of the systems with parameters (α and w) that would be considered sub-critical and super-critical in the zero input case are also shown and these will be denoted the 'sub-critical' and 'super-critical' parameters respectively. The dynamics in the 'critical' case are 'avalanche-like' with bursts of neuronal firing interspersed with periods of relatively few or no neurons firing. As might be expected, in the 'sub-critical'

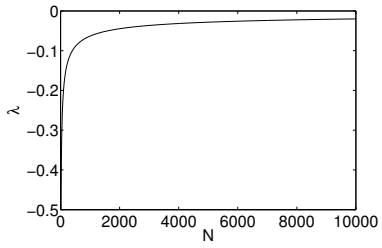

Figure 4.3: Plot of the eigenvalue of the system against the system size. With $w = 1,\ h = \frac{1}{N} \Rightarrow \lambda = -\frac{1}{N} - \frac{2}{N}\left(-\frac{1}{2} \pm \sqrt{\frac{1}{4} + N}\right) = -\sqrt{\frac{1}{N^2} + \frac{4}{N}}$. Thus as $N \to \infty$, $\lambda \to 0$.

case the activity appears to die out quicker than in the 'critical' case and the bursts of activity involve smaller numbers of neurons. In the 'super-critical' case the firing rate is much higher than for the other two parameter sets and, though there are still fluctuations in the firing rate, the bursts are much less distinct. This is also reflected in the number of active neurons at each simulation step which does not return to 0 in this simulation. In contrast, in the 'sub-critical' case the number of active neurons returns to zero frequently and in the simulation with 'critical' parameters the number of active neurons also returns to zero, though less frequently than in the 'sub-critical' simulation.

The burst behaviour observed in these raster plots cannot be predicted from evaluating the mean field equations. Evaluating the mean field equation (equation 4.1.2) with the 'critical' parameters, the results quickly tend towards the fixed point as would be expected, see Fig. 4.5. The burst dynamics observed in the simulations occur due to the stochastic nature of the neurons. As this cannot be predicted from the mean field equations of the dynamics of the individual neurons such behaviour might be termed *emergent* [60]. Averaging the dynamics across a number of simulations the burst dynamics are no longer apparent, see Fig. 4.5. For the 'sub-critical' parameter set, the average across the simulations approximates the solution of the mean field equations. However, in the 'critical' case the average rests at a lower firing rate than the mean field solution. This is a known phenomenon of the mean field approach and the invalidity for critical parameters due to so called *critical fluctuations* [200–202].

Having determined parameters which lead to burst behaviour in the dynamics we now investigate whether these emergent burst dynamics have properties reflecting critical state dynamics. Do the bursts exhibit power-law distributions similar to those of neuronal avalanches? Do the burst characteristics exhibit LRTCs similar to those observed in the preterm EEG? Before analysing the avalanche (burst) dynamics of these simulations let us first examine the *inter-spike interval (ISI)* statistics. This gives an idea of the individual neuronal properties and enables comparison with previous models. Specifically, *Benayoun et al.* examined this property in their simulations of both excitatory and inhibitory neurons, observing an exponential distribution of ISIs [61]. Fig. 4.6 shows the ISI distributions from the simulations for each of the three parameter

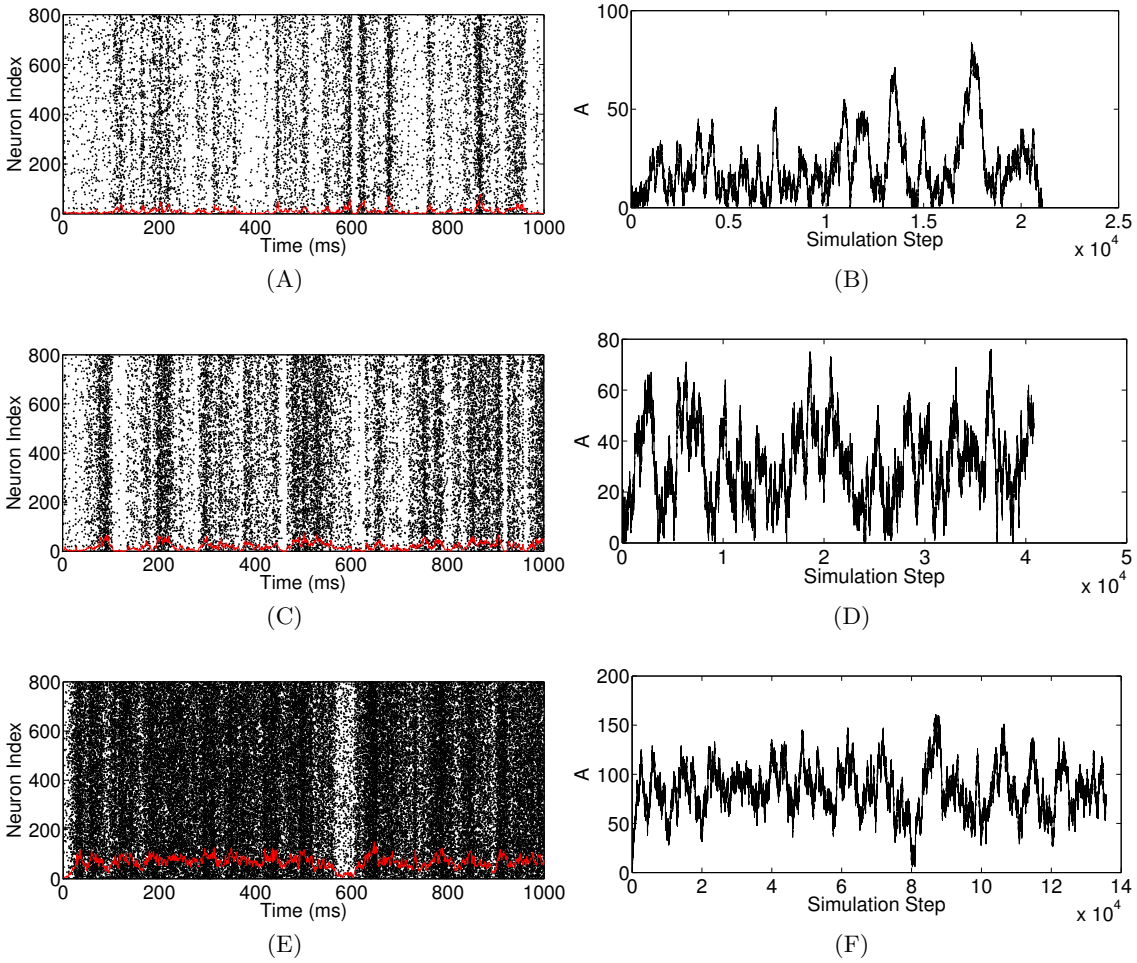

Figure 4.4: Simulations of the network with linear activation function and parameters of $N = 800$, $w = 1$, $h = 1/N$ and α chosen so that the system is approximately (would be in the presence of zero input) (A,B) sub-critical - $\alpha = 1.1$, (C,D) critical - $\alpha = 1$ and (E,F) super-critical - $\alpha = 0.9$. (A,C,E) Raster plots of the firing dynamics of the simulations. Red line indicates a simple count of the number of firings binned in 1ms intervals. (B,D,F) Number of active neurons at each step of the simulations.

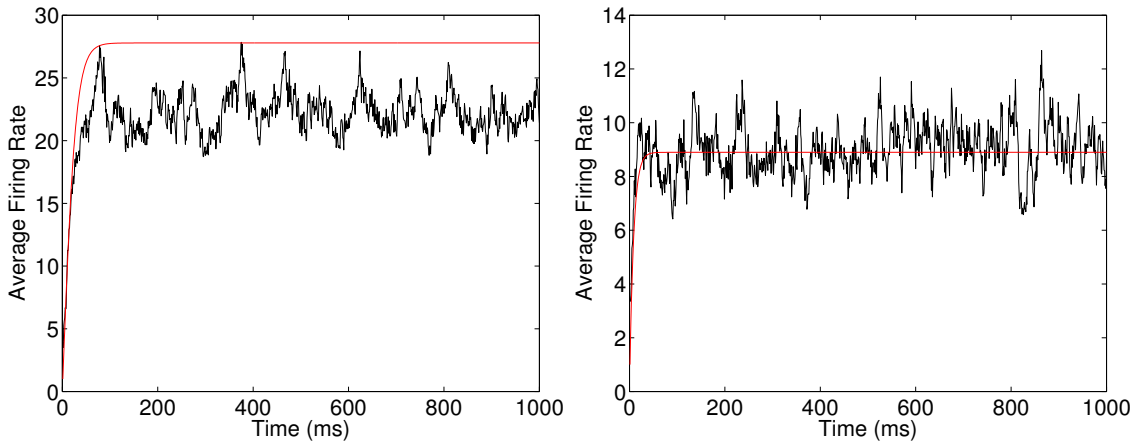

(A) (B)

Figure 4.5: Solution to the mean field equation, shown in red, for the system with linear activation function and parameters $N = 800$, $w = 1$, $h = 1/N$ and (A) $\alpha = 1$, (B) $\alpha = 1.1$. The mean field solution quickly converges to the fixed point (A) $A = -\frac{1}{2} \pm \sqrt{\frac{1}{4} + N} = 27.79$ (B) $A = 8.90$. Overlaid (black) is the average number of active neurons per unit time for 100 simulations. This averaging shows that the bursts do not have a characteristic timescale which would be observed in all simulations. However, in the 'critical' case (A) there is some discrepancy between the average of the simulations and the mean field. This is unlike what is observed when averaging simulations with parameters away from the critical point as seen in (B), where the simulations are noisy but approximate the fixed point.

sets ('sub-critical','critical' and 'super-critical') on a semi-logarithmic axis. A linear trend can be observed indicating an exponential distribution of ISIs. LRTCs in the sequences of ISIs were also analysed using DFA. For the 'critical' parameters the ISI sequences had an average exponent of 0.52 (range 0.45-0.57), indicating no correlations in the ISI sequences. Similarly with the 'subcritical' parameters the average exponent was 0.51 (range 0.42-0.60) and with 'supercritical' parameters the average exponent was 0.51 (range 0.46-0.56).

The firing activity from simulations was divided into avalanches using the binning method from *Benayoun et al.* [61] (see Appendix 3). Consecutive neuronal firing is separated into avalanches based on the average firing rate from the full simulation. Two consecutive neuronal spikes are separated into different avalanches if the time difference between these two spikes is greater than the average firing rate. Note that these are consecutive spikes in terms of the whole network firing - no neuron fires during an inter-avalanche interval; it is a period of silence throughout the whole network. From this the size of the avalanche is defined as the number of neuronal firings within the avalanche (if a neuron fires more than once it is counted more than once), the avalanche duration is the time between the start of the avalanche and the end (in ms), and the inter-avalanche interval (IAI) is defined as the time between the end of one avalanche and the start of the next (in ms). The distribution of avalanche sizes, IAIs and avalanche durations for simulations with the three parameter sets - 'sub-critical',

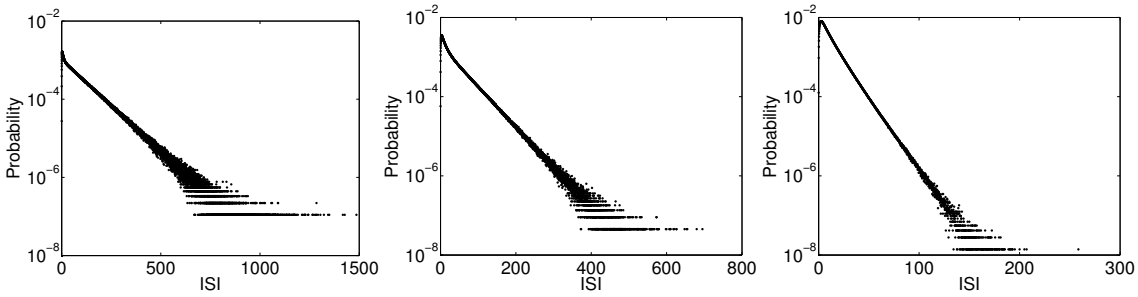

Figure 4.6: ISI distributions (in ms) for simulations with parameters that are (A) 'sub-critical', (B) 'critical' and (C) 'super-critical' shown on a semi-logarithmic axis. For all three simulations $N = 800,\ w = 1,\ h = 1/N$ and the simulation length was 1000 seconds. In the 'sub-critical' case $\alpha = 1.1$, in the 'critical' case $\alpha = 1$ and in the 'super-critical' case $\alpha = 0.9$. Note, there is a slight deviation from the trend in the distribution of all plots for very small ISIs - with a smaller probability of ISIs of this size than would be expected. In general though a linear trend is observed indicating that the ISIs are exponential distributed.

'critical' and 'super-critical' - are shown in Fig. 4.7. For all three parameter sets there is not a power-law relationship in avalanche size or duration and the distributions are curved on the double-logarithmic scale. This is in contrast to the results of *Benayoun et al.* and other models examining neuronal avalanches [37, 61, 149, 159]. This observation will be discussed in greater detail later on. In contrast, the IAIs do appear to follow a straight line indicative of a power-law distribution in the 'critical' case. This is also observed in the 'subcritical' case, though the straight line relationship does not extend as far as in the 'critical' case. The distribution is more obviously disrupted in the 'super-critical' case.

As the distribution of IAIs in the 'critical' parameter case appears to follow a power-law, goodness of fit to a power-law distribution was assessed using the approach[4] of *Clauset et al.* [134]. The best-fit to the original and truncated IAI distribution by a power-law is shown in Fig. 4.8. In both cases the p-values suggested that a power-law was not a good-fit to the data. However, it is worth noting that the approach of *Clauset* uses the Kolmogrov-Smirnov test to compare the distribution to generated power-law distributions. With this test, as the sample size increases the likelihood of rejection also increases. The original IAI distribution was composed of over 6,000,000 IAIs. Taking the first 100,000 IAIs from the simulation only and analysing these in the same way yields a p-value of 0.44 indicating a good-fit of the data to a power-law distribution, see Fig. 4.8. This clearly highlights a flaw in this statistical approach which should be considered when analysing data of this type.

Though the distribution does not rigorously pass this statistical testing, it still appears

[4] As there was a large number of data points the calculation using the code of *Clauset* proved too time consuming. Therefore, the data was first binned and normalised (dividing by the minimum IAI) and a modified version of the code was used (code from Timothy Taylor, University of Sussex).

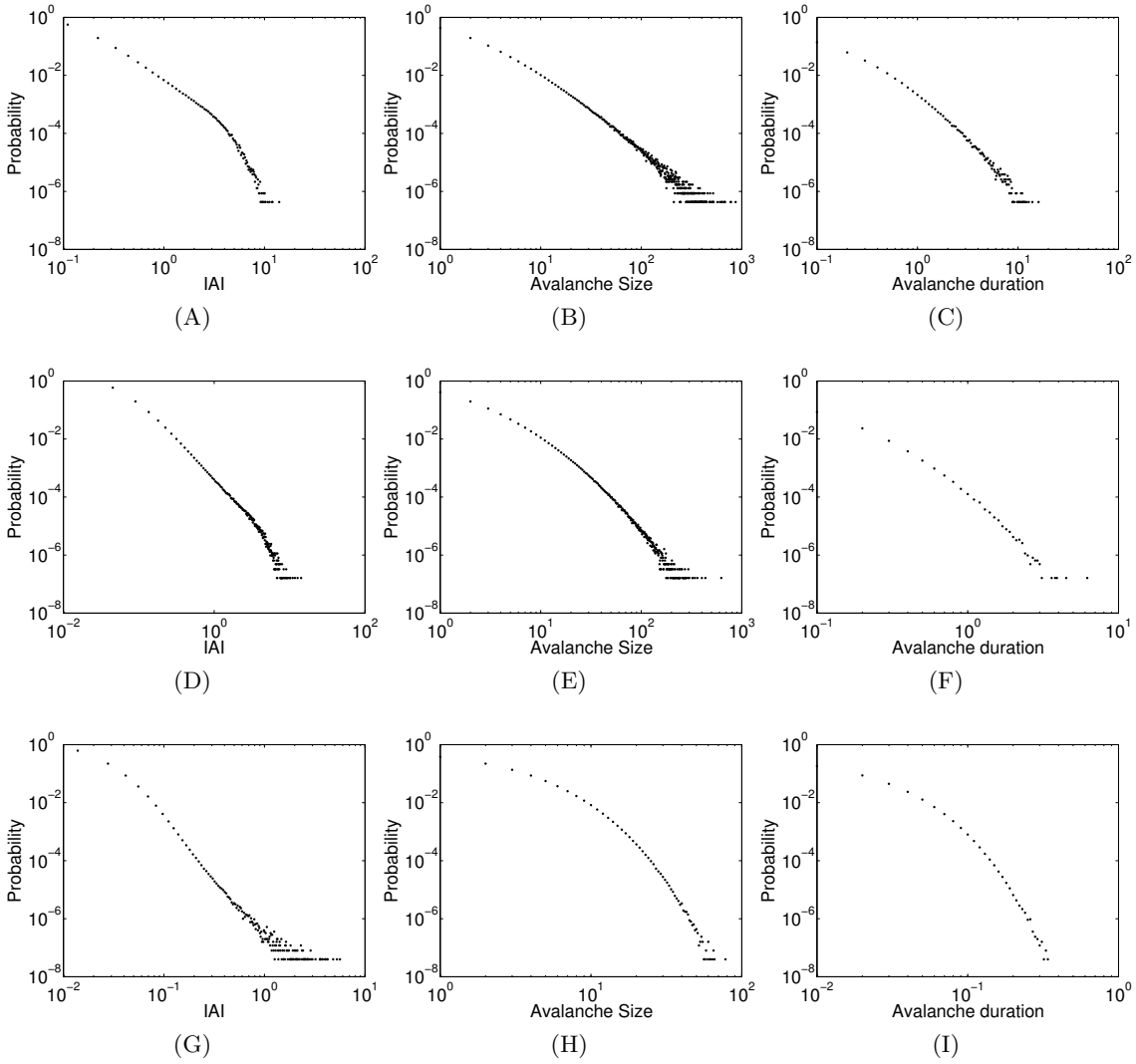

Figure 4.7: Avalanche statistics for simulations of the dynamics evaluated through binning of the network firing. (A,D,G) IAI distributions, (B,E,H) distributions of avalanche size and (C,F,I) distributions of avalanche duration for parameters that are 'sub-critical' (A,B,C), 'critical' (D,E,F) and 'super-critical' (G,H,I). For all simulations $N = 800$, $w = 1$, $h = 1/N$ and the simulation length was 1000 seconds. In the 'sub-critical' case $\alpha = 1.1$, in the 'critical' case $\alpha = 1$ and in the 'super-critical' case $\alpha = 0.9$. Note that throughout this chapter all IAIs and durations are given in ms.

by eye to follow a power-law. As most of the work examining power-laws distributions has just examined the appearance of the distribution on double-logarithmic axes and has not carried out statistical testing, the distribution of IAIs found appears to be 'as close' to a power-law as the empirically observed 'power-law' distributions are. Thus, even though the external input perturbs the system away from the critical fixed point apparent power-law distributions can still be observed.

As the distributions of avalanche size and duration in the 'critical' case were curved on the double-logarithmic scale the possibility that they were exponentially distributed was examined. Fig. 4.9 shows the distributions of the 'critical' regime on semi-logarithmic axes. For all three characteristics (IAI, size and duration) there is clearly not a linear trend across any scale, indicating that the distributions are not a single exponential. In section 4.1.4 a theoretical approach will be taken to more closely examine the distributions of the different avalanche attributes. However, before this the analysis of the simulations themselves will be completed, assessing the presence of LRTCs in the avalanches. The simulations will also be extended to different levels of external input and variations in the distributions will be examined.

LRTCs in avalanches?

As with the EEG data analysis the Hurst exponent can be estimated for the *sequences* (defined in temporal order of occurrence within the simulation) of avalanche size, duration and IAIs using DFA and the Whittle estimator. Example DFA plots for each of these three characteristics and for each of the three parameter sets ('sub-critical', 'critical' and 'super-critical') are shown in Fig. 4.10. From visual inspection of the plots it can be noted that for none of the characteristics or conditions does a single linear fit seem appropriate. All plots appear to have 'crossover' points - a point at which there is a switch in the linear trend - with box sizes either side of these points exhibiting different linear trends in the fluctuations [179]. In the 'sub-critical' case there is a single crossover, while for the 'critical' and 'super-critical' parameters there are two crossover points, i.e. three regions with different linear fits.

For the plots with 'critical' parameters, setting the condition that two crossover points exist, the best-fit to the data by three linear regions was found using Matlab's nonlinear regression function 'nlinfit'. For example, Fig. 4.11 shows this fit to the DFA plot for an IAI sequence in the 'critical' case. The lower (with smallest box sizes) and middle regions have exponents that are 0.75 and 0.89 respectively whereas the upper region has an exponent of 0.56. So, while the first two regions exhibit exponents indicating LRTCs, the upper region has an exponent which is closer to 0.5, indicating only short-range correlations across these larger box sizes.

This crossover behaviour is in contrast to the trend across box sizes observed for the

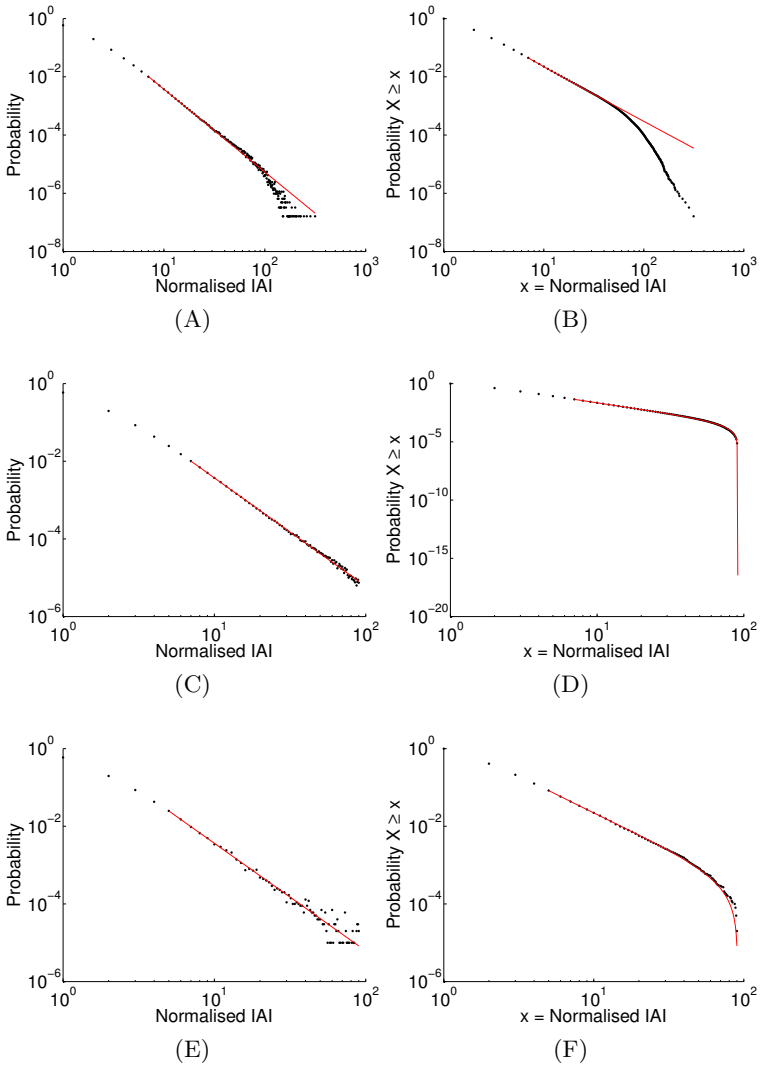

Figure 4.8: The IAI distribution in the 'critical' parameter case was examined for fit to a power-law using the *Clauset et al.* [134] approach modified for discrete data. The line of best-fit is shown in red on both the distribution (A) and the cumulative distribution (B). For this fit $\gamma = 2.84,\ x_{min} = 0.32,\ p = 0$ (where the value for x_{min} is in terms of the actual IAI length and has a normalised value of 7). The fit to a truncated power-law was also examined (C,D). The distribution was truncated at a size of 90 for the normalised IAIs, which was a value of 4.06 seconds for the un-normalised IAIs. For this fit $\gamma = 2.79,\ x_{min} = 0.32,\ p = 0.001$. Finally the fit to a truncated power-law of the first 100,000 IAIs was examined (E,F). Again the distribution was truncated at a value of 90 in the normalised IAIs. For this fit $\gamma = 2.77,\ x_{min} = 0.23,\ p = 0.44$, indicating a good-fit to a power-law distribution.

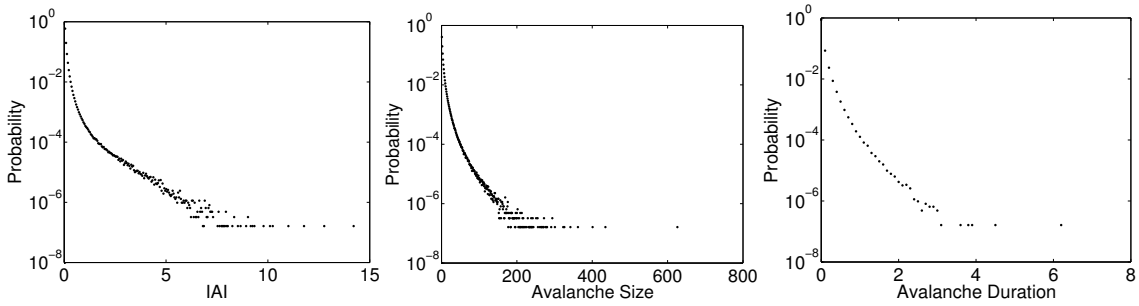

(A) (B) (C)

Figure 4.9: Distributions from simulations with 'critical' parameters as in Fig. 4.7(D-F) plotted on a semi-logarithmic axis. These plots clearly indicate that none of the distributions are exponential.

DFA plots of the shuffled sequences. Fig. 4.11(B) shows an example of the DFA plot for a randomly shuffled sequence. As would be expected any LRTCs are destroyed and the sequence has an exponent of 0.51, with the same linear trend across all box sizes. Shuffling the same sequence 500 times, the average exponent was 0.50 (range: 0.48-0.52).

What might be the reason for the crossover in the original sequences? The addition of the external input means that the eigenvalue is no longer exactly zero at the fixed point and so the fixed point is no longer critical but can perhaps be considered close to the critical point. A crossover in the DFA plot indicates that the LRTCs only extend to a certain box length, i.e. the correlations extend across a certain range. Thus, they are 'partial' LRTCs as they do not extend across all lengths. Recall that with $h = 1/N$ as $N \to \infty,\ \lambda \to 0$ and so it seems plausible to hypothesise that as N is increased the crossover will increase to larger box sizes with the correlations extending over longer sections of the sequences as the fixed point becomes closer to a critical state.

Changing the number of neurons

The system dynamics were investigated for a range of system sizes with $N = \{3200, 6400, \ldots, 57600, 64000, 70400, 73600, 86400, 172800\}$. All other parameters were kept constant and set to the 'critical' condition with $\alpha = 1,\ w = 1$; however, the external input $h = 1/N$ and so the actual value of the external input did change with system size even though the value in relation to the system is kept constant. With alterations in system size there was some change in burst frequency - for a single simulation with $N = 3200$ the minimum IAI was 0.02 ms and the maximum was 11.56 ms, compared with a single simulation at the largest network size $N = 172800$ where the minimum IAI was 0.003 ms and the maximum IAI was 7.00 ms. Despite the slight increase in burst rate, the firing rate of an individual neuron in the system decreased as the system size increased (with $N = 3200$ the minimum ISI was 0.015 ms and the maximum was 1260.7 ms, whereas with $N = 172800$ the minimum ISI was 0.032 ms and

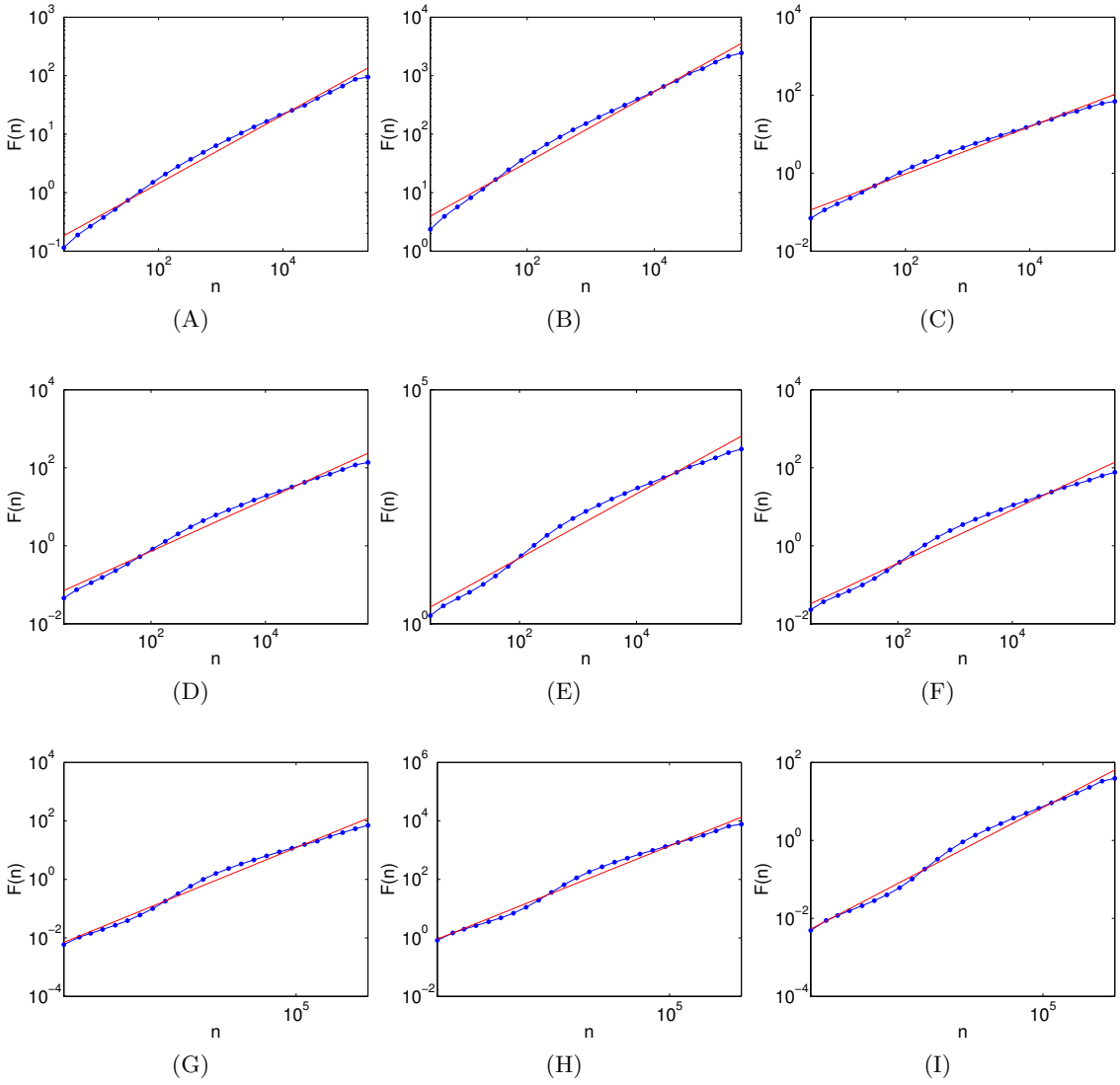

Figure 4.10: DFA plots for sequences of each of the three avalanche characteristics: IAI (A,D,G), avalanche size (C,F,I) and avalanche duration (G,H,I). Sequences of data were from the same simulations whose distributions are shown in Fig. 4.7 with parameters that are 'sub-critical' (A,B,C), 'critical' (D,E,F) and 'super-critical' (G,H,I). Exponents from a single linear fit were (A) 0.59, (B) 0.60, (C) 0.61, (D) 0.66, (E) 0.69, (F) 0.68, (G) 0.72, (H) 0.70 and (I) 0.69. However, from visual inspection of the plots it can be seen that they are not best fit by the single straight line. In fact there appears to be crossovers between linear trends.

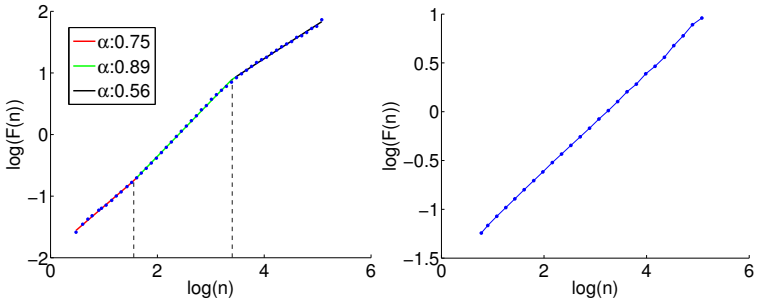

Figure 4.11: DFA plot for the IAI sequence of the simulation with 'critical' parameters and $N = 3200$ (A). The lines indicate the best-fit to the data by three different linear regions (two crossover points). The two regions with lower box sizes have exponents indicating LRTCs (the exponents are 0.75, 0.89), while the upper region has an exponent indicative of short range correlations only (0.56). This is in contrast to the DFA plot for the shuffled IAI sequence which was best-fit by a single linear trend (B). The exponent of this shuffled sequence was 0.51 indicating no correlations in the data.

the maximum was 7214.4 ms).

For each value of N, ten simulations were carried out. For all network sizes two crossovers between three different linear trends were observed in the DFA plots. The DFA exponents and the lower crossover (the crossover at the lower box size) did not change with system size other than within measurement error. As the burst frequency increased as the network size increased, the IAI sequence length also increased. Therefore the upper crossover value was compared with network sizes by normalising by sequence length, see Fig. 4.12. As was expected the upper crossover does indeed increase to even larger box sizes as the system size increases. Fig. 4.13 shows two example DFA plots for the smallest and largest network sizes. The increase in the upper crossover point is clearly visible. This is strong evidence that the correlations extend as the eigenvalue of the fixed point tends to the critical value through increasing the system size.

Similar patterns were observed in the DFA plots of the sequences of avalanche size and duration (plots not shown). For both measures the upper crossover increased with increasing system size.

For each of the sequences (IAI, avalanche size and duration) and system sizes the Whittle exponent was also calculated. Due to the length of the sequences, the program used could not calculate the exponent for the entire sequence and so exponents of fixed length sequences of the first 1,000,000 data points were calculated. However, this requirement also means that the Whittle exponent (here and for all future values given of the Whittle exponent of data from the model) is less effected by the crossover behaviour compared with the DFA. Across all sequences and system sizes the exponent ranged from 0.65 - 0.77, indicating LRTCs in all the sequences.

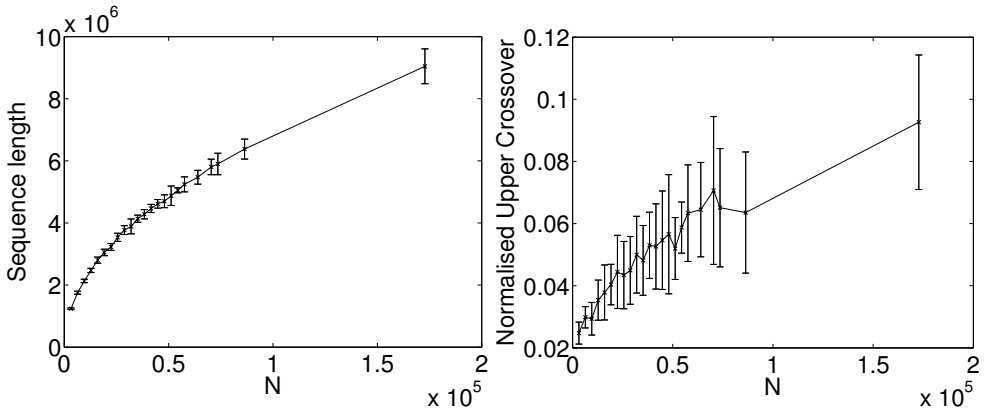

(A) (B)

Figure 4.12: (A) Average sequence length of the IAI sequences from the simulations for network size N. (B) The upper crossover point (normalised by sequence length) increases as the network size increases. Simulations were carried out 10 times for each network size with error bars indicating standard deviation. We concentrate here on the upper crossover point as at this box size there is a switch in the exponent from one that exhibits LRTCs to an exponent closer to 0.5.

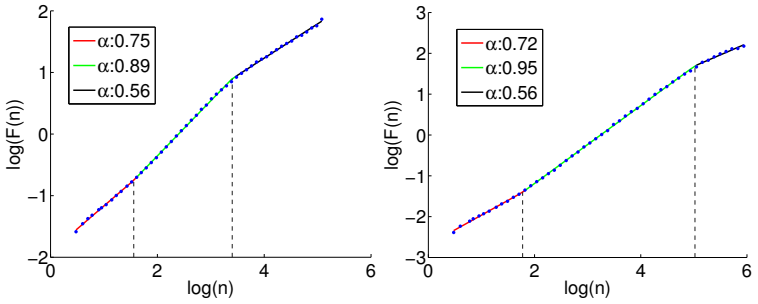

(A) (B)

Figure 4.13: DFA plot for the IAI sequence of the simulation with 'critical' parameters and $N = 3200$ (A) and $N = 172800$ (B) (i.e. the smallest and largest networks studied in Fig. 4.12). The lines indicate the best-fit to the data by three different linear regions (two crossover points). The two regions with lower box sizes have exponents indicating LRTCs (the exponents are 0.75, 0.89, 0.72 and 0.95), while the upper region has an exponent indicative of short range correlations only (0.56 in both cases).

Finally the distribution of IAIs and avalanche size were compared for different system sizes, by collapsing the distributions for different sizes. Recall that the IAI distribution appears to follow a power-law whereas the distribution of avalanche size does not (for this level of external input, which moves the system away from the critical point - this was not the case when there was no external input). Therefore, it is expected that the power-law in IAI distribution will extend with the system size similar to finite-size scaling (see Chapter 1). Note that as the IAIs are not directly related to the number of neurons within the system (i.e. the IAIs are not integer values) the distribution is scaled instead by the mean IAI, as was the approach of *Beggs and Plenz* [49]. For consistency the avalanche size distribution was also scaled by the average avalanche size. Fig. 4.14 shows the scaled distributions. As expected the IAI distributions show the same slope and extend across larger values for larger system sizes. In contrast the avalanche size distributions do not exhibit a power-law and the tail of the distribution does not change with the system size.

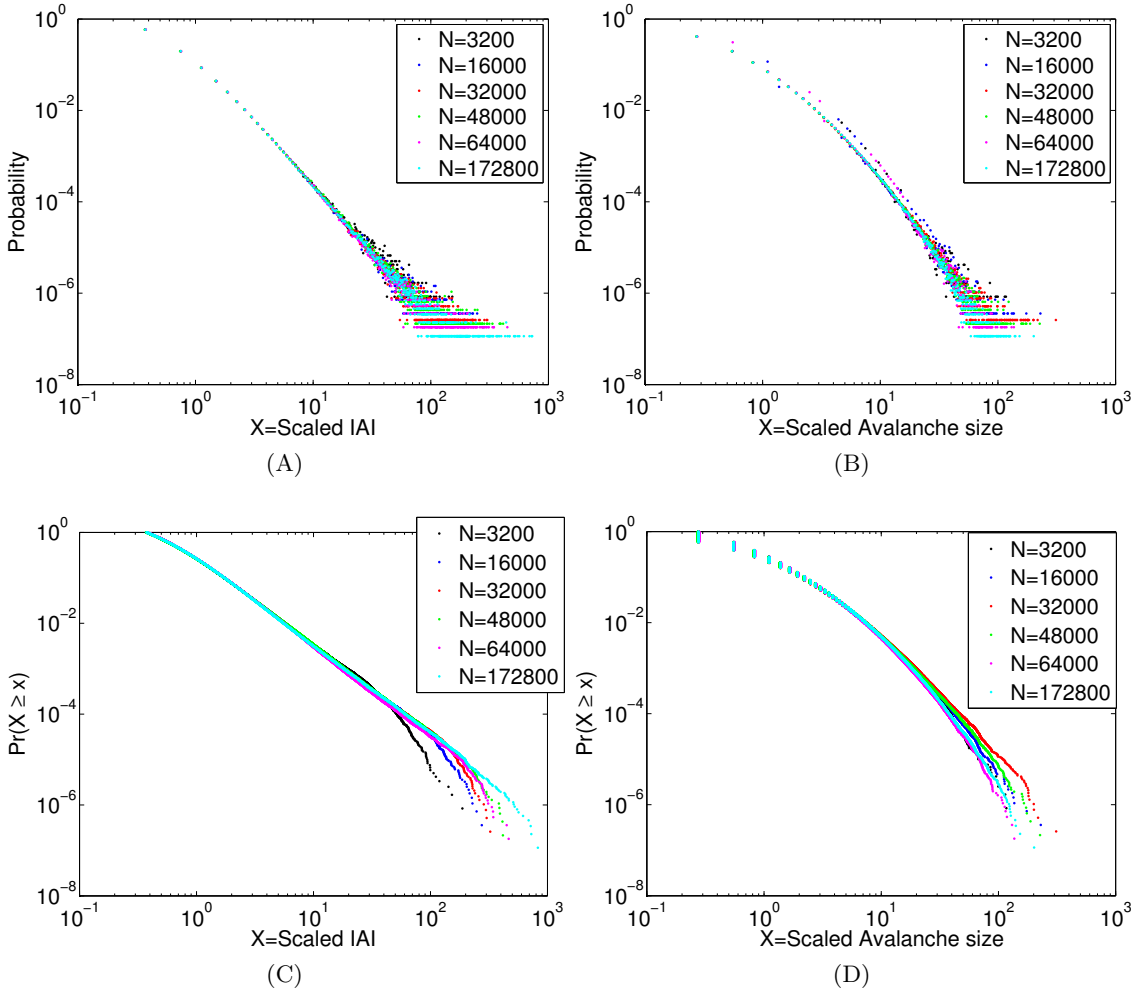

Figure 4.14: IAI (A) and avalanche size (B) distributions for 5 different network sizes rescaled by the mean IAI and avalanche size for each network respectively. The distributions show similar shape for all network sizes. (C,D) The corresponding cumulative distributions. For IAI (C) it can be seen that the larger networks have straight line slopes which extend further than smaller networks. There is no such relationship with avalanche size (D).

Changing the value of the external input

For the system with no external input the distribution of avalanche sizes followed a power-law (when the branching parameter was equal to 1), as is also observed experimentally in neuronal avalanches [49, 50]. However, as was observed in Fig. 4.7, the distribution of the sizes of avalanches in the presence of external input at the level $h = 1/N$ does not obey a power-law. This is likely due to a superposition of avalanches caused by the external input effectively initiating another avalanche before the first avalanche has time to complete. If this is the case then one would expect smaller values of h to lead to less of a superposition effect and so a shift in the distribution of the size of avalanches to become more like a power-law. In order to test this, and so as to better understand the dynamics of the system, the value of h was systematically varied.

For all simulations in this section $\alpha = 1,\ w = 1,\ N = 800$. The value of h will (as previously) depend on the number of neurons with $h = c/N$ where c is a constant (in previous simulations $c = 1$), and the value of c will be varied to change the level of external input. By equation 4.1.2 the fixed points and corresponding eigenvalue (with $\alpha = w = 1$) are:

$$A = -\frac{c}{2} \pm \sqrt{\frac{c^2}{4} + cN}$$
$$\lambda = \pm\sqrt{\frac{c^2}{N^2} + \frac{4c}{N}}$$

Let $c \in \{0.01, 0.1, 2, 10\}$. For each of these values 10 simulations of the firing dynamics were carried out. Fig. 4.15 shows the raster plots of the first 1 second of a simulation for each of these values of c. As expected the firing density is decreased for lower levels of the external input (i.e. smaller values of c) and so the bursts of activity are more distinct. This difference in firing density can also be observed in the inter-spike intervals of the neurons - see Fig. 4.16. Note that the ISIs are exponentially distributed for all levels of the external input.

Fig. 4.17 shows the distributions of burst characteristics for different levels of external input. This should be compared with Fig. 4.7(D-F) which showed the distributions for $h = 1/N$. We see that, as expected, for lower levels of the external input the distribution of avalanche sizes follows a power-law. For low levels of the external input, there also appears to be a linear relationship (on this double-logarithmic scale) over a range of scales in the duration distribution, although this does not hold for the smallest or largest durations. The distributions for both avalanche size and duration can therefore be understood in terms of previous results that have suggested that both exhibit power-laws [49, 55] when there is a separation of timescales (i.e. the avalanches occur on a much faster time-scale than the initiation of the avalanches) [56, 58]. As the

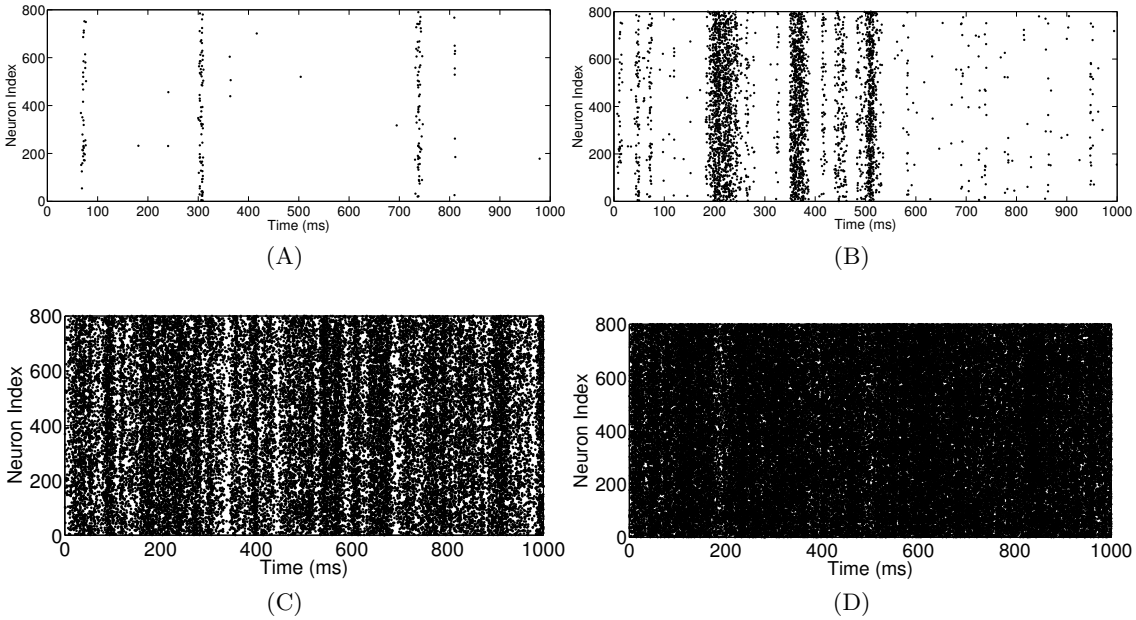

Figure 4.15: Raster firing plot for simulations with $h = \frac{c}{N}$ where (A) c=0.01, (B) c=0.1, (C) c=2 and (D) c=10. The other parameters were set to the 'critical' values with $\alpha = 1,\ w = 1,\ N = 800$. For smaller values of the external input the firing dynamics are sparser, which is also reflected in the network ISI distributions, see Fig. 4.16. For the highest level of external input (D) burst dynamics are no longer as obvious, though periods of less dense firing can be observed. These figures can be compared with Fig. 4.4(C) where $h = 1/N$.

level of the external input is increased there is no longer a separation of timescales and superposition of the avalanches occurs, disrupting the distributions.

In contrast the IAIs, do not exhibit power-law behaviour for small external input, but a power-law relationship emerges at higher levels. The distributions were also examined on semi-logarithmic axes to investigate the possibility that the data was exponentially distributed. For small levels of the external input (c=0.01,0.1) the IAI distributions did exhibit linear scaling indicating that these distributions were indeed exponential, see Fig. 4.18. This was not the case for any of the other distributions (not shown). This coincides with other modelling results that have shown exponential distributions of IAIs for the same (slow driving) external input as gives rise to power-law distributions in avalanche size and duration [56, 138].

The DFA and Whittle exponents were also calculated for each of the simulations for each level of the external input. Summary statistics for the exponents are given in Table 4.1. For $c = 0.01, 0.1$ the DFA plots followed a single trend across all box sizes (i.e. there were no crossovers) with exponents that were close to 0.5 indicating no LRTCs in the data. For $c = 2, 10$ there were two crossover points in the plots. For $c = 10$, the (middle) DFA exponent was lower than for $c = 2$. A similar pattern was seen in the Whittle exponent, where the highest exponent values were seen for the input level with $c = 2$. Intuitively this can be understood as for low levels of external input the

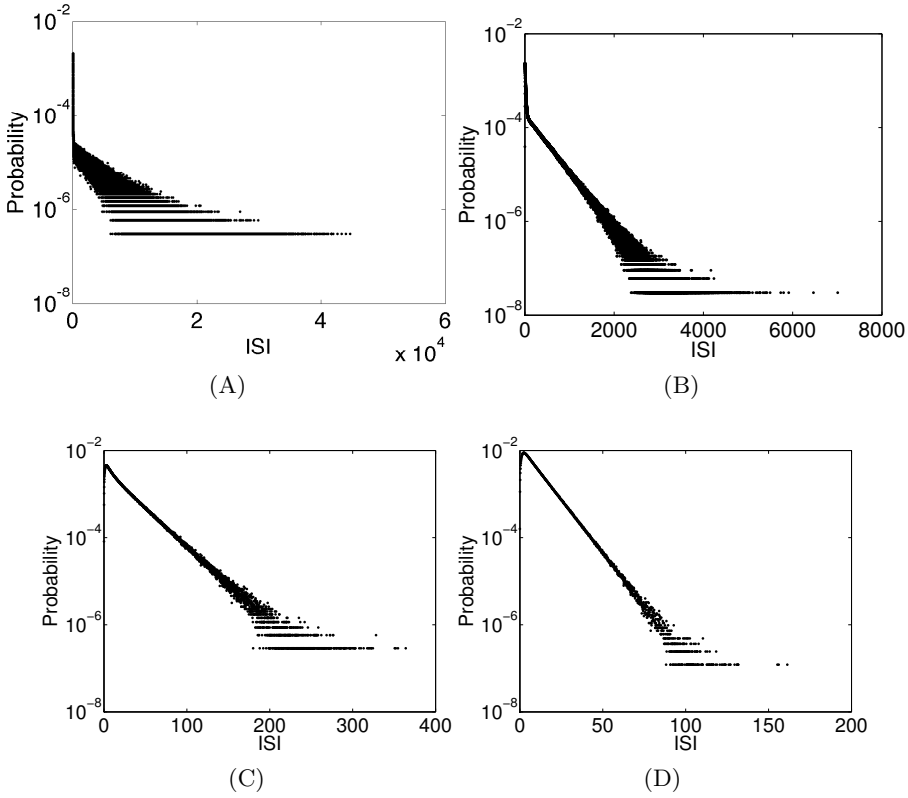

Figure 4.16: ISI distributions for simulations with $h = \frac{c}{N}$ where (A) c=0.01, (B) c=0.1, (C) c=2 and (D) c=10. The distribution is from a single simulation at each level of the external input and is shown on a semi-logarithmic scale. This can be compared with the ISI distribution for a simulation with c=1, shown in Fig. 4.6. For c=2,10 analysis was only carried out to a simulation length of 100 seconds due to the density of firing.

bursts are far apart and so may have less influence on one another. For high levels of external input there is a high firing rate and all avalanches merge together. This result indicates that there is an 'optimal' level of external input for LRTCs, where the bursts are not so far apart that there is no relationship between them but they are not so close that they completely overlap.

In summary, with no external input the system exhibits power-law distributions of avalanche size, as is also the case for experimentally observed neuronal avalanches [49, 50], but there is no way of measuring IAIs. For very small levels of the external input the system exhibits distinct avalanche behaviour with a power-law distribution of avalanche size and an exponential distribution of IAIs. This is the same type of distributions observed, for example, in the avalanches in the sandpile model which is slowly driven and has a separation of timescales [56, 138]. For this level of the external input the sequences of avalanche size, duration and IAI do not exhibit LRTCs. However, as the input is increased there is a superposition effect, with the next avalanche starting before the previous one has finished. With this the power-law in avalanche size and duration is lost but a power-law distribution of IAIs emerges. For this level of the

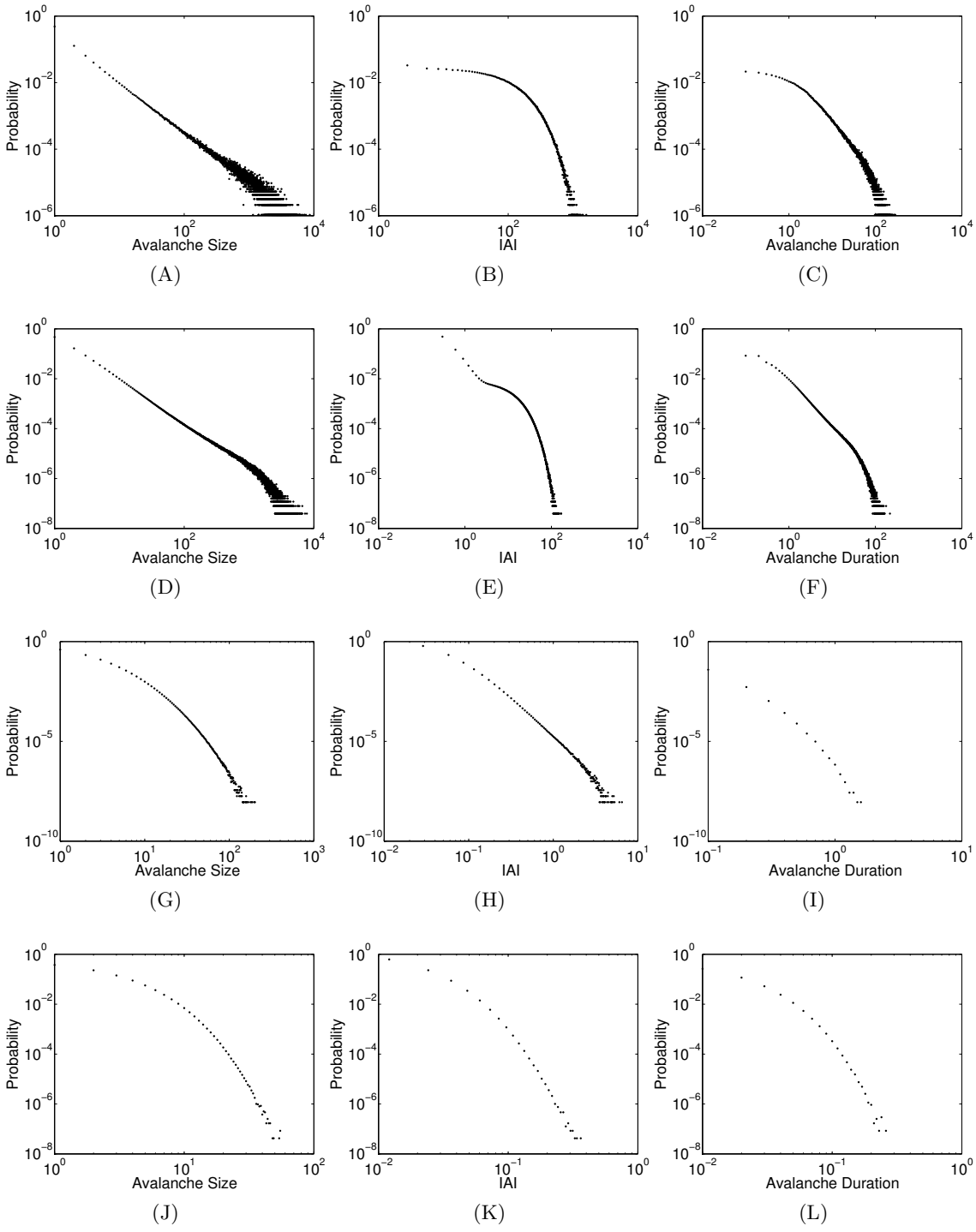

Figure 4.17: Distribution plots for c=0.01 (A-C), c=0.1 (D-F), c=2 (G-I) and c=10 (J-L). These can be compared with the distributions with $c = 1$ in Fig. 4.7(D,E,F). Here changes in avalanche size distributions (A,D,G,J), IAI distributions (B,E,H,K) and duration distributions (C,F,I,L) with the level of external input can be observed. Distributions are pooled values from 10 simulations at each value.

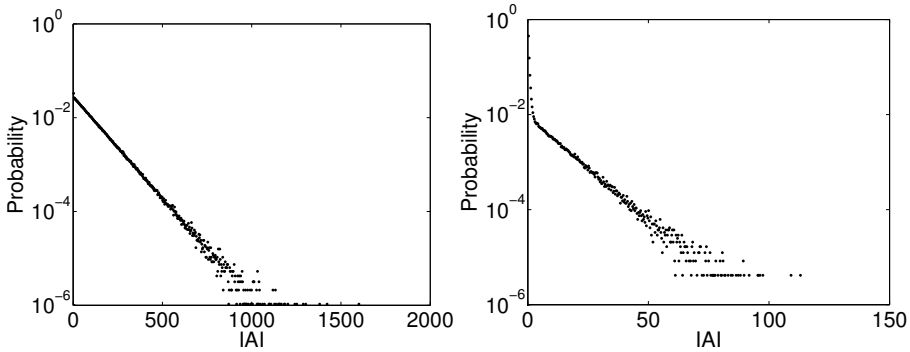

(A) (B)

Figure 4.18: IAI distributions plotted on semi-logarithmic scale for (A) c=0.01 and (B) c=0.1. For the smallest level of external input (c=0.01) the whole distribution seems to be well fit by a single linear trend on this scale indicating that the distribution is an exponential. For c=0.1 (as would be expected from Fig. 4.17(E)) the distribution has two different sections, with a much stepper gradient at very small IAI.

	IAI - DFA			Size - DFA			Duration - DFA		
c	Mean	Min.	Max.	Mean	Min.	Max.	Mean	Min.	Max.
0.01	0.50	0.49	0.51	0.49	0.48	0.51	0.50	0.48	0.52
0.1	0.56	0.55	0.57	0.54	0.52	0.56	0.56	0.54	0.58
2	0.93	0.91	0.95	0.98	0.96	1.00	0.95	0.93	0.97
10	0.85	0.82	0.86	0.88	0.86	0.90	0.83	0.81	0.84
	IAI - Whittle			Size - Whittle			Duration - Whittle		
c	Mean	Min.	Max.	Mean	Min.	Max.	Mean	Min.	Max.
0.01	0.50	0.50	0.50	0.50	0.50	0.51	0.50	0.50	0.51
0.1	0.64	0.63	0.65	0.57	0.55	0.58	0.61	0.60	0.63
2	0.71	0.70	0.71	0.69	0.69	0.69	0.66	0.66	0.66
10	0.58	0.57	0.58	0.59	0.59	0.59	0.57	0.57	0.57

Table 4.1: Tables indicating the DFA and Whittle exponents for different values of c where $h = c/N$. Summary statistics (mean, minimum and maximum) for the 10 simulations carried out at each of the values of c for IAIs, size of avalanches and duration of avalanches. For $c = 2, 10$ the DFA plots had 2 crossovers and the summaries are of the central region of boxes between the two crossovers. However, note that for $c = 2$ for 2 IAI sequences the exponents were excluded as the lower crossover was very close to the upper crossover. Whittle exponents are for fixed length sequences of the first 1,000,000 data points.

external input, LRTCs are observed in the sequences of IAIs, avalanche size and duration (up to a crossover dependent on system size). It is important to remember that the external input itself is not structured and the LRTCs exhibited by the avalanches are an emergent property of the system - a signature of the system being close to a critical point.

The original observation of neuronal avalanches was in spontaneous activity in neuronal cultures [49, 50]. If an external input was applied to the system at a level equivalent to simulated levels here, a superposition effect would also be observed and it would be interesting to see if this activity displayed LRTCs. The results here suggest that the LRTCs observed in the human brain could be a consequence of an optimal level of external input displacing the system from the critical point. Indeed, it has been suggested that the LRTCs observed in the fluctuations of oscillation amplitude in continuous data may be a result of a network which is slightly supercritical [159].

4.1.4 A probability tree approach to calculating avalanche distributions

Finally in this chapter we take a theoretical approach to understand the avalanche attributes. This approach does not detract from the results of the simulations but on the contrary aids in our understanding of the system. Indeed, using this theoretical approach the overall distributions of the avalanches can be derived. However, the burst behaviour itself cannot be observed and LRTCs cannot be assessed. As the model is a fully connected system avalanche distribution statistics can be analysed directly through assessment of the probabilities at each simulation step. This analysis was not carried out by *Benayoun et al.* [61] and is investigated in this type of model for the first time here.

Firstly, in this section the theoretical probability distribution of IAIs is derived. An IAI is a period during which no neuronal firing occurs, but any number of active neurons can switch back into their quiescent state. Thus, the probability distribution of IAIs is equivalent to the distribution of all possible continuous sequences of active to quiescent ($a \to q$) transitions. For the moment, the binning used to attain IAIs is neglected and the possibility that $a \to q$ transitions can occur within an avalanche (and so not within an IAI) is therefore also neglected. The effect this has on the distribution will be returned to later.

As the Gillespie algorithm was used for simulations then exactly one neuron changes its state at each simulation step. Thus, given a certain number of active neurons, at each step in the simulation one of two possible transitions must occur - either (1) a new neuron switches into the active state or (2) a neuron becomes inactive. Let N_0 be the initial number of active neurons (here initial should be taken to imply a starting point from any number of active neurons and does not just mean the number of active neurons at the very start of the simulation). The number of active neurons after a single simulation step will be $N_0 + 1$ or $N_0 - 1$. Let q_i be the probability that a neuron goes back to the quiescent state given i active neurons. So the probability that there are $N_0 - 1$ active neurons after a single simulation step is q_{N_0} and the probability that there is $N_0 + 1$ active neurons is $1 - q_{N_0}$. Note that from the transition rates of the neurons:

$$q_i = \frac{\alpha i}{(\frac{w}{N} i + h)(N - i) + \alpha i} = \frac{\alpha i N}{(wi + hN)(N - i) + \alpha i N}$$

An IAI is formed from a period of consecutive $a \to q$ transitions (without any neurons firing within the system). Thus, from the description above and starting with N_0 initially active neurons (assuming a neuron has just fired for the system to enter that state) then the probability of an IAI of k $a \to q$ transitions can be calculated. This can be depicted using a probability tree, see Fig. 4.19, which pays particular attention to the $a \to q$ transitions (i.e. $N_0 \to N_0 - 1 \to N_0 - 2 \to ...$), as once a $q \to a$ transition occurs

the IAI has ended. Note that in the case where there are no active neurons, as the system has an external input, after the next simulation step there will be a single active neuron with probability 1.

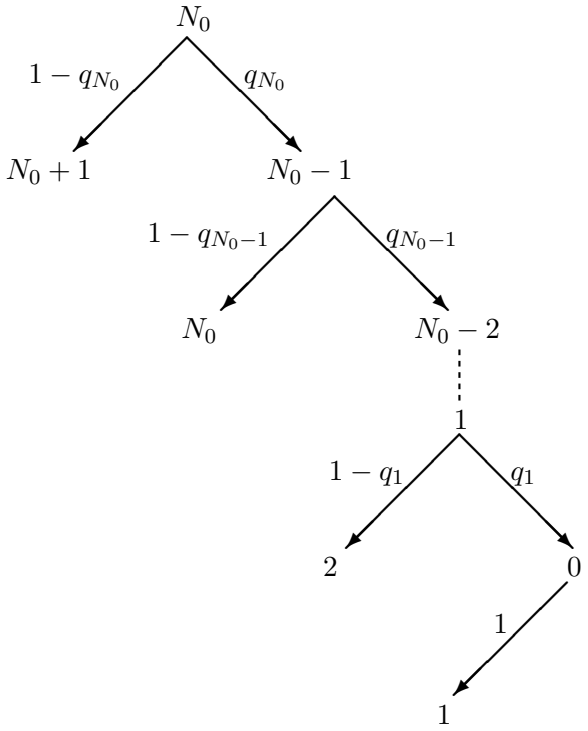

Figure 4.19: Probability tree of IAIs

Starting with N_0 active neurons the probability of an IAI of *at least* k transitions is therefore

$$P(IAI_{\geq k}) = p(N_0, \geq k) = \prod_{j=0}^{k-1} q_{N_0-j}$$

and the probability of the IAI consisting of *exactly* k transitions (and so it must be ended by a $q \to a$ transition) is

$$P(IAI_{=k}) = p(N_0, k) = (1 - q_{N_0-k}) \prod_{j=0}^{k-1} q_{N_0-j}$$

Given this probability of an IAI consisting of a set number of transitions, to obtain a probability distribution for IAIs (i.e. the actual time periods) the time for each transition must be calculated. The length of the IAI is then given by the sum of the times for each of the transitions. As the Gillespie algorithm is used, at each simulation step the time to the next transition changes and is related to the total transition rates of all the neurons in the system. Given i active neurons, then the sum of the rates within the system is $R_i = \alpha i + (\frac{w}{N} i + h)(N - i)$ and the time to the next transition is drawn at random from an exponential distribution with rate R_i. So the average time to the next

transition is $\tau_i = \frac{1}{R_i}$.

Starting with N_0 active neurons and for an IAI of k transitions, the average length of time for this IAI will therefore be:

$$T = \sum_{j=0}^{k-1} \tau_{N_0-j}$$

However, if this IAI, with equal starting conditions, were to be simulated a number of times then a distribution of IAI lengths would be found. The total IAI length is a sum of exponentially distributed variables drawn from distributions of different rates. This implies that the IAI will be drawn from a *hypoexponential* distribution[5]. The probability distribution function of a hypoexponentially distributed variable x, if all the rates of the individual exponentials are independent ($\lambda_i \neq \lambda_j \; \forall i \neq j$), is given by [203]:

$$\sum_{j=1}^{n} \lambda_j e^{-\lambda_j x} \left(\prod_{i=1, i\neq j}^{k} \frac{\lambda_i}{\lambda_i - \lambda_j} \right)$$

where the λ_j are the rates of the exponential distributions. So in this context the distribution, $f(x, N_0, k)$ of IAIs (where x is the length of the IAI) consisting of k transitions and starting with N_0 active neurons, is given by

$$f(x, N_0, k) = \sum_{j=0}^{k-1} R_{N_0-j} e^{-R_{N_0-j}x} \left(\prod_{i=0, i\neq j}^{k-1} \frac{R_{N_0-i}}{R_{N_0-i} - R_{N_0-j}} \right) \tag{4.1.4}$$

Fig. 4.20 compares the resulting distribution of IAIs from a number of simulations[6], each with the same starting value and number of transitions, and the probability density function for the corresponding hypoexponential. A good comparison is shown between the two.

However, equation 4.1.4 just gives us the distribution of the IAI lengths for a set starting point and number of transitions. What we want is the distribution of all possible IAIs, that is the distribution starting from any number of active neurons and for any number of transitions. First let us consider what happens when we have any number of transitions for a set initial number of active neurons. As was shown above, the probability for all possible numbers of transitions can be calculated and for each of these the hypoexponential distribution can also be found. So the overall distribution

[5] A hypoexponential distribution is defined as a sum of exponentially distributed variables. Each exponential can have a different rate.

[6] Unless otherwise stated the simulations in this section do not use binning as was carried out for pervious simulations, but keep track of transitions within the network to better compare with the theoretical approach. Thus, single $a \rightarrow q$ transitions are included as IAIs when they probably would not be with the binning approach. At the end of the section the theoretical distributions are compared to the normal simulation with binning results.

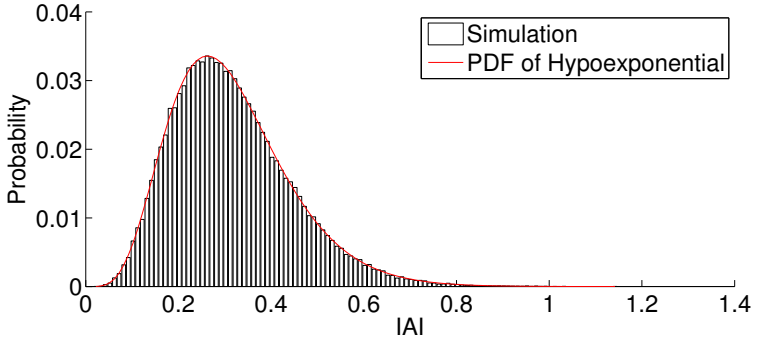

Figure 4.20: Histogram shows 100,000 IAIs from a simulation with 20 neurons, 18 initially active neurons and 5 transitions. The simulated IAIs were calculated by drawing a random value from an exponential distribution with rate equal to the total rates of the neurons in the network at each step of the simulation, and summed over the 5 transitions. The red line shows the probability density function of the corresponding hypoexponential distribution, calculated from equation 4.1.4.

will be a weighted sum of hypoexponentials which depends on the probability of an IAI of k transitions occurring.

Thus, the probability density function, $F(x, N_0)$, of these IAIs (with different numbers of transitions but for a given initial number of active neurons N_0) is given by:

$$F(x, N_0) = \sum_{m=1}^{N_0} f(x, N_0, m) p(N_0, m) \tag{4.1.5}$$

where $p(N_0, m)$ is (as above) the probability of an IAI of m transitions given N_0 initially active neurons, found using the probability tree. The sum is taken across all possible numbers of transitions, the greatest of which is N_0 corresponding to all of the initially active neuron becoming inactive before a single $q \to a$ transition occurs.

Fig. 4.21 compares the resulting distributions of IAIs from a simulation starting with the same number of initially active neurons with the probability density function of the weighted sum of hypoexponentials. Again a good comparison is found.

Finally, to calculate the full probability density function of IAIs for a network of set system size we must consider all possible values for the initial number of active neurons, $N_0 \in \{1, 2, ...N\}$ (note that 0 is not considered as the next transition will necessarily be an activation). This overall distribution will therefore be the weighted sum of the above calculated distribution, i.e. a *weighted sum of a weighted sum of hypoexponentials*. The weighting for this final part of the distribution comes from the probability of having a certain number of active neurons. Assuming that the simulation starts from a state with no active neurons (which has been the case in all simulations in this thesis for which an external input is present). Then straight away at the next simulation step there will be a single active neuron. At all steps after this the number of active neurons will increase or decrease and so higher numbers of active neurons will occur less frequently than

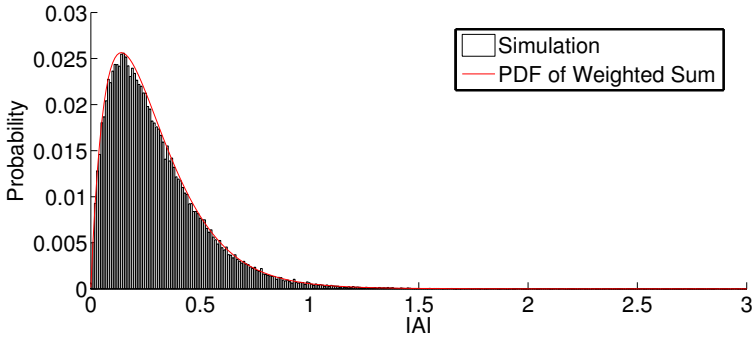

Figure 4.21: Histogram of 100,000 IAIs simulated from a network with 20 neurons and 18 initially active neurons. The IAI is calculated as the sum of transition times chosen from exponential distributions and the number of transitions is chosen probabilistically using the normal simulation approach. The red line shows the probability density function of the weighted sum of hypoexponentials, as given in equation 4.1.5.

states with lower number of active neurons.

To calculate the probability of a certain number of active neurons we make use of a probability tree where this time we are interested in all transitions and not just those that lead to the extension (or termination) of an IAI. The tree will therefore start from 0 active neurons (as simulations start from this state) and consider all possible transitions. First let us consider the simple case of $N = 3$. Fig. 4.22 shows all possible transitions for a network of this size.

From the tree it can be observed that the probabilities, $P(i)$, of the number of active neurons being equal to i, where i is one of the four possibilities $\{0, 1, 2, 3\}$ are:

$$\begin{aligned} P(0) &= q_1 P(1) \\ P(1) &= P(0) + q_2 P(2) \\ P(2) &= (1 - q_1)P(1) + P(3) \\ P(3) &= (1 - q_2)P(2) \end{aligned} \tag{4.1.6}$$

Rearranging and substituting to write the equations in terms of $P(1)$:

$$\begin{aligned} P(0) &= q_1 P(1) \\ P(2) &= \frac{(1 - q_1)}{q_2} P(1) \\ P(3) &= \frac{(1 - q_1)(1 - q_2)}{q_2} P(1) \end{aligned} \tag{4.1.7}$$

Furthermore, the sum of all the probabilities must equal 1 and so

$$\left(q_1 + 1 + \frac{(1 - q_1)}{q_2} + \frac{(1 - q_1)(1 - q_2)}{q_2} \right) P(1) = 1 \tag{4.1.8}$$

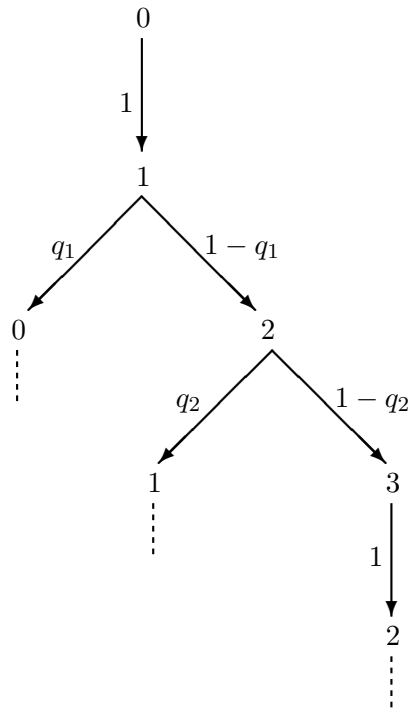

Figure 4.22: Probability tree of all possible transitions in a network of size $N = 3$. Dots indicate transitions that are already shown elsewhere in the tree.

Therefore

$$P(1) = \frac{q_2}{q_1 q_2 + q_2 + (1 - q_1) + (1 - q_1)(1 - q_2)} \tag{4.1.9}$$

Substituting this value back into equations 4.1.8 the probabilities for the full system can be calculated.

This approach can be extended to obtain equations for the probabilities of the number of active neurons for any system size N. Firstly, as in equations 4.1.7 the probabilities can be written as:

$$\begin{aligned}
P(0) &= q_1 P(1) \\
P(1) &= P(0) + q_2 P(2) \\
P(2) &= (1 - q_1) P(1) + P(3) \\
&\vdots \\
P(k) &= (1 - q_{k-1}) P(k-1) + q_{k+1} P(k+1) \\
&\vdots \\
P(N-1) &= (1 - q_{N-2}) P(N-2) + q_N P(N) \\
P(N) &= (1 - q_{N-1}) P(N-1)
\end{aligned} \tag{4.1.10}$$

where $q_N = 1$ but it will remain in the equations so as to aid notation. Rearranging gives

$$P(2) = \frac{(1-q_1)}{q_2} P(1)$$

and by induction:

$$\begin{aligned} P(k+1) &= \frac{1}{q_{k+1}} \left(P(k) - (1-q_{k-1}) P(k-1) \right) \\ &= \frac{(1-q_1)(1-q_2)\dots(1-q_k)}{q_2 q_3 \dots q_{k+1}} P(1) \end{aligned} \tag{4.1.11}$$

Summing all the probabilities and setting this equal to 1:

$$P(1) = \frac{q_2 q_3 \dots q_N}{q_1 q_2 \dots q_N + q_2 q_3 \dots q_N + (1-q_1) q_3 \dots q_N + \dots + (1-q_1)(1-q_2)\dots(1-q_N)} \tag{4.1.12}$$

To check these theoretical values of the probabilities, the values were compared to the probabilities obtained from a simulation of a network with $N = 100$. The results are shown in Fig. 4.23.

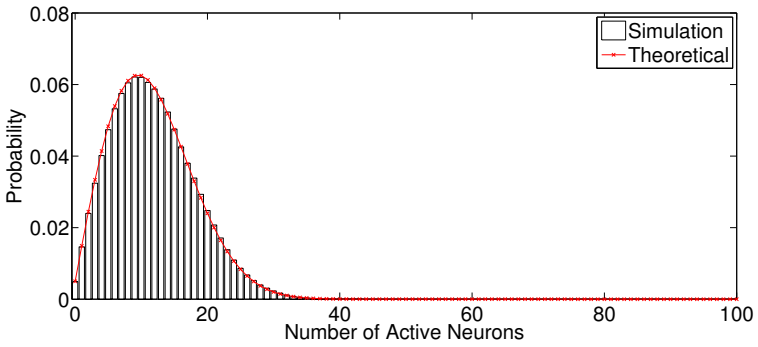

Figure 4.23: Histogram of probabilities of the number of active neurons from a simulation of network size $N = 100$. The simulation lasted for 1,000,000 transitions. The probabilities are compared to the theoretical values, obtained from equations 4.1.11,4.1.12, shown in red.

With these probabilities the full probability distribution for the IAIs of the system can now be calculated. As was shown above, for a set initial number of active neurons, the probability distribution of IAIs is given by a weighted sum of hypoexponentials. Thus, the distribution of all IAIs, across all possible initial numbers of active neurons, is a weighted sum of a weighted sum of hypoexponentials, where the first weighting is given by $P(N_0)$ (the probability of the number of active neurons being equal to N_0) and the second weighting is $p(N_0, m)$ (the probability given N_0 initially active neurons that the IAI has exactly m transitions). Thus, the overall probability distribution is given by

$$\wp(x) = \sum_{i=0}^{N} \left(P(i) \sum_{m=1}^{i} f(x,i,m) p(i,m) \right) \tag{4.1.13}$$

Fig. 4.24 shows an example comparison of IAIs from a simulation and the theoretically expected value given by equation 4.1.13. Note that this distribution, like a power-law, has a fat-tail. This explains why, as we will see below, the distribution can appear linear on a double-logarithmic scale.

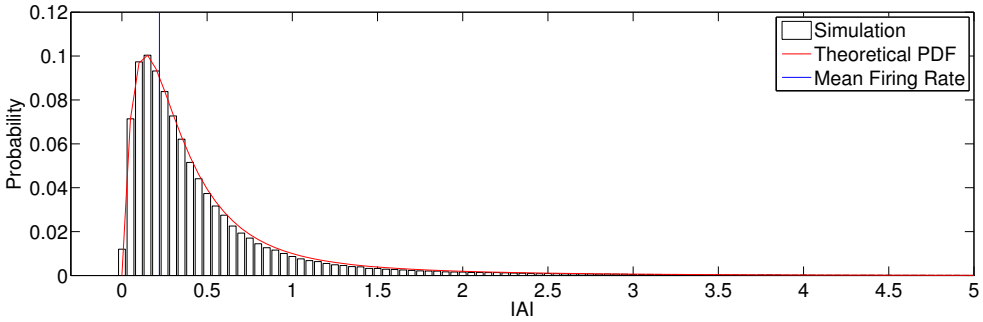

Figure 4.24: Histogram of IAIs from a simulation with 20 neurons considering all $a \to q$ transitions as an IAI. The theoretical distribution calculated from equation 4.1.13 is shown in red. The mean firing rate of the simulation is also indicated in blue - note that this is calculated including all the intervals between firing (including consecutive firing) and so it is not the mean of the IAI distribution.

How is the distribution affected by the binning method?

In previous simulations firing dynamics were binned into avalanches in a similar way to that which is carried out in experimental settings. Firing was separated into avalanches dependant on the average firing rate in the system. Thus, a minimum IAI equal to the average time between consecutive spikes in the network was imposed on the simulation results. How does taking into account this binning affect the theoretical distributions? As was shown in Fig. 4.24, the average firing rate is close to the peak of the IAI distribution. Only the section of the distribution to the right of this threshold needs to be considered when comparing with the simulation results. Fig. 4.25 shows the theoretical IAI distribution, above the average firing rate compared with a the IAIs found from the simulation using the standard binning method to define the avalanches. Fig. 4.26 shows this theoretical distribution extended for $N = 800$ and compared with the simulation results found earlier (Fig. 4.7). The theoretical distribution is close to the simulated data, giving rise to the 'drop-off' at the same IAI value. The theoretical distribution also appears to follow a straight-line on this double-logarithmic scale and so the weighted sum of hypoexponential distributions provides an explanation as to why the simulated IAI data appears to follow a power-law. We have seen in Fig. 4.24 that the weighted sum of hypoexponentials is a 'fat-tail' distribution (as is a power-law) and so this provides an explanation for the linear relationship on the double-logarithmic axis.

The theoretical distribution was also a good-fit to the data when the distribution did not appear to follow a power-law, as was observed at lower values of the external input.

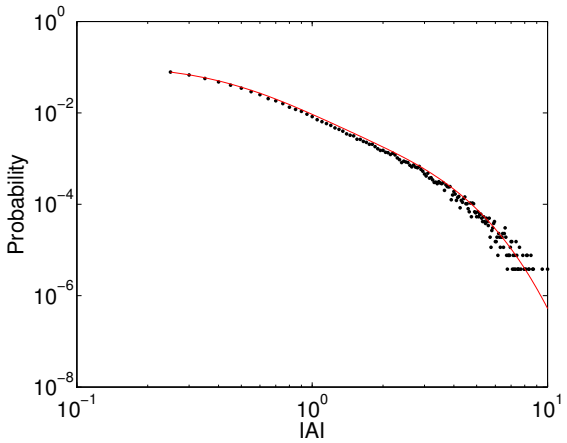

Figure 4.25: Theoretical and simulated distribution of IAI shown on a double-logarithmic scale. The distribution is the same as that shown in Fig. 4.24 but only those IAI greater than the mean firing rate (blue line in Fig. 4.24) are included, as would have been the case with the binning method for the other simulations in this chapter.

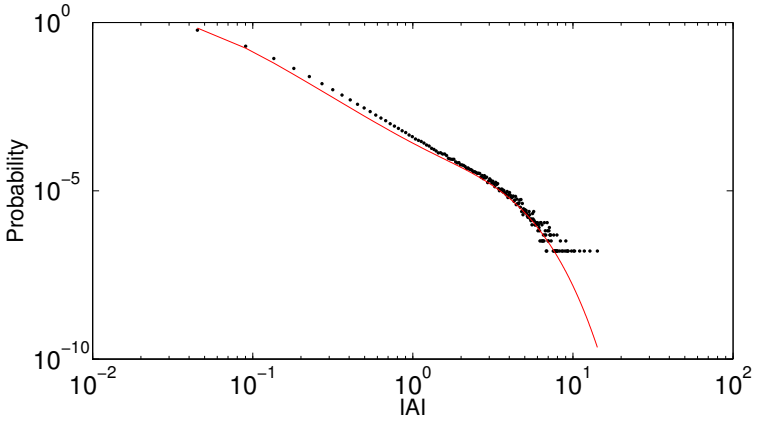

Figure 4.26: Theoretical (red) and simulated (black) distributed of IAIs for a network of $N = 800$ neurons and $\alpha = 1,\ w = 1,\ h = 1/N\ (c = 1)$.

Fig. 4.27 shows the theoretical distributions and corresponding distributions from the simulated data for $h = c/N$ with $c = 0.01$ and $c = 0.1$. This theoretical derivation therefore provides an explanation for the IAI distribution at different levels of the external input. Thus, we can conclude from this section that the IAI distribution is a weighted sum of hypoexponentials. This fat-tail distribution results in the apparent power-law scaling of the distribution from the simulations.

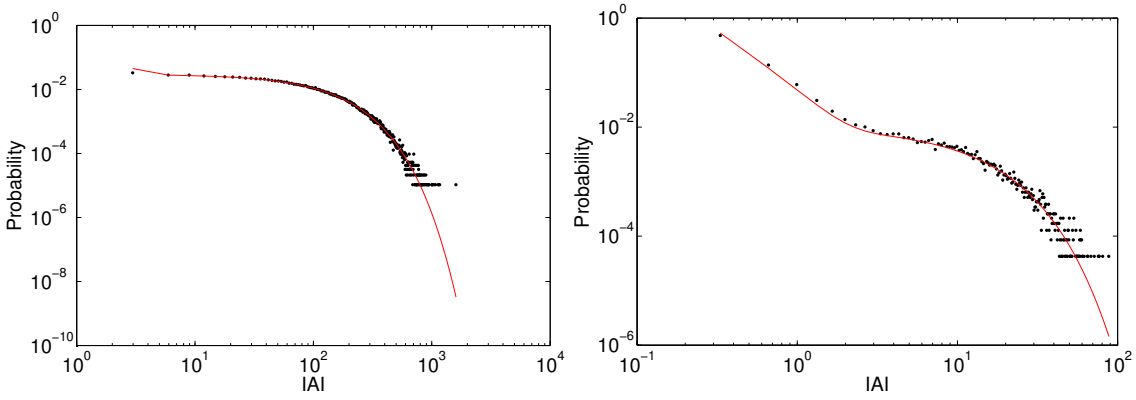

(A) (B)

Figure 4.27: Theoretical (red) and simulated (black) distributed of IAIs for a network of $N = 800$ neurons, $\alpha = 1,\ w = 1,\ h = c/N$ where (A) $c = 0.01$ and (B) $c = 0.1$.

It is worth recalling here that LRTCs in data sequences are a result of a complex relationship in the temporal distribution of the data and the underlying probability distribution of that data need not be a power-law. Therefore, the fact that the distribution of IAI is a weighted sum of hypoexponentials does not imply that the LRTCs in the data are also due to a hypoexponential in the autocorrelation function (or a distribution other than a power-law). The tree approach used here examines directly the distribution of avalanche characteristics but does not examine the temporal ordering of these characteristics and so cannot be used to evaluate the distribution of the autocorrelation function.

It is also worth considering what this means for the system, given that we know that the system is near a critical point. Would we not expect the distribution to be a power-law? However, note that the fact that the distribution is a hypoexponential is related to the simulation steps - as the Gillespie algorithm was used the time between transitions is drawn from an exponential distribution. Therefore, one would expect the IAI distribution to be somehow related to an exponential distribution. This is also the case for the duration distribution but is not the case for the distribution of avalanche size - as we will see the distribution of avalanche size does not need to take into account these transition rates only the transitions themselves.

A probability tree approach to calculating avalanche size and duration

The above method for calculating the probability distribution for IAIs can be used in a similar way to calculate the distribution of avalanche durations, and in a slightly simplified way to calculate avalanche size. Note first that an avalanche consists of periods of neuronal firing, i.e. $q \to a$ transitions. Thus, an avalanche can be of size k if there are exactly k $q \to a$ transitions. The size of the avalanche increases by 1 for each of these transitions and does not need to factor in the transition time. Thus, the distribution of avalanche sizes is simply the weighted sum of the probabilities of avalanches of all sizes; for example, an avalanche of exactly k transitions (and therefore of size k) starting with an initial number of active neurons of N_0 is

$$Pr(S = k) = q_k \prod_{j=0}^{k-1} (1 - q_{N_0+j})$$

and this is weighted, as above - see equations 4.1.11,4.1.12 - by the probability, $P(N_0)$, of starting with N_0 active neurons. Note that the distribution of avalanche sizes is not weighted by a hypoexponential.

This is simply extended to yield the distribution for avalanche duration, by noting that the duration should take into account the transition times. Thus, the distribution of avalanche durations will also be a weighted sum of a weighted sum of hypoexponentials, with the hypoexponential taking rates $R_{N_0}, R_{N_0+1}, \ldots R_{N_0+j}$ as the number of active neurons will increase for the duration of the avalanche.

Fig. 4.28 compares these full probability distributions for avalanche size and duration with results from simulations. As was the case with the IAI distributions a good agreement is seen between the theoretical and simulated values.

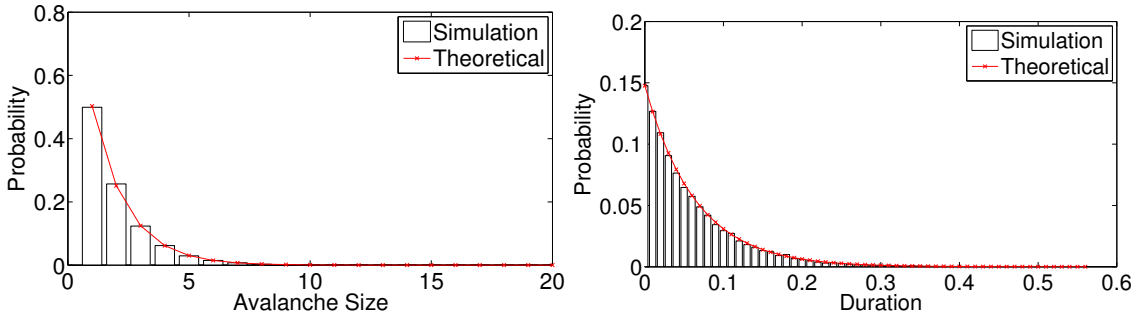

(A) (B)

Figure 4.28: Avalanche size (A) and duration (B) distributions, with the theoretical distribution shown in red and the simulation values (which are calculated without binning to define the avalanche) shown in black. Both are calculated for a network size of 20 neurons.

For the size and duration distributions this simulation binning method to define

avalanches will cause a larger alteration than was the case for IAIs. For example a series of transitions $q \to a,\ q \to a,\ a \to q,\ q \to a,\ q \to a$ may be one avalanche with a size of 4 and a duration that is the sum of the time for each of the transitions. It is therefore not clear how the distribution of size and duration from the binning method can be directly related to their theoretical distributions. However, the example given here is the joining together of two avalanches, each of size two (assuming that at either end an IAI occurs). Therefore, the simulated distributions will be related to the theoretical distributions given here by a superposition effect.

4.2 Summary of the model and results

- In early development some neurotransmitters (in particular GABA) have altered effects. While presynaptic inhibition is thought to occur from early stages of development, postsynaptic inhibition is altered. In this chapter the altered postsynaptic effects during development were considered and the question of whether a purely excitatory system can produce burst dynamics with the type of complex behaviour observed in the EEG was addressed.

- A simple excitatory neuronal model was constructed. The model is a fully connected system with simple 'switch' neurons that can be in one of two states: active or quiescent. Their state changes stochastically depending on transition rates which, in the case of $q \to a$ transitions, are related to the activity in the rest of the network.

- With no external input, parameter values can be derived so that the system has a critical (zero eigenvalue) fixed point. This is equivalent to saying that the branching parameter of the system is equal to one and the dynamics are balanced. For critical parameters the distribution of avalanche sizes follow a power-law. This behaviour is similar to that observed experimentally in the form of neuronal avalanches [49, 50] for which there is a power-law distribution in avalanche size.

- However, with no external input the activity is not continuous and $A = 0$ is an absorbing state. To achieve a higher level of biological realism and to allow for the possibility of emergent burst dynamics, a non-zero tonic external input was added to the system.

- With a linear activation function and non-zero input it is not possible to derive parameters such that the fixed point of the system is critical. However, dynamics were assessed with parameters that were sub-critical, critical and super-critical in the zero input case, with the small external input only perturbing the dynamics slightly from the fixed points. In simulations with 'critical' parameters burst dynamics were observed and are an 'emergent' property of the collective dynamics

of the system. For 'subcritical' parameters the bursts die out quickly, while for 'supercritical' parameters the bursts are (on average) more sustained.

- With $h = 1/N$ the distribution of IAIs appears to follow a power-law distribution while the distributions of avalanche size and duration do not show a straight line relationship on the double-logarithmic scale. For different system sizes the distributions exhibit the same behaviour with the apparent power-law relationship in IAIs extending to larger values for larger system sizes. This is not the case for the distribution of avalanche sizes.

- For lower levels of the external input the distribution of avalanche size and duration appears to follow a power-law suggesting that the lack of this relationship for higher levels of external input is due to a superposition effect. At these lower levels of the external input the IAI distribution no longer follows an apparent power-law. For higher levels of the external input none of the avalanche characteristics are power-law distributed.

- The distributions can be derived theoretically by assessment of the probabilities at each transition - a probability tree approach. The distribution of IAIs is shown theoretically to be a weighted sum of hypoexponentials, which appears approximately linear on a double-logarithmic scale (for $h = 1/N$) and is in good agreement for the distributions from the simulations, above the low cut-off imposed by the binning method of simulations. Therefore, the apparent power-law distributions found in the simulations are actually related to sums of hypoexponentials - another 'fat-tailed' distribution. This distribution was related to the fact that simulations are carried out using the Gillespie algorithm which draws transition rates randomly from an exponential distribution.

- With $h = 1/N$, DFA of the sequences of burst characteristics (size, duration and IAI) yields plots with crossovers. This was not the case for shuffled sequences which had a single linear trend across all box sizes with a slope of approximately 0.5. This indicates that the correlations within the actual sequences extend up to a certain box size, i.e. the correlations extend to a certain length. It was shown that increasing the system size increases the extent of the correlations (the crossover point increases). Theoretically, as $N \to \infty$, $\lambda \to 0$. Thus, it appears that LRTCs with infinite correlation length will occur in the limit of system size.

- For low and high levels of external input the DFA and Whittle exponents were close to 0.5. This indicates that there is an 'optimal' level of external input with which to obtain LRTCs which is neither so low that the avalanches are completely separate or so high that there is no clear distinction of the avalanches.

4.3 Discussion

To my knowledge this chapter provides the first analysis of LRTCs of avalanche/burst dynamics in a neuronal network model. The results presented here indicate that, in this excitatory neuronal network model, there is both an optimal level of input for LRTCs and also that LRTCs exist across an infinite sequence length (in the case of this particular level of external input) in the limit of system size. This coincides with the eigenvalue of the fixed point tending to zero, i.e. a branching parameter of one.

4.3.1 Two routes to criticality?

In this chapter we considered levels of the external input $h = c/N,\ c \in \{0.01, 0.1, 1, 2, 10\}$ and an 'optimal' level of the external input in terms of LRTCs was observed for $h = 1/N$. In this case as $N \to \infty,\ h \to 0 \Rightarrow \sigma \to 1$ and LRTCs with no upper crossover and the same linear trend extending across all box sizes exist in the limit of system size. However, it is also true that as $c \to 0,\ h \to 0 \Rightarrow \sigma \to 1$. So why do we not observe LRTCs for small values of c? Note that, while in both cases the actual value of h (the input received by each neuron in the system) tends to zero, if $h = 1/N$ and the system size changes then the overall level of external input to the system does not change. However, when $c \to 0$ the overall input to the system also decreases. So the critical eigenvalue is 'approached' in a different way. From the raster firing plots, we have seen that as c decreases the firing rate also decreases and the average IAI increases. With larger gaps between the avalanches one might hypothesise that the influences the avalanches have on each other decreases which explains the loss in the temporal correlations of the activity. By contrast, with $h = 1/N$ for different size systems the average burst rate is not greatly different and the bursts remain close (but not 'too' close) together. In this way correlations can extend across the temporal domain.

Similarly, as the level of external input changes there are also differences in the overall distributions of the avalanches. For low levels of the external input the distribution of avalanche sizes exhibits an apparent power-law. This agrees with previous results of neuronal avalanches and computational models describing neuronal avalanches [38, 49, 50, 61, 159]. As the level of external input is increased, the power-law distribution in avalanche size disappears. This can be explained by a superposition effect - for low levels of external input there is an effective separation of timescales with the time between the avalanches large so that (in general) an avalanche will finish before the next one begins. A separation of timescales has been noted by previous authors as an important system characteristic needed for power-laws in avalanche sizes [56, 58]. As the external input increases, the inter-avalanche intervals decrease and new avalanches can start before the previous avalanche finishes leading to a distribution that is a

superposition of avalanches.

As the level of external input changes there are also changes in the IAI distribution. For low levels of external input the distribution follows an exponential, whereas with $h = 1/N$ the distribution appears to follow a power-law. Theoretical analysis in fact indicates that these distributions (in both cases) are a weighted sum of hypoexponentials. As this distribution is a so-called 'fat-tailed' distribution this explains why it appears similar to a power-law on double-logarithmic axes. The same relationship was observed in the case of duration distributions, which appeared to exhibit a power-law over a range of scales for low levels of the external input. The observations again highlight the need for caution when evaluating distributions based on their linearity on double-logarithmic scales. The presence of hypoexponentials in the IAI and duration distributions was related to simulations using the Gillespie algorithm in which the time to the next transition is drawn from an exponential distribution. The avalanche size distribution is not affected by these transition times.

4.3.2 Relationship with experimental data

The aim of this chapter was to determine whether a purely excitatory neuronal network system could produce burst dynamics with LRTCs similar to that observed in the EEG recordings from preterm subjects. The question was reduced into its simplest form (i.e. whether an excitatory system alone can exhibit this type of dynamics *not* how does the preterm EEG exhibit this type of dynamics) and the model was therefore not expected to be an exact representation of the EEG. It was then intended that the model might generate an hypothesis as to how the complex temporal dynamics might occur in the premature brain and perhaps provide a basis for the construction of a more biophysically realistic model of the preterm brain. To this end, it is important to consider the differences between the model dynamics and that of the preterm EEG to decide whether the hypothesis generated by the model is viable.

It was found that LRTCs in burst characteristics occur for system parameters such that the branching parameter is one (in the limit of system size). This implies that the network is in a balanced state of activity such that on average an active neuron will in turn activate one other neuron. Therefore, this result predicts that a possible mechanism underlying the burst activity with LRTCs in the preterm EEG is this type of balanced activity. Intuitively this is an attractive mode for brain dynamics - one in which activity does not quickly die out nor cause run away excitation. In the preterm EEG the bursts have different amplitudes, suggesting that these are not all-or-nothing events encompassing all neurons despite the fact that the brain at this age has an imbalance of excitation and inhibition. This therefore supports the suggestion that the brain is in a balanced state. However, future work would be needed to determine

whether this hypothesis is true. Experimentally, the idea that a balance of excitation and inhibition is needed for power-laws in more mature systems has been tested by pharmacologically manipulating neurotransmitter receptors [37, 38, 160]. It may be possible to conduct similar experiments in the developing nervous system to test the effect that different levels of excitation have on the dynamics.

Examining DFA plots for the sequences of burst characteristics in the model, two crossover points were observed with three different linear trends across box sizes. As the system size increases the upper crossover also increases, extending the range of the correlations. The presence of crossovers in these plots contrasts with the DFA plots for the sequences from the preterm EEG, for which no crossover points were observed and the same linear trend was found to occur across all box sizes. However, the average sequence length for the preterm data was 3403. This is at approximately the same level as the upper crossover point in the smallest network analysed (compare with Fig. 4.11 - the sequences analysed from model simulations were much longer) and so it is possible that if the EEG data had been longer a crossover would have occurred. However, if the same underlying mechanism were to apply to the EEG data, as for the model, then the number of neurons in the brain would suggest that the upper crossover would be close to infinity. On the other hand, there was no 'lower' crossover (i.e. there was no crossover point at all) in the EEG data, perhaps indicating that a different mechanism is involved.

The model predicts that LRTCs in the bursts occur for an 'optimal' level of the external input which appears to be related to the fact that bursts are then 'close enough' to affect each other. However, in the preterm EEG the bursts can be hundreds of seconds apart. It therefore seems unlikely that these bursts are 'close' in the same way they are in the model. This suggests that the model constructed here does in fact not behave in the same way as the preterm EEG. Having said this, it may still be that the balance in activity is applicable to the preterm given that a balance of activity appears to relate to apparent critical dynamics and LRTCs in the more mature brain [159]. As will be discussed below, there are a number of ways in which this model could be extended to increase the biological realism. Perhaps these extensions will lead to burst dynamics that occur less frequently but that also exhibit LRTCs? Furthermore, it is worth remembering that the EEG is not a direct recording from a neural network but is the synchronised activity of a population of neurons distorted by the scalp. This leads to changes in the dynamics that are observed, with very small bursts of neuronal activity not being detected at the scalp.

Due to the simplicity of the model (which was required for analytical tractability) there are a number of other differences between the model dynamics and that of the preterm EEG. Primarily, the bursts of activity in the model were not nested oscillations. Recent interest in nested oscillations in the computational literature has been inspired by the observation of nested theta/gamma oscillations in the hippocampus and other brain

regions which have been suggested to relate to memory [204–206]. Several models have therefore examined nested oscillations in neuronal populations where inhibition is though to play an important role [207, 208]. It would be interesting to extend this work to examine nested oscillations in purely excitatory populations to generate hypotheses of how such activity is generated in the preterm brain. This could then be combined with the current model to achieve a model of BNOs with LRTCs.

Additionally, the distribution of burst characteristics in the model appear to be different from those in the preterm EEG. This may be for several reasons. Firstly, as stated above the EEG is a measure of scalp electrical activity not neuronal firing. This could lead to a subsampling effect, which has been shown to change the appearance of distributions [209]. Secondly, as was described, particularly in relation to the amplitude of the BNOs, for low values the distribution was likely distorted by the extraction algorithm. On the other hand, this is perhaps due to the general differences we see between the model and the EEG (such as the long time difference between bursts in the EEG which is not found in the model when the bursts exhibit LRTCs) and an increase in biological realism may aid us in our understanding of these differences.

4.3.3 A critical discussion of the model

The model analysed in this chapter was a simple stochastic network. The network was fully connected, the synaptic weights were the same for all connections, the external input was the same for all neurons and simulations steps, and each neuron could be in one of two states. However, as pointed out by *Benayoun et al.*, "simple stochastic models may produce qualitatively the same network dynamics as more biophysically detailed models, while their simplicity enables them to give insight into the mechanisms of emergent phenomena" [61]. Indeed, the simplifications imposed on the model here enabled analytical analysis of the model and insights into the dynamics that might not have been obtained had a more complex model been analysed. Having used a greatly simplified model to understand a purely excitatory neuronal system it is possible with future work to adapt this model or apply the mechanisms to a more complex model so as to characterise the dynamics in a more biophysically realistic system.

The theoretical derivation of the distributions showed that the IAI and avalanche duration distributions are a weighted sum of hypoexponentials. However, the exponential timescales relates directly to the fact that simulations were carried out using the Gillespie algorithm which selects the time to the next event from an exponential distribution. This algorithm was chosen as it is an efficient method for simulating stochastic models [61]. If a different simulation method had been chosen then the resultant distributions may not have been hypoexponentials. However, they also may not have exhibited apparent power-laws. This result clearly shows that apparent

power-law distributions can result from data that is in fact not power-law distributed.

The binning method used to define avalanches in the simulations was the same used by *Benayoun et al.* and similar to the approach used in experimental data [49, 50] - see Appendix 3. This method separates consecutive spikes into different avalanches if they are greater than average firing rate apart. While this method is appropriate if the dynamics are such that avalanches are well spaced with high density firing within the avalanches, it is important to note that no matter what the firing dynamics 'avalanches' will still be defined using this approach. This was seen in the case with increased external input. In this case, the dynamics appear continuous but, as some spikes must be greater than the average firing rate apart (due to stochasticity in selecting the time to the next event in the Gillespie algorithm) these will necessarily be separated into distinct avalanches. Despite this separation this activity cannot really be described as bursts/avalanches of activity and care needs to be taken when using this approach.

Parameter tuning or SOC?

The model examined here involves parameter tuning to reach a state of balanced activity. It is therefore not a SOC model. Despite this it is possible that, if a balanced activity state does exist, an alternative SOC model of the brain during early development could be constructed that also reaches the same 'critical' state. Thus, this model should not be taken to discount the possibility that the brain is a SOC system. It is worth noting that the neuronal dynamics studied here are non-conserving and so if the same neuronal dynamics were used in a self-organising system this would lead to a SOqC state (see Chapter 1). In either case (the model presented in this chapter which was perturbed away from the critical state by the external input, or a SOqC system which also 'hovers' close to a critical point [58]) it is worth noting that from the experimental observations of neuronal avalanches the branching parameter was calculated as 1.04 ± 0.19 [49]. The fact that this value is not exactly 1 is of course most likely due to experimental noise (particularly as the branching parameter in experiments can only be estimated). However, it may be because the system is not actually exactly critical but only close to a critical point.

4.3.4 Extensions to the model

Throughout this chapter the network examined has been a fully connected system so as to be analytically tractable and enable the construction of the mean field equations. However, the real nervous system is not a fully connected network. As has been indicated by previous work, the topology of the network can have a large affect on its dynamics [168–171]. It is therefore of interest to investigate the dynamics for different

connection topologies and determine whether the burst dynamics can also be observed in these cases. This will be investigated in the next chapter of this thesis.

Another obvious extension to the model is to examine the effect of different types of input. In this chapter the external input has been a single tonic source equal for all neurons and at all simulation steps. Again, this will not be the case physiologically and it would be interesting to examine input which is not tonic and exhibits different temporal patterns (including LRTCs) as well as input which is different for different populations of neurons within the network. Such an extension is important in understanding the early developing brain where input to the cortex is from both sensory and spontaneously generated activity and is not continuous.

Another natural extension would be to add an explicit refractory period to the individual neuronal dynamics. While *Benayoun et al.* [61] suggest that the active period might be considered to incorporate the refractory period, it would be of interest to separate the two so that an understanding of the the importance of a refractory period within the dynamics of the system can be gained. Indeed, in the current model a neuron in the active period continues to affect the neighbouring neurons throughout its active period which would not be the case for a physiological neuron in the refractory period. The addition of an explicit refractory period may well have an affect on the dynamics, in particular on the waiting times between avalanches. A similar model with a refractory period was constructed by *Kinouchi and Copelli* [36] but this included set time steps and rates (the model was not stochastic). They also did not consider the temporal ordering in the activity. One of the limitations of the model investigated here is that the bursts occur on a much quicker timescale than the bursts observed in the preterm EEG. Therefore, in order to better represent the EEG dynamics the bursts must be slowed down while retaining the dynamics and correlations of burst occurrence. Adding a refractory period may be a way to achieve this.

Considering possible extensions to the model from a wider perspective, the dynamics of this model may be of interest in the field of epidemiology. The system studied here is essentially also the system studied in the epidemiology literature as a classical infectious disease model known as the *SIS, susceptible-infectious-susceptible* model [210]. In this model an individual can either be susceptible (in state S) or infectious (in state I). A susceptible individual becomes infectious at a rate dependent on the number of infectious neighbours it has (which is the same as a quiescent neuron becoming active dependent on the number of neighbouring active neurons it has) and an infectious individual goes back to the susceptible state at a set rate (α). Therefore this work may also be applicable to the epidemiology field, perhaps in examining recurrence of diseases within populations.

Chapter 5

Long-range temporal correlations and connectivity formation

5.1 Introduction

In the last chapter LRTCs were observed in the burst dynamics of a purely excitatory neuronal network model. For analytical tractability, the networks analysed were fully connected. However, a physiological neural network will not be fully connected[1]. Previous research (with other models) has shown that connection topology can have a large effect on the emergent dynamics of a network [168–171]. Intuitively, this can be easily understood. Consider the extreme example where a neuron has lost all its connections to other neurons within the network. Therefore (in our case) this neuron is only driven by the external input and so will fire less often. Similarly, if a particular neuron loses (or gains) connections it is likely to fire less (more) regularly. Additionally, particular connection topologies may lead to interesting spatial patterns. For example, if neurons are generally connected together in small 'sub-networks' then the neurons within these sub-networks are likely to fire together. This may then lead to distinct groups of firing which can be observed as spatial clustered bursts within the whole network firing dynamics.

In this chapter the model will be extended to examine the effect on the dynamics of different connection topologies. In particular, for different topologies we will ascertain whether it is possible for burst (avalanche) dynamics to occur and whether these avalanche dynamics exhibit LRTCs in the sequences of size, duration and IAI. The effect of connection topology has been considered by previous authors in relation to the branching parameter and power-law statistics [212–214]. However, no consideration has

[1] Except perhaps approximately for a small group of neurons with close proximity to one another [211]

been made of the effects of topology on LRTCs and whether networks with different topologies can exhibit this type of critical behaviour.

During the early preterm period the dominant developmental process is connectivity formation - both within the cortex and the formation of thalomocortical connections, at first via the subplate [65, 69]. Therefore, it is not only important to extend the model to examine more physiologically realistic connection topologies, but also to consider the dynamics as connectivity changes. Recall that in terms of the preterm EEG, despite the differences in cortical connectivity that occur during the period studied, all of the EEGs had discontinuous BNO activity and there was no change in the Hurst exponent of the BNO sequences with age. This would suggest that this type of dynamics can occur with different connection densities and possibly different connection topologies[2]. We will therefore also investigate the dynamics with changing connectivity. Can burst dynamics be maintained for different levels of connection density and as connections are updated? Extending this slightly further we can then ask, how do connectivity formation and activity interact? That is, how does connectivity update with respect to the system activity and in turn how does this altered connectivity affect the dynamics?

This type of question has led to a new area of research in the field of complex systems. Examining the dynamics of the system with different topologies can be referred to as examining the dynamics *on* the network, whereas examining changes in the connection topology (such as wiring rules based on preferential attachment [215] or rewiring [216]) can be described as the dynamics *of* the network [217]. Often only one of these types of network dynamics are investigated and it is not until recently that they have been investigated together. Networks which exhibit both types, where there is a feedback loop such that the topology of the network is tuned based on the dynamics on the network, are described as *adaptive* networks [217–219]. *Meisel and Gross* examined connectivity formation dependent on activity in a neuronal network model and showed that the model could 'self-organise' to a balanced connectivity level which is the same irrespective of the initial connectivity level [219]. In the second part of this chapter, we will extend the model to examine the adaptive dynamics of the network, considering connectivity formation as a function of the dynamics of the network.

An adaptive model is crucial to understand the developing nervous system. As was discussed previously activity-dependent mechanisms play a crucial role in connectivity formation. During the early preterm period external input is via the subplate [6, 8] and it is thought that subplate activity generates the delta waves observed (as part of the BNO activity) on the preterm EEG [97]. Previous experimental research examining the effect of bursts of activity on connectivity development has investigated the effect of preventing or reducing the activity [18, 73, 74]. These results showed that

[2]To my knowledge the topological characteristics in the early developing brain have not been investigated. This would certainly be a question worthy of study in the future.

thalamocortical connections are weaker and cortical patterning is altered if activity has been reduced. These results therefore imply that the activity itself is important for development. Fish reared in an environment with only synchronous visual input have an altered topographic map [220] and periodic pulses of electrical stimulation to the ferret optic nerve, leading to the synchronous activation of retinal ganglion cells, result in weaker orientation selectivity of neurons in the cortex [221]. Therefore, it seems that disrupting the temporal patterning of activity can have a detrimental effect on connectivity. Completely synchronous input leads to problems in connectivity formation, but in a different way to silencing the activity altogether. However, no consideration of the overall temporal patterning (i.e. LRTCs compared with random temporal correlations) has been made. This question lends itself to analysis using a computational approach where the temporal dynamics of processes can easily be altered. We will analyse the effects of LRTCs on connectivity formation, comparing this with randomly shuffled processes.

A number of computational models have been constructed by other authors to examine network connectivity formation in early development. Models examining axonal growth through molecular gradients have been extensively studied, see for example [222, 223]. Other authors have examined morphology of the developing neuron, for example neurite branching [224, 225], producing realistic cell morphologies from rules based on within cell factors such as the level of microtubules. Many of these factors are regulated by Ca^{2+} concentration which in turn is regulated by the activity of the neuron and the surrounding cells [226]. Therefore, there is a clear connection between these models and activity-dependent development. Several models have taken a more direct approach to examining the effect of activity dependence. A simple model of connectivity formation, with growth and retraction of dendritic and axonal 'fields' based on neuronal activity, leads to an equilibrium in connectivity (after an initial overshoot in the number of connections) [226, 227]. Interestingly, at the equilibrium connectivity level the network exhibits neuronal avalanches [228]. As described above *Meisel and Gross* examined an adaptive model when investigating connectivity formation [219]. While the model analysed by *Meisel and Gross* was adaptive and so connectivity formation was activity-dependent, they did not take into account any specific temporal relationships of the activity. To my knowledge, no models have examined the effect of activity with LRTCs on connectivity formation. Given the observation of LRTCs in the preterm EEG during the main period of cortical connectivity formation, examining the effect of LRTCs on connectivity formation will lead to an understanding of this complex temporal activity pattern in the developing brain. Specifically, can connectivity patterns that are seen in the more mature brain emerge from random networks when they are subjected to external input which exhibits LRTCs?

5.2 Extending the model - the interplay between connectivity and model dynamics

5.2.1 The effect of connection topology on network dynamics

Two different topologies will be investigated in this section: *random* and *small-world*. A random network is perhaps the simplest topology and the most straightforward extension that can be made. On the other hand, there is evidence that the brain has a small-world architecture [216, 229–232] and so this structural topology increases the physiological realism of the model. A *small-world* network is one which is highly clustered but which also has a few long range connections (between clusters) which enable fast communication between the clusters [216]. Thus, small-world networks are thought to be important for brain function as they permit efficient integration and segregation of information [229, 232, 233]. Measures used to determine whether a network has a small-world topology will be discussed below.

Note: all the networks constructed in this chapter will be directed, i.e. each connection has a pre-synaptic neuron and a post-synaptic neuron and there will not necessarily be a connection in both directions (although this is a possibility). The networks are directed as physiological neuronal networks also have a clearly defined direction of communication with a pre-synaptic and post-synaptic neuron at every synapse.

Dynamics on a random network

Random networks are constructed by connecting any two nodes with a set probability, where the probability relates to the number of connections required within the system. Any two nodes have the same probability of connection. This type of graph is also known as an Erdős-Rényi network [234].

Fig. 5.1 shows simulations of the network dynamics for a random network of size $N = 800$ and parameters described as 'critical' in the previous chapter. Four different levels of connectivity were simulated. As can be seen, as the connection density decreases the firing became sparser and the burst like appearance of the dynamics disappears.

Of course upon decreasing the number of connections in relation to the number of neurons the dynamics of the network are likely to change - with fewer presynaptic neighbours a quiescent neuron is less likely to enter the active state and vice versa: an active neuron is less likely to activate a post-synaptic neighbour. The model can no longer be fully described by the mean field equations as it is not a fully connected

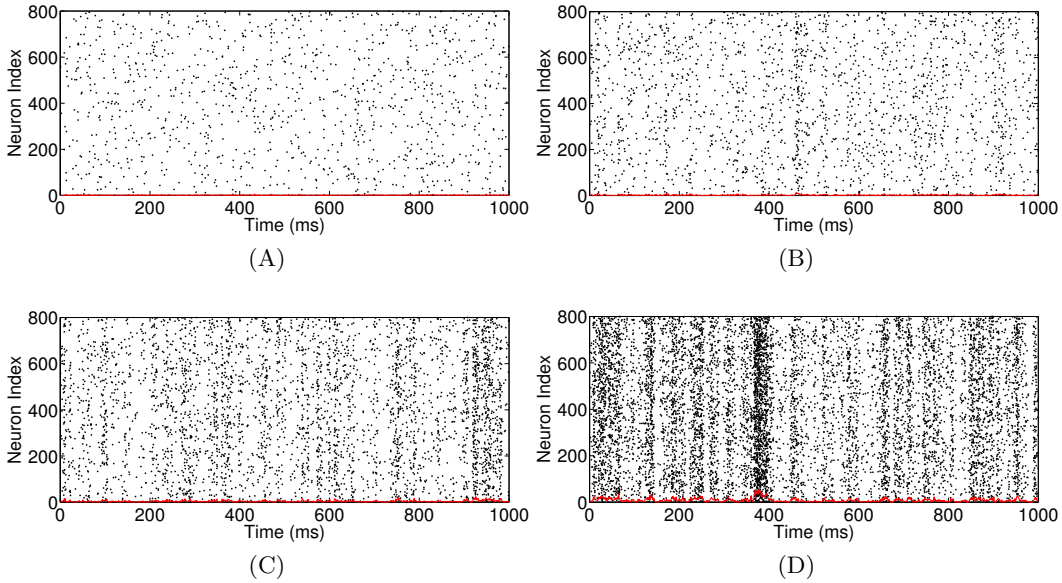

Figure 5.1: Simulations of the excitatory stochastic network (as in Chapter 4) but with random network topology. For all four simulation $N = 800$, $\alpha = 1$, $w = 1$, $h = 1/N$. (A) 10% connectivity, (B) 50% connectivity, (C) 75% connectivity and (D) 90% connectivity. The red line (which in some cases is at very low levels and so close to the line y=0) indicates the rate of firing binned in 1 ms intervals.

network and so the neurons do not have the same numbers of connections[3]. However, the mean field equations and the analysis in the last chapter can perhaps be used to inspire the analysis here if we consider an 'average' neuron (i.e. a neuron with an average number of connections). In the previous simulations of the fully connected system, burst dynamics were observed for parameters close to points such that the branching parameter was equal to 1. Reconsidering the dynamics of the fully connected network for parameters far away from the critical state (for example, when the parameters are such that the network is subcritical) we also observe a loss in the bursting behaviour, see Fig. 5.2, similar to that at low connection densities. Thus, it seems likely that the lower connection density has pushed the system far away from the critical point. How has this occurred? Previously, with $w = 1$, given a single active neuron (and ignoring the external input) on average 1 new neuron would be activated. Thus, the branching parameter was equal to 1. However, if the connectivity is a proportion p of this fully-connected network level then on average only $p < 1$ neurons are activated from this single neuron. For example, if a neuron has 80 connections in a network of 800 then on average this pre-synaptic neuron would have to activated 10 times before it activated a single one of its post-synaptic targets. Thus, the branching parameter is lower than one (the dynamics are sub-critical) and the activity in the

[3]The mean field equation describes the rate of change of a quiescent neuron into the active state based on the number of active neurons in the network. This is therefore only an accurate description if the quiescent neurons are connected to all of those active neurons - which occurs when the network is fully connected.

network is no longer balanced, see also the example in Fig. 5.3. If burst dynamics are related to a critical state (i.e. if they are an emergent behaviour related to a critical state) then this explains the loss of burst dynamics.

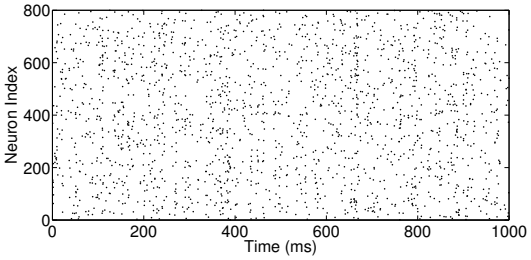

Figure 5.2: Firing dynamics in the fully connected network with the branching parameter far from the critical value. The parameters were set as $N = 800,\ w = 1,\ \alpha = 2 \Rightarrow \sigma = 0.5$ and $h = 1/N$. For this subcritical branching parameter there are no apparent bursts within the dynamics, similar to the dynamics of the network with low connection densities - see Fig. 5.1.

Therefore, it seems plausible that retuning the parameters for the networks with lower connection densities so as to achieve a branching parameter equal to 1 will also lead to bursting dynamics within these networks. As the network is not fully connected the mean field equations cannot be used and it is not possible to derive the fixed point and branching parameter directly. However, intuitively from the above description it seems likely that tuning w in relation to the proportion of connections will once again lead to a branching parameter close to the critical level and so the emergence of burst dynamics, see the example in Fig. 5.3. Fig. 5.4 shows network simulations with the same topologies as those in Fig. 5.1 but with $w = 1/p$ where p is the proportion of connections in the network - in this way for each network the branching parameter is set (close) to 1 (note that this is effectively the average branching parameter for the overall network - individual neurons may have more or fewer connections than the average leading to them on average activating more or fewer postsynaptic neurons on average). From the simulations it can be seen that changing the synaptic weights as described has a dramatic effect on the network dynamics and burst activity is present even for the lowest connection density.

For each of these connection densities (and with $w = 1/p$) the firing dynamics were simulated for 100 seconds and the summary statistics for the IAIs, avalanche size and avalanche duration are shown in Table 5.1. Fig. 5.5 shows the IAI, size and duration distributions for each of the connection densities, pooled across five simulations of networks of that density. The distributions for different densities coincide well with each other. These distributions are also similar to the distributions seen for the fully connected network with the same level of parameters as the simulations here (i.e. $h = 1/N,\ \alpha = 1,\ w = 1$). The IAI distribution appears straight on this scale, whereas both the size and duration distributions appear curved indicating a superposition of avalanches, as was discussed in Chapter 4.

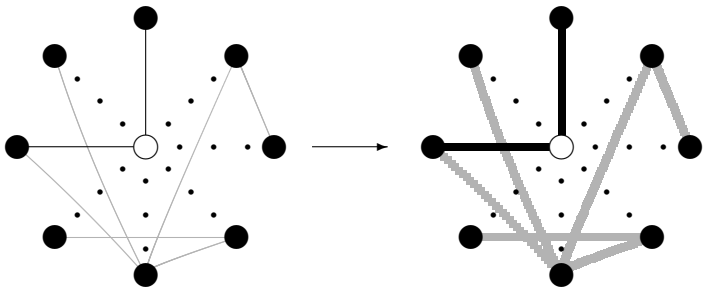

Figure 5.3: Schematic of the change required in the synaptic weights to re-balance network activity in a network which is not fully connected. Suppose that the central neuron (shown as a white circle) is active. There are no other active neurons within the network. This neuron is connected to two other neurons as indicated by the black lines (left plot). If the network were fully connected then the neuron would be connected to the other neurons as indicated by the dotted black lines. Let the synaptic weights be given by $w = 1$. In this case each neighbouring neuron has a probability equal to $\frac{w}{N} = \frac{1}{9}$ of becoming active. If the network is fully connected then, as there are 8 neighbouring neurons, this means that on average 1 will be activated each time the central neuron is active. Now suppose the connectivity is as shown. With $w = 1$ the probability of either of the two neurons becoming active is still $\frac{1}{9}$. This means that there is a probability of $\sim \frac{1}{4}$ of either becoming active and so the central neuron needs to be activated 4 times before it will activate a single one of its neighbours - the branching parameter is less than 1. Suppose therefore that the synaptic weights are increased (right plot - increase of synaptic weights indicated by increase in the thickness of the lines). Let $w = 4 = 8/2 = 1/p$, i.e. the inverse of the proportion, p, of connections within the network. Then, on average, each time the central neuron is activated the probability of each of its neighbours entering the active state becomes $\frac{w}{N} = \frac{4}{9}$ and so now on average each time the central neuron is activated it will activate one of its two neighbours - the branching parameter is approximately one. (Note that in this case the probability is slightly less than 1 but this is related to the small size of the network and the fact that a neuron cannot connect with itself. This difference decreases as the network size increases and we are examining much larger network sizes in simulation.) For simulations all synaptic weights were changed according to the average connectivity within the network. Thus, all other connection strengths are increased in the same proportion as indicated here by the grey lines which show connections between other neurons.

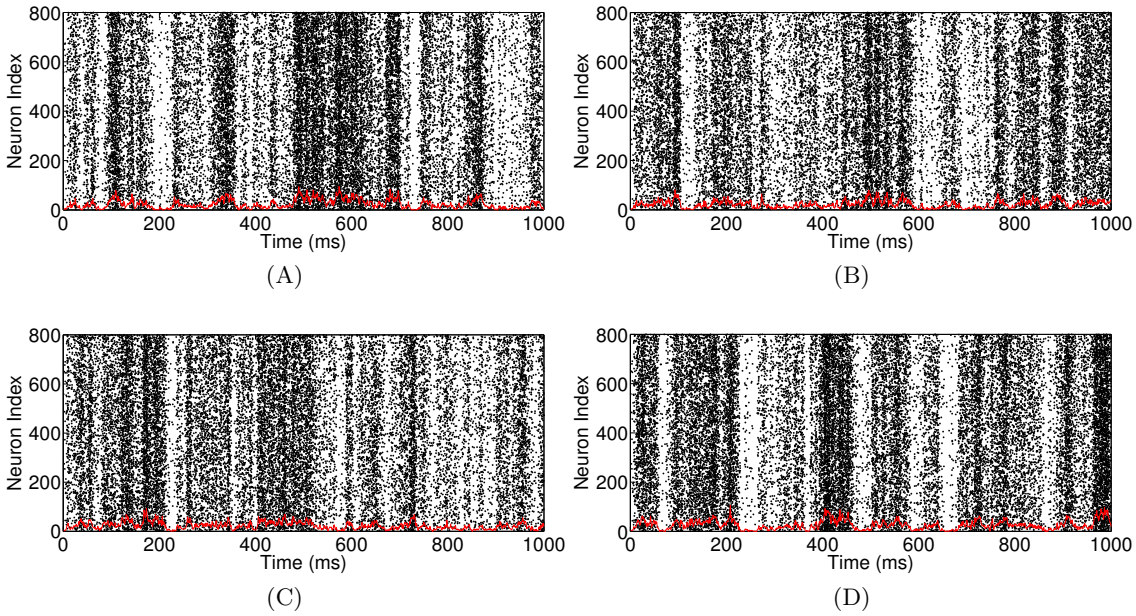

Figure 5.4: Simulations of the same networks (with the same topologies) as in Fig. 5.1 but with the synaptic weights changed in proportion to the level of connectivity, $w = \frac{1}{p}$. (A) 10% connectivity $\Rightarrow w = 10$, (B) 50% connectivity $\Rightarrow w = 2$, (C) 75% connectivity $\Rightarrow w = 4/3$ and (D) 90% connectivity $\Rightarrow w = 10/9$. The red line indicates the amount of firing binned in 1 ms intervals.

The DFA and Whittle exponents for the sequences of avalanche size, duration and IAI were also calculated, see Table 5.2. The DFA plots had a single crossover, with the linear trend for box sizes above this crossover indicating Hurst exponents close to 0.5. The table shows the average of the exponents from the lower region below the crossover point (averages across 5 simulations). The presence of only a single crossover point may relate to the shorter simulations carried out here compared with those in the last chapter. For all networks the exponents indicated LRTCs in the data suggesting that the dynamics on a random network can exhibit burst dynamics with (partial) LRTCs when the synaptic weight is tuned to relate to the number of connections within the

	Avalanche size			Avalanche duration			IAI		
Density	Mean	Min.	Max.	Mean	Min.	Max.	Mean	Min.	Max.
10%	3.60	1	394	0.046	0	4.03	0.13	0.048	7.55
50%	3.59	1	302	0.042	0	2.71	0.12	0.045	11.12
75%	3.58	1	296	0.042	0	3.03	0.12	0.042	8.07
90%	3.56	1	302	0.040	0	2.66	0.11	0.043	8.45

Table 5.1: Summary statistics for networks with different connection densities. Network parameters were $N = 800,\ \alpha = 1,\ h = 1/N,\ w = 1/p$ where p is the proportion of connections (across the whole network). Avalanches were determined using the binning approach of *Benayoun et al.* [61] as in the last chapter. The simulation length was 100 seconds and averages were taken across 5 simulations. The overall distributions from these simulations are shown in Fig. 5.5. Recall that an avalanche duration of 0 indicates a single neuron firing.

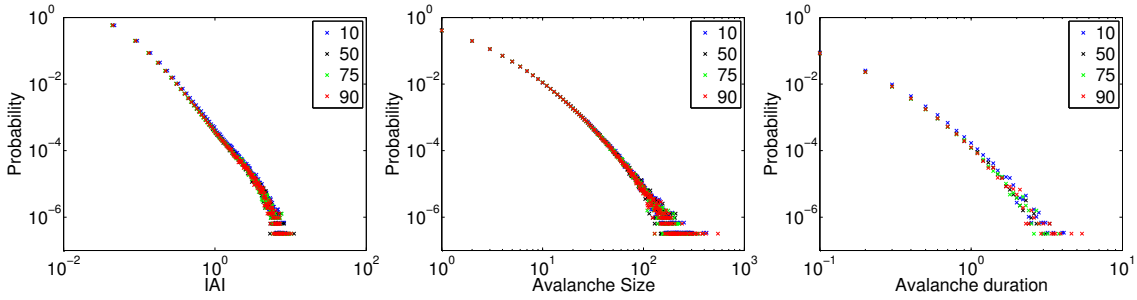

(A) (B) (C)

Figure 5.5: IAI (A), avalanche size (B) and avalanche duration (C) distributions for the simulations of the random networks with different connection densities (as indicated in the legends). Distributions for each connection density are pooled from 5 simulations. The IAI distribution appears linear over a range of scales and the slope of the line of best fit for all connection densities is ~ 2.6. The distributions overlay well with each other and are also similar to the distributions (with $h = 1/N$) of the fully connected network shown in Chapter 4.

network so that the (average network) branching parameter is equal to 1.

Connection	DFA exponent			Whittle exponent		
Density	IAI	Size	Duration	IAI	Size	Duration
10	0.82	0.88	0.86	0.73	0.75	0.72
50	0.82	0.88	0.86	0.74	0.74	0.70
75	0.83	0.88	0.86	0.74	0.74	0.71
90	0.82	0.88	0.86	0.76	0.73	0.70

Table 5.2: DFA and Whittle exponents for the sequences of avalanche sizes, duration and IAI from the random networks with connection density as indicated. Synaptic weights were set to $w = 1/p$ where p is the proportion of connections. There was a single crossover in the DFA plots and the lower exponent (averaged across the 5 simulations) is given here. The upper exponent was approximately 0.5.

Dynamics on a modular network

Define a modular network as one which can be divided into a number of modules, where each module is fully connected and inter-module connections are sparse and random. The random inter-module connections allow for fast communication between modules while the modules themselves are highly clustered as they are fully connected and so this representation is an example of a small-world network. Let m be the number of modules and N_m the number of neurons in the the module. For simplicity, all modules were set to be equal in size so $N = mN_m$.

Fig. 5.6 shows the connectivity of an example modular network compared with a random network of the same connectivity level. Two statistics that can be used to quantitatively assess a network's topology are the *clustering coefficient* and the *average path length*. These are defined as follows.

- For an undirected network the *clustering coefficient* is defined as the ratio of the number of triangles to the number of connected triples, where a triangle is any three completely connected *nodes* (in our case neurons) and a triple is three nodes where at least one node is connected to the other two. For a directed network, the definition is equivalent but the direction of connections must be taken into account, see [216, 235]. Thus, the clustering coefficient examines how likely any two neighbouring neurons of a single neuron are themselves likely to be connected.
- Given any two nodes in a network, the *(shortest or geodesic) path length* between them (also known as the distance between them) is the length of the smallest path needed to be traversed when going from one to the other (note that in a directed network the directions also need to be taken into account). The *mean (average) path length*, also known as the diameter of the network, is defined as the mean distance between all nodes in the network [216, 235].

Small-world networks have a higher clustering coefficient than a random network with the same number of connections, but the average path length of the two networks will be approximately equal [216]. As expected the clustering coefficient of the modular network shown in the Fig. 5.6 is much higher than that of the random network (0.97 and 0.25 respectively) while the average path lengths are approximately equal (1.85 and 1.75 respectively). These values were calculated using code available from the Brain Connectivity Toolbox [236].

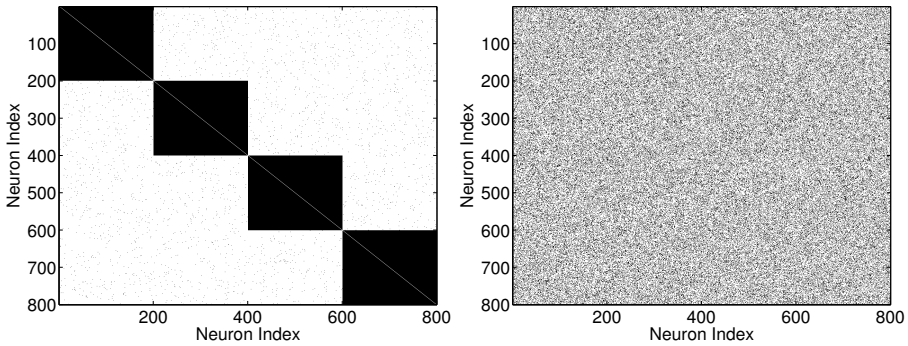

(A) (B)

Figure 5.6: (A) Example of the connectivity within a modular network with $m = 4$ modules. Each module is itself fully connected. Inter-module connections are random and in this network there is on average 1 connection per neuron in any module to any of the other modules. This plot is read as the neuron index along the x and y axis so that if there is a connection between neuron i and neuron j the point (i, j) is black. (B) A network with the same number of connections (on average 203 per neuron) but random connectivity.

Fig. 5.7 shows simulations of firing dynamics for modular networks. Networks with four different connectivity levels of the random inter-module connections are simulated, including the network whose topology is shown in Fig. 5.6. The synaptic weights were (as with the random network topology) weighted according to the proportion of

connections within the network: $w = 1/p$. For a low density of inter-module connections (at an average of around 1 or fewer connections per neuron to a neuron in each of the other module) the dynamics of each module exhibit burst behaviour which are generally distinct between the modules. As the inter-module connection density is increased this distinction between the modules becomes less apparent.

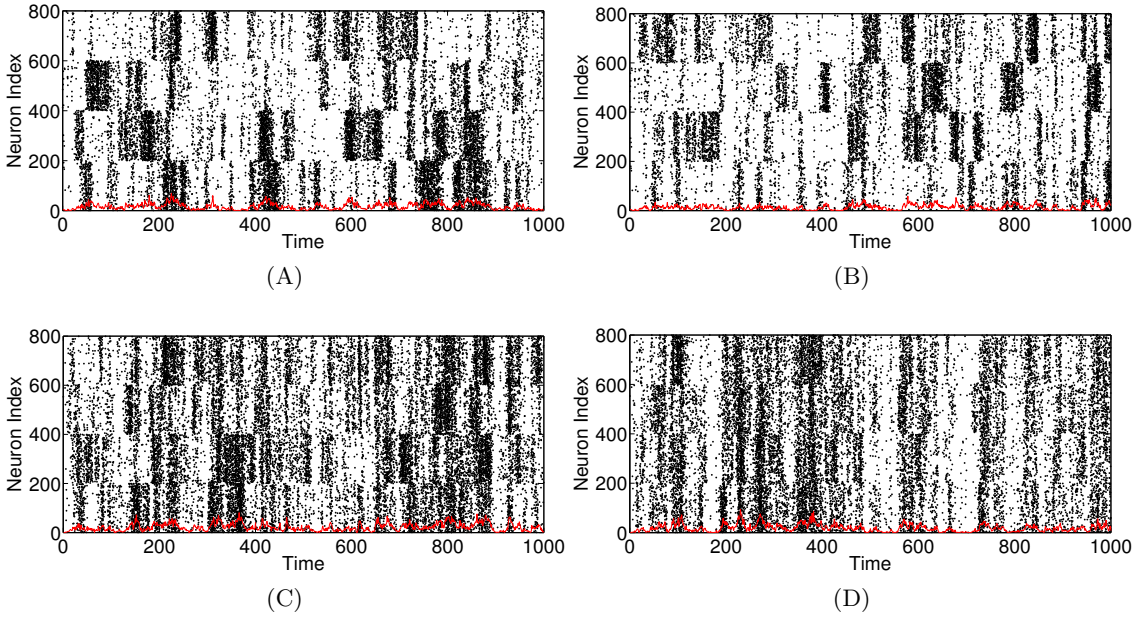

Figure 5.7: Simulation of dynamics on a modular network. For all four simulations $N_m = 200,\ m = 4,\ \alpha = 1,\ h = 1/N$ and $w = 1/p$ where p is the proportion of connections (on average) that a neuron makes to post-synaptic neurons. Within each module neurons were fully connected. From one module to each other module each neuron made an average of (A) 0.5, (B) 1, (C) 5 and (D) 10 connections. For low density inter-module connections each module has distinct behaviour. For a connectivity level of only $10/200 = 5\%$ between modules, as in (D), this distinction is not so apparent. The red line indicates the amount of firing binned in 1 ms intervals.

Longer simulations were carried out for each of the four connection densities. Avalanches were then defined on a per module basis (i.e. clusters of firing within a single module) and summary statistics for the avalanche characteristics are given in Table 5.3. With higher connection densities between modules the IAIs decrease as do the avalanche sizes and durations. Probability distributions for the avalanche characteristics for the different connections are shown in Fig. 5.8. As the connection density increases there is a decrease in all three characteristics most apparent in the IAI distributions. This change can be understood by examining the raster plots of the firing dynamics, Fig. 5.7. Considering a single module, for low connection densities the activity will be less likely to be affected by other modules leading to longer IAIs. However, as the synaptic weighting takes into account all connections within the network $w >> 1$. Therefore, when an avalanche is initiated within a module it is likely to last longer than for a fully connected network as the within module branching parameter is effectively super-critical. None of the distributions appear to exhibit a power-law, including the IAI

distributions which appear to have a slight 'bump' at large IAI values. However, as the connection densities is increased the bump is not as clear. This may reflect the fact that with a higher number of connections between the modules, the dynamics of the modules are less distinct (see Fig. 5.7) and the avalanches themselves are less segregated.

Connection	IAI			Avalanche size			Avalanche duration		
Number	Mean	Min.	Max.	Mean	Min.	Max.	Mean	Min.	Max.
0.5	1.18	0.24	25.98	6.11	1	484	0.36	0	21.74
1	1.16	0.25	32.47	5.85	1	651	0.36	0	28.21
5	0.76	0.21	22.76	4.69	1	345	0.25	0	17.47
10	0.64	0.20	19.42	4.23	1	284	0.22	0	11.39

Table 5.3: Summary statistics for the modular networks with different connection densities (an average of 0.5, 1, 5 or 10 connections per neuron to neurons within each of the other modules). Avalanches were determined for individual modules and average statistics calculated across all four modules.

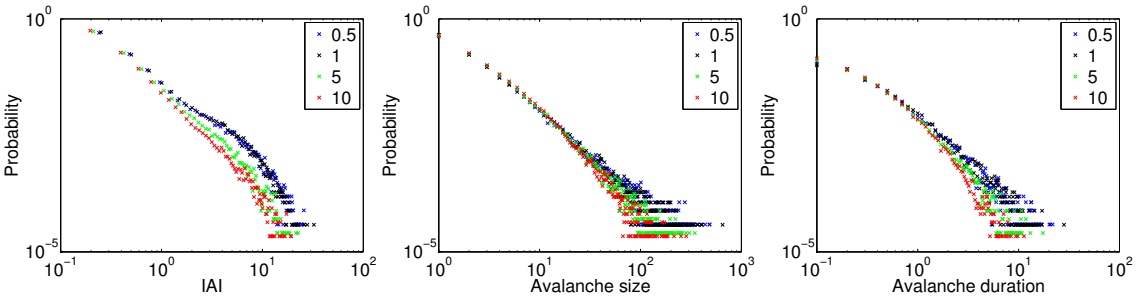

Figure 5.8: Probability distributions for IAI, avalanche size and duration for the modular network with different average numbers of connections per neuron to the other modules (as indicated in the legends). Avalanches were determined for each of the four modules separately using the standard binning approach and the distributions pooled from all the modules. The simulations lasted for 100 seconds.

On a per module basis the DFA and Whittle exponents were also calculated for the sequences of the avalanche sizes, durations and IAIs. DFA exponents again appeared to exhibit a single crossover, with the linear trend across box sizes above the crossover indicating a Hurst exponent of approximately 0.5. Summaries of the exponents for the box sizes below the crossover for different connectivity levels are listed in Table 5.4. Again the exponents indicated LRTCs within the burst dynamics.

Dynamics on a non-modular small-world network

Though modular networks are a type of small-world network, it is possible for a non-modular network to be a small-world network. For example, if neurons are arranged on a spatial configuration such as a ring and connected with outgoing connections to their k nearest neighbours and additionally a small proportion of these connections are

Connection Number	DFA exponent			Whittle exponent		
	IAI	Size	Duration	IAI	Size	Duration
0.5	0.70	0.68	0.73	0.66	0.68	0.70
1	0.70	0.71	0.71	0.66	0.67	0.69
5	0.71	0.76	0.73	0.68	0.70	0.70
10	0.75	0.72	0.74	0.69	0.71	0.70

Table 5.4: DFA and Whittle exponents of the sequences for each of the avalanche characteristics from each module separately. Neurons had an average number of connections of 0.5, 1, 5 or 10 to neurons to each of the other modules. Exponents indicated are averages across the four modules for each simulation. DFA exponents are from the lower region of box sizes below the crossover point.

randomly chosen and re-wired to form 'long-distance' connections (i.e. connections to neurons other than those that are their neighbours) then this network is clustered and has a low path length, i.e. it is a small-world network [216] - see Fig. 5.9. Our interest in this network stems from the fact that the clusters overlap to a much greater degree than in the modular network. Will spatially distinct bursts still be observed? Or will this overlap lead to whole network avalanches (i.e. avalanches that are not spatially well-defined, though they may not involve all neurons within the network) as in the random and fully connected case?

Figure 5.9: **Figure removed from online version of the thesis due to copyright - see *Watts and Strogatz* [216].** (A) The rewiring procedure for creating a small-world network. Starting from a regular network with all neurons connecting to their nearest neighbours (in this case the four nearest neighbours with two either side of the neuron) a small proportion p of the connections are randomly rewired leading to long-range connections. For high proportions of rewiring the network generated has a random topology. (B) The clustering coefficient, C, and mean path length, L, normalised by the values for a regular network and plot against the proportion of rewiring p. For low levels of rewiring the network exhibits a high clustering coefficient and a low mean path length indicative of a small-world network. Figures from *Watts and Strogatz* [216].

An example of a connectivity matrix of a network with such topology is shown in Fig. 5.10. The clustering coefficient for this network was 0.69 and the mean path length was 1.76. As would be expected the mean path length is similar to the values of the random and modular network (of the same size and same number of connections, see above). The clustering coefficient was smaller than the modular network but much larger than the random network. This indicates that the network has small-world topology (as was desired). Fig. 5.10 also shows an example of the simulated dynamics on this network. Unlike in the case of the modular network, there are no clearly defined spatial clusters, though occasionally bursts appear denser in some network areas.

Perhaps these clusters of firing will become better defined as the connection density is varied, as this will vary both the size of the neighbourhoods of the neurons and the number of long-range connections across the network? Fig. 5.11 shows the firing dynamics for small-world networks with four different connection densities. Indeed, as the number of connections per neuron decreases clusters of firing dynamics become much

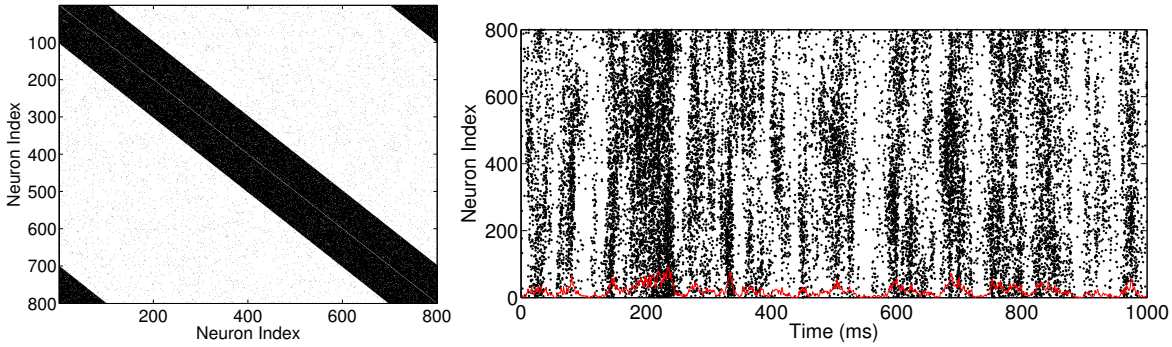

(A) (B)

Figure 5.10: Non-modular small-world topology. (A) An example of the connectivity matrix for a small-world (non-modular) network. Overall connection density for this network was the same as the networks in Fig. 5.6, whose density was an average of $k = 203$ connections per neuron. Connections were made with 203 of the 204 nearest neighbours (102 on each side with the neurons arranged on a ring) and then a random proportion of up to 0.05 of these were rewired to form long-range connections (algorithm for construction of this type of small-world network from *Watts and Strogatz*, 1998 [216]). (B) Raster plot of the firing dynamics for this network with $\alpha = 1,\ h = 1/N,\ w = 1/p$ where $p = k/N$. The red line indicates the amount of firing binned in 1 ms intervals.

more defined. What is interesting about this type of network as well is that, in contrast to the modular network, as the neighbourhoods of the neurons overlap significantly the clusters of firing involve different neurons rather than the distinct modules.

Table 5.5 shows the summary statistics for the avalanche characteristics. Avalanches were defined in these simulations using the usual approach - binning across the whole network. Fig. 5.12 shows the distributions of the data for the different connection densities. The overall distributions appear to have similar shapes to the distributions of the fully connected and random networks, with the IAI distribution exhibiting a linear relationship over a range of scales. Interestingly, there is a decrease in both IAI and duration as connection density increases but there is not such an apparent difference in the distribution of avalanche sizes.

Connection	IAI			Avalanche size			Avalanche duration		
Density	Mean	Min.	Max.	Mean	Min.	Max.	Mean	Min.	Max.
20	0.31	0.12	9.47	3.59	1	569	0.11	0	12.25
50	0.21	0.078	12.93	3.62	1	487	0.074	0	7.76
100	0.16	0.060	10.93	3.62	1	498	0.058	0	7.36
300	0.12	0.046	8.85	3.60	1	474	0.045	0	4.89

Table 5.5: Summary statistics for avalanches from the small-world (non-modular) networks for different connection densities. The avalanches were defined using the usual binning method across the whole network. Averages were taken across 5 simulations for each connection density.

The DFA and Whittle exponents for the sequences of avalanches characteristics are shown in Table 5.6. The exponents once again indicate the presence of LRTCs in the sequences of all the avalanche characteristics.

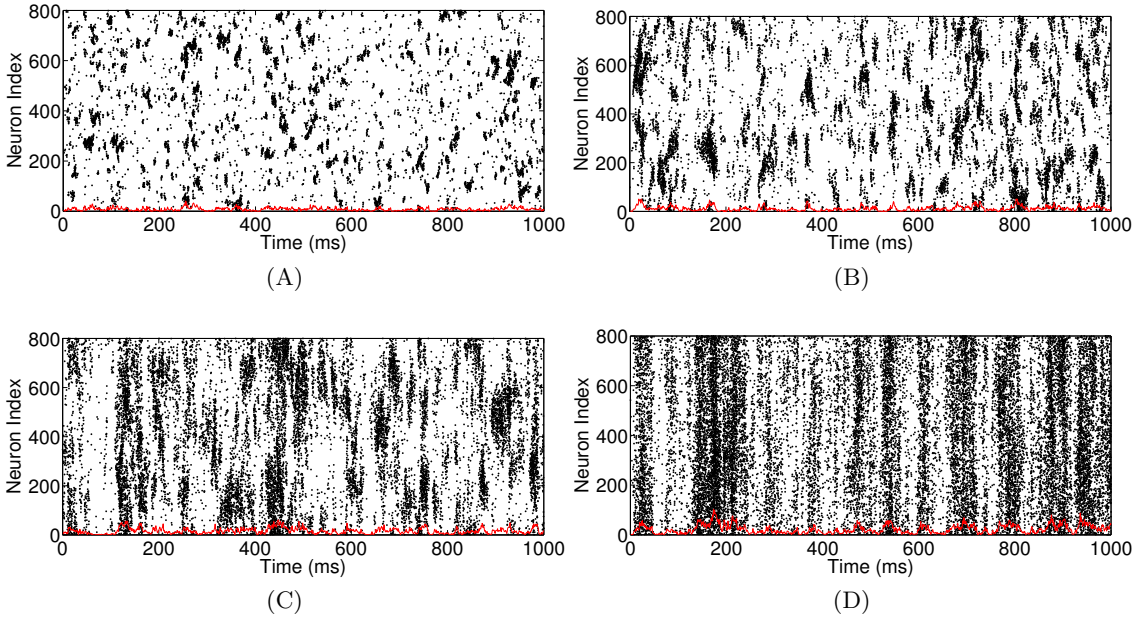

Figure 5.11: Raster plots for simulations of a small-world network for different levels of connection density. (A) $k = 20$, (B) $k = 50$, (C) $k = 100$ and (D) $k = 300$ where k is the number of outgoing connections per neuron. For all simulations $N = 800$, $\alpha = 1$, $h = 1/N$, $w = 1/p$ where $p = k/N$. The red line indicates the amount of firing binned in 1 ms intervals.

In summary, in this section three different connection topologies were examined. It was seen that adapting the synaptic weights to $w = 1/p$, where p is the proportion of connections in the network, on average balances the activity such that a single active neuron activates a single postsynaptic neighbour. With this parameter rescaling, bursts were observed in the dynamics of all three connection topologies. In the case of the modular network, for low numbers of inter-module connections the bursts were spatially segregated within the modules. Similarly, in a non-modular small-world network, for low connection densities, the bursts appear spatially clustered (despite the overlap in clusters within the connectivity itself). For all three connection topologies LRTCs were also observed (up to a crossover). Thus, a purely excitatory network can produce

Connection	DFA exponent			Whittle exponent		
Density	IAI	Size	Duration	IAI	Size	Duration
20	0.74	0.80	0.78	0.71	0.73	0.71
50	0.78	0.84	0.82	0.72	0.75	0.72
100	0.80	0.86	0.84	0.74	0.78	0.74
300	0.82	0.88	0.86	0.74	0.76	0.72

Table 5.6: DFA and Whittle exponents for the avalanche data sequences of the non-modular small-world networks. Avalanches were defined by binning the firing activity across the whole network. A single crossover was observed, with Hurst exponents for box sizes above the crossover of approximately 0.5. The exponent listed here is that of the lower box sizes, below the crossover point. Whittle exponents were analysed across the first 10,000 points. Averages were taken across 5 simulations for each of the connection densities.

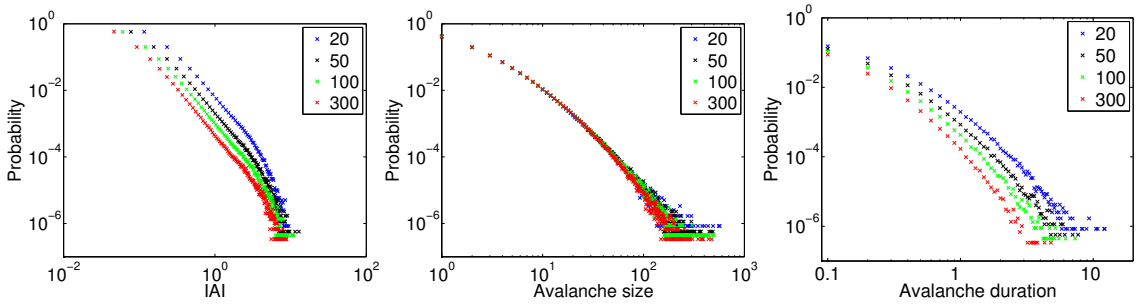

(A) (B) (C)

Figure 5.12: Distributions of the avalanche characteristics for the small-world (non-modular) networks for different connection densities (as indicated by the legends). For each of the IAI distributions the slopes of the lines of best fit are 2.62, 2.57, 2.52, 2.44 in order of increasing connection density. The distributions are pooled from five simulations.

spatially and temporally confined bursts of activity given particular (physiologically realistic) network topologies and a balance in the activity. These bursts exhibit temporally complex dynamics, as was observed in the preterm EEG recordings.

5.2.2 Connectivity formation

During the period of early brain development covered by the EEG recordings examined in this thesis connectivity formation is the main developmental process of the cortex. Therefore, while the last section enabled an understanding of the adaptation required in the parameters to achieve 'critical' dynamics for different (physiologically realistic) topologies, given the developmental context of this work a more interesting question is to consider changing connectivity within a model. In this section we consider activity-dependent connectivity formation and specifically address whether LRTCs have an effect on connectivity formation. An adaptive model approach will be used so that connectivity changes based on activity within the network, which in turn updates the network dynamics.

Activity-dependent connectivity formation

In modelling activity-dependent connectivity formation we will be inspired by the idea that "cells that fire together wire together". This idea, a summarised form of Hebb's 1949 theory [237], implies that when the activity of one neuron regularly facilitates the activity of the other then the connection between the two will be strengthened. This concept underlies spike-timing dependent plasticity (STDP). STDP (in its simplest form) is a mechanism by which synaptic connection strengths are adjusted based on the relative firing of the presynaptic and postsynaptic neurons [31, 172, 238, 239]. So if a presynaptic neuron fires just before the postsynaptic neuron then the connection will be

strengthened. Conversely, if the presynaptic neuron fires just after the postsynaptic neuron then the connection weight decreases.

Here the interest is not with connection weights but with connectivity formation through the loss and addition of the synaptic connections themselves. After an initial outgrowth of the axons and dendrites, reorganisation and refinement of developing synapses is dependent on activity and this activity dependence is similar to STDP in that neurons that fire in a correlated manner retain their connections [173, 240–242]. Therefore, we will examine activity dependence through considering spike-timing. Hence our approach might be described as 'spike-timing dependent connectivity formation'. If a neuron spikes just before another neuron then a connection will be more likely to form/be retained between these neurons with the connection directed in the way in which the action potentials occur.

Let L be a matrix of values where $L(i,j)$ indicates the likelihood of losing/gaining a connection from neuron i (presynaptic) to neuron j (postsynaptic). $L(i,j)$ is modified by

$$L(i,j) = L(i,j) + A_P \exp\left(-\frac{\Delta t_i}{\tau}\right)$$

following a spike in neuron j, where Δt_i is the time since the last spike in neuron i, τ is a decay constant and $A_P > 0$ is the amplitude change when $\Delta t_i = 0$, and by

$$L(i,j) = L(i,j) - A_D \exp\left(-\frac{\Delta t_j}{\tau}\right)$$

following a spike in neuron i, where Δt_j is the time since the last spike in neuron j and $A_D > 0$ is the amplitude change when $\Delta t_j = 0$.

A connection from i to j is gained (if there is not already a connection present) when $L(i,j)$ increases beyond the threshold value g. A connection from i to j is lost when $L(i,j)$ decreases beyond the threshold value l. In order to better take into account temporal dynamics within the system (for example if two neurons only spike together rarely) the values of L decay with rate τ_L. Thus, at each time-step:

$$L(i,j) = L(i,j) \exp\left(-\frac{1}{\tau_L}\right)$$

The loss-likelihood was initially set to zero for all connections: $L(i,j) = 0\ \forall i,j$ and the thresholds for the gain and loss of a connection were $g = 3,\ l = -3$. As in *Song et al.* [243] depression was set to be slightly stronger than potentiation. We set $A_P = 1,\ A_D = 1.1$.

In this section the effect of LRTCs on connectivity formation is investigated by examining the effects of two different types of external inputs on connectivity formation

- the first input exhibits LRTCs whereas the second does not. The input is generated by thresholding a *fractional Gaussian noise process* as described in Appendix 1. This generates an input process that has 'up' and 'down' periods of activity, for which the sequence of periods (both up and down periods separately) exhibit LRTCs. The down periods were set to a value of $0.5/N$ and the up periods to $1.5/N$. Note that the down periods were not set to zero as if there is no external input to the particular system studied here and if the number of active neurons $A = 0$ then the simulation will stop. The function was also 'smoothed' across time so that the external input switches to the next value in the sequence every 1 ms. For example, if the fractional Gaussian noise (once thresholded) led to a sequence of points: $\{0.5, 0.5, 1.5, 0.5, \ldots\}/N$, then the external input would be $0.5/N$ for the first 2 ms, then $1.5/N$ for the next millisecond, then back to $0.5/N$ at the next millisecond and so on. This approach was used as, if the input was changed at each simulation step (for example the average simulation step from the simulation in Fig. 5.14(B) is 0.11 ms) then, as the Gillespie algorithm updates using an exponential time step, the LRTCs in the input would effectively be lost. An example of this input is shown in Fig. 5.13.

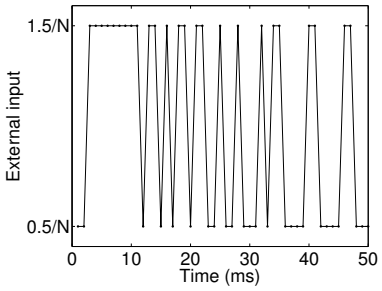

Figure 5.13: An example of the external input for 50 ms. The input is constructed by thresholding a fractional Gaussian noise process, see Appendix 1. This generates an input that has 'up' and 'down' periods, i.e. periods of higher and lower levels of the external input respectively. These periods exhibit LRTCs and were set to values of $0.5/N$ and $1.5/N$.

First let us investigate the firing dynamics attained with an LRTC input. Fig. 5.14 shows the raster plot of the network firing for the first and last second of two simulations. In the first simulation the synaptic weights are kept constant throughout. In the second simulation the synaptic weights are recalculated at each step in the simulation so that $w = 1/p$ where p is the proportion of connections throughout the network at each instance. This rescaling of the synaptic weights might be considered a form of global homeostatic plasticity[4]. As can be seen (and would be expected from the analysis of the previous section) the synaptic weight rescaling leads to burst dynamics continuing to occur throughout the simulation. It is also worth noting that these burst dynamics emerge with the LRTC input, as was the case previously with the constant

[4]The balance of activity within neuronal systems is maintained through a variety of homeostatic plasticity mechanisms that regulate both neuronal and circuit excitability. This theory was originally developed (and shown experimentally) to explain why other plasticity mechanisms such as STDP do not lead to 'run'away' increases in synaptic strength [244].

external input.

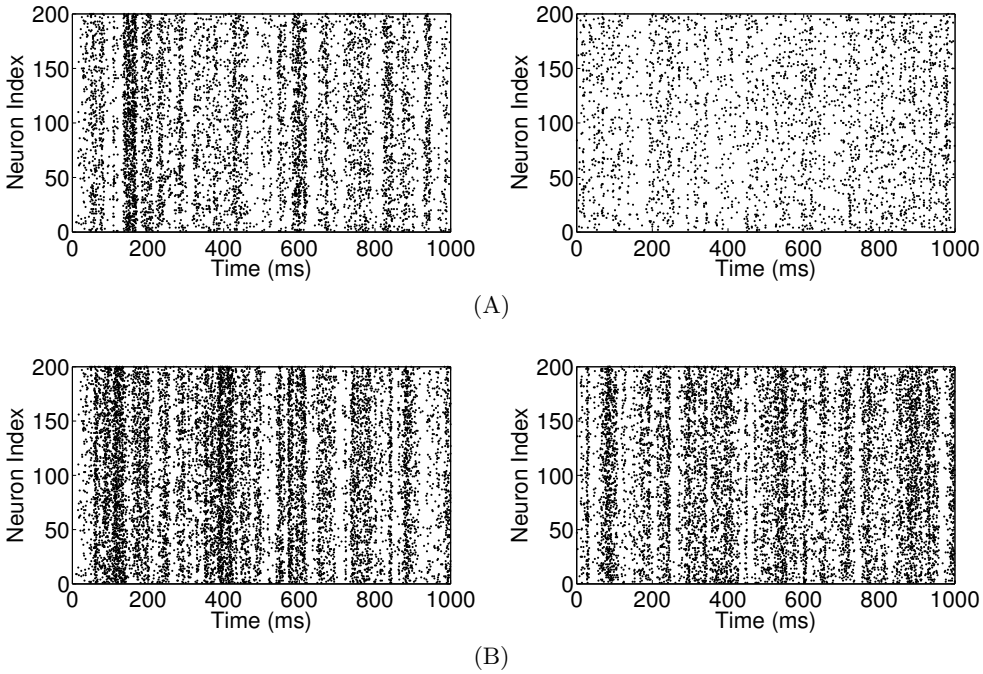

Figure 5.14: Raster firings plots for a network which is initially fully connected and for a simulation with (A) constant synaptic weights $w = 1$ throughout, (B) synaptic weights updated at each simulation step $w = 1/p$, where p is the proportion of connections within the network at that instance. For each, the left hand-side plot shows the first second for the simulation and the right hand-side shows the last second of the 50 second simulation. For both simulations $\tau = 5$ and $\tau_L = 100$.

Fig. 5.15 shows the change in proportion of connections across time for different values of τ, the spike-timing decay constant, and τ_L the decay in the loss-likelihood values over time. Higher values of both these decay constants appear to lead to higher proportions of connections in the network. For higher values of τ the effect of a neighbouring spiking neuron on another neuron lasts across a wider range of time differences and so more changes in the connectivity are likely to occur in a shorter time window. Similarly for higher values of τ_L, L decays at a slower rate and so is more likely to cross the threshold for the gain (loss) of a connection.

We now investigate changes in the connectivity for the two different external inputs - input with LRTCs and the same input randomly shuffled (shuffling the 'up' and 'down' periods not the individual values of the input at each time step). We employ the approach of random shuffling as in this way other aspects of the input, such as the length of the 'up' and 'down' periods, remain constant and only the temporal ordering is changed. Fig. 5.16 shows the change in the proportions of connections for five simulations with each of the inputs for two different parameter sets. Though there is individual variation between the simulations, there is no apparent difference between the simulations with the two types of input. Why might this be the case?

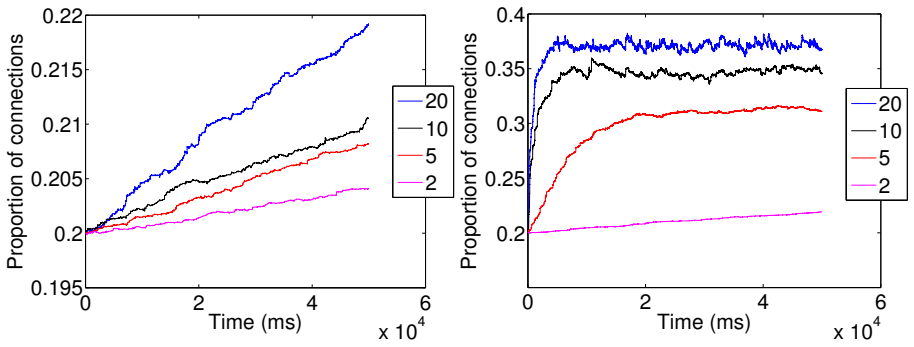

Figure 5.15: (A) The change in proportion of connections over time for different decay constants for the spike-timing. $\tau_L = 20$ and $\tau \in \{2, 5, 10, 20\}$ (as indicated in the legend). (B) The change in proportion of connections over time for different rates of the decay of the values of L. $\tau = 2$ and $\tau_L \in \{2, 5, 10, 20\}$ (as indicated in the legend).

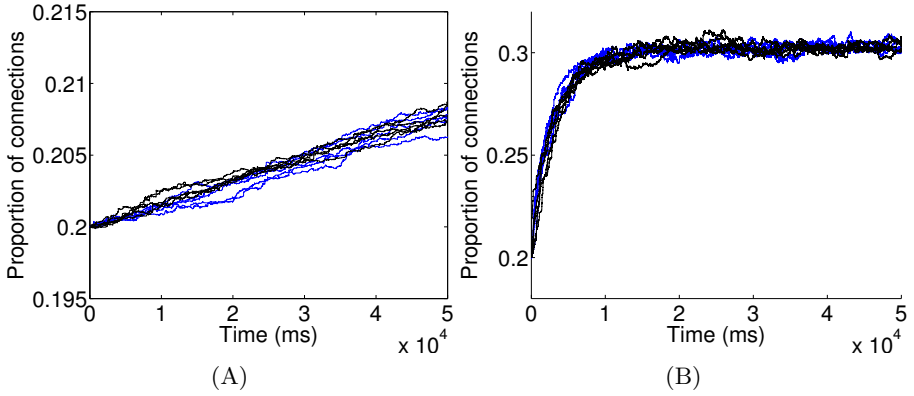

Figure 5.16: (A) 5 simulations of the network with $\tau = 2$ and $\tau_L = 5$ and with an external input with LRTCs (blue) compared with 5 simulations with external input without LRTCs ($H \sim 0.5$, black). (B) Similarly, there is no difference in the results for the different external inputs with $\tau = 5$ and $\tau_L = 100$.

Problems with this approach

As we are using the Gillespie algorithm for simulating the network dynamics this appears to give rise to several problems with regards to investigating the adaptation of the network in response to patterned external input. Firstly, the external input (and also the input from other neurons in the network) are effectively evaluated at each simulation step but they only affect the neuron on that simulation step and are not 'remembered'. When a real neuron receives input this leads to an EPSP (excitatory postsynaptic potential[5] - a small temporary depolarisation of the cell which decays over a short time [245]). If several inputs are received in relatively quick succession the neuron can then reach threshold and an action potential is initiated. If no other input is received then the effect of the EPSP decays and the neuron returns to its resting state.

[5]IPSPs (inhibitory postsynaptic potentials) can also occur in the more mature nervous system.

However, with the Gillespie algorithm two neurons with the same input will not both enter the active state - only a single neuron at each simulation step can switch states. The input that the other neuron (the one that does not enter the active state) had at that simulation step is then lost at the next simulation step. In this way the neurons in the network can be thought of subsampling the external input. Subsampling of power-law dynamics has been shown to prevent the observation of power-law dynamics within a network [209] and in a similar way here the neurons will not receive power-law correlated input. Therefore, any temporal patterning within the external input is lost.

Another problem with this approach is that, with this level of the external input, for both cases (i.e. input with LRTCs and input without LRTCs) the bursts of network activity themselves exhibit LRTCs. For example, the average DFA exponent of the IAI sequences for 5 simulations with a shuffled external input was 0.66 (range: 0.65-0.69, simulation with $\tau = 2,\ \tau_L = 100$). This is not related to any temporal structure of the external input (recall that with a constant input - as in Chapter 4 and the start of the first half of this chapter - LRTCs can be observed within the network avalanche activity) but in fact highlights the loss of the temporal patterning of the input due to the Gillespie algorithm. When there are no LRTCs within the external input, the network still exhibits LRTCs in neuronal avalanches. These dynamics will have a large effect on the connectivity formation and will override the effects of patterning within the external input.

5.2.3 LRTCs in a leaky integrate-and-fire neuronal network

For these reasons connectivity formation was also examined in a network of *integrate-and-fire* neurons. Such neurons will sum input and all input is taken into account. The same method as above was used to update the connectivity - based on the activity of the neurons and the likelihood matrix L. Therefore, the network is still adaptive, with network topology updating based on the dynamics of the system. The individual neuron dynamics were modelled as leaky integrate-and-fire neurons, following the equation:

$$\frac{dV}{dt} = -g_L(V - V_r) + I(t)$$

where V is the membrane potential of the neuron, V_r is the resting potential, g_L is the leak conductance and $I(t)$ is the input. The input at each time step varies depending on the external input to the neuron and the input from other neurons in the network (i.e. from presynaptic spiking neurons). When the neuron reaches a threshold membrane potential V_{thres} it fires and is reset to V_{reset}. Fig. 5.17 shows the membrane potential over time for a single neuron modelled in this way. For all neurons in the simulations $V_{thres} = -54\ mV$, $V_r = -70\ mV$, $V_{reset} = -60\ mV$ [246]. The leak conductances were

randomly chosen from a normal distribution with mean 0.025 and standard deviation 0.005. This heterogeneity in the conductances stops all the neurons firing at exactly the same time throughout the simulation (in response to the external input). The membrane potential of all the neurons are updated synchronously in 1 ms time steps.

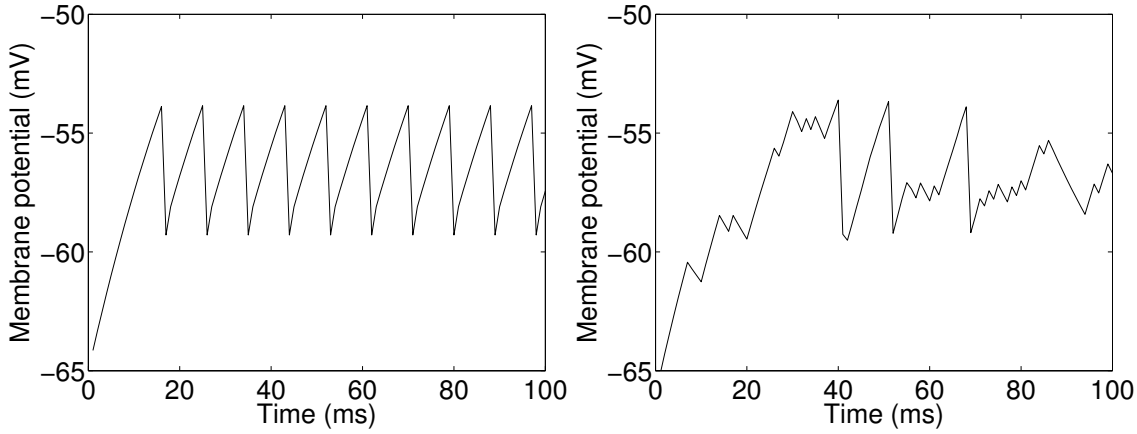

Figure 5.17: Membrane potential of a single leaky integrate-and-fire neuron in the presence of (A) constant external input (1 mV at each time step) and (B) input with LRTCs. The latter input is constructed using the thresholded fractional Gaussian noise approach as before, with the 'up' periods set to 1 mV and the 'down' periods to 0 mV. Thus, in the 'down' periods the membrane potential of the neuron starts to decay back to the resting state.

For the simulations examining connectivity formation, all the neurons had the same external input which as before was constructed from thresholding a fractional Gaussian noise process. In the 'up' periods the external input increased the membrane potential of the neurons by 1 mV and in the 'down' periods there was no external input[6]. This value of the external input was chosen as smaller values lead to network quiescence. Fig. 5.18 shows the firing dynamics across 1 second of simulation with an external input with LRTCs and the same input shuffled. With LRTCs in the external input the firing dynamics appear to display longer bursts as well as longer periods in which there is almost no firing. Firing dynamics were binned (as before using the approach of *Benayoun et al.* [61]) and the Hurst exponent, estimated using DFA, of the temporal occurrence of the bursts of activity within the network was found to be almost identical to the Hurst exponent of the sequences of 'down' periods in the external input (0.669 compared with 0.665 respectively, 'up' periods had an exponent of 0.672). Similarly, when the external input was shuffled both the inter-burst intervals of the bursts within the network and the 'down' periods of the external input showed no correlations (DFA exponents of 0.507 and 0.512 respectively, 'up' periods had an exponent of 0.493). This transfer of the temporal dynamics of the input to the output of the network might be expected given the individual neuronal dynamics. However, it highlights that the

[6]Note that in the case of integrate-and-fire neurons, no external input does not stop the simulation unlike in the case of the active-quiescent neuron model examined previously.

problem with the previous network, with the loss of the temporal patterning relating to the use of the Gillespie algorithm, does not happen in this type of network.

Neurons were initially connected randomly with 50% connectivity. Synaptic weights were set to $\frac{0.5}{pN}$ where N is the number of neurons and p is the proportion of connections. Thus, if all the presynaptic neurons spike at once then the membrane potential of the postsynaptic neuron is increased by 0.5 mV. This value was chosen so that the network was not saturated. The synaptic weights were adjusted accordingly when network connections were changed.

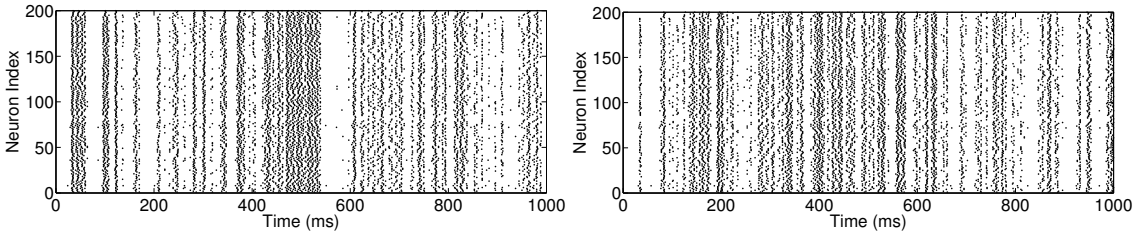

(A) (B)

Figure 5.18: Raster plots of the firing dynamics for networks of leaky integrate-and-fire neurons with external input (A) with LRTCs and (B) the same input randomly shuffled so that all LRTCs are lost. Heterogeneity in the neuron dynamics comes from the variability in the leak conductances (each neuron has a constant conductance throughout the simulation). In this case the leak conductances were randomly chosen from a normal distribution with mean 0.025 and standard deviation 0.005. The external input was the same to all neurons and there was 50% connectivity within the network.

Simulations examining the evolution of connectivity were carried out with $\tau = 5$ and $\tau_L = 100$. These values were chosen so as to take into account the network dynamics. In particular, relatively slow decay of the values in L (the likelihood of gaining/losing a connection) allows for the temporal dynamics of a number of spikes to be taken into account (i.e. the decay is not so fast that every time a neuron spikes the likelihood of gaining/losing a connection to all other neurons has decayed back to zero). The decay for the spike timing τ was set to be relatively short so as to allow the temporal dynamics of the external input to take affect.

Fig. 5.19 shows the evolution in the proportion of connections, the *normalised* clustering coefficient and the *normalised* mean path length across time for 10 simulations of the network with LRTC external input compared with simulations where the same input has been randomly shuffled. Both the clustering coefficient and mean path length were *normalised* by the average value of 50 random networks with the same number of connections. In this way it is possible to determine how the network compares with a random network, with a normalised value of 1 indicating that the clustering coefficient/mean path length is the same as that of a random network [229]. For example, in one of the simulations with LRTCs in the external input the clustering coefficient of the final connectivity matrix was 0.19 and the mean path length was 2.04.

However, these values alone cannot tell you anything about whether the network exhibits, for example, small-world properties with a clustering coefficient higher than that of a random network and a mean path length approximately the same as a random network. Fifty random networks with the same number of connections had an average clustering coefficient of 0.12 (range: 0.120 - 0.123) and a mean path length of 1.93 (range: 1.922-1.929). Thus, the normalised values of the clustering coefficient and mean path length for the network are $\frac{0.19}{0.12} = 1.58$ and $\frac{2.04}{1.93} = 1.06$ respectively. One can then also calculate the small-world index defined as the ratio of these two values [229], in this case $\frac{1.58}{1.06} = 1.49$. A value close to one would be indicative of a random network. The value here instead indicates that the network is more clustered than a random network but has similar mean path length - the network displays small-world properties. In contrast, the network with shuffled external input had a random final network topology - see Fig. 5.19. Across all 10 simulations the network with LRTC input showed an average small-world index of the final network of 1.49 (range: 1.27-1.69), whereas for the shuffled external input the average small-world index was 1.01 (range: 1.00-1.01).

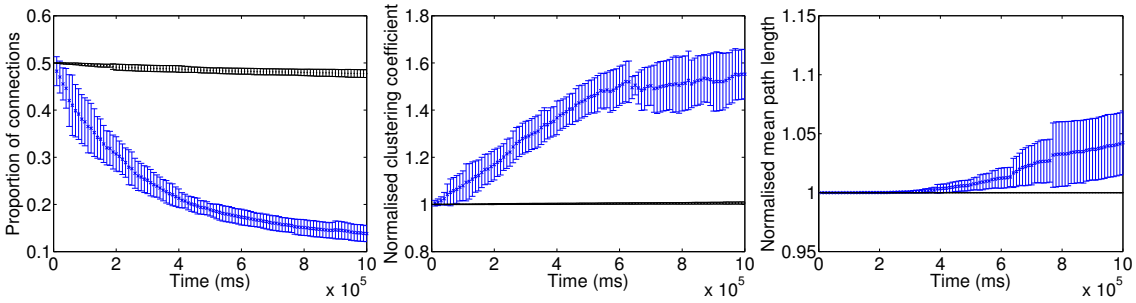

(A) (B) (C)

Figure 5.19: Evolution of the proportion of connections (A), normalised clustering coefficient (B) and normalised mean path length (C) over time for 10 simulations of a network of leaky integrate and fire neurons with external input with LRTCs (blue) and with the same randomly shuffled input (black). Values were measured every 10 seconds. For all simulations the leak conductances were randomly chosen from a normal distribution with mean 0.025 and standard deviation 0.005. Error bars indicate standard deviation.

The results clearly show a difference between the simulations with LRTCs in the input and those without. This can be understood by considering the firing dynamics of the network (see Fig. 5.18) and the LRTCs within the external input. LRTCs implies that a long (short) period is more likely to be followed by a long (short) period. In the case of the external input, this applies to both the 'up' and 'down' periods so that a long (short) period of actual input to the neurons is more likely to be followed by a long (short) period of input and a short (long) period of zero input is more likely to be followed by a short (long) period of zero input - both of which lead to periods of higher (lower) levels of the external input. This is reflected in the firing dynamics of the network where there are long bursts of activity as well as long periods of silence. There are not such long periods within the network firing in the case of the shuffled external

input. Therefore, in the case of the shuffled external input the bursts of activity are not often long enough to have an effect on the activity, but the longer bursts (and silences) with LRTCs in the external input allow for connectivity evolution.

In the case of the network with LRTCs in the external input, as the connectivity changes the normalised clustering coefficient increases. The normalised mean path length also increases, but only slightly. This indicates that as the network connectivity evolves the network topology changes from random (all simulations were started from a random connection topology) to a small-world. As there is evidence to suggest that real neural networks have small-world topologies [216, 229–232] this is particularly interesting.

Fig. 5.20 shows the network connectivity matrices at the end of two simulations - one with LRTCs in the external input and one with shuffled external input - and the degree distribution for the final networks. As expected the network which was subject to LRTCs in the external input has a lower average degree per node (as more connections are lost). However, the distribution for this network also appears more skewed than the distribution for the network with shuffled external input - there are a few nodes with a high degree. This is also of interest as there is evidence that some regions in the brain are so called 'hub' nodes - with a very high degree [247]. Due to their high connectivity these regions are thought to be key to integration and fast communication throughout the network [247].

Fig. 5.21 shows the connectivity evolution for simulations with a lower initial connectivity. There remains a clear difference between the network evolved under input with and without LRTCs, but the overall connectivity change is greatly reduced. However, despite this reduction in change in the proportion of connections, the normalised clustering coefficient (in the case of LRTC input) increases indicating a change towards a more clustered network. There is also an increase in the normalised mean path length. The final network connectivity had an average small-world index of 1.15 (with input with LRTCs, range: 1.06-1.37) and 1.00 (shuffled input, range: 0.99-1.02). Examining the degree distributions for the initial and final networks, see Fig. 5.22, after the connectivity has evolved under the external input with LRTCs, some nodes have increased their degree while others have decreased. Once again this final distribution appears to exhibit hub nodes with very high degree. These results suggest that, starting from a lower degree distribution the network evolved under external input with LRTCs still takes on properties characteristic of networks of the brain.

Fig. 5.23 compares the connectivity evolution between external input with and without LRTCs, with a slight increase in the heterogeneity of the neuronal dynamics. A similar pattern is observed, with a large difference between the connectivity for the two different inputs. Comparing with Fig. 5.19 the average resulting number of connections and clustering coefficient (at the end of the simulation) is increased (i.e. fewer connections

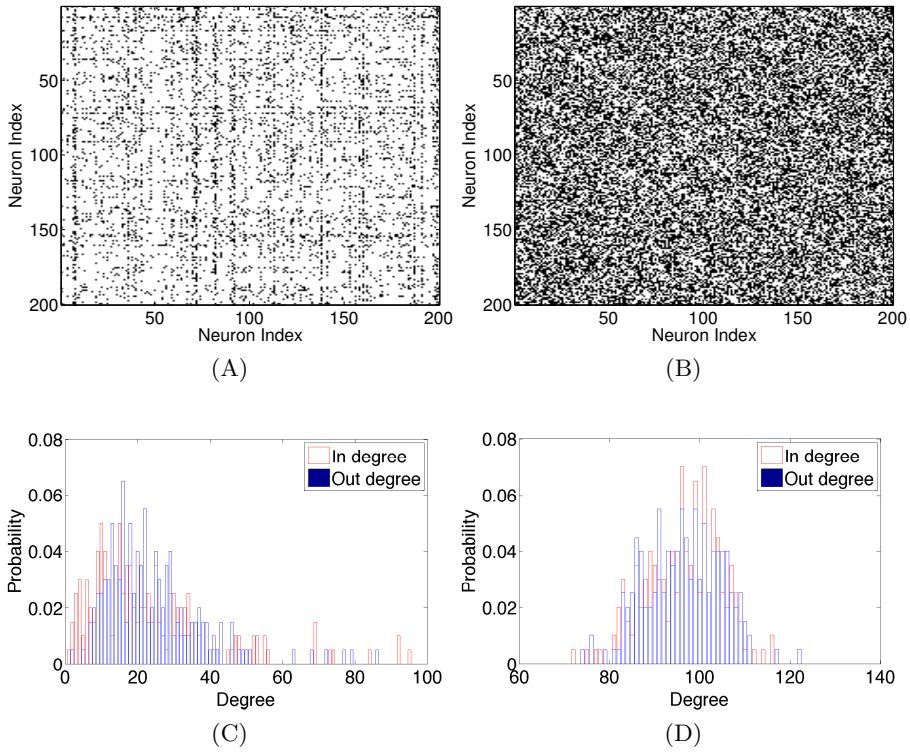

Figure 5.20: (A) Final network connectivity in a simulation with LRTCs in the external input. (B) Final connectivity in a simulation with the same input shuffled. (C) Degree (in and out degree as indicated, i.e. the distribution of presynaptic contacts to neurons and postsynaptic contacts respectively) distribution of the final network in the simulation with LRTCs in the external input. (D) Degree distribution of the final network with shuffled external input.

are lost) with this increase in heterogeneity. This is perhaps related to the fact that with an increase in heterogeneity spikes are more likely to be spread further apart and so the update of the likelihood in relation to the spike-timing will be decreased.

To further confirm that the differences in the evolution of connections are related to the LRTCs, an external input with no LRTCs (constructed from a fractional Gaussian noise process with a Hurst exponent of ~ 0.5) was compared with the network dynamics with the same input shuffled. In both cases the input is uncorrelated and so we would expect there to be no measurable difference in the way in which connectivity changes. Indeed, this was the case - see Fig. 5.24. This shows that the difference in the dynamics shown previously is a result of the LRTCs in the input and is not a spurious result from shuffling the input.

Finally, we examine connectivity formation on a larger network with N=1000. Again we see that an external input with LRTCs has a large effect on connection topology in this adaptive network, see Fig. 5.25. With an external input with LRTCs the network exhibits higher clustering than a random network with the same degree. This is in contrast to the network which received the same input randomly shuffled. The

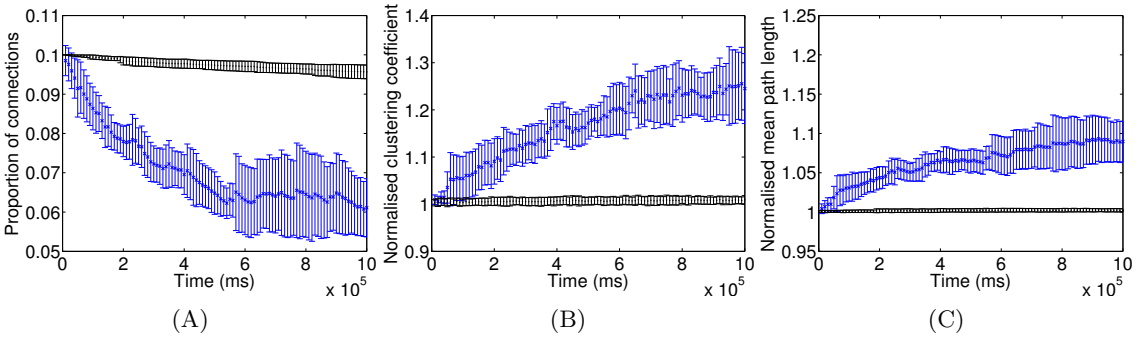

(A) (B) (C)

Figure 5.21: Evolution of the proportion of connections (A), normalised clustering coefficient (B) and normalised mean path length (C) over time for 10 simulations starting from a random network with a lower connection density that the simulations in Fig. 5.19. Again the external input either exhibited LRTCs (blue) or was randomly shuffled (black). Error bars indicate standard deviation.

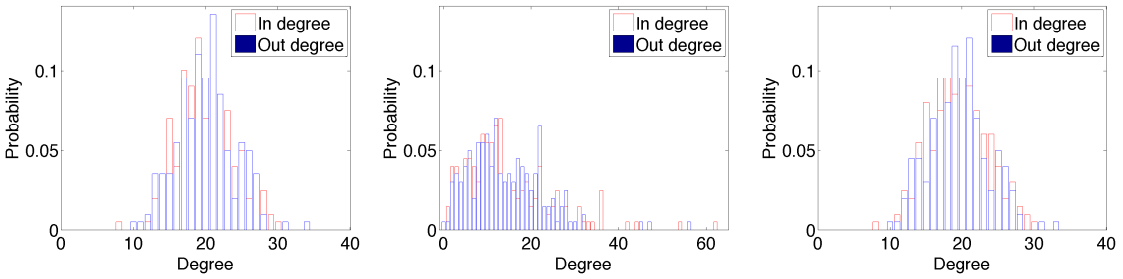

(A) (B) (C)

Figure 5.22: Degree distributions for (A) the initial network, (B) the final network having evolved under external input that exhibits LRTCs, (C) the final network after evolution of the connectivity under the same input randomly shuffled. The initial connectivity was reduced compared with the networks whose degree distributions are shown in Fig. 5.20. Note that some of the nodes in the network with LRTC input have much higher degrees than were present in the initial network.

small-world index of the final network connectivity had an average value of 2.16 (for networks with LRTC external input, range: 1.74-2.41) and 1.01 (shuffled input, range: 1.00-1.02). As observed previously, the network which received input with LRTCs exhibits hub neurons in the final network topology, see Fig. 5.26.

5.3 Discussion

Connectivity formation is the main developmental process in the early preterm period across which EEG recordings were studied in Chapters 2 and 3. Here we investigated the effects of different topologies on the temporal characteristics of the burst dynamics in the excitatory stochastic neuronal network model constructed in the previous chapter. This was then extended further to investigate the effect of LRTCs on connectivity formation.

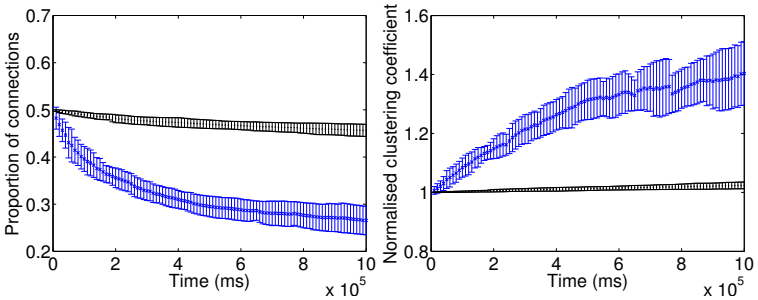

(A) (B)

Figure 5.23: Evolution of the proportion of connections (A) and normalised clustering coefficient (B) over time for 10 simulations of a network of leaky integrate and fire neurons with external input with LRTCs (blue) and with the same randomly shuffled input (black). For all simulations the leak conductances were randomly chosen from a normal distribution with mean 0.025 and standard deviation 0.01, i.e. the variance in conductances was increased from the simulations whose results are given in Fig. 5.19. Error bars indicate standard deviation.

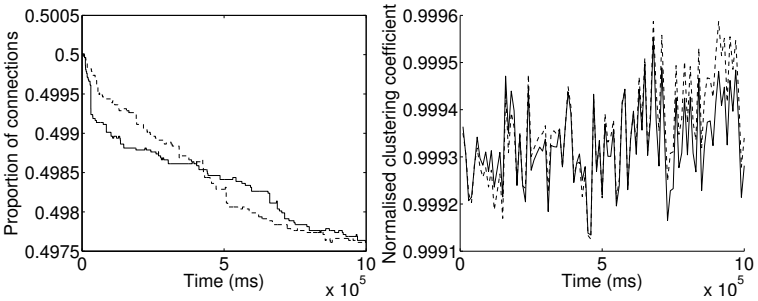

(A) (B)

Figure 5.24: Change in the proportion of connections (A) and normalised clustering coefficient (B) in a network with external input constructed from a fractional Gaussian noise process with no correlations (so that the Hurst exponent of the periods within the external input is approximately 0.5, dashed line). This is compared with the evolution under the same input shuffled (solid line). Note the scale on the y-axis - in both simulations very few connections are lost. The change in normalised mean path length was less than 0.0001 in both cases.

As was shown to be the case with previous models, topology has a major effect on network dynamics [168–171]. In particular, in random networks bursts tended to occur across the network with no distinct spatial pattern. In contrast, the bursts within the modular network tended to occur within the modules and in the case of the non-modular small-world network the bursts occurred in discrete spatial groupings. To my knowledge the topological properties of the preterm brain have not been investigated[7]. However, considering what are likely (by extension of the topological properties in the adult) to be physiologically realistic network topologies, this work shows that a *purely excitatory* system can have spatially distinct (as well as temporally

[7]One study has investigated functional connectivity in *full-term* infants suggesting that functional 'hubs' - nodes with a very high number of connections - are present in the brain at full-term but these occur in different brain regions to the hub regions in adults [248].

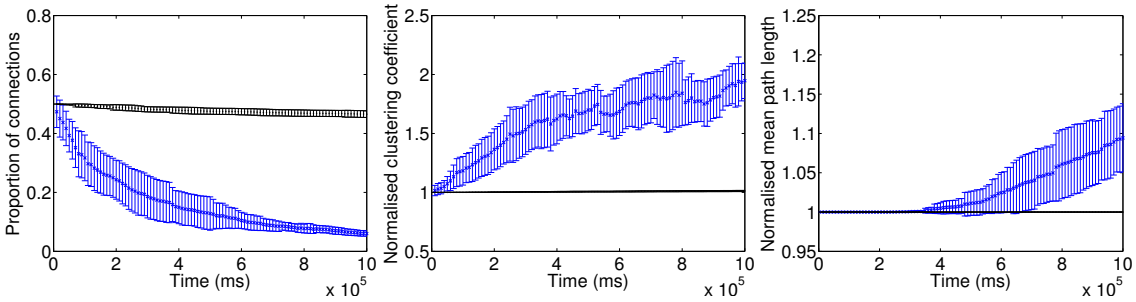

(A) (B) (C)

Figure 5.25: Change in proportion of connections (A), normalised clustering coefficient (B) and normalised mean path length (C) for a network with size N=1000. Connectivity in the network was evolved either in the presence of an external input with LRTCs (blue) or with the same input shuffled (black). The clustering coefficient was normalised by the clustering coefficient of 20 random networks of the same size. Error bars indicate standard deviation.

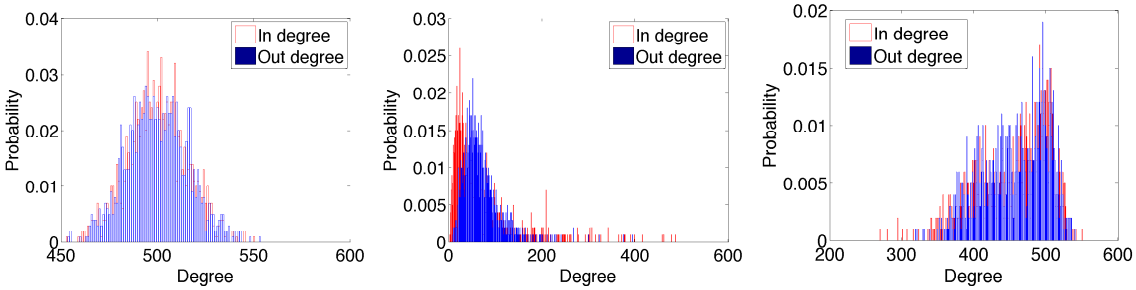

(A) (B) (C)

Figure 5.26: (A) Network degree at the start of the simulation for a network with size N=1000. (B) After connectivity changes under an input with LRTCs, the final network topology exhibits hub neurons. (C) Final network degree in the network following evolution under a shuffled distribution.

distinct) bursts of activity. In this way - with few long-range connections - excitation does not lead to 'spatial saturation'.

Kaiser et al. [196, 197] investigated the spreading of activity on networks with different topologies and showed that hierarchical networks topologies (networks with modules on at least two different levels, i.e. modules within modules) can allow for sustained activity (without the need for external input) and that this topology also leads to more segregated activity when compared with random networks where activity either quickly died out or saturated the network. The results presented here coincide with this analysis in that both modular and small-world networks showed spatially segregated dynamics. However, we do not examine sustained activity but instead show that activity can occur in bursts within the modules. From this perspective, the results of *Kaiser et al.* were limited as it appears that when the activity was sustained, this coincided with saturation in a single module/hierarchical cluster within the network. Furthermore, *Kaiser et al.* did not examine temporal pattering within their network activity nor the

effect of temporal patterning within external input - they seeded the network with active neurons and did not have another source of external input.

As connection densities were varied, it was shown that in order to maintain a balanced level of activity within the network the synaptic weights needed to be varied according to the connection density. For example given a connection density of 50% this implies that in a network of N=100, a single neuron will have (on average) 50 postsynaptic neighbours. Thus, with synaptic weights that have not been updated $w = 1$ implies that on average 0.5 neurons will become active from a single presynaptic active neuron. To maintain a branching parameter of 1 we must therefore update the synaptic weights in proportion to the number of connections. However, it is important to note that with all the network topologies studied here individual neurons have different numbers of connections. Therefore, this global homeostasis will not necessarily lead to a branching parameter of one exactly on a local level. For example, a neuron may have only 48 postsynaptic neurons (while on average across the network neurons have 50 postsynaptic contacts). Each of these connections has a weight adapted to the average network level ($w = 1/p = 1/0.5 = 2$). Thus, on average for every activation of this neuron $(2/100) \times 48 = 0.96$ neurons are activated. However, the branching parameter itself is an average measure - a branching parameter of one implies than *on average* a neuron activates one other neuron. Therefore, this global maintenance of the branching parameter will be sufficient to generate a balanced state of network activity. Indeed despite the global rather than local homeostasis, LRTCs indicative of a critical state were observed in the dynamics.

Larremore et al. [212, 213] suggest that for different network topologies a critical state can be achieved by setting the dominant eigenvalue in the adjacency matrix (the matrix describing the networks connections) equal to one. Table 5.7 shows the eigenvalues of the adjacency matrices for the topologies studied in this chapter. All the eigenvalues are very close to one. From the results of *Larremore et al.* this suggests that the networks are not exactly, but almost, at a critical state. Recall that the external input anyway perturbs the system away from the critical point. So again apparent 'critical' dynamics (such as LRTCs) can be achieved in the system when it is close to, but does not need to be at, the critical point. In terms of the biophysical realism of the system, the approach taken here (adjusting the synaptic weights) seems more appropriate than adjusting the eigenvalue of the adjacency matrix. An individual neuron within a network is unlikely to be able to 'realise' the adjacency matrix of the whole network, whereas maintaining a balanced level of activity is physiologically appealing.

Connectivity	Eigenvalue for topology type		
	Random	Modular	Non-modular small-world
1	0.9997	0.9950	1.0000
2	1.0000	0.9951	1.0000
3	1.0000	0.9954	1.0000
4	1.0000	0.9957	1.0000

Table 5.7: Average (across simulations) maximum eigenvalue of the adjacency matrices, where each element of the adjacency matrix (i, j) is either 0 if there is no connection from neuron i to neuron j or equal to $1/(pN)$ if there is a connection from neuron i to j, where p is the proportion of connections in the network and N is the total number of neurons. Connectivity indicates the level of connectivity as investigated for each of the networks. So for random networks this indicates a connection density of 10, 50, 75, 90 (in that order 1, 2, 3, 4), for modular networks this indicates a number of connections between the modules of 0.5, 1, 5, 10; and for non-modular small-world networks this indicates a connection density of 20, 50, 100, 300 respectively.

5.3.1 LRTCs and connectivity formation

In the second part of this chapter the effect of LRTCs in the external input was investigated in a adaptive network model. An adaptive network model was chosen specifically as it enables connectivity to be updated dependent on the dynamics and vice versa creating a feedback loop. Given that connectivity formation involves activity-dependent mechanisms, but that connectivity can also influence dynamics, such an approach is essential to understand connectivity formation.

To my knowledge, this is the first investigation of the effect of LRTCs on connectivity formation. After exploration of the effects of LRTC input in the stochastic neuronal network model, a network of leaky integrate and fire neurons was examined. This approach allowed for a direct investigation of the question as the leaky integrate and fire neurons were found to fire in relation to the external input. This was unlike the other model which was not directly influenced by the patterning in the input (and for example continued to display LRTCs in the bursts within the network even when the external input itself did not display LRTCs).

It was found that, in the leaky integrate and fire model, the proportion of connections throughout the course of the simulations differed greatly when the network was subject to an external input with LRTCs compared with randomly shuffled external input (without LRTCs). The randomly shuffled input had all the same characteristics of the input with LRTCs except for the temporal ordering, i.e. the length of the 'up' and 'down' periods are the same. Thus, the differences in connectivity were solely influenced by the temporal ordering of the external input.

While this model did not attempt to be physiologically realistic in terms of the final topology and level of connectivity that is reached, it demonstrates that LRTCs can have an effect on activity-dependent connectivity formation. It is worth noting that the rate of the external input and the rate of adaptation of the connectivity are on a much faster

timescale than the LRTCs observed in the preterm EEG. Future work is therefore required to extend this investigation to fully understand the effects of LRTCs in the burst dynamics of the preterm EEG. Nonetheless, the results of this section suggest that the LRTCs in the bursts (not just the bursts of activity themselves) of the early developing nervous system may be important in connectivity formation.

Most interestingly, there was not only a difference in the way the connectivity evolved in the presence of the different inputs, but in the resultant topology as well. With an external input with LRTCs there was an increase in the normalised clustering coefficient. As the increase in normalised mean path length was not as great, this indicates that the final network had a small-world connection topology. Additionally, the degree distributions for the final network showed some neurons had become hub nodes - with a much higher number of connections compared with other neurons. There was no pre-programming within the model to lead to this network topology, and the network started with random connectivity. The final topology is purely a result of the network adapting its connectivity in relation to the dynamics of the network driven by the external input. This topology - a small-world network with hub nodes - has been observed in brain networks [216, 229–232, 247] and so is of particular significance

There is experimental evidence to suggest that in pathological states brain connectivity is closer to a random network, with lower clustering and fewer hub nodes [249]. Other authors have shown in computational models that changes in network structure can give rise to epileptic activity [171, 250]. Connection topology is therefore important for the proper function of the brain and this connection topology is formed during development. Small-world topology has been suggested previously to arise due to constraints such as efficient neuronal communication and metabolic costs which are related to neuronal wiring and signal propagation (which increase with increasing separation of the neurons) [249]. The presence of modularity within a network has also been suggested to evolve in the presence of varying 'modular' input [251]. The results of the model presented in this chapter suggest that the LRTCs observed in early brain activity may also be crucial for the formation of cortical connectivity formation. How exactly LRTCs in early brain dynamics aid in the construction of brain networks warrants future experimental investigation.

5.3.2 Connectivity formation and critical state dynamics

LRTCs are a possible indication that the brain is in a critical state. However, critical states may emerge as a function of the connectivity - for example this has been suggested to be the case in cultures where power-law distributions are not observed when the cultured neurons have few connections during the early stages of development [54]. So *if* a certain level of connectivity is required for LRTCs, how would LRTCs

influence activity-dependent connectivity formation?

It is important to recall that LRTCs were observed even in the youngest preterm subject studied. Therefore, it appears that LRTCs are exhibited by the bursts of cortical activity before cortical connectivity formation is fully formed. I speculate that, as the subplate develops before the cortical plate [7, 10] and as there is some suggestion that the delta wave of the BNO activity is a result of subplate activity [97], that the subplate may be a source of external input to the cortex which exhibits LRTCs. That is to say that the subplate does not just drive the cortex but it does so in a temporally complex manner crucial for proper connectivity formation. If this is the case, then there would be no stable cortical connectivity required for LRTCs in the dynamics and LRTCs could influence cortical connectivity formation.

Chapter 6

General discussion

This thesis examined the temporal dynamics of the electrical activity of the early developing brain through the analysis of very preterm human EEG and the construction and analysis of computational neuronal network models. Particular attention was paid to the LRTCs of burst dynamics and this thesis presents the first observations of LRTCs both in the preterm EEG and in the 'avalanche' dynamics of an artificial neuronal network. This temporal patterning suggests a greater degree of complexity in very early brain dynamics than was previously appreciated and may be crucial for connectivity formation.

6.1 Summary of the main results

- LRTCs were consistently observed in the ordering of BNO activity within the EEG recordings of all preterm subjects assessed, both in the initial study (Chapter 2) and the study conducted afterwards on a larger sample set (Chapter 3) - a total population size of 52.
- The degree of the LRTCs did not vary with gestational age but there was a significant effect of the time since birth (in the case of IEI sequence exponents) and EEG channel location (in the case of duration sequence exponents).
- No difference in the Hurst exponent was found between those children with normal and abnormal neurological outcome at two years of age. Having said this, there was a significant difference within the group of children with intracranial haemorrhages at birth, with those with an abnormal outcome at two years having higher exponents compared with those with normal outcome.
- With system parameters such that the branching parameter is one, a purely excitatory neuronal network was shown to display burst dynamics. For different

levels of the external input different distributions were observed for avalanche (burst) size, duration and IAIs. For low levels of the external input power-law distributions were observed in avalanche size and duration, coinciding with previous work examining neuronal avalanches [38, 49, 50]. As the external input was increased there was a superposition effect in the distribution of avalanches but an emergence of a power-law in the distribution of IAIs.

- For an optimal level of external input the sequences of avalanche characteristics exhibit LRTCs, with LRTCs extending across an infinite sequence length in the limit of system size. The results from this modelling study suggest that a possible mechanism leading to LRTCs in the preterm EEG is a balanced state of network activity with a branching parameter of 1.

- LRTCs were observed in the dynamics of networks with different connection topologies, provided that the synaptic weights were updated so that a balanced state of activity remained.

- Updating the synaptic weights continually while the topology changes - in particular by changing the synaptic weights in proportion to the level of connectivity within the network - may be a homeostatic mechanism by which the brain remains in a balanced state throughout the period of cortical connectivity formation.

- External input that exhibit LRTCs, compared with input that did not, was shown to have a pronounced effect on connectivity formation in a model composed of leaky integrate and fire neurons. Furthermore, the resulting connectivity following evolution under the input with LRTCs was shown to be a small-world network - the connection topology observed in physiological neuronal networks.

6.2 Outlook and future directions

6.2.1 Criticality and the brain

The idea that the brain is a critical system has received much attention in recent years [38, 60, 148, 252]. As discussed in the first chapter of this thesis, the basis for this idea is the observation of power-law distributions in neuronal systems including neuronal avalanches - a power-law distribution in the size of cascades of neuronal firing [49, 50] - and power-law distributions in the autocorrelation (LRTCs) of fluctuations in oscillation amplitude in EEG and MEG recordings [39, 44, 45]. These observations, combined with the enthusiasm for the SOC framework in the wider literature [56, 148], has fuelled the hypothesis that the brain is a SOC system. However, it is important to remember that

while power-laws are a necessary condition for a system to be critical they are not sufficient. The current literature is therefore, for the most part, inconclusive - power-law dynamics are suggestive of a system at criticality but further evidence is needed.

Tetzlaff et al. [54] provided evidence for self-organisation to a critical state in cultured neural networks during connectivity formation, showing that the firing dynamics exhibit first supercritical behaviour, then subcritical, before finally entering a regime exhibiting critical power-law dynamics. However, there is currently no evidence for such behaviour *in vivo*. In this thesis critical power-law dynamics were observed even in the youngest subject studied. Thus, there was no evidence for a period of self-organisation to a critical state across the age range studied. I speculate that, as the subplate develops at an earlier stage to the cortical plate [6, 8, 9], *if* the brain is a SOC system then a self-organisation process may occur in the subplate at an earlier developmental stage to the one studied here. The subplate may then project 'critical' dynamics onto the cortical plate during a period of self-organisation in the cortex. As SOC systems self-organise without particular external driving [55, 56], if the cortical plate organises under the influence of critical dynamics from the subplate this would suggest that the cortex is not a SOC system.

On the other hand, perhaps our perspective of SOC and the brain needs to be altered. If the subplate is wired early in development so as to project critical LRTC dynamics onto the cortical plate generating a small-world connectivity then there is a fitness gain in the developing brain having a subplate which acts in this way. Previously we had thought that the brain self-organises to a critical state during the lifetime of the individual, making the brain a SOC system. Could the brain instead be a SOC system from an evolutionary perspective? This idea is speculative and could not readily be tested other than to perhaps test whether animals with less well developed nervous systems do not exhibit critical state dynamics. However, it is stated here as an interesting alternative view to the current SOC brain hypothesis within the literature.

From our modelling approach we have seen that LRTCs can be observed in avalanche dynamics when there is a balanced state of activity. Therefore, a third interpretation of the results might be that, if the healthy brain remains within a balanced state of activity, then we will never see non-critical dynamics. In this way, a self-organisation process of the dynamics may not be observed as from the very earliest stages of nervous system development the cells may be maintaining a balanced state. In fact, as we have seen, the system may not need to be exactly at the critical balanced state for power-law dynamics to be observed. A system very close to the critical state can also exhibit apparent power-law dynamics, as has been observed by other authors [58, 149, 151, 159]. *Poil et al.* [159] suggested that, in their computational model, LRTCs in the fluctuations of oscillation amplitude and neuronal avalanches corresponding to those observed experimentally, occur when the network is in a slightly supercritical regime. In

the computational model constructed in this thesis, the external input perturbed the system into a subrcritical state. Whether the brain is a system slightly perturbed away from the critical state, in either the supercritical or subcritical directions remains to be investigated.

Power-laws have been observed at different scales from the neuronal level (i.e. in neuronal avalanches [49, 50]) to wider brain networks in the analysis of EEG, MEG and fMRI [39, 40, 44–46]. They have also been observed in different types of activity: for example neuronal avalanches occur across a spatial region and exhibit power-laws in avalanche sizes up to the system size. Conversely LRTCs examine power-laws in the autocorrelation function. Here we examined the temporal structure of discrete bursts of activity. However, it was not possible to carry out a spatial analysis similar to that of the neuronal avalanche analysis as there were only (approximately) 10 electrodes used for recording. This does not give a large enough spatial range with which to conduct this type of spatial analysis. It was therefore not possible to try to connect the work here more directly with the observations of neuronal avalanches. Furthermore, the LRTCs examined were in discrete activity and so it was not possible to directly connect these observations with the LRTCs shown in more mature subjects in the fluctuations of oscillation amplitude in continuous data. Whether and how these observations of power-laws at different levels can be related remains an unresolved issue [159]. However, connecting all of this work will aid in our understanding of this type of dynamics and is likely to be an important question of future research. Recently, *Poil et al.* [159] showed that in a computational model the same mechanism can give rise to neuronal avalanches and, on a longer timescale, LRTCs in the fluctuations of oscillation amplitude. Here we have shown in a computational model that LRTCs may also occur in the temporal sequences of the avalanche dynamics themselves. Future experimental work is needed to fully connect the dynamics on the different scales within the nervous system.

What is crucially lacking from the literature is an understanding of why LRTCs are important. Are they just a product of the brain being in a critical state or do they perform a useful function? Critical systems have been shown to give rise to optimal dynamic ranges [36] and optimal information transfer [160]. It is known that LRTCs (by their definition - see Chapter 1) 'carry a memory' of past events. Could they somehow be related to human memory, perhaps through synaptic strength modification? Through the modelling work in this thesis we have seen how LRTCs can have an effect on connectivity formation, significantly also leading to the small-world network topology seen in neural networks [229, 232, 249]. The modelling approach taken examined an adaptive model in which connectivity was updated through an activity-dependent rule. From this we might ask whether, in more mature subjects, LRTCs play a similar role in plasticity through the alteration of synaptic weights by spike-timing dependent plasticity. This leads to future interesting experimental studies both in the developing and more mature nervous system. For example, one could envisage examining synaptic

connectivity in cultures driven with input with LRTCs compared with input without LRTCs. This could either compare connectivity in a developing culture, combining with the computational model studied here, or a more mature culture - examining changes in synaptic strength. Considering development, synchronous periodic electrical stimulation of the ferret optic nerve leads to weaker orientation patterning of cells within the visual cortex [221]. A similar experiment could be conducted whereby input with LRTCs or without LRTCs is compared. The results of such studies may emphasise the need for this type of dynamics in the brain.

6.2.2 The temporal dynamics of activity

This thesis has considered the temporal dynamics of the early preterm EEG. As was discussed, this is an abnormal state where the developing brain is subject to the *ex-utero* environment. The activity studied in these recordings cannot be assumed to be the same as in a normal developing foetal brain. However, through MEG recordings it has been shown that the foetus *in-utero* exhibits nested activity similar to that in the preterm EEG [116] suggesting that the preterm brain exhibits similar activity to that of the foetal brain. Having said this, there has been no extensive study comparing, for example, the rate of activity or indeed the temporal characteristics of the burst activity. Such an analysis will be imperative in furthering our understanding of the differential development of the preterm brain.

Niemarkt et al. [84] observed cyclic behaviour in the inter-burst ratio in 4 hour recordings which they suggest confirms the concept of sleep-wake cycles in very early preterm subjects, as have been observed by other authors [27, 89]. Sleep is crucial for brain functioning later in life, in particular in memory consolidation [253], and the disruption of sleep-wake cycling in the preterm period may indicate an underlying pathology [254]. Therefore, sleep may be important for early brain formation. However, the particular temporal characteristics of different sleep stages during development have not been well studied. Do bursts occur with a different temporal ordering in different sleep stages? This analysis could be achieved using the recently developed time-varying adaptive DFA algorithm [255] for the characterisation of time-varying exponents, modified for discontinuous data. If different sleep stages do have different temporal dynamics, coinciding with the modelling work of this thesis, this might then generate a hypothesis that some sleep stages are more important for neuronal connectivity formation than others.

In relation to the preterm brain it is important to consider directly how the external environment might be affecting nervous system activity. Responses can be observed on the EEG following tactile [29, 90, 91], painful [91], visual [256] and auditory [257] stimuli. The responses that have been examined in relation to these stimuli are single

evoked potentials. However, if a potential is evoked when the brain is not 'expecting' it, could this have a deleterious effect by disrupting the temporal patterning within the bursts? Earthquakes are an example of a system which exhibits power-law statistics. After an earthquake has occurred, smaller earthquakes (aftershocks) follow with a power-law relationship to the initial earthquake [135]. Might an external stimulus be a 'neurological earthquake' with aftershocks affecting the temporal dynamics for more than just a few seconds? If so, could this (transient) disruption in the temporal patterning lead to an explanation as to why preterm children are more likely to have neurological problems later in life in comparison to their term born peers [111–113]?

Between 31 - 35 weeks gestational age (just older than the age range investigated here) subplate neurons start to apoptose and the switch occurs in GABA to the mature inhibitory effect [4, 65]. With these changes the EEG gradually becomes more continuous. What does this mean for the temporal dynamics of the system? LRTCs have been observed after birth in the fluctuations of oscillation amplitude in the continuous activity. Before 31 weeks (i.e. the maximum age studied in this thesis) LRTCs were observed in this thesis in the temporal pattern of the discontinuous burst activity. Investigating the changing temporal pattern between these two age ranges will enhance our knowledge of the two major underlying changes in the brain at this stage and may also lead to a better understanding of the connection between these two observations of LRTCs in different types of activity.

6.3 Conclusions

The burst dynamics of the human very preterm EEG exhibit LRTCs, suggestive of critical state dynamics. The early developing brain has altered neurotransmitter effects compared with the mature nervous system with a delay in postsynaptic inhibition. A balance of activity in an excitatory neuronal network model leads to LRTCs in burst dynamics. This suggests that a possible underlying mechanism for this type of dynamics in the early developing nervous system is the maintenance of a balanced state, which need not be from a balance of excitation and inhibition as was suggested in the case of the mature nervous system. Homeostatic tuning of the synaptic weights may explain the continual observation of LRTCs over a period of development during which cortical connectivity changes. Moreover, the evidence to indicate that the majority of cortical activity is attributed to the subplate leads to the suggestion that the subplate may drive the cortical plate with LRTC input.

Early spontaneous and sensory driven activity is crucial for proper connectivity formation in the brain. The results of this thesis suggest that not just the activity itself but also its temporal ordering may be critical. In particular, LRTCs can result in different connectivity compared with input without LRTCs, and significantly, with

LRTCs, the resultant network has a small-world topology also seen in physiological neural networks. These results pave the way for future work investigating the exact role of these complex temporal dynamics in the early developing brain.

Chapter 7

Appendices

7.1 LRTCs in thresholded fractional Gaussian noise

Fractional Gaussian Noise (FGN) is a process that exhibits long-range dependencies. The process $\{y_t : t \in \mathbb{Z}\}$ is defined by [139]:

$$y_t = B_d(t+1) - B_d(t)$$

where $B_d(t)$ is fractional Brownian motion.

The points y_t have a Gaussian distribution, thus, this is an example of a process that does not have a power-law distribution of points but does exhibit LRTCs in the temporal distribution of these points.

Whilst trying to find processes that exhibit LRTCs in waiting times between bursts of activity I investigated thresholding of a FGN process and observed, through DFA analysis, that this did indeed yield LRTCs in waiting times. To my knowledge this has not been discussed by previous authors and therefore a brief exploration is undertaken here. However, a theoretical proof will not be given.

FGN processes were constructed using the code of Little et al. [258, 259]. Fig. 7.1 shows an example of a FGN process. The distribution of the points is Gaussian with mean zero. Therefore to create waiting times (IEIs), the process was thresholded at zero, creating bursts of activity where the process was above zero and periods of silence (set to zero) where the process was negative. An IEI was defined as one of these periods below zero. Fig. 7.1 shows an example of an IEI sequence constructed in this way. Fig. 7.2 shows example DFA plots for the FGN process itself (as expected this has a Hurst exponent $H > 0.5$) and the DFA plot for the sequence of IEIs lengths from the thresholded sequence. This figure also shows a comparison of the exponents of the FGN processes and the IEI sequences. It was found that the IEI sequences did exhibit

LRTCs, though the exponent was lower than the exponent of the FGN sequence and there was a saturation effect of the exponents at ~ 0.75. Nevertheless, this provides a useful method for the construction of a sequence with waiting periods with LRTCs. This process was used to construct external input with LRTCs for the system studied in the second half of Chapter 5.

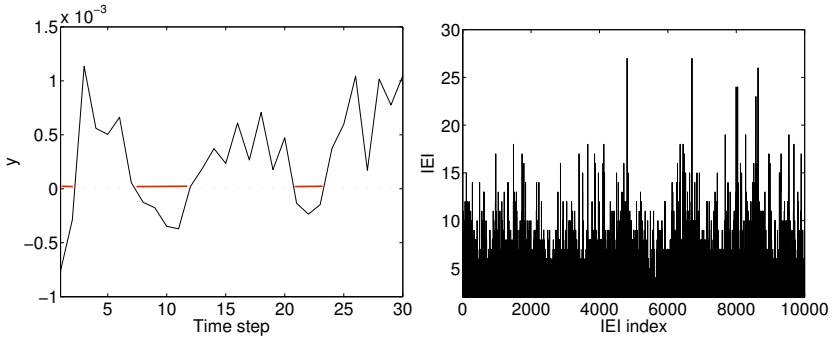

(A) (B)

Figure 7.1: (A) An example of a short section of fractional Gaussian noise (y, defined as in text). Waiting times (IEI) between bursts were set as periods for which $y < 0$ and are shown in red. The length of the IEI was set as the number of points for which $y < 0$. (B) An example of an IEI sequence formed in this way.

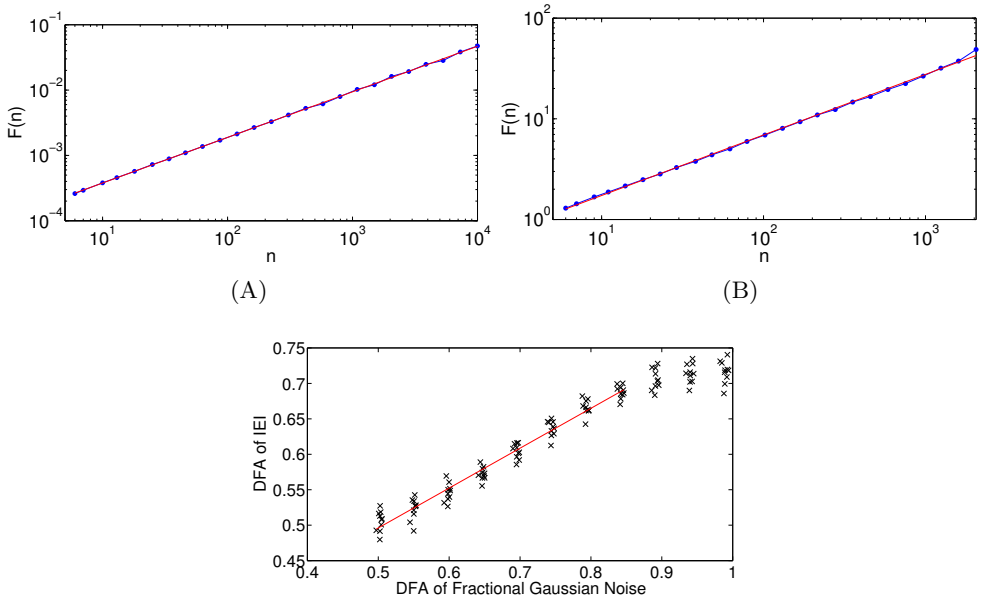

(A) (B)

(C)

Figure 7.2: (A) DFA plot of a FGN process, here the exponent was 0.70. (B) DFA plot of IEI sequence from the FGN process whose DFA plot was shown in (A). For the IEI sequence the exponent was 0.60. (C) Plot of DFA exponents for the IEI sequence compared with DFA exponents of the original FGN process. The line of best-fit taken for values of the exponent for the FGN up to 0.85 (red line) had a slope of 0.56 and an intercept at 0.21.

7.2 A system with a critical fixed point in the presence of non-zero external input

In Chapter 4 it was shown that it is not possible for there to exist a critical fixed point in the presence of non-zero external input with the linear activation function. In order to achieve parameters such that the branching parameter is equal to 1 (a balanced activity state) the activation function must therefore be altered. In this section the activation function is chosen from a purely theoretical perspective in order to achieve this and understand the dynamics when this criteria is for-filled.

Consider the quadratic activation function $g(A) = \frac{w}{N}A^2 + h$. The mean-field equation is given by:

$$\frac{dA}{dt} = \left(\frac{w}{N}A^2 + h\right)(N - A) - \alpha A$$

The equations for the fixed points of the system and the eigenvalue at the fixed points are given by:

$$\begin{aligned} f(A) = \frac{dA}{dt} &= -\frac{w}{N}A^3 + wA^2 - (h + \alpha)A + hN = 0 \\ \lambda = f'(A) &= -3\frac{w}{N}A^2 + 2wA - h - \alpha \end{aligned} \tag{7.2.1}$$

Solving these simultaneously gives:

$$\begin{aligned} \alpha &= -3\frac{w}{N}A^2 + 2wA - h \\ 2wA^3 &- wNA^2 + hN^2 = 0 \end{aligned} \tag{7.2.2}$$

Which defines the parameter space and value of the fixed point for which a critical fixed point can be obtained.

First, considering the case with $h = 0$ we see that the fixed points are given by $A^2(2wA - wN) = 0$. So $A^* = 0$ or $A^* = N/2$. However, note that when $A^* = 0$ then $\alpha = 0$ which is not a valid parameter choice for our system. When $A^* = N/2$, $\alpha = (1/4)wN$ in order for the fixed point to be critical. However, note that in this case there is another fixed point of the system ($A^* = 0$) and this fixed point is stable. So how will this other fixed point affect the dynamics? Letting $N = 800,\ w = 1$ we see (Fig. 7.3) that eventually the dynamics reach the fully quiescent state, however, the dynamics do depend on the initial condition of the network. If a single neuron is used to seed the network (as was done with simulations with zero input and the linear activation function) then the activity quickly (usually at the first step in the simulation) dies out as it is attracted to the stable fixed point $A = 0$ - results not shown. Similarly, if the initial number of active neurons is between 1 and $N/2$ then the activity will decrease to

zero, though if the number of active neurons is initially close to $N/2$ then it appears that the dynamics start to be affected by the critical fixed point. If the initial number of active neurons is above $N/2$ then the activity eventually dies out, but appears to 'hover' around the critical fixed point for a period before doing so.

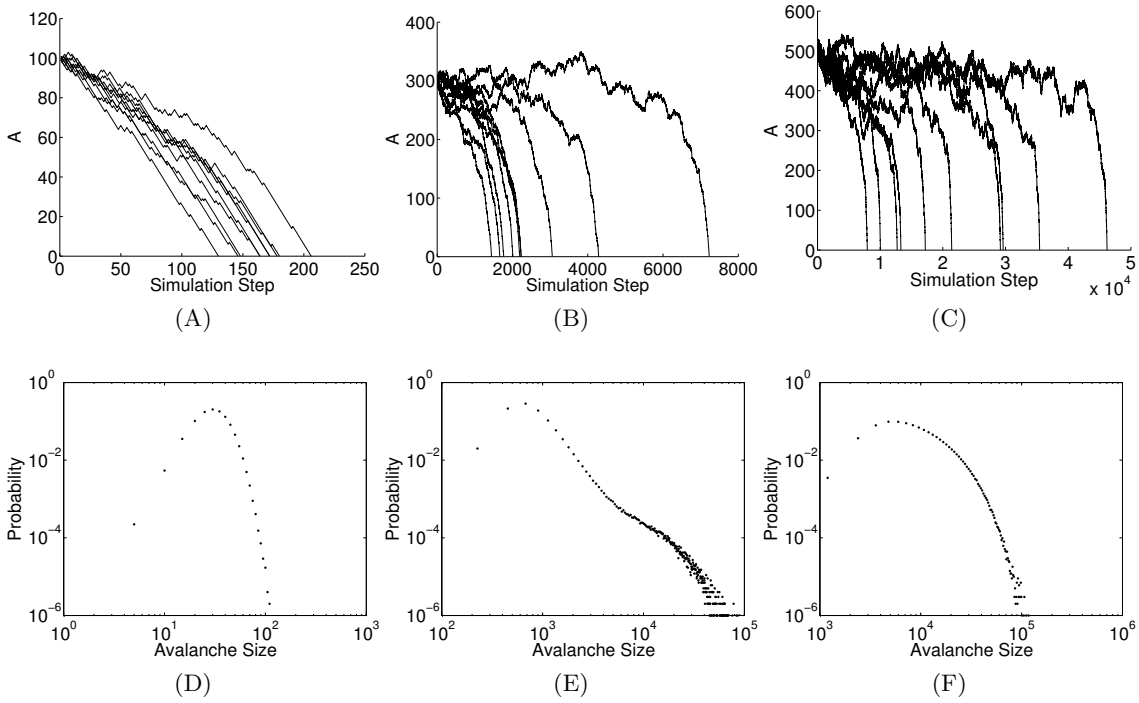

Figure 7.3: (A-C) Number of active neurons at each simulation step for 10 simulations of the system with the quadratic activation function and no external input. (D-F) Number of neurons that fire until the activity dies out for 1,000,000 simulations of the same system. Initially 100 (A,D), 300 (B,E) and 500 (C,F) neurons were randomly chosen and set to the active state. For all simulations the parameters were $N = 800,\ w = 1,\ \alpha = (1/4)wN$. The system has two fixed points: 0 (stable, absorbing state) and $N/2 = 400$ (critical eigenvalue).

Recall that the single seeding of an active neuron in the case of the linear activation function perturbs the system away from the critical fixed point (at zero) by one. Therefore the analogous situation here is not in fact to consider the return to the absorbing fully quiescent state, as was examined in Fig. 7.3, but to perturb the system 1 above the critical fixed point, that is to set the number of initial active neurons to $(N/2) + 1$. The avalanche is then finished when the dynamics reach this critical point (i.e. when the number of active neurons first equals $N/2$). The size of the avalanche is again defined as the number of neurons that fire within the avalanche. The distribution of avalanche sizes is shown in Fig. 7.4. This figure also shows the distribution of avalanche sizes for sub-critical and super-critical parameter sets. The parameters for these simulations come from setting the fixed point to be $A^* = N/2$. From this the eigenvalue of the fixed point (and therefore the branching parameter) can be calculated and so we find that $\alpha = \frac{wN}{4\sigma}$. Simulations were carried out with $\sigma = 0.9$ (subcritical) and $\sigma = 1.1$ (supercritical).

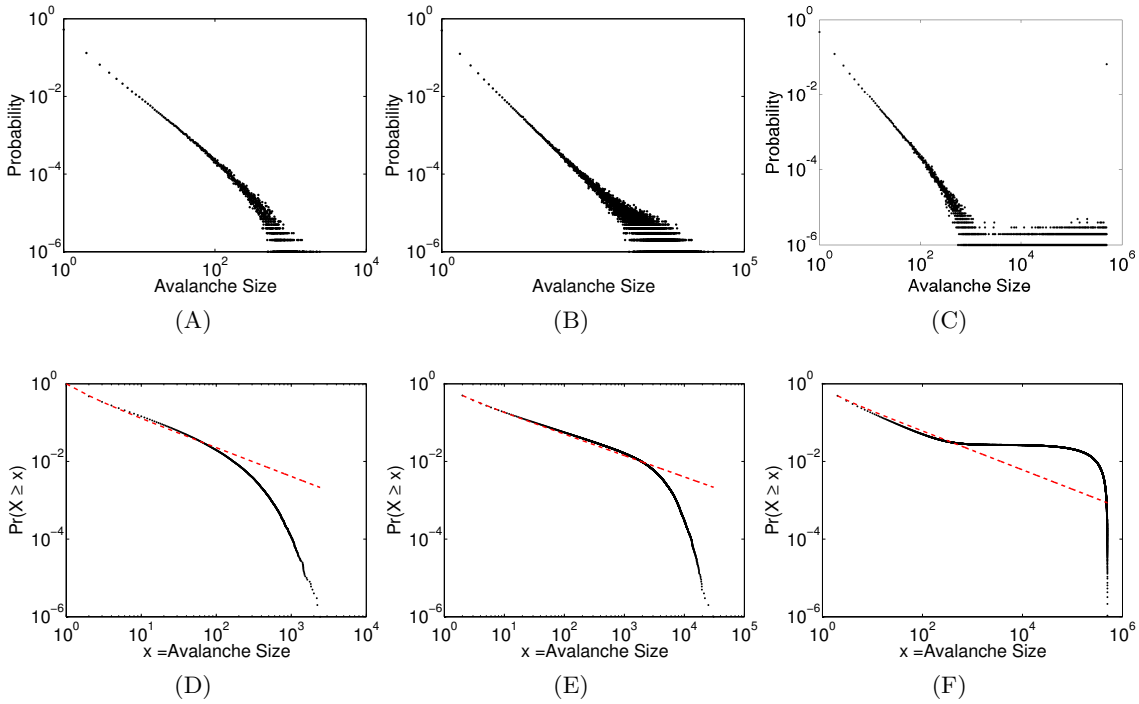

Figure 7.4: (A-C) Distribution of avalanche sizes for the system with the quadratic activation function and no external input and the corresponding cumulative distributions (D-F). (A,D) Parameters are such that the branching parameter is sub-critical: $N = 800,\ w = 1,\ \alpha = 0.25(wN/0.9) = 222.22$. (B,E) Parameters such that the fixed point is critical: $N = 800,\ w = 1,\ \alpha = 0.25wN = 200$. (C,F) Parameters such that the fixed point is super-critical: $N = 800,\ w = 1,\ \alpha = 0.25(wN/1.1) = 181.82$. All simulations began with $401 = (N/2) + 1$ randomly chosen neurons set to the active state. An avalanche was defined as the network firing until the number of active neurons reached the fixed point $(N/2)$. Note that in the super-critical case, avalanche simulations were stopped when the avalanche size reached 500,000 due to simulation speed. The outlier at 500,000 indicates that a number of avalanches reached this threshold. However, even with this threshold imposed, it is clear that the network dynamics for these parameter values are supercritical, with a large proportion of very large avalanches. Note that these outliers were removed from the cumulative distribution. The best fit of the distribution by a power-law are shown in red on the cumulative plots and have exponents (using the approach of [134]) of (D) $\gamma = 1.74,\ x_m = 1$ (E) $\gamma = 1.55,\ x_m = 2$, (F) $\gamma = 1.5,\ x_m = 2$.

Now consider positive external input: $h > 0$. Parameters can be chosen in such a way as to satisfy equation 7.2.2. For example, setting $N = 800,\ w = 0.001,\ h = 1/N$ the critical fixed point is $A = 33.01$ and $\alpha = 0.061$. An example simulation with such parameters is shown in Fig. 7.5. We see that the dynamics quickly make a transition from an initially low level of activity to a higher activity level. From the mean field equations (7.2.1) one can see that there is another (positive) fixed point at $A = 734.0$ of the system with these parameters. This fixed point is stable and acts as an attractor for the dynamics - Fig. 7.5B shows that the number of active neurons quickly increases to be in the region of this fixed point. As the dynamics are attracted to this other fixed point they are not affected by the critical fixed point. Therefore, it appears an additional constraint is required in order to obtain power-law dynamics with the system at a critical fixed point - the system must have a single fixed point which is critical.

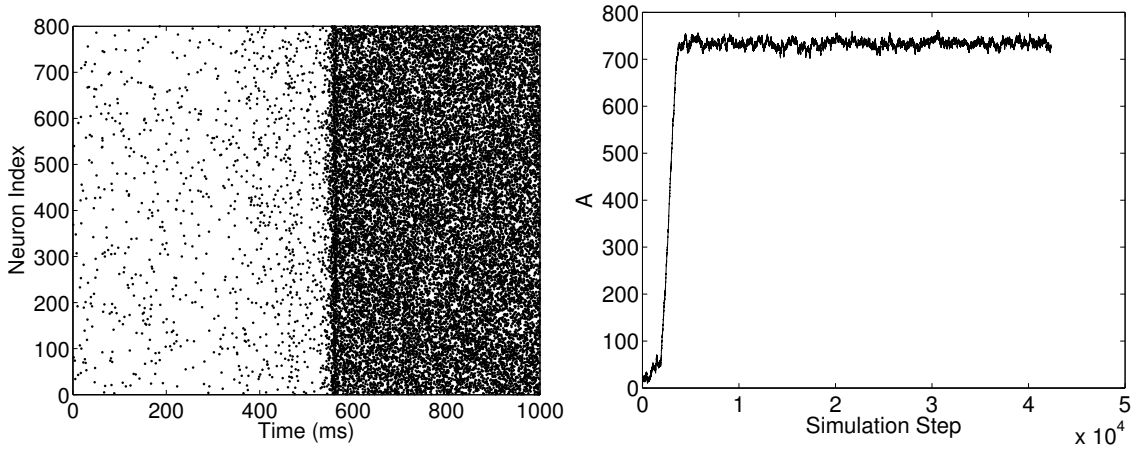

(A) (B)

Figure 7.5: Dynamics for a network with quadratic activation function and non-zero input. (A) Raster firing plot of network dynamics. (B) Number of active neurons at each step in the simulation. Network parameters were $N = 800,\ w = 0.001,\ h = 1/N$, which leads to a critical fixed point (by equation 7.2.2) at $A = 33.01$ and with $\alpha = 0.061$. However, the system also has a stable fixed point (eigenvalue = -0.61) at 734.0. The dynamics appear to quickly move away from the critical fixed point and are attracted to this stable fixed point.

Given that $f(A)$ is a cubic equation, to achieve a single fixed point which is critical, this point must be an inflection point with $f'(A) = 0$ and $f''(A) = 0$. From the second equality:

$$2wN - 6wA = 0 \ \Rightarrow \ A = N/3$$

Substituting this value of A into equation 7.2.2 we have that $h = \frac{wN}{27}$ and $\alpha = \frac{8wN}{27}$. So for any values of w and N this parameter set will lead to a system with a single critical fixed point. An example simulation of such a system with $N = 800,\ w = 0.01$ is shown in Fig. 7.6.

To assess the dynamics, a analogous approach to the one used above is employed. An avalanche is defined as a single excursion from the fixed point. However, note that as the

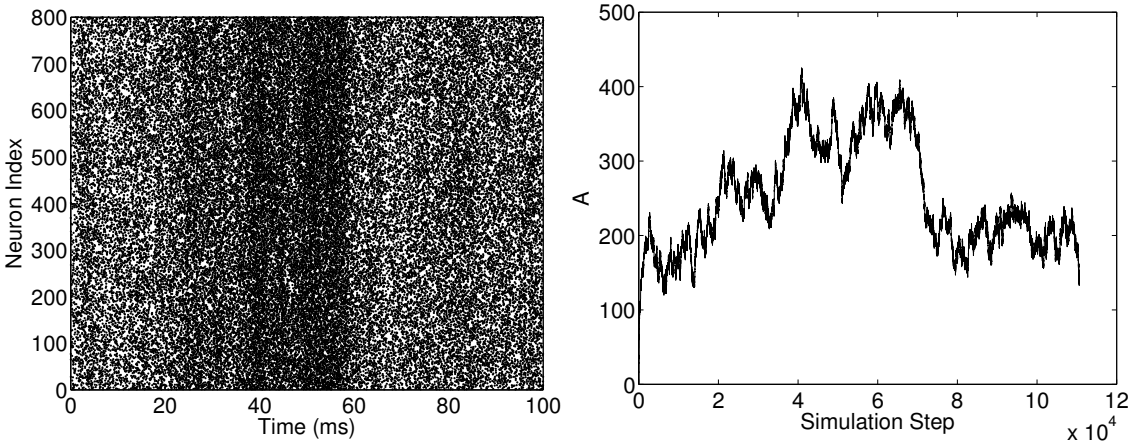

(A) (B)

Figure 7.6: Simulation of network dynamics for a network with quadratic activation function, non-zero input and a single fixed point which is critical. (A) Raster plot of firing dynamics. Note the slight increase in firing between 40-60ms. Longer simulations also exhibit these fluctuations in firing rate, giving an indication that the dynamics are non-trivial. (B) The number of active neurons, A, at each simulation step. The single critical fixed point of the system is $A = N/3 = 266.67$ as $N = 800$. The other parameters were set to $w = 0.01,\ h = \frac{wN}{27}$ and $\alpha = \frac{8wN}{27}$. Note that for this (short) simulation the number of active neurons fluctuates about the fixed point. Fig. 7.7 shows the level of the fluctuations about this fixed point for much longer simulations.

fixed point is positive and is the single fixed point (so zero is not an absorbing state) the excursion can start with either an increase or decrease away from the fixed point and the avalanche finishes when the dynamics next cross the fixed point i.e. the number of active neurons $A = N/3$. Fig. 7.7 shows the distributions of sizes of these avalanches. The figure also shows the distribution of sizes of avalanches which are formed from positive excursions only, in order to check that both types (positive and negative) of excursions are the same. Indeed, as would be expected from a critical system the distribution in both cases (all excursions and only positive excursions) appears to follow a power-law.

If the dynamics at this critical point are indeed 'critical' then one would expect that the power-law distributions are lost if the parameters are perturbed away from this critical state. For consistency within the simulations $N/3$ should remain a fixed point while the parameters are changed so that the branching parameter is altered. Recall that $\sigma = (\lambda/\alpha) + 1$. Therefore, from equations 7.2.1 and letting $A = N/3$:

$$\begin{aligned} \alpha &= \frac{wN}{3\sigma} - \frac{h}{\sigma} \\ \Rightarrow h &= \frac{(3 - 2\sigma)wN}{9(2\sigma + 1)} \end{aligned} \tag{7.2.3}$$

Setting $N = 800,\ w = 0.001$ as before, for $\sigma = 0.9 \Rightarrow h = 0.38,\ \alpha = 2.54$ and for $\sigma = 1.1 \Rightarrow h = 0.22,\ \alpha = 2.22$. Distributions of avalanche sizes (again excursions from the fixed point) for simulations with these sub and super-critical parameter values are

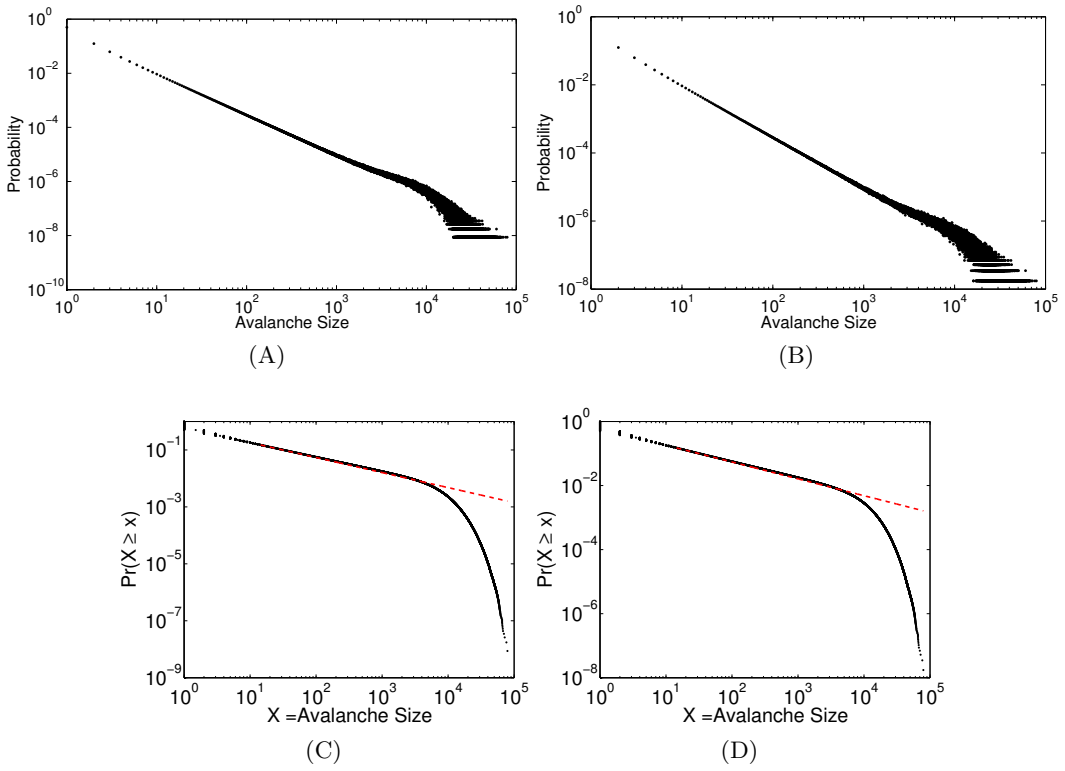

Figure 7.7: 20 simulations of length 1,000 seconds were carried out for networks with parameters $N = 800,\ w = 0.01,\ h = \frac{wN}{27} = 0.30,\ \alpha = \frac{8wN}{27} = 2.37$. This system therefore had a single fixed point at $A = N/3$ and the fixed point is critical. Avalanches were defined as excursions (either positive or negative) from the critical fixed point and the size of the avalanche was defined as the number of neurons that fire during the avalanche. (A) Distribution of avalanche sizes pooled from all 20 simulations. (B) Distribution of avalanche sizes from positive excursions only. (C,D) The corresponding cumulative distributions, with the red line indicating the best-fit to the data by a power-law following the approach of [134]. This yielded exponents of (C) $\gamma = 1.527,\ x_m = 14.5$ and (D) $\gamma = 1.525,\ x_m = 14.5$.

shown in Fig. 7.8. For the super-critical case the distribution clearly has a high proportion of large avalanches. The difference in the sub-critical case is not so apparent, however, comparing with the critical case (Fig. 7.7) one can see that the tail of the distribution is different between the two and in the critical case the power-law extends to a larger size.

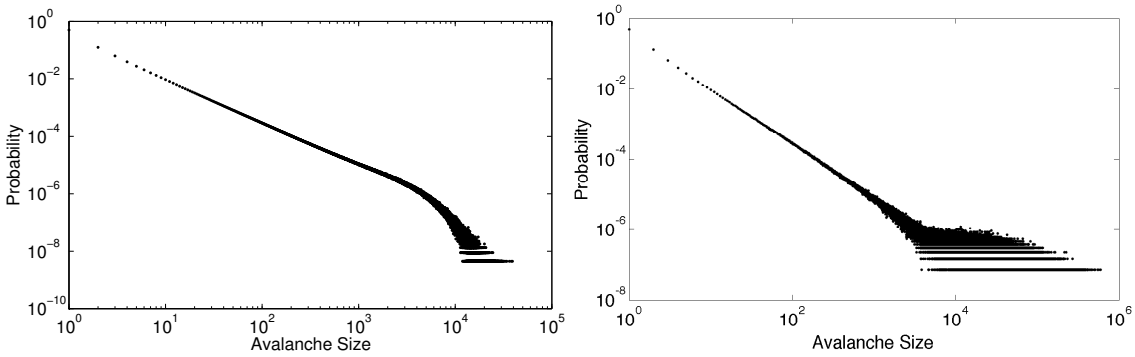

(A) (B)

Figure 7.8: Distribution of avalanche sizes (defined as excursions from the fixed point) from the system dynamics with parameters such that the branching parameter is (A) sub-critical $\sigma = 0.9,\ N = 800,\ w = 0.01,\ h = 0.38,\ \alpha = 2.54$ and (B) super-critical $\sigma = 1.1,\ N = 800,\ w = 0.01,\ h = 0.22,\ \alpha = 2.22$. This should be compared with Fig. 7.7 where the parameters were such that the branching parameter is critical.

Through this analysis we have seen that there is evidence of power-law dynamics at critical fixed points for the system in the presence of non-zero external input. However, analysing the dynamics in this way, by assessing the excursion from the fixed point, does not examine the firing dynamics of the system in a way that would be carried out in an experimental setting and furthermore it does not yield statistics that are analogous to those observed experimentally such as inter-avalanche intervals. Therefore to analyse the simulations further the binning method of *Benayoun et al.* [61] was used to separate the firing dynamics into avalanches, as has been done in the previous chapters. Fig. 7.9 shows the distributions found using this approach. Both avalanche size and IAI appeared to be exponentially distributed. This is interesting as we have seen that from the more analytical approach to define the avalanches they did indeed exhibit apparent power-law behaviour. The discrepancy here is likely to be as the firing is fairly dense - see Fig. 7.6 - and as the binning method necessarily divides the firing into avalanches. Given that the binning is related to the average firing rate, this division into separate avalanches is likely to occur when there are higher number of active neurons (and so $a \to q$ transitions are more likely), which is unrelated to passing the critical fixed point, as was used in the other approach to define the avalanches. This finding highlights the fact that binning of (experimental) data may not always reveal underlying 'critical' behaviour.

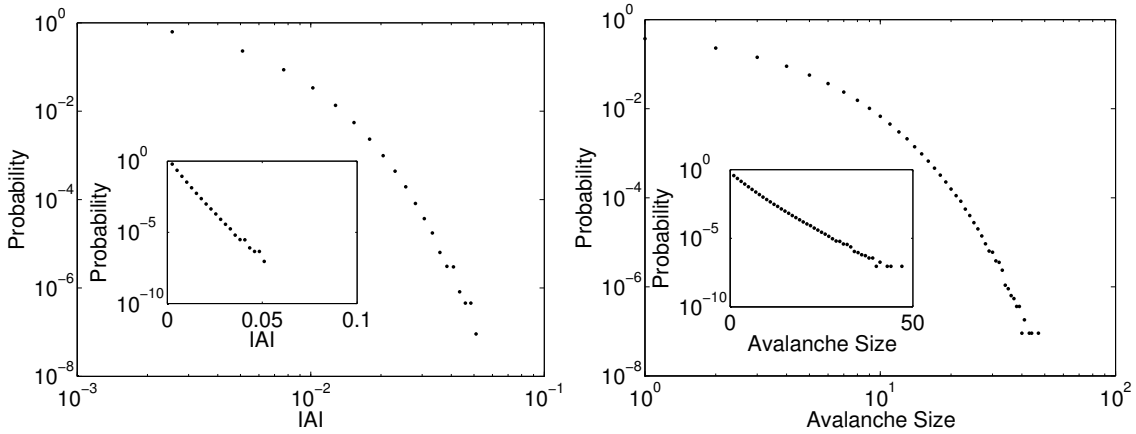

(A) (B)

Figure 7.9: IAI (A) and avalanche size (B) calculated using the firing binning method [61]. Insets for each show the same distribution plotted on a semi-logarithmic axis. Both exhibit a linear relationship on this scale suggesting that the distributions are exponential.

7.3 Avalanche binning method

Avalanches were assessed in two ways. For the system with no external input, a single neuron was set to the active state and an avalanche was defined as the firing that occurred until the system returned to the absorbing fully quiescent fixed point. This approach is similar to the definition of an avalanche in a SOC system [55] where the avalanche is the 'firing' that occurs until the system returns to an equilibrium. However, this approach does not take into account the burst nature of the dynamics and does not lead to periods of inter-avalanche intervals, even in the presence of external input (as was seen in the previous section). Furthermore, this approach does not take into account the temporal characteristics of the neuronal firing and so is not similar to how avalanches are defined in the experimental setting. For these reasons a different method was used when examining continuous firing activity. This method uses a binning approach to divide neuronal firing into avalanches and so takes into account the temporal characteristics of the firing and leads directly to measurements of IAIs.

The binning method used is from *Benayoun et al.* [61], where an avalanche is defined as a sequence of spikes such that no two consecutive spikes in the avalanche are separated by a time greater than dt, where dt is the average time between consecutive spikes within the network. Thus, the minimum IAI is dt. This method differs slightly from that used in experimental definitions of neuronal avalanches [49, 50] where firing is binned into bins of width dt. An avalanche is then defined as consecutive bins in which at least one neuron fires, preceded by and followed by a bin with no firing. With this method, it is possible for two consecutive neurons to fire with a difference between spikes of greater than dt but to be within the same avalanche. This is unlike the method of *Benayoun et al.* - which was used in this thesis - where such spikes will always be separated into two avalanches, for example see Fig. 7.10. This leads to some differences in the distributions, though overall the shape of the distributions is the same - see Fig. 7.11.

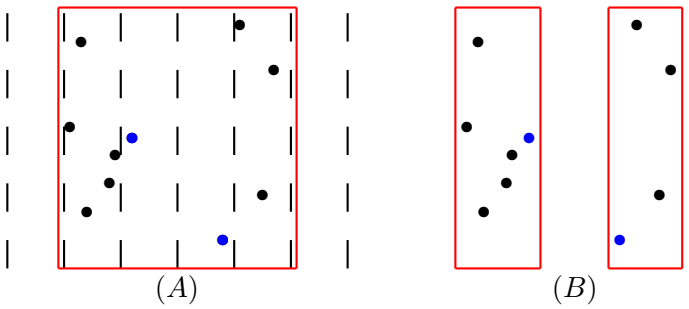

Figure 7.10: Firing dynamics binned using the two different methods into avalanches as indicated by the red boxes. (A) Binning using the experimental method [49, 50], with bins (as indicated by the dashed lines) of equidistant width dt. Avalanches are defined by consecutive bins in which there is spiking present so this firing pattern is a single avalanche. Note however, that the two blue spikes are actually greater than dt apart. Therefore, the same firing pattern when separated using the *Benayoun et al.* [61] method (B) is separated into two avalanches.

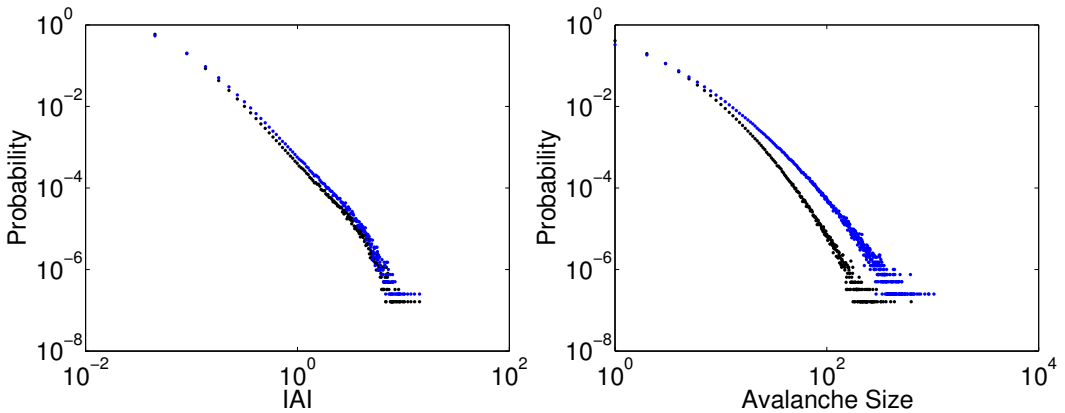

Figure 7.11: (A) IAI and (B) avalanche size distributions from a simulation with $N = 800$, $\alpha = 1$, $w = 1$, $h = 1/N$ using the two binning approaches. The distributions shown in blue were those found using the experimental binning approach [49, 50] - Fig. 7.10(A). The black distributions are found using the approach that has been used throughout the rest of this thesis [61]. As expected from Fig. 7.10, the number of avalanches detected using the experimental method was considerably lower than the number detected using the other approach - 3992082 in comparison with 6181142 avalanches respectively. This accounts for the higher probability of larger avalanches from the experimental binning method.

Chapter 8

References

[1] Gould, E. (2007) *Nat Rev Neurosci* **8(6)**, 481–8.

[2] Cherubini, E., Gaiarsa, J. L., and Ben-Ari, Y. (1991) *Trends Neurosci* **14(12)**, 515–9.

[3] Rivera, C., Voipio, J., Payne, J. A., Ruusuvuori, E., Lahtinen, H., Lamsa, K., Pirvola, U., Saarma, M., and Kaila, K. (1999) *Nature* **397(6716)**, 251–5.

[4] Ben-Ari, Y. (2002) *Nat Rev Neurosci* **3(9)**, 728–39.

[5] Voigt, T., Opitz, T., and deLima, A. D. (2001) *J Neurosci* **21(22)**, 8895–905.

[6] Allendoerfer, K. L. and Shatz, C. J. (1994) *Annu Rev Neurosci* **17**, 185–218.

[7] Bystron, I., Blakemore, C., and Rakic, P. (2008) *Nat Rev Neurosci* **9(2)**, 110–22.

[8] Friauf, E., McConnell, S. K., and Shatz, C. J. (1990) *J Neurosci* **10(8)**, 2601–13.

[9] Kostović, I. and Judas, M. (2010) *Acta Paediatr* **99(8)**, 1119–27.

[10] Meyer, G., Schaaps, J. P., Moreau, L., and Goffinet, A. M. (2000) *J Neurosci* **20(5)**, 1858–68.

[11] Katz, L. C. and Shatz, C. J. (1996) *Science* **274(5290)**, 1133–8.

[12] Kilb, W., Kirischuk, S., and Luhmann, H. J. (2011) *Eur J Neurosci* **34(10)**, 1677–86.

[13] Huttenlocher, P. R. and Dabholkar, A. S. (1997) *J Comp Neurol* **387(2)**, 167–78.

[14] Pascual-Leone, A., Amedi, A., Fregni, F., and Merabet, L. B. (2005) *Annu Rev Neurosci* **28**, 377–401.

[15] Galli, L. and Maffei, L. (1988) *Science* **242(4875)**, 90–1.

[16] Meister, M., Wong, R. O., Baylor, D. A., and Shatz, C. J. (1991) *Science* **252(5008)**, 939–43.

[17] Wong, R. O., Meister, M., and Shatz, C. J. (1993) *Neuron* **11(5)**, 923–38.

[18] Shatz, C. J. and Stryker, M. P. (1988) *Science* **242(4875)**, 87–9.

[19] O'Donovan, M., Sernagor, E., Sholomenko, G., Ho, S., Antal, M., and Yee, W. (1992) *J Exp Zool* **261(3)**, 261–73.

[20] Ren, J. and Greer, J. J. (2003) *J Neurophysiol* **89(3)**, 1187–95.

[21] Baker, R. E., Corner, M. A., and Habets, A. M. (1984) *J Neurosci* **4(5)**, 1187–92.

[22] Jansen, J. K., Lomo, T., Nicolaysen, K., and Westgaard, R. H. (1973) *Science* **181(4099)**, 559–61.

[23] Dupont, E., Hanganu, I. L., Kilb, W., Hirsch, S., and Luhmann, H. J. (2006) *Nature* **439(7072)**, 79–83.

[24] Khazipov, R., Sirota, A., Leinekugel, X., Holmes, G. L., Ben-Ari, Y., and Buzsáki, G. (2004) *Nature* **432(7018)**, 758–61.

[25] Khazipov, R. and Luhmann, H. J. (2006) *Trends Neurosci* **29(7)**, 414–8.

[26] André, M., Lamblin, M.-D., d'Allest, A. M., Curzi-Dascalova, L., Moussalli-Salefranque, F., S Nguyen The, T., Vecchierini-Blineau, M.-F., Wallois, F., Walls-Esquivel, E., and Plouin, P. (2010) *Neurophysiol Clin* **40(2)**, 59–124.

[27] Selton, D., Andre, M., and Hascoët, J. M. (2000) *Clin Neurophysiol* **111(12)**, 2116–24.

[28] Hellström-Westas, L. and Rosén, I. (2005) *Early Hum Dev* **81(3)**, 255–61.

[29] Milh, M., Kaminska, A., Huon, C., Lapillonne, A., Ben-Ari, Y., and Khazipov, R. (2007) *Cereb Cortex* **17(7)**, 1582–94.

[30] Thornorsteinsson, H., Reynisson, H. M., Sigurethardóttir, L. Y., Dagbjartsson, A., and Karlsson, K. A. E. (2010) *Behav Brain Res* **211(1)**, 11–5.

[31] Bi, G. Q. and Poo, M. M. (1998) *J Neurosci* **18(24)**, 10464–72.

[32] Engel, A. K., Kreiter, A. K., König, P., and Singer, W. (1991) *Proc Natl Acad Sci U S A* **88(14)**, 6048–52.

[33] Farmer, S. F. (1998) *J Physiol* **509 (Pt 1)**, 3–14.

[34] von derMalsburg, C. (1995) *Curr Opin Neurobiol* **5(4)**, 520–6.

[35] Schumacher, E. M., Westvik, A. S., Larsson, P. G., Lindemann, R., Westvik, J., and Stiris, T. A. (2011) *Pediatr Res* **69(5 Pt 1)**, 413–7.

[36] Kinouchi, O. and Copelli, M. (2006) *Nature Physics* **2(5)**, 348–352.

[37] Shew, W. L., Yang, H., Petermann, T., Roy, R., and Plenz, D. (2009) *J Neurosci* **29(49)**, 15595–600.

[38] Shew, W. L. and Plenz, D. (2012) *Neuroscientist*.

[39] Linkenkaer-Hansen, K., Nikouline, V. V., Palva, J. M., and Ilmoniemi, R. J. (2001) *J Neurosci* **21(4)**, 1370–7.

[40] Linkenkaer-Hansen, K., Nikulin, V. V., Palva, J. M., Kaila, K., and Ilmoniemi, R. J. (2004) *Eur J Neurosci* **19(1)**, 203–11.

[41] Nikulin, V. V. and Brismar, T. (2004) *Clin Neurophysiol* **115(8)**, 1896–908.

[42] Nikulin, V. V. and Brismar, T. (2005) *Neuroscience* **130(2)**, 549–58.

[43] Linkenkaer-Hansen, K., Smit, D. J. A., Barkil, A., vanBeijsterveldt, T. E. M., Brussaard, A. B., Boomsma, D. I., vanOoyen, A., and deGeus, E. J. C. (2007) *J Neurosci* **27(50)**, 13882–9.

[44] Berthouze, L., James, L. M., and Farmer, S. F. (2010) *Clin Neurophysiol* **121(8)**, 1187–97.

[45] Smit, D. J. A., deGeus, E. J. C., van deNieuwenhuijzen, M. E., vanBeijsterveldt, C. E. M., vanBaal, G. C. M., Mansvelder, H. D., Boomsma, D. I., and Linkenkaer-Hansen, K. (2011) *J Neurosci* **31(37)**, 13128–36.

[46] Kitzbichler, M. G., Smith, M. L., Christensen, S. R., and Bullmore, E. (2009) *PLoS Comput Biol* **5(3)**, e1000314.

[47] Parish, L. M., Worrell, G. A., Cranstoun, S. D., Stead, S. M., Pennell, P., and Litt, B. (2004) *Neuroscience* **125(4)**, 1069–76.

[48] Bhattacharya, J., Edwards, J., Mamelak, A. N., and Schuman, E. M. (2005) *Neuroscience* **131(2)**, 547–55.

[49] Beggs, J. M. and Plenz, D. (2003) *J Neurosci* **23(35)**, 11167–77.

[50] Beggs, J. M. and Plenz, D. (2004) *J Neurosci* **24(22)**, 5216–29.

[51] Gireesh, E. D. and Plenz, D. (2008) *Proc Natl Acad Sci U S A* **105(21)**, 7576–81.

[52] Petermann, T., Thiagarajan, T. C., Lebedev, M. A., Nicolelis, M. A. L., Chialvo, D. R., and Plenz, D. (2009) *Proc Natl Acad Sci U S A* **106(37)**, 15921–6.

[53] Hahn, G., Petermann, T., Havenith, M. N., Yu, S., Singer, W., Plenz, D., and Nikolic, D. (2010) *J Neurophysiol* **104(6)**, 3312–22.

[54] Tetzlaff, C., Okujeni, S., Egert, U., Wörgötter, F., and Butz, M. (2010) *PLoS Comput Biol* **6(12)**, e1001013.

[55] Bak, P., Tang, C., and Wiesenfeld, K. (1987) *Phys Rev Lett* **59(4)**, 381–384.

[56] Jensen, H. J. (1998) Self-organized criticality: emergent complex behaviour in physical and biological systems, Cambridge University Press, .

[57] Wagenmakers, E.-J., Farrell, S., and Ratcliff, R. (2004) *Psychon Bull Rev* **11(4)**, 579–615.

[58] Bonachela, J. A. and Muñoz, M. A. (2009) *J. Stat. Mech.* p. P09009.

[59] Bak, Tang, and Wiesenfeld (1988) *Phys Rev A* **38(1)**, 364–374.

[60] Chialvo, D. R. (2010) *Nature Physics* **6(10)**, 744–750.

[61] Benayoun, M., Cowan, J. D., vanDrongelen, W., and Wallace, E. (2010) *PLoS Comput Biol* **6(7)**, e1000846.

[62] Yang, H., Shew, W. L., Roy, R., and Plenz, D. (2012) *J Neurosci* **32(3)**, 1061–72.

[63] Holmes, G. L., Khazipov, R., and Ben-Ari, Y. Jan 2002 *Neuroreport* **13(1)**, A3–8.

[64] Bystron, I., Rakic, P., Molnár, Z., and Blakemore, C. (2006) *Nat Neurosci* **9(7)**, 880–6.

[65] Kostovic, I. and Rakic, P. (1990) *J Comp Neurol* **297(3)**, 441–70.

[66] Kanold, P. O. and Luhmann, H. J. (2010) *Annu Rev Neurosci* **33**, 23–48.

[67] Caviness, Jr, V. S. (1982) *Brain Res* **256(3)**, 293–302.

[68] Angevine, Jr, J. B. and Sidman, R. L. (1961) *Nature* **192**, 766–8.

[69] Kostović, I. and Jovanov-Milosević, N. (2006) *Semin Fetal Neonatal Med* **11(6)**, 415–22.

[70] Sur, M. and Rubenstein, J. L. R. (2005) *Science* **310(5749)**, 805–10.

[71] Wiesel, T. N. (1982) *Nature* **299(5884)**, 583–91.

[72] Kanold, P. O., Kara, P., Reid, R. C., and Shatz, C. J. (2003) *Science* **301(5632)**, 521–5.

[73] Kanold, P. O. and Shatz, C. J. (2006) *Neuron* **51(5)**, 627–38.

[74] Tolner, E. A., Sheikh, A., Yukin, A. Y., Kaila, K., and Kanold, P. O. (2012) *J Neurosci* **32(2)**, 692–702.

[75] Ghosh, A. and Shatz, C. J. (1992) *Science* **255(5050)**, 1441–3.

[76] Kanold, P. O. (2009) *Front Neuroanat* **3**, 16.

[77] Kostović, I. and Judas, M. (2002) *Anat Rec* **267(1)**, 1–6.

[78] Dubois, J., Benders, M., Cachia, A., Lazeyras, F., Ha-Vinh Leuchter, R., Sizonenko, S. V., Borradori-Tolsa, C., Mangin, J. F., and Hüppi, P. S. (2008) *Cereb Cortex* **18(6)**, 1444–54.

[79] Toga, A. W. and Thompson, P. M. (2003) *Nat Rev Neurosci* **4(1)**, 37–48.

[80] Sidman, R. L. and Rakic, P. (1973) *Brain Res* **62(1)**, 1–35.

[81] Dreyfus-Brisac, C., Samsondollfus, D., and Fischgold, H. (1955) *Sem Hop* **31(3)**, 1783–90.

[82] Lamblin, M. D., André, M., Challamel, M. J., Curzi-Dascalova, L., d'Allest, A. M., De Giovanni, E., Moussalli-Salefranque, F., Navelet, Y., Plouin, P., Radvanyi-Bouvet, M. F., Samson-Dollfus, D., and Vecchierini-Blineau, M. F. (1999) *Neurophysiol Clin* **29(2)**, 123–219.

[83] Anderson, C. M., Torres, F., and Faoro, A. (1985) *Electroencephalogr Clin Neurophysiol* **60(2)**, 95–105.

[84] Niemarkt, H. J., Andriessen, P., Peters, C. H. L., Pasman, J. W., Zimmermann, L. J., and Bambang Oetomo, S. (2010) *Early Hum Dev* **86(4)**, 219–24.

[85] Flores Guevara, R., Giannuzzi, R., Nosralla, M. d. O., Vignolo, P., Moriette, G., and Maier, M. A. (2008) *Clin Neurophysiol* **119(1)**, 180–9.

[86] Hayakawa, M., Okumura, A., Hayakawa, F., Watanabe, K., Ohshiro, M., Kato, Y., Takahashi, R., and Tauchi, N. (2001) *Arch Dis Child Fetal Neonatal Ed* **84(3)**, F163–7.

[87] Bell, A. H., McClure, B. G., McCullagh, P. J., and McClelland, R. J. (1991) *J Clin Neurophysiol* **8(3)**, 312–9.

[88] Niemarkt, H. J., Jennekens, W., Pasman, J. W., Katgert, T., Van Pul, C., Gavilanes, A. W. D., Kramer, B. W., Zimmermann, L. J., Bambang Oetomo, S., and Andriessen, P. (2011) *Pediatr Res* **70(5)**, 529–34.

[89] Vecchierini, M.-F., d'Allest, A.-M., and Verpillat, P. (2003) *Brain Dev* **25(5)**, 330–7.

[90] Vanhatalo, S., Jousmäki, V., Andersson, S., and Metsäranta, M. (2009) *Pediatr Res* **66(6)**, 710–3.

[91] Fabrizi, L., Slater, R., Worley, A., Meek, J., Boyd, S., Olhede, S., and Fitzgerald, M. (2011) *Curr Biol* **21(18)**, 1552–8.

[92] Hanganu, I. L., Ben-Ari, Y., and Khazipov, R. (2006) *J Neurosci* **26(25)**, 6728–36.

[93] Vanhatalo, S. and Kaila, K. (2006) *Semin Fetal Neonatal Med* **11(6)**, 471–8.

[94] Vanhatalo, S., Tallgren, P., Andersson, S., Sainio, K., Voipio, J., and Kaila, K. (2002) *Clin Neurophysiol* **113(11)**, 1822–5.

[95] Vanhatalo, S., Palva, J. M., Andersson, S., Rivera, C., Voipio, J., and Kaila, K. (2005) *Eur J Neurosci* **22(11)**, 2799–804.

[96] Hellström-Westas, L. and Rosén, I. The Newborn Brain, Chapter 14 Cambridge University Press (2010).

[97] Vanhatalo, S. and Lauronen, L. (2006) *Semin Fetal Neonatal Med* **11(6)**, 464–70.

[98] Biagioni, E., Frisone, M. F., Laroche, S., Rutherford, M., Counsell, S., Cioni, G., Azzopardi, D., Mercuri, E., and Cowan, F. (2000) *Clin Neurophysiol* **111(12)**, 2145–9.

[99] Okumura, A., Hayakawa, F., Kato, T., Maruyama, K., Kubota, T., Suzuki, M., Kidokoro, H., Kuno, K., and Watanabe, K. (2003) *J Pediatr* **143(1)**, 26–30.

[100] Marret, S., Parain, D., Jeannot, E., Eurin, D., and Fessard, C. (1992) *Arch Dis Child* **67(7)**, 948–51.

[101] Benda, G. I., Engel, R. C., and Zhang, Y. P. (1989) *Electroencephalogr Clin Neurophysiol* **72(3)**, 189–97.

[102] Clancy, R. R. and Tharp, B. R. (1984) *Electroencephalogr Clin Neurophysiol* **57(5)**, 395–404.

[103] Connell, J., Oozeer, R., Regev, R., De Vries, L. S., Dubowitz, L. M., and Dubowitz, V. (1987) *Arch Dis Child* **62(10)**, 1019–24.

[104] Connell, J., deVries, L., Oozeer, R., Regev, R., Dubowitz, L. M., and Dubowitz, V. (1988) *Pediatrics* **82(3)**, 337–43.

[105] Watanabe, K., Hayakawa, F., and Okumura, A. (1999) *Brain Dev* **21(6)**, 361–72.

[106] Pitt, M. and Pressler, R. Dec 2005 *Early Hum Dev* **81(12)**, 939–46.

[107] Radvanyi-Bouvet, M. F., deBethmann, O., Monset-Couchard, M., and Fazzi, E. (1987) *Brain Dev* **9(4)**, 399–405.

[108] Biagioni, E., Bartalena, L., Boldrini, A., Cioni, G., Giancola, S., and Ipata, A. E. (1994) *Electroencephalogr Clin Neurophysiol* **91(3)**, 154–62.

[109] Le Bihannic, A., Beauvais, K., Busnel, A., deBarace, C., and Furby, A. (2012) *Arch Dis Child Fetal Neonatal Ed* **97(2)**, F106–9.

[110] Wikström, S., Pupp, I. H., Rosén, I., Norman, E., Fellman, V., Ley, D., and Hellström-Westas, L. (2012) *Acta Paediatr* **101(7)**, 719–26.

[111] Johnson, S., Fawke, J., Hennessy, E., Rowell, V., Thomas, S., Wolke, D., and Marlow, N. (2009) *Pediatrics* **124(2)**, e249–57.

[112] Johnson, S., Hennessy, E., Smith, R., Trikic, R., Wolke, D., and Marlow, N. (2009) *Arch Dis Child Fetal Neonatal Ed* **94(4)**, F283–9.

[113] Moster, D., Lie, R. T., and Markestad, T. (2008) *N Engl J Med* **359(3)**, 262–73.

[114] Field, D. J., Dorling, J. S., Manktelow, B. N., and Draper, E. S. (2008) *BMJ* **336(7655)**, 1221–3.

[115] Hahn, J. S., Monyer, H., and Tharp, B. R. (1989) *Electroencephalography and Clinical Neurophysiology* **73(5)**, 410–418.

[116] Eswaran, H., Haddad, N. I., Shihabuddin, B. S., Preissl, H., Siegel, E. R., Murphy, P., and Lowery, C. L. (2007) *Clin Neurophysiol* **118(9)**, 1940–6.

[117] Eswaran, H., Preissl, H., Wilson, J. D., Murphy, P., Robinson, S. E., Rose, D., Vrba, J., and Lowery, C. L. (2002) *Neurosci Lett* **331(2)**, 128–32.

[118] Eswaran, H., Wilson, J., Preissl, H., Robinson, S., Vrba, J., Murphy, P., Rose, D., and Lowery, C. (2002) *Lancet* **360(9335)**, 779–80.

[119] Arichi, T., Moraux, A., Melendez, A., Doria, V., Groppo, M., Merchant, N., Combs, S., Burdet, E., Larkman, D. J., Counsell, S. J., Beckmann, C. F., and Edwards, A. D. (2010) *Neuroimage* **49(3)**, 2063–71.

[120] Doria, V., Beckmann, C. F., Arichi, T., Merchant, N., Groppo, M., Turkheimer, F. E., Counsell, S. J., Murgasova, M., Aljabar, P., Nunes, R. G., Larkman, D. J., Rees, G., and Edwards, A. D. (2010) *Proc Natl Acad Sci U S A* **107(46)**, 20015–20.

[121] Scher, M. S., Sun, M., Steppe, D. A., Guthrie, R. D., and Sclabassi, R. J. (1994) *Pediatr Neurol* **10(2)**, 104–8.

[122] Slater, R., Fabrizi, L., Worley, A., Meek, J., Boyd, S., and Fitzgerald, M. (2010) *Neuroimage* **52(2)**, 583–9.

[123] Monod, N., Pajot, N., and Guidasci, S. (1972) *Electroencephalogr Clin Neurophysiol* **32(5)**, 529–44.

[124] Buzsáki, G. (2006) Rhythms of the brain, Oxford University Press, Oxford.

[125] Campbell, I. G. and Feinberg, I. (2009) *Proc Natl Acad Sci U S A* **106(13)**, 5177–80.

[126] Clarke, A. R., Barry, R. J., McCarthy, R., and Selikowitz, M. (2001) *Clin Neurophysiol* **112(5)**, 806–14.

[127] Gasser, T., Verleger, R., Bächer, P., and Sroka, L. (1988) *Electroencephalogr Clin Neurophysiol* **69(2)**, 91–9.

[128] Murthy, V. N. and Fetz, E. E. (1992) *Proc Natl Acad Sci U S A* **89(12)**, 5670–4.

[129] Conway, B. A., Halliday, D. M., Farmer, S. F., Shahani, U., Maas, P., Weir, A. I., and Rosenberg, J. R. (1995) *J Physiol* **489 (Pt 3)**, 917–24.

[130] Fries, P., Reynolds, J. H., Rorie, A. E., and Desimone, R. (2001) *Science* **291(5508)**, 1560–3.

[131] Schevon, C. A., Cappell, J., Emerson, R., Isler, J., Grieve, P., Goodman, R., McKhann, Jr, G., Weiner, H., Doyle, W., Kuzniecky, R., Devinsky, O., and Gilliam, F. (2007) *Neuroimage* **35(1)**, 140–8.

[132] Uhlhaas, P. J. and Singer, W. (2010) *Nat Rev Neurosci* **11(2)**, 100–13.

[133] James, L. M., Halliday, D. M., Stephens, J. A., and Farmer, S. F. (2008) *Eur J Neurosci* **27(12)**, 3369–79.

[134] Clauset, A., Shalizi, C. R., and Newman, M. E. J. (2009) *Siam Review* **51(4)**, 661–703.

[135] Omori, F. (1894) *J. Coll. Sci. Imper. Univ. Tokyo* **7**, 111–200.

[136] Guzzetti, F., Malamud, B., Turcotte, D., and Reichenbach, P. (2002) *Earth and Planetary Science Letters* **195(3-4)**, 169–183.

[137] Birkeland, K. and Landry, C. (2002) *Geophysical Research Letters* **29(11)**, 1554.

[138] Boffetta, G., Carbone, V., Giuliani, P., Veltri, P., and Vulpiani, A. (1999) *Physical Review Letters* **83(22)**, 4662–4665.

[139] Palma, W. (2007) Long-memory time series: theory and methods, Wiley-Interscience, Hoboken, N.J.

[140] Hurst, H. (1951) *Trans. Am. Soc. Civil Eng.* **116**, 770–808.

[141] Peng, C. K., Havlin, S., Stanley, H. E., and Goldberger, A. L. (1995) *Chaos* **5(1)**, 82–7.

[142] Linkenkaer-Hansen, K., Monto, S., Rytsälä, H., Suominen, K., Isometsä, E., and Kähkönen, S. (2005) *J Neurosci* **25(44)**, 10131–7.

[143] Montez, T., Poil, S.-S., Jones, B. F., Manshanden, I., Verbunt, J. P. A., vanDijk, B. W., Brussaard, A. B., vanOoyen, A., Stam, C. J., Scheltens, P., and Linkenkaer-Hansen, K. (2009) *Proc Natl Acad Sci U S A* **106(5)**, 1614–9.

[144] Nikulin, V. V., Jönsson, E. G., and Brismar, T. (2012) *Neuroimage* **61(1)**, 162–9.

[145] Gao, J., Hu, J., Tung, W.-W., Cao, Y., Sarshar, N., and Roychowdhury, V. P. (2006) *Phys Rev E Stat Nonlin Soft Matter Phys* **73(1 Pt 2)**, 016117.

[146] Binney, J., Dowrick, N., Fisher, A., and Newman, M. E. J. (1992) The Theory of critical phenomena: an introduction to the renormalization group, Clarendon Press, Oxford.

[147] Bak, P. (1990) *Physica A* **163**, 403–409.

[148] Bak, P. (1996) How nature works: the science of self-organized criticality, Copernicus, New York, NY, USA.

[149] Levina, A., Herrmann, J. M., and Geisel, T. (2007) *Nature Physics* **3(1)**, 857–860.

[150] Bonachela, J. A., deFranciscis, S., Torres, J. J., and Muñoz, M. A. (2010) *J. Stat. Mech.* p. P02015.

[151] Olami, Z., Feder, H., and Christensen, K. (1992) *Phys Rev Lett* **68(8)**, 1244–1247.

[152] Corral, A., Pérez, C., Díaz-Guilera, A., and Arenas, A. (1995) *Phys Rev Lett* **74(1)**, 118–121.

[153] daSilva, L., Papa, A., and deSouza, A. (1998) *Physics Letters a* **242(6)**, 343–348.

[154] Lin, M. and Chen, T. (2005) *Physical Review E* **71(1)**, 016133.

[155] Touboul, J. and Destexhe, A. (2010) *PLoS One* **5(2)**, e8982.

[156] Hausdorff and Peng (1996) *Phys Rev E Stat Phys Plasmas Fluids Relat Interdiscip Topics* **54(2)**, 2154–2157.

[157] Torre, K. and Wagenmakers, E.-J. (2009) *Hum Mov Sci* **28(3)**, 297–318.

[158] Chen, Y., Ding, M., and Kelso, J. A. (2001) *J Mot Behav* **33(1)**, 3–8.

[159] Poil, S.-S., Hardstone, R., Mansvelder, H. D., and Linkenkaer-Hansen, K. (2012) *J Neurosci* **32(29)**, 9817–23.

[160] Shew, W. L., Yang, H., Yu, S., Roy, R., and Plenz, D. (2011) *J Neurosci* **31(1)**, 55–63.

[161] Klaus, A., Yu, S., and Plenz, D. (2011) *PLoS One* **6(5)**, e19779.

[162] Taqqu, M., Teverovsky, V., and Willinger, W. (1995) *Fractals* **3(4)**, 785–798.

[163] Peng, C. K., Buldyrev, S. V., Havlin, S., Simons, M., Stanley, H. E., and Goldberger, A. L. (1994) *Phys Rev E Stat Phys Plasmas Fluids Relat Interdiscip Topics* **49(2)**, 1685–9.

[164] McSharry, P. (2005, Last checked: 11 January 2011) *DFA Matlab code found on the website of the Systems analysis, modelling and prediction group, Department of Engineering Sciences, University of Oxford. Available: http://www.eng.ox.ac.uk/samp/software/ cardiodynamics/dfa.m.*

[165] Wilson, C. J. and Kawaguchi, Y. (1996) *J Neurosci* **16(7)**, 2397–410.

[166] Lombardi, F., Herrmann, H. J., Perrone-Capano, C., Plenz, D., and deArcangelis, L. (2012) *Phys Rev Lett* **108(22)**, 228703.

[167] Victor, S., Appleton, R. E., Beirne, M., Marson, A. G., and Weindling, A. M. (2005) *Pediatr Res* **57(3)**, 336–41.

[168] Lago-Fernández, L. F., Huerta, R., Corbacho, F., and Sigüenza, J. A. (2000) *Phys Rev Lett* **84(12)**, 2758–61.

[169] Percha, B., Dzakpasu, R., Zochowski, M., and Parent, J. (2005) *Phys Rev E Stat Nonlin Soft Matter Phys* **72(3 Pt 1)**, 031909.

[170] Grinstein, G. and Linsker, R. (2005) *Proc Natl Acad Sci U S A* **102(28)**, 9948–53.

[171] Netoff, T. I., Clewley, R., Arno, S., Keck, T., and White, J. A. (2004) *J Neurosci* **24(37)**, 8075–83.

[172] Bi, G. and Poo, M. (2001) *Annu Rev Neurosci* **24**, 139–66.

[173] Constantine-Paton, M. and Cline, H. T. (1998) *Curr Opin Neurobiol* **8(1)**, 139–48.

[174] Biagioni, E., Frisone, M. F., Laroche, S., Kapetanakis, B. A., Ricci, D., Adeyi-Obe, M., Lewis, H., Kennea, N., Cioni, G., Cowan, F., Rutherford, M., Azzopardi, D., and Mercuri, E. (2007) *Clin Neurophysiol* **118(1)**, 53–9.

[175] Hartley, C., Berthouze, L., Mathieson, S. R., Boylan, G. B., Rennie, J. M., Marlow, N., and Farmer, S. F. (2012) *PLoS One* **7(2)**, e31543.

[176] Klem, G. H., Lüders, H. O., Jasper, H. H., and Elger, C. (1999) *Electroencephalogr Clin Neurophysiol Suppl* **52**, 3–6.

[177] Palmu, K., Wikström, S., Hippeläinen, E., Boylan, G., Hellström-Westas, L., and Vanhatalo, S. (2010) *Clin Neurophysiol* **121(7)**, 1015–22.

[178] Chan, D. W. S., Yamazaki, M., Akiyama, T., Chu, B., Donner, E. J., and Otsubo, H. (2010) *Brain Dev* **32(6)**, 482–6.

[179] Hu, K., Ivanov, P. C., Chen, Z., Carpena, P., and Stanley, H. E. (2001) *Phys Rev E Stat Nonlin Soft Matter Phys* **64(1 Pt 1)**, 011114.

[180] Segev, R., Benveniste, M., Hulata, E., Cohen, N., Palevski, A., Kapon, E., Shapira, Y., and Ben-Jacob, E. (2002) *Phys Rev Lett* **88(11)**, 118102.

[181] Thompson, D. K., Warfield, S. K., Carlin, J. B., Pavlovic, M., Wang, H. X., Bear, M., Kean, M. J., Doyle, L. W., Egan, G. F., and Inder, T. E. (2007) *Brain* **130(Pt 3)**, 667–77.

[182] Barry, R. J., Clarke, A. R., McCarthy, R., and Selikowitz, M. Mar 2005 *Int J Psychophysiol* **55(3)**, 313–21.

[183] Epstein, C. M. and Brickley, G. P. Apr 1985 *Electroencephalogr Clin Neurophysiol* **60(4)**, 287–92.

[184] Hohlefeld, F. U., Huebl, J., Huchzermeyer, C., Schneider, G.-H., Schönecker, T., Kühn, A. A., Curio, G., and Nikulin, V. V. Sep 2012 *Eur J Neurosci* **36(6)**, 2812–21.

[185] Battin, M. R., Maalouf, E. F., Counsell, S. J., Herlihy, A. H., Rutherford, M. A., Azzopardi, D., and Edwards, A. D. (1998) *Pediatrics* **101(6)**, 957–62.

[186] Kostović, I., Lukinović, N., Judas, M., Bogdanović, N., Mrzljak, L., Zecević, N., and Kubat, M. (1989) *Metab Brain Dis* **4(1)**, 17–23.

[187] Ishiwa, S., Ogawa, T., and Sonoda, H. (1991) *Brain Topogr* **4(1)**, 23–30.

[188] Jennekens, W., Niemarkt, H. J., Engels, M., Pasman, J. W., vanPul, C., and Andriessen, P. (2012) *Clin Neurophysiol*.

[189] Curzi-Dascalova, L., Figueroa, J. M., Eiselt, M., Christova, E., Virassamy, A., d'Allest, A. M., Guimarâes, H., Gaultier, C., and Dehan, M. Nov 1993 *Pediatr Res* **34(5)**, 624–8.

[190] Faul, F., Erdfelder, E., Buchner, A., and Lang, A.-G. Nov 2009 *Behav Res Methods* **41(4)**, 1149–60.

[191] Nakagawa, S. and Cuthill, I. C. Nov 2007 *Biol Rev Camb Philos Soc* **82(4)**, 591–605.

[192] Cohen, J. Jul 1992 *Psychol Bull* **112(1)**, 155–9.

[193] Manneville, P. (1980) *Journal De Physique* **41(11)**, 1235–1243.

[194] Heagy, J., Platt, N., and Hammel, S. (1994) *Physical Review E* **49(2)**, 1140–1150.

[195] Harris, T. E. (1963) The theory of branching processes, Die Grundlehren der mathematischen Wissenschaften in EinzeldarstellungenSpringer, Berlin.

[196] Kaiser, M., Goerner, M., and Hilgetag, C. (2007) *New J. Phys.* **9**, 110.

[197] Kaiser, M. and Hilgetag, C. C. (2010) *Front Neuroinform* **4**, 8.

[198] Gillespie, D. (1977) *Journal of Physical Chemistry* **81(25)**, 2340–2361.

[199] Zapperi, K, B. L., and Stanley (1995) *Phys Rev Lett* **75(22)**, 4071–4074.

[200] Buice, M. A. and Cowan, J. D. (2009) *Prog Biophys Mol Biol* **99(2-3)**, 53–86.

[201] Buice, M. A. and Cowan, J. D. (2007) *Phys Rev E Stat Nonlin Soft Matter Phys* **75(5 Pt 1)**, 051919.

[202] Buice, M. A., Cowan, J. D., and Chow, C. C. (2010) *Neural Comput* **22(2)**, 377–426.

[203] Ross, S. M. (2010) Introduction to probability models, Academic Press, Amsterdam 10th ed edition.

[204] Lisman, J. E. and Idiart, M. A. (1995) *Science* **267(5203)**, 1512–5.

[205] Penttonen, M., Kamondi, A., Acsády, L., and Buzsáki, G. (1998) *Eur J Neurosci* **10(2)**, 718–28.

[206] Düzel, E., Penny, W. D., and Burgess, N. (2010) *Curr Opin Neurobiol* **20(2)**, 143–9.

[207] Wulff, P., Ponomarenko, A. A., Bartos, M., Korotkova, T. M., Fuchs, E. C., Bähner, F., Both, M., Tort, A. B. L., Kopell, N. J., Wisden, W., and Monyer, H. (2009) *Proc Natl Acad Sci U S A* **106(9)**, 3561–6.

[208] Neymotin, S. A., Lazarewicz, M. T., Sherif, M., Contreras, D., Finkel, L. H., and Lytton, W. W. (2011) *J Neurosci* **31(32)**, 11733–43.

[209] Priesemann, V., Munk, M. H. J., and Wibral, M. (2009) *BMC Neurosci* **10**, 40.

[210] Keeling, M. J. and Rohani, P. (2008) Modeling infectious diseases in humans and animals, Princeton University Press, Princeton.

[211] Hellwig, B. (2000) *Biol Cybern* **82(2)**, 111–21.

[212] Larremore, D. B., Shew, W. L., and Restrepo, J. G. (2011) *Phys Rev Lett* **106(5)**, 058101.

[213] Larremore, D. B., Shew, W. L., Ott, E., and Restrepo, J. G. (2011) *Chaos* **21(2)**, 025117.

[214] Serrano, M. A. and Boguñá, M. (2006) *Phys Rev Lett* **97(8)**, 088701.

[215] Barabasi and Albert (1999) *Science* **286(5439)**, 509–12.

[216] Watts, D. J. and Strogatz, S. H. (1998) *Nature* **393(6684)**, 440–2.

[217] Gross, T. and Blasius, B. (2008) *J R Soc Interface* **5(20)**, 259–71.

[218] Gross, T., D'Lima, C. J. D., and Blasius, B. (2006) *Phys Rev Lett* **96(20)**, 208701.

[219] Meisel, C. and Gross, T. (2009) *Physical Review E* **80(6)**, 061917.

[220] Schmidt, J. T. and Eisele, L. E. (1985) *Neuroscience* **14(2)**, 535–46.

[221] Weliky, M. and Katz, L. C. (1997) *Nature* **386(6626)**, 680–5.

[222] Goodhill, G. J., Gu, M., and Urbach, J. S. (2004) *Neural Comput* **16(11)**, 2221–43.

[223] Goodhill, G. J. and Xu, J. (2005) *Network* **16(1)**, 5–34.

[224] Kiddie, G., McLean, D., Van Ooyen, A., and Graham, B. (2005) *Prog Brain Res* **147**, 67–80.

[225] Van Pelt, J., Dityatev, A. E., and Uylings, H. B. (1997) *J Comp Neurol* **387(3)**, 325–40.

[226] Van Ooyen, A. (2003) Modeling neural development, MIT Press, Cambridge, Mass.

[227] Van Ooyen, A. and Van Pelt, J. (1994) *J Theor Biol.* **167**, 27–43.

[228] Abbott, L. F. and Rohrkemper, R. (2007) *Prog Brain Res* **165**, 13–9.

[229] Bassett, D. S. and Bullmore, E. (2006) *Neuroscientist* **12(6)**, 512–23.

[230] Bassett, D. S., Meyer-Lindenberg, A., Achard, S., Duke, T., and Bullmore, E. (2006) *Proc Natl Acad Sci U S A* **103(51)**, 19518–23.

[231] Sporns, O., Chialvo, D. R., Kaiser, M., and Hilgetag, C. C. (2004) *Trends Cogn Sci* **8(9)**, 418–25.

[232] Sporns, O., Tononi, G., and Edelman, G. M. (2000) *Cereb Cortex* **10(2)**, 127–41.

[233] Bullmore, E. and Sporns, O. (2012) *Nat Rev Neurosci* **13(5)**, 336–49.

[234] Erdős, P. and Rényi, A. (1959) *Publicationes Mathematicae* **6**, 290–297.

[235] Costa, L. D. F., Rodrigues, F. A., Travieso, G., and Boas, P. R. V. (2007) *Advances In Physics* **56(1)**, 167–242.

[236] Rubinov, M. and Sporns, O. (2010) *Neuroimage* **52(3)**, 1059–69.

[237] Hebb, D. O. (1949) The organization of behavior: a neuropsychological theory, A Wiley book in clinical psychologyWiley, New York.

[238] Abbott, L. F. and Nelson, S. B. (2000) *Nat Neurosci* **3 Suppl**, 1178–83.

[239] Sjöström, P. J., Rancz, E. A., Roth, A., and Häusser, M. (2008) *Physiol Rev* **88(2)**, 769–840.

[240] Zhang, L. I., Tao, H. W., Holt, C. E., Harris, W. A., and Poo, M. (1998) *Nature* **395(6697)**, 37–44.

[241] Zhang, L. I. and Poo, M. M. (2001) *Nat Neurosci* **4 Suppl**, 1207–14.

[242] Cramer, K. S. and Sur, M. (1995) *Curr Opin Neurobiol* **5(1)**, 106–11.

[243] Song, S., Miller, K. D., and Abbott, L. F. (2000) *Nat Neurosci* **3(9)**, 919–26.

[244] Turrigiano, G. (2011) *Annu Rev Neurosci* **34**, 89–103.

[245] Pitman, R. M. (1984) *J Exp Biol* **112**, 199–224.

[246] Liu, Y. H. and Wang, X. J. (2001) *J Comput Neurosci* **10(1)**, 25–45.

[247] van denHeuvel, M. P. and Sporns, O. (2011) *J Neurosci* **31(44)**, 15775–86.

[248] Fransson, P., Skiöld, B., Horsch, S., Nordell, A., Blennow, M., Lagercrantz, H., and Aden, U. (2007) *Proc Natl Acad Sci U S A* **104(39)**, 15531–6.

[249] Sporns, O. (2011) *Front Comput Neurosci* **5**, 5.

[250] Terry, J. R., Benjamin, O., and Richardson, M. P. (2012) *Epilepsia* **53(9)**, e166–9.

[251] Kashtan, N. and Alon, U. (2005) *Proc Natl Acad Sci U S A* **102(39)**, 13773–8.

[252] Beggs, J. M. and Timme, N. (2012) *Front Physiol* **3**, 163.

[253] Stickgold, R. (2005) *Nature* **437(7063)**, 1272–8.

[254] Soubasi, V., Mitsakis, K., Sarafidis, K., Griva, M., Nakas, C. T., and Drossou, V. (2012) *Eur J Paediatr Neurol*.

[255] Berthouze, L. and Farmer, S. F. (2012) *J Neurosci Methods* **209(1)**, 178–88.

[256] Pike, A. A., Marlow, N., and Reber, C. (1999) *Early Hum Dev* **54(3)**, 215–22.

[257] Suppiej, A., Mento, G., Zanardo, V., Franzoi, M., Battistella, P. A., Ermani, M., and Bisiacchi, P. S. (2010) *Early Hum Dev* **86(12)**, 807–12.

[258] Little, M. A., McSharry, P. E., Roberts, S. J., Costello, D. A. E., and Moroz, I. M. (2007) *Biomed Eng Online* **6**, 23.

[259] Little, M. A. Last checked: 21/08/2012. http://www.maxlittle.net/software/index.php.